STATE OF CALIFORNIA • DEPARTMENT OF TRANSPORTATION

# TECHNICAL REPORT DOCUMENTATION PAGE

TR0003 (REV 10/98)

**ADA Notice**

For individuals with sensory disabilities, this document is available in alternate formats. For information call (916) 654-6410 or TDD (916) 654-3880 or write Records and Forms Management, 1120 N Street, MS-89, Sacramento, CA 95814.

| 1. REPORT NUMBER | 2. GOVERNMENT ASSOCIATION NUMBER | 3. RECIPIENT'S CATALOG NUMBER |
|---|---|---|
| CA14-2414 | | |

**4. TITLE AND SUBTITLE**

Evaluation of the Efficacy of Some Promising Algorithms for Damage Detection, Location, and Quantification in Seismic Response Modification Devices and Flexible Bridges

**5. REPORT DATE**

11/11/2013

**6. PERFORMING ORGANIZATION CODE**

**7. AUTHOR**

A. Derkevorkian, S. F. Masri, G. Benzoni, G. Lomiento, and N. Bonessio

**8. PERFORMING ORGANIZATION REPORT NO.**

**9. PERFORMING ORGANIZATION NAME AND ADDRESS**

University of Southern California
METRANS
650 Childs Way
Los Angeles, CA 90089-0193

**10. WORK UNIT NUMBER**

**11. CONTRACT OR GRANT NUMBER**

65A0213

**12. SPONSORING AGENCY AND ADDRESS**

California Department of Transportation
Division of Research, Innovation and System Information (MS-83)
P. O. Box 942873
Sacramento, CA 94273-0001

**13. TYPE OF REPORT AND PERIOD COVERED**

Final Report
7/1/2005-9/30/2013

**14. SPONSORING AGENCY CODE**

**15. SUPPLEMENTARY NOTES**

**16. ABSTRACT**

Structural health monitoring of large multi-span flexible bridges is particularly important because of their important role in civil infrastructure and transportation systems. In this study, the response of the Yokohama Bay Bridge (YBB), a three-span cable-stayed bridge, to the 2011 Great East Japan earthquake is used to perform multi-input-multi-output (MIMO) system identification studies. The extensive multi-component measurements are also used to develop and validate data driven nonlinear mathematical models that can predict the response of YBB to various earthquake records and can accurately estimate its damping characteristics when the system is driven into the nonlinear response range. A combination of least-square (parametric) and neural network (nonparametric) approaches are used to develop the mathematical models, along with time-marching techniques for dynamic response calculations. It is shown that the nonlinear mathematical models perform better than the equivalent linear models, both for response prediction and damping estimation. The importance of having an accurate approach for quantifying the damping due to the variety of nonlinear features in the YBB response is shown. This study demonstrates the significance of constructing robust mathematical models that can capture the correct physics of the underlying system, and that can be used for computational purposes to augment experimental studies. Given the lack of suitable data sets for full-scale structures under extreme loads, the availability of the long-duration measurements from the 2011 Great East Japan earthquake and its many strong aftershocks provides an excellent opportunity to perform the analyses presented in this study.

| 17. KEY WORDS | 18. DISTRIBUTION STATEMENT |
|---|---|
| large multi-span flexible bridges, Yokohama Bay Bridge (YBB), 2011 Great East Japan earthquake, multi-input-multi-output (MIMO), least-square (parametric), and neural network (nonparametric). | No Restrictions. This document is available through the National Technical Information Service, Springfield, VA 22161 |

| 19. SECURITY CLASSIFICATION *(of this report)* | 20. NUMBER OF PAGES | 21. COST OF REPORT CHARGED |
|---|---|---|
| Unclassified | 175 | |

## DISCLAIMER STATEMENT

This document is disseminated in the interest of information exchange. The contents of this report reflect the views of the authors who are responsible for the facts and accuracy of the data presented herein. The contents do not necessarily reflect the official views or policies of the State of California or the Federal Highway Administration. This publication does not constitute a standard, specification or regulation. This report does not constitute an endorsement by the Department of any product described herein.

For individuals with sensory disabilities, this document is available in Braille, large print, audiocassette, or compact disk. To obtain a copy of this document in one of these alternate formats, please contact: the Division of Research and Innovation, MS-83, California Department of Transportation, P.O. Box 942873, Sacramento, CA 94273-0001.

# Evaluation of the Efficacy of Some Promising Algorithms for Damage Detection, Location, and Quantification in Seismic Response Modification Devices and Flexible Bridges

by

A. Derkevorkian, S. F. Masri
Astani Department of Civil and Environmental Engineering
University of Southern California

and

G. Benzoni, G. Lomiento, and N. Bonessio
Department of Structural Engineering
University of California San Diego

Final Report

11 November 2013

11 November 2013 10:04
CaltransFinalReport˙2013˙november˙11a

# Contents

# List of Figures

# List of Tables

# Chapter 1

# USC FINAL REPORT

## 1.1 INTRODUCTION

### 1.1.1 Research Summary

As part of the collaboration with Prof. Yozo Fujino of University of Tokyo, a manuscript was submitted to the Journal of *Earthquake Engineering and Structural Dynamics*. Further discussion was incorporated in the manuscript as a result of the analysis performed on a series of small earthquake measurements received from Prof. Fujino, confirming the accuracy of the ambient vibration results reported in the paper. Extensive literature review was performed and the latest relevant publications were identified and referenced in the manuscript. The manuscript is titled *"Development and Validation of Nonlinear Computational Models of Dispersed Structures Under Strong Earthquake Excitation"*, and reports the important contributions of this research relevant to developing the nonlinear mathematical models as well as the proposed framework to estimate the nonlinear damping characteristics of the Yokohama Bay bridge. The abstract of the paper is as follows:

"Structural health monitoring of large multi-span flexible bridges is particularly important because of their important role in civil infrastructure and transportation systems. In this study, the response of the Yokohama Bay Bridge (YBB), a three-span cable-stayed bridge, to the 2011 Great East Japan earthquake is used to perform multi-input-multi-output (MIMO) system identification studies. The extensive multi-component measurements are also used to develop and validate data-driven nonlinear mathematical models that can predict the response of YBB to various earthquake records and can accurately estimate its damping characteristics when the system is driven into the

nonlinear response range. A combination of least-square (parametric) and neural network (non-parametric) approaches are used to develop the mathematical models, along with time-marching techniques for dynamic response calculations. It is shown that the nonlinear mathematical models perform better than the equivalent linear models, both for response prediction and damping estimation. The importance of having an accurate approach for quantifying the damping due to the variety of nonlinear features in the YBB response is shown. This study demonstrates the significance of constructing robust mathematical models that can capture the correct physics of the underlying system, and that can be used for computational purposes to augment experimental studies. Given the lack of suitable data sets for full-scale structures under extreme loads, the availability of the long-duration measurements from the 2011 Great East Japan earthquake and its many strong aftershocks provides an excellent opportunity to perform the analyses presented in this study."

The paper was submitted to the journal after receiving approval from the Tokyo Metropolitan Express Highway Corporation who provided the data used in the analyses. Furthermore, the contributions of Caltrans and Dr. Charles Sikorsky are acknowledged in the paper. The paper was accepted for publication after performing minor changes suggested by the reviewers.

We have also collaborated with Prof. Gianmario Benzoni of UCSD on planning of tests at UCSD to provide data to USC to evaluate damage detection algorithms in conjunction with Caltrans Structural Response Modification Devices (SRMD). Furthermore, some of the damage detection algorithms (i.e., neural networks, Chebyshev Polynomials, SubSpace Method, etc.) have been further tested and tuned using synthetic data, in preparation to be used on the experimental data from UCSD.

### 1.1.2 Background

Structural health monitoring and system identification of multi-span bridges is particularly important because of the vital role they play in civil infrastructure systems. System identification of a complex multi-input-multi-output (MIMO) system during strong earthquakes allows the identification of dominant dynamic features of the system from structural measurements. The development of data-driven reduced-order mathematical models of such systems is important for several control and health monitoring applications. Furthermore, constructing robust mathematical models that capture the correct physics of the underlying system are important for computational purposes to augment experimental studies. While there have been several studies in developing reduced-order linear mathematical models, not much work has been performed in developing nonlinear reduced-order mathematical models based on vibration measurement analysis of multi-span bridges. Many studies use ambient vibration data to perform system identification of various structural systems.

One of the advantages of ambient measurements is that they can be recorded for a long time (hours or even days), resulting in a very accurate equivalent linear estimates of the system parameters. On the other hand, one disadvantage of earthquake records is their duration, which is usually relatively short ($20 - 30$ seconds). As a result, there is a lack of suitable data sets for full-scale structures under extreme loads, that are crucial for the proper characterization of nonlinear behavior of such structures.

Several works have been performed in the identification of bridges. [1] performed system identification of the Vincent Thomas suspension bridge using earthquake records, [2] studied the observed dynamic performance of the Yokohama Bay bridge from system identification using seismic records, [3] studied the dynamic characteristics of a curved cable-stayed bridge identified from strong motion records, [4] applied system identification techniques to long-span cable-supported bridges using seismic records, [5] analyzed the characteristics of suspension bridge using ambient vibration response, [6] studied the dynamic characteristics of an overpass bridge in a full-scale destructive test, [7] investigated the continuous dynamic monitoring of a lively footbridge for serviceability assessment and damage detection. [8, 9] performed the response analysis of Yokohama Bay Bridge after the 2011 Great East Japan Earthquake. Other relevant works include [10, 11], [12], [13], [14], [15], amongst others. There is a small number of publications that treat the response of such nonlinear distributed-parameter systems as multi-input-multi-output. [1] incorporated the MIMO approach in the analysis of the Vincent Thomas bridge. The lack of such studies is not only due to the complexity of the analysis when adopting the approach, but also due to lack of the necessary sensor resolution on most of the bridges (not enough sensors) to perform such analysis. Another important dynamic feature of a multi-span cable-stayed bridge is its damping characteristics. An accurate damping ratio estimate is particularly important from the design standpoint, as such an estimate cannot be easily obtained from engineering drawings. While equivalent linear models can provide relatively accurate estimates of the damping ratio when modeled using ambient vibration data, it may not accurately reflect the inherent damping encountered during strong earthquakes.

### 1.1.3 Motivation

This study analyzes the response of a relatively large (three-span) cable-stayed bridge, Yokohama Bay bridge, to the 2011 Tohoku earthquake (the Great East Japan earthquake). A total of 10 datasets (1 main shock, and 9 strong aftershocks) are used in the analysis. Response from 66 channels located at various parts of the bridge is analyzed. System identification is preformed using well-known state-of-the-art methodologies. A unique aspect of this study is the availability of relatively long strong earthquake records (the main shock is 600 seconds), which significantly

helps to improve the accuracy of the vibration-signature based analysis and thus obtain an accurate nonlinear model of the system. Another important feature of the study is the availability of extensive multi-component measurements from a relatively dense sensor array (66 channels) that allows a meaningful analysis of the system. The available measurements are used to develop a reduced-order nonlinear mathematical model of the bridge. The mathematical model is used to predict important system dynamic characteristics such as natural frequency, damping ratio, and is also used to predict the response of the system to other earthquake records. The robustness of the proposed model is assessed by comparing it to an equivalent linear mathematical model, as well as by comparing the obtained system characteristics to results from previous analyses from ambient monitoring of the Yokohama Bay Bridge. Given the lack of recorded response of large flexible bridges driven into nonlinear response range, this study provides an excellent opportunity to assess the viability of the developed MIMO nonlinear mathematical models in accurately characterizing the Yokohama Bay Bridge.

### 1.1.4 Scope

With the preceding in mind, Section 2 describes the Yokohama Bay Bridge (YBB) including its general characteristics, the sensor network, and the dynamic characteristics based on ambient measurements. Section 3 describes the 2011 East Japan Earthquake including the earthquake response of the Yokohama Bay Bridge and an overview of the earthquake response data sets. In Section 4, system identification studies are presented. The identification methods are discussed and the results based on equivalent-linear systems are reported. Also, the nonlinearities in the YBB response are detected and quantified. Section 5 presents the development of the reduced-order nonlinear mathematical models. Architecture of neural networks used to identify the nonlinear forces are discussed, as well as the training results from the neural networks. In Section 6, validation of the reduced-order nonlinear mathematical models is performed. Sections 7 and 8 are discussion and conclusions, respectively.

## 1.2 YOKOHAMA BAY BRIDGE (YBB)

### 1.2.1 Characteristics

The Yokohama Bay Bridge was completed in 1988 and is located at the entrance of Yokohama Harbor, see Fig. 1.1(a). The left subfigure in Fig. 1.1(b) shows the map of Japan and the locations of Yokohama Bay Bridge (denoted as A) and the epicenter of the 2011 East Japan Earthquake

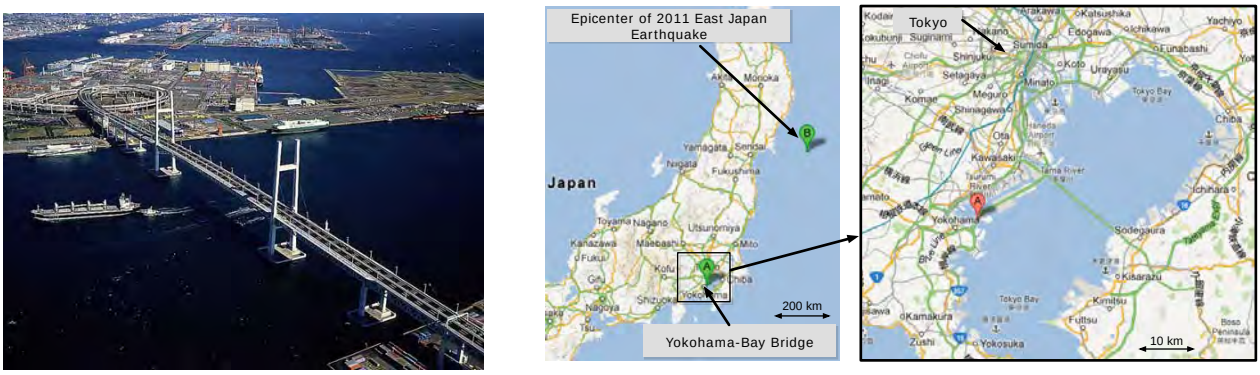


(a) View of YBB.

(b) Location of YBB.

Figure 1.1: View and the location of the Yokohama Bay Bridge (Source: Google).

(denoted as B). The right subfigure in Fig. 1.1(b) shows a zoomed version of the map where YBB is denoted as A. The bridge is at a distance of about 42 km south of Tokyo and is a crucial part the Yokohama-Tokyo bay-shore expressway. It is a continuous three-span cable-stayed bridge. The main girder consists of a double-deck steel truss-box. The mid-span is 460 m and each side-span is 200 m. The bridge has two H-shaped towers of 172 m height and 29.25 m width. The upper deck has 6 lanes and is part of the Yokohama expressway bay-shore Route, while the lower deck has 2 lanes and is part of the National Route.

### 1.2.2 Sensor Network

There are 85 acceleration sensors (66 of which are available and used for the analysis in this study) installed at 36 locations throughout the bridge. The sensors on the middle girder are located at a spacing of 115 m. Figure 1.2 shows the location of the sensors installed on the Yokohama Bridge. The measurements are in X (longitudinal), Y (lateral), and Z (vertical) directions. Each sensor has a frequency measurement range from 0.05 to 35 Hz, and an accuracy of $15 \times 10^{-3}$ amp/cm/$s^2$. The sampling frequency of the records used in this study is 100 Hz. As seen from Fig. 1.2, sensors are attached on the piles of the bridge which makes it a great opportunity to assess multi-input modeling approaches. On the other hand, it is seen that there is lack of sensors on the bridge cables.

### 1.2.3 Natural Frequencies Based on Ambient Measurements

The natural frequencies of the bridge corresponding to the first few modes were identified from ambient measurements. The results were published by the Metropolitan Expressway Public Corpo-

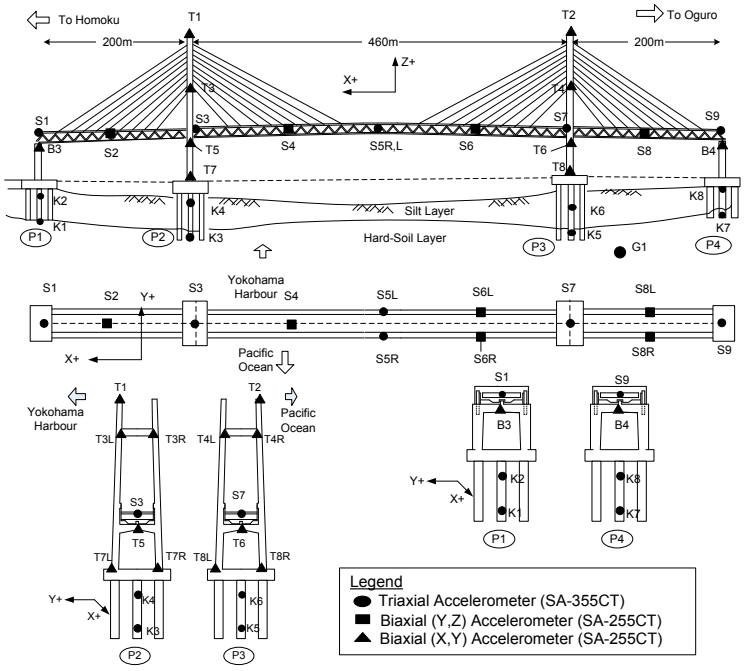


Figure 1.2: Sensor map on Yokohama Brige.

ration in 1991, and were later reported and compared to finite-element-analysis (FEA) results by [2]. The results are summarized in Table 1.1. As seen in the table, the frequencies are identified using sensors in the lateral and vertical directions only. There is a good match between the FEA and the ambient measurements results. The fundamental frequency corresponding to the $1^{st}$ symmetric bending was identified to be 0.27 Hz.

## 1.3 GREAT EAST JAPAN 2011 EARTHQUAKE

### 1.3.1 Overview

On March 11, 2011, at 14:46 Japan Standard Time (JST), NorthEastern Japan was struck by the Great East Japan Earthquake with a moment magnitude of 9.0. It was the most powerful earthquake to have hit Japan, and the fifth most powerful earthquake in the world since the modern recording began in early 1900s.

Table 1.1: Identified natural frequencies from ambient measurements and FEA.

| Mode | Frequency (Hz) | |
|---|---|---|
| Lateral-Vertical | Ambient | FEA |
| $1^{st}$ symmetric bending (tower-girder same phase) | 0.27 | 0.28 |
| $1^{st}$ asymmetric bending (tower anti phase) | 0.38 | 0.42 |
| $1^{st}$ asymmetric bending (tower-girder anti phase) | 0.68 | 0.70 |
| $2^{nd}$ symmetric bending | n/a | 1.08 |

### 1.3.2 Earthquake Response of Yokohama Bay Bridge

Yokohama Bay Bridge is the second longest-span cable-stayed bridge in the Eastern part of Japan. Japan Meteorological Agency (JMA) seismic intensity of more than 5 (out of maximum scale of 7) was recorded at the bridge location during the 2011 Great East Japan Earthquake. The epicenter of the earthquake was about 398 km away from the bridge (see Fig. 1.1(b)), with focal depth of 24 km. The response from the bridge superstructure was represented by large vibration in the transverse direction. The maximum girder displacement and acceleration were recorded in the transverse direction at the center of the mid-span of the girder (see sensor S5 in Fig. 1.2). The values of the maximum displacement and the maximum acceleration were 60 $cm$ and 299.2 $cm/s^2$, respectively. The maximum transverse displacement in the towers was 54.6 $cm$ (at location T1) and the maximum transverse acceleration was 656.9 $cm/s^2$ (at location T2). See Fig. 1.2 for the location of the sensors.

### 1.3.3 Earthquake Response Data Sets

There are a total of 10 data sets available for the analyses in this study. Table 1.2 presents a brief description of each available data set. As seen, there is 1 main shock and 9 aftershocks. It should be noted that the length of the response data corresponding to the main shock is 600 $sec$. Furthermore, looking at the intensity of the aftershocks, it is seen that some of the aftershocks are strong earthquakes in their own right.

Figure 1.3 shows sample records in the transverse (Y) direction with the corresponding Fast-Fourier-Transform (FFT) plots. The sensors used in the figure are sensor G1 (located in the ground - free field measurement) and sensor S5R (located) at the center of the mid-span of the bridge-deck

Table 1.2: List of the earthquake records.

| Earthquake ID | Mw | JMA | Description | Data Length (sec) | Max Input Acc ($cm/s^2$) |
|---|---|---|---|---|---|
| EQ1 | 9.0 | 5 | Main shock | 600 | 83.32 |
| EQ2 | 7.7 | 4 | Aftershock 1 | 480 | 35.27 |
| EQ3 | 7.5 | 3 | Aftershock 2 | 240 | 6.06 |
| EQ4 | 6.5 | 2 | Aftershock 3 | 60 | 3.84 |
| EQ5 | 6.1 | 3 | Aftershock 4 | 150 | 7.16 |
| EQ6 | 6.7 | 3 | Aftershock 5 | 120 | 3.11 |
| EQ7 | 6.4 | 3 | Aftershock 6 | 120 | 3.82 |
| EQ8 | 6.2 | 4 | Aftershock 7 | 60 | 5.31 |
| EQ9 | 6.4 | 4 | Aftershock 8 | 120 | 15.65 |
| EQ10 | 6.1 | 3 | Aftershock 9 | 120 | 5.62 |

(girder). The strength of the main shock (EQ1) and its length can be seen in Fig. 1.3. As mentioned earlier, the response of the girder in the lateral (transverse) direction at the center of the mid-span is just below 300 $cm/s^2$.

## 1.4 SYSTEM IDENTIFICATION STUDIES

### 1.4.1 Overview of Some System Identification Methods

Three state-of-the-art system identification techniques are used to identify the modal parameters of the bridge. The methods are: (1) MNExT-ERA, (2) SRIM, and (3) LSID. It should be noted that these methods are developed based on linear system theory and the parameters obtained from them represent an equivalent-linear system. Given the linearity assumption, only linear viscous damping is considered in the damping estimations. Any other source of inherent energy dissipation mechanism such as, cables, friction, and connections, is modeled as part of the equivalent-linear damping. As a result, the modal parameters obtained from these techniques are associated with both estimation and modeling errors.

A brief summary of each method is provided in this section. The measured acceleration data was sampled at 100 Hz with a corresponding Nyquist frequency of 50 Hz. The frequencies of interest in this study are much less than 35 Hz, therefore the measured acceleration data was band-pass filtered between 0.05 and 30 Hz. The results presented in the next section are obtained using the main shock (EQ1) dataset.

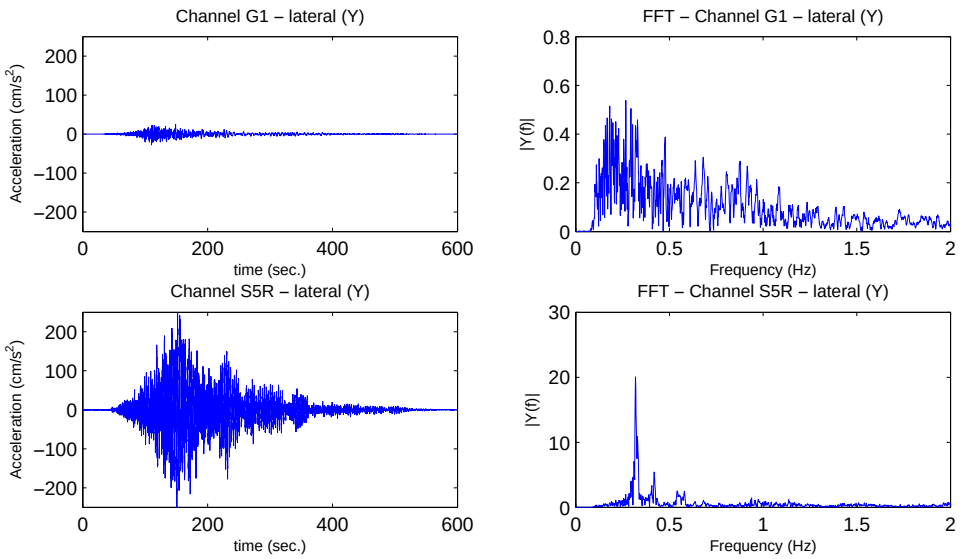


Figure 1.3: Sample time histories and corresponding FFT plots corresponding to EQ1.

### Multiple-Reference Natural Excitation Technique Combined with Eigensystem Realization Algorithm (MNExT-ERA)

The natural excitation technique is based on obtaining the cross-correlation function between the acceleration responses of two degrees of freedoms in the structure that is subjected to a broad-band excitation. The obtained cross-correlation function has the same analytical form as the free-vibration of the structure [16]. The Eigensystem Realization Algorithm (ERA) can then be used to extract the modal parameters from the cross-correlation function [17]. While in the case of building-like structures it is much easier to choose a single reference degree-of-freedom to calculate the cross-correlation functions, it is much more challenging in bridges to choose a single reference DOF that assures the identification of all the dominant modes. Therefore, multiple references (vector of references) were chosen in this study [18]. Six reference channels were chosen for this study (S5R(X,Y,Z) and S6R(X,Y,Z)). Accelerations were used from 49 channels on the superstructure in all three directions (i.e., X, Y, and Z). The response cross-correlation functions were estimated by calculating the inverse Fourier transform of the corresponding cross-spectral density (CSD). CSD was estimated using Welch's averaged modified periodogram method of spectral estimation, using Hanning windows with 50% overlap.

Table 1.3: Summary of the methodologies used for system identification.

| Method | Input/Output |
|---|---|
| MNExT-ERA | Output-Only |
| SRIM | Input-Output |
| LSID | Input-Output |

**System Realization Using Information Matrix (SRIM)**

In this approach, a state-space-based realization is used to identify the system observability matrix from the information matrix consisting of input-ouput data correlation [19]. The system matrices are then identified, from which the modal parameters are estimated. It should be noted that this is an input-output method, as opposed to the NExT-ERA method which is an output-only method. In this method, acceleration response from 49 (output) channels on the superstructure were used, along with acceleration response from 9 (input) channels (i.e., K1(X,Y,Z), K2(X,Y,Z), and K3(X,Y,Z)).

**Time-Domain Least-Square Identification (LSID)**

The time-domain least-square identification approach is an input-output method that estimates the system matrices, appearing in the vector equation of motion, by reducing the estimation error in a least-square sense, see [20, 21]. Further details on the approach are presented in the upcoming sections. As in the SRIM method, 49 output channels and 9 input channels are used for the identification purposes.

The methods are briefly summarized in Table 1.3.

### 1.4.2 System Identification Results Based on Equivalent-Linear System

The results of the identification are summarized in Table 1.4. The table shows the frequencies and the damping ratios identified from the first 10 modes using the three above-listed methods. It is seen that the frequency estimates from all three methods are fairly consistent and within the same range. However, the identified damping ratios vary quite a bit from one method to another. This is mainly due to the fact that all three methods are based on linear system theory and the identified damping ratio is an equivalent viscous damping and does not take into account other major sources of energy dissipation such as materials, connections, cables, etc. Depending on the method used, the error can be due to other contributing factors as well. In the case of MNExT-ERA, one major

Table 1.4: System identification results.

| Mode | MNExT-ERA | | SRIM | | LSID | |
|---|---|---|---|---|---|---|
| | $\omega$ (Hz) | $\zeta$ % | $\omega$ (Hz) | $\zeta$ % | $\omega$ (Hz) | $\zeta$ % |
| 1 | 0.319 | 4.81 | 0.316 | 1.80 | 0.320 | 1.76 |
| 2 | 0.422 | 4.85 | 0.384 | 3.20 | 0.335 | 1.63 |
| 3 | 0.467 | 5.69 | 0.481 | 2.59 | 0.417 | 1.58 |
| 4 | 0.570 | 3.18 | 0.521 | 7.09 | 0.478 | 1.96 |
| 5 | 0.780 | 4.24 | 0.728 | 2.61 | 0.557 | 3.77 |
| 6 | 0.885 | 6.48 | 1.006 | 3.33 | 0.667 | 6.63 |
| 7 | 1.006 | 3.57 | 1.141 | 2.89 | 0.755 | 5.49 |
| 8 | 1.117 | 1.89 | 1.254 | 1.85 | 0.827 | 2.63 |
| 9 | 1.336 | 5.64 | 1.615 | 3.55 | 0.931 | 1.81 |
| 10 | 1.759 | 1.98 | 1.774 | 1.38 | 1.010 | 2.88 |

assumption is that the excitation is broadband (white noise) signal. This is clearly not the case with the main shock (EQ1) dataset, therefore it is a violation of one of the assumptions in the method, and might be a contributing factor in the estimation error. Nevertheless, with all three methods, consistent frequency estimations are obtained. It should also be noted that since the analyses are performed using data in all three directions (X,Y, and Z), most of the identified modal parameters are coupled, and do not necessarily represent one distinct direction.

### 1.4.3 Detection and Quantification of Nonlinearities in Response

This least-square time-domain system identification (LSID) approach depends on two stages. The first stage is the identification of the reduced-order equivalent-linear model. During the second stage, instead of treating the unmodeled response as an error, it is assumed to be the non-linear dynamics yet to be modeled. The equation of motion can be written as follows:

$$\mathbf{M_{11}^{-1}C_{11}\dot{x}_1}(t) + \mathbf{M_{11}^{-1}K_{11}x_1}(t) + \mathbf{M_{11}^{-1}M_{10}\ddot{x}_0}(t) + \mathbf{M_{11}^{-1}C_{10}\dot{x}_0}(t) + \mathbf{M_{11}^{-1}K_{10}x_0}(t) = -\mathbf{I\ddot{x}_1}(t) \quad (1.1)$$

where $\mathbf{x_1}(t) = [x_{11}(t), ..., x_{1n_1}(t)]^T$, $\dot{\mathbf{x}}_\mathbf{1}(t) = [\dot{x}_{11}(t), ..., \dot{x}_{1n_1}(t)]^T$, and $\ddot{\mathbf{x}}_\mathbf{1}(t) = [\ddot{x}_{11}(t), ..., \ddot{x}_{1n_1}(t)]^T$ represent the measured displacement, velocity, and acceleration, respectively. While, $\mathbf{x_0}(t) = [x_{01}(t), ..., x_{0n_0}(t)]^T$, $\dot{\mathbf{x}}_\mathbf{1}(t) = [\dot{x}_{11}(t), ..., \dot{x}_{1n_1}(t)]^T$, and $\ddot{\mathbf{x}}_\mathbf{1}(t) = [\ddot{x}_{11}(t), ..., \ddot{x}_{1n_1}(t)]^T$ represent the measured base (ground) displacement, velocity, and acceleration, respectively. The symbol $n_1$ represents the number of degrees-of-freedom of the system and the symbol $n_0$ represents the number of base excitations. The matrices $\mathbf{M_{11}}$,$\mathbf{C_{11}}$, and $\mathbf{K_{11}}$ are the discretized system matrices corresponding

Table 1.5: The abbreviated notation for the identified system matrices.

| Matrix Product | $\mathbf{M_{11}^{-1}C_{11}}$ | $\mathbf{M_{11}^{-1}K_{11}}$ | $\mathbf{M_{11}^{-1}M_{10}}$ | $\mathbf{M_{11}^{-1}C_{10}}$ | $\mathbf{M_{11}^{-1}K_{10}}$ |
|---|---|---|---|---|---|
| Abbreviation | $\mathbf{^2A}$ | $\mathbf{^3A}$ | $\mathbf{^4A}$ | $\mathbf{^5A}$ | $\mathbf{^6A}$ |
| Dimension | $n_1 \times n_1$ | $n_1 \times n_1$ | $n_1 \times n_0$ | $n_1 \times n_0$ | $n_1 \times n_0$ |

to the mass, damping and the stiffness matrices. The system matrices can be represented using a abbreviated notation as in Table 1.5:

Applying Eq. 1.1 to discrete time-steps, $t = [t_1, ..., t_N]$, where $N$ is the time step index, yields parallel matrix equations as follows:

$$\begin{gathered}\mathbf{M_{11}^{-1}C_{11}\dot{x}_1}(t_1) + \mathbf{M_{11}^{-1}K_{11}x_1}(t_1) + \mathbf{M_{11}^{-1}M_{10}\ddot{x}_0}(t_1) + \mathbf{M_{11}^{-1}C_{10}\dot{x}_0}(t_1) + \mathbf{M_{11}^{-1}K_{10}x_0}(t_1) = -\mathbf{I\ddot{x}_1}(t_1) \\ \vdots \\ \mathbf{M_{11}^{-1}C_{11}\dot{x}_1}(t_N) + \mathbf{M_{11}^{-1}K_{11}x_1}(t_N) + \mathbf{M_{11}^{-1}M_{10}\ddot{x}_0}(t_N) + \mathbf{M_{11}^{-1}C_{10}\dot{x}_0}(t_N) + \mathbf{M_{11}^{-1}K_{10}x_0}(t_N) = -\mathbf{I\ddot{x}_1}(t_N)\end{gathered} \tag{1.2}$$

The components of $^j\mathbf{A}$ matrices mentioned above (i.e., the components of the mass, damping and stiffness matrices) are unknowns and need to be identified. The above equation can be written in the following form:

$$\hat{\mathbf{R}}\hat{\boldsymbol{\alpha}} = \hat{\mathbf{b}} \tag{1.3}$$

$$\hat{\mathbf{R}} = \begin{bmatrix} \boldsymbol{R} & \mathbf{0} & \mathbf{0} & \cdots & \mathbf{0} \\ \mathbf{0} & \boldsymbol{R} & \mathbf{0} & \cdots & \mathbf{0} \\ \mathbf{0} & \mathbf{0} & \boldsymbol{R} & \mathbf{0} & \mathbf{0} \\ \vdots & \vdots & \cdots & \ddots & \vdots \\ \mathbf{0} & \mathbf{0} & \cdots & \cdots & \boldsymbol{R} \end{bmatrix} \tag{1.4}$$

$$\hat{\boldsymbol{\alpha}} = \begin{bmatrix} \boldsymbol{\alpha}_1 \boldsymbol{\alpha}_2 \cdots \boldsymbol{\alpha}_{n1} \end{bmatrix}^T \tag{1.5}$$

$$\hat{\mathbf{b}} = \begin{bmatrix} \mathbf{b}_1 \mathbf{b}_2 \cdots \mathbf{b}_{n1} \end{bmatrix}^T \tag{1.6}$$

where $\hat{\boldsymbol{\alpha}}$ contains all the unknown parameters to be identified, $\hat{\mathbf{R}}$ is equivalent to a coefficient matrix assembled from data measurements, and $\hat{\mathbf{b}}$ is the right-hand-side of Eq. 1.1. The coefficient can be calculated using $\hat{\boldsymbol{\alpha}} = \hat{\mathbf{R}}^{\dagger}\hat{\mathbf{b}}$, where $\dagger$ represents the psuedoinverse of a matrix. The identified equivalent linear system matrix coefficients can be inserted back into equation 1.3 to obtain an

estimate of the acceleration vector $\hat{\mathbf{b}}$, which can be denoted as $\mathbf{b}_{est}$. Then, the difference $(\hat{\mathbf{b}} - \mathbf{b}_{est})$ is treated as the nonlinear residual $\mathbf{F}_{nl}$ (instead of treating it as error). The residual can be modeled using several techniques. Some of these techniques include non-parametric methods such as neural networks, basis function fitting, amongst others. Neural networks are used in this study to model the nonlinear residual.

It is possible to obtain the modal properties of the structure using the identified system matrices $\mathbf{M_{11}^{-1}C_{11}}$ and $\mathbf{M_{11}^{-1}K_{11}}$. It should be noted that in practical base-excitation problems the mass matrix $\mathbf{M_{11}}$ is unknown. The modal frequencies, damping coefficients, and mode shapes can be derived by solving a classical eigenvalue problem as follows:

$$\mathbf{Az} = \lambda\mathbf{z} \tag{1.7}$$

$$\mathbf{A} = \begin{bmatrix} \mathbf{0} & \mathbf{I} \\ -\mathbf{M_{11}^{-1}K_{11}} & -\mathbf{M_{11}^{-1}C_{11}} \end{bmatrix} \tag{1.8}$$

Since the above system matrices are identified, the matrix $\mathbf{A}$ is known and has a dimension of $2n_1 \times 2n_1$. The eigenvalues $\lambda_k$ and the eigenvectors $\mathbf{z}_k$ may be complex numbers and come in complex conjugate pairs. The physical modal frequencies, $\omega_i$, and the modal damping coefficients, $\zeta_i$, are related to the obtained eigenvalues as follows:

$$\omega_i = \sqrt{\Re(\lambda_{2i-1})^2 + \Im(\lambda_{2i-1})^2} = \sqrt{\Re(\lambda_{2i})^2 + \Im(\lambda_{2i})^2}, \quad i = 1, \cdots, n_1 \tag{1.9}$$

$$\zeta_i = \frac{-\Re(\lambda_{2i-1})}{\sqrt{\Re(\lambda_{2i-1})^2 + \Im(\lambda_{2i-1})^2}} = \frac{-\Re(\lambda_{2i})}{\sqrt{\Re(\lambda_{2i})^2 + \Im(\lambda_{2i})^2}}, \quad i = 1, \cdots, n_1 \tag{1.10}$$

where $\Re(.)$ denotes the real part of a complex number and $\Im(.)$ denotes the imaginary part of a complex number.

The time-domain identification approach was implemented using data in the longitudinal, lateral, and vertical directions. A total of 58 channels were used for the analysis. A total of 49 channels from the superstructure (i.e., $n_1 = 49$), and a total of 9 channels were used from the base and the foundation of the bridge (i.e., $n_0 = 9$).

Figures 1.4(a) and 1.4(b) show the system identification results from a representative channel (S5RY). Figure 1.4(a) corresponds to the results from dataset (EQ1), and Figure 1.4(b) corresponds to dataset (EQ2). As seen in both figures, the equivalent linear estimate captures the main oscillations of the measured acceleration very well. The difference between the estimate and the measured acceleration is treated as the nonlinear residual and is plotted on the third row of each figure.

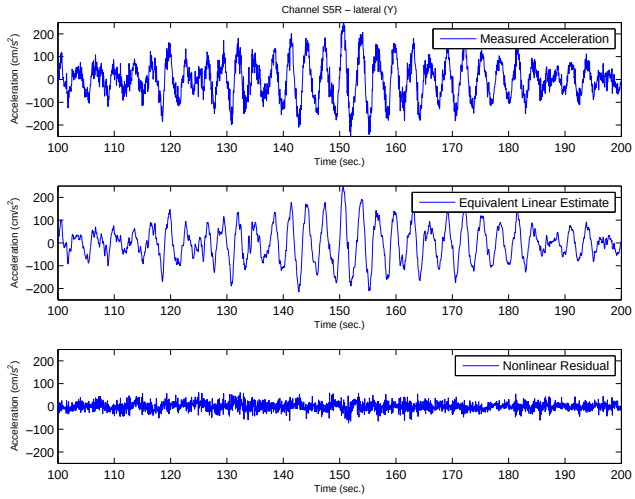


(a) The main shock (EQ1) dataset is used.

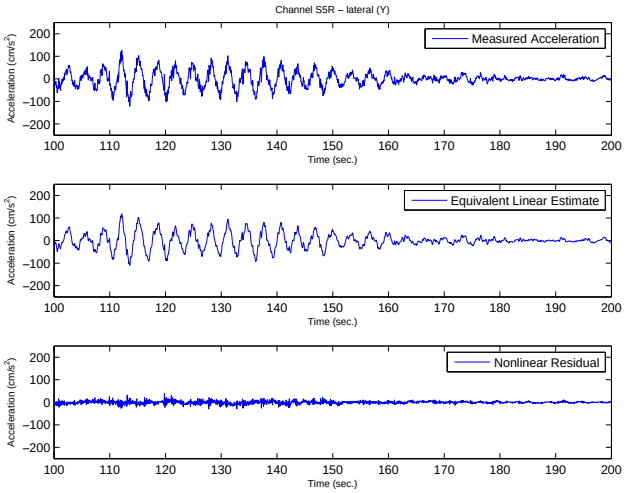


(b) The first aftershock (EQ2) dataset is used.

Figure 1.4: In the top figure, the measured channel S5R - lateral (Y) acceleration is shown. Below this is the linear model estimate using least-square method. The third figure shows the non-linear residual (i.e., the difference of the previous two signals.

Figure 1.5 shows the identified fundamental natural frequencies ($\omega$) and the corresponding damping ratios ($\zeta$) for all available datasets. The left sub-figure shows the identified natural frequencies for each dataset. It is seen that the highest fundamental natural frequency is observed during the main shock (dataset EQ1). This is not surprising, as during the main shock (the strongest ground motion), the system will undergo most of the nonlinearities which might cause increase in the stiffness (induced partly by the bridge cables) and correspondingly increase in the natural frequency. It should be noted that the intensity of the ground motion does not decrease gradually from aftershock EQ2 through EQ10. Some aftershocks are stronger than the other, the epicenter is closer to the bridge, the strong motion part of the record is longer in some records. Because of all the mentioned factors, it is difficult to observe a trend in the identified natural frequencies corresponding to aftershocks EQ2 to EQ10. However, it is seen in the left sub-figure that all the identified frequencies during the aftershocks are less than the frequency identified during the main shock, which is consistent with the expectations discussed above. Is it seen that the average natural frequency identified during the aftershocks is about 0.27 Hz, which matches the identified fundamental frequency obtained from ambient vibration tests reported in the literature, [4].

The right sub-figure in Fig. 1.5 shows the identified damping ratios from all 10 datasets. It is seen that the damping ratio corresponding to the main shock is $\zeta = 1.5\%$. Considering the extent of the inherent nonlinearities during the main shock (EQ1), the equivalent linear estimate of the damping ratio is much lower than expected. The estimates using the aftershock datasets (where the contribution of nonlinearities are less than the main shock) seem to be reasonable. In the upcoming

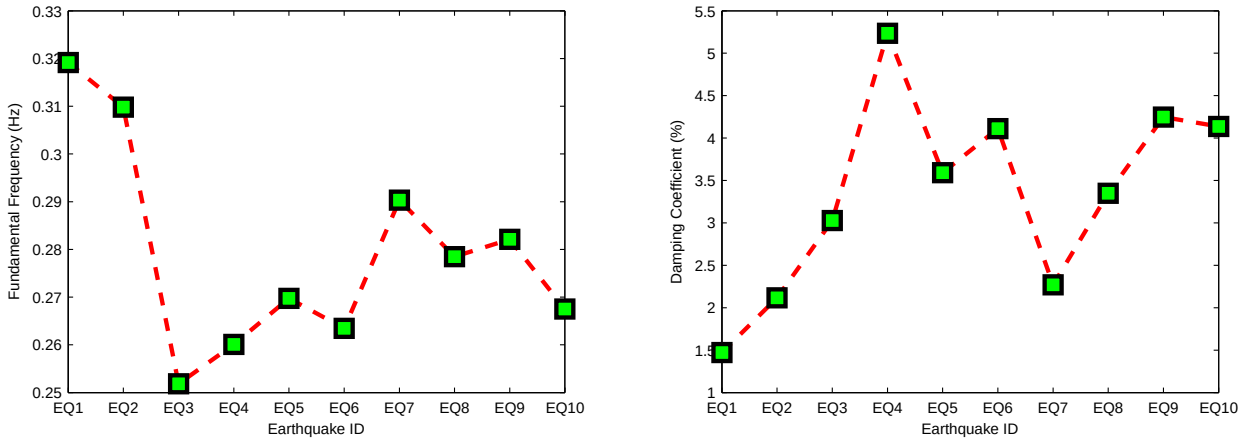


Figure 1.5: Identified fundamental natural frequencies and damping ratios from all 10 datasets.

sections, the accuracy of the obtained damping results from EQ1 will be validated using a linear computational model and the significance of including the nonlinear terms will be investigated using the nonlinear computational model.

## 1.5 DEVELOPMENT OF REDUCED-ORDER NONLINEAR COMPUTATIONAL MODELS

There is a paucity of publications dealing with measurements from large-scale real structural systems for developing data-driven reduced-order nonlinear models of complex bridge systems. In this study, such reduced-order nonlinear models were developed by using a combination of parametric and nonparametric approaches, and employing both physical and computational tools. Two models are developed and investigated in this study: an equivalent linear model and a nonlinear model. In both cases, the system matrices identified using the least-square approach are used.

### 1.5.1 Equivalent Linear Model

In the equivalent linear model, the Fourth-Order Runge-Kutta (RK4) method is used to solve the differential equation governing the motion of the bridge given by:

$$\mathbf{I}\ddot{\mathbf{x}}_{\mathbf{1}}(t) = -^{\mathbf{2}}\mathbf{A}\dot{\mathbf{x}}_{\mathbf{1}}(t) - ^{\mathbf{3}}\mathbf{A}\mathbf{x}_{\mathbf{1}}(t) - ^{\mathbf{4}}\mathbf{A}\ddot{\mathbf{x}}_{\mathbf{0}}(t) - ^{\mathbf{5}}\mathbf{A}\dot{\mathbf{x}}_{\mathbf{0}}(t) - ^{\mathbf{6}}\mathbf{A}\mathbf{x}_{\mathbf{0}}(t) \tag{1.11}$$

where the system matrices are identified using the time-domain identification approach explained earlier, the base motion $(\mathbf{x_0}(t), \dot{\mathbf{x}}_\mathbf{0}(t), \ddot{\mathbf{x}}_\mathbf{0}(t))$ are earthquake-specific measurements, and the bridge motion $(\mathbf{x_1}(t), \dot{\mathbf{x}}_\mathbf{1}(t))$ is calculated using the ordinary differential equation (ODE) solver, by providing their respective initial conditions $(\mathbf{x_1}(0), \dot{\mathbf{x}}_\mathbf{1}(0))$.

### 1.5.2 Noninear Model

In the nonlinear model, the Fourth-Order Runge-Kutta method is also used to solve the differential equation governing the bridge motion, given by:

$$\mathbf{I}\ddot{\mathbf{x}}_\mathbf{1}(t) = -^{\mathbf{2}}\mathbf{A}\dot{\mathbf{x}}_\mathbf{1}(t) - ^{\mathbf{3}}\mathbf{A}\mathbf{x}_\mathbf{1}(t) - ^{\mathbf{4}}\mathbf{A}\ddot{\mathbf{x}}_\mathbf{0}(t) - ^{\mathbf{5}}\mathbf{A}\dot{\mathbf{x}}_\mathbf{0}(t) - ^{\mathbf{6}}\mathbf{A}\mathbf{x}_\mathbf{0}(t) - \mathbf{F}_{nl}(t) \tag{1.12}$$

The additional term in the right hand side of the equation ($\mathbf{F}_{nl}(t)$) is the nonlinear residual defined as the difference between the measured acceleration and the equivalent linear estimate obtained by the least-square approach. In order for this nonlinear (new) term to be used in a time-marching module such as the Runge-Kutta, it has to be modeled in a robust way so that it is sensitive to various earthquake records. In this study, the neural network approach is used to model the nonlinear part of the response.

#### Architecture of Neural Network Used to Identify the Nonlinear Forces

A typical neural network architecture used in this study is shown in Fig. 1.6. The neural network has an input layer, one hidden layer, and an output layer. The hidden layer has 15 hidden neurons. The hidden layer has hyperbolic tangent sigmoid transfer functions, while the output layer has a linear transfer function. These neural transfer functions calculate the layers' output from their input. As seen from the figure, the weighted inputs are summed with the bias before going in the transfer function. Both the weights and the biases are initialized using a random scheme. Initially, the inputs of the neural network were chosen to be the displacements ($\mathbf{y}_k$), velocities ($\dot{\mathbf{y}}_k$), and base accelerations ($\ddot{\mathbf{s}}_k$) at time $t_k$. The outputs are the nonlinear residuals ($\hat{\mathbf{F}}nl_k$). However, given the complex dynamic system subjected to severe non-stationary excitations, delayed inputs were used to incorporate the response from the system memory (i.e., from previous time steps), hence to enhance the training of the neural network and better capture the nonlinear characteristics of the system. As a result, the nonlinear residual at delayed time step ($\hat{\mathbf{F}}nl_{k-1}$) is provided as an additional input. The components of the input and output layers can be seen in Fig. 1.6.

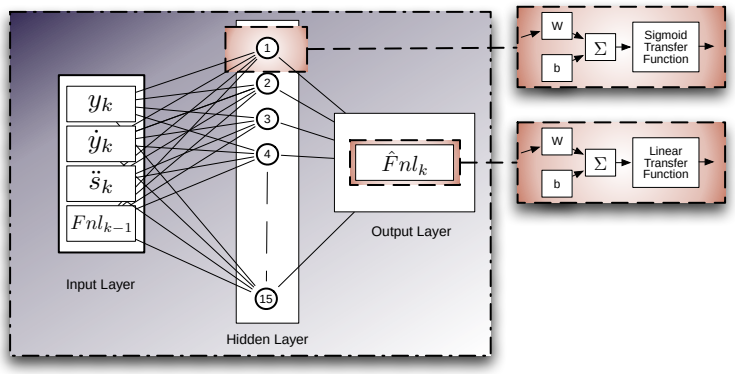


Figure 1.6: Architecture of the neural network used in this study.

**Neural Network Training**

Many training algorithms have been developed by researchers. One of the effective techniques is the adaptive random search method (ARS) proposed by [22], that promises an improved convergence rate of the minimizer of a given cost function. An improved optimization procedure based on the adaptive random search algorithm is also proposed by [23]. In some more recent works, [24] presents the Levenberg-Marquardt backpropagation algorithm and describes it as the harmonization between the Gauss-Newton method and the the steepest descent method. Furthermore, [25] studies and compares the performance of various neural network training algorithms and suggests that the Levenberg-Marquardt backpropagation algorithm provides the best results for the purposes of vibration-based damage detection in structural systems. In this study, batch mode of training was adopted using the Levenberg-Marquardt backpropagation algorithm. In the batch mode of training, the weights and the biases are updated once in each epoch, after all the inputs are presented. The mean-squared normalized error (mse) was used as the performance function during the training. Most of the trained networks satisfied the specified (mse) performance criteria within an average of 30 epochs. A sample neural network output is shown in Fig. 1.7. The first row shows the entire record of the nonlinear residual from channel S5R(Y) superposed on the corresponding neural network estimate. The second row shows the time-history of the error (i.e., the difference between the nonlinear residual and the neural network estimate). The third row depicts a 5 *sec.* segment from the plot in the first row. As seen in the figure, the neural network output and the target nonlinear residual force match very well.

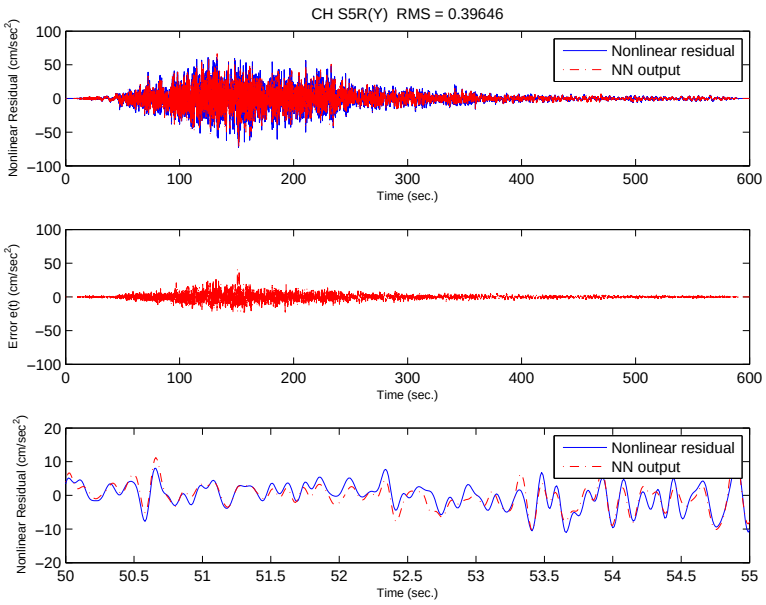


Figure 1.7: The neural network estimates of the nonlinear residual. The first row represents the entire record of the nonlinear residual from channel S5R(Y) superposed on the corresponding neural network estimate. The second row shows the error $e(t)$ plot. The third row shows a segment of 5 sec. from the same record.

## 1.6 VALIDATION OF REDUCED-ORDER NONLINEAR COMPUTATIONAL MODELS

### 1.6.1 Overview of Time-Marching Approaches for Dynamic Response Calculations

One of the most common and well-established time-marching approaches to solve ordinary differential equations (ODEs) is the fourth-order Runge-Kutta Method. In this approach, the value at the next time-step is determined based on the value at the present time-step and the weighted average of four increments, where each increment is a function of the integration step-size and the estimated slope specified by the right-hand side of the differential equation to be solved. In this study, the integration step-size was chosen to be $1/10^{th}$ of the sampling time-step. The fourth-order Runge-Kutta Method was used to solve Eq.1.11 (for the linear mathematical model) and EQ. 1.12 (for the nonlinear mathematical model).

In the case of the nonlinear mathematical model, the implementation of the procedure is particularly challenging because of the two sources of error involved in the procedure: the neural network estimation error, and the truncation error associated with the ODE solver at each time-step. As

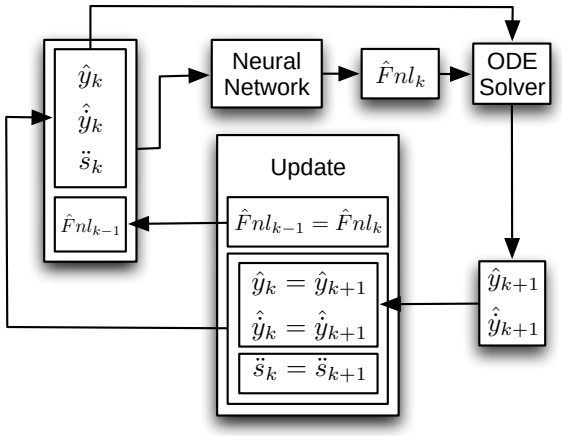


Figure 1.8: Flowchart of the developed nonlinear computational model.

mentioned earlier, the neural network performance was enhanced by providing the nonlinear residual estimate at time $k$, $(\hat{F}nl_k)$, as an additional input to the network at time $k+1$, along with $\hat{y}_{k+1}$, $\hat{\dot{y}}_{k+1}$, and $\ddot{s}_{k+1}$. While the truncation error of the ODE solver was decreased by using a relatively smaller integration step-size (i.e., $\Delta t = 0.001$). A detailed flowchart of the nonlinear computational model is shown in Fig. 1.8. As seen in Fig. 1.8, at each time-step the nonlinear force is estimated using the neural network and added to the right-hand side of Eq. 1.12 along with the velocity, displacement, and base motion, then the ODE solver is used to solve the equation and estimate the response at the next time-step.

### 1.6.2 Assessing the Accuracy of Linear vs Nonlinear Dynamic Response Calculations

In order to assess the viability of the developed linear and nonlinear computational models, testing and validation is performed using various available earthquake records. During the testing stage, the same earthquake data used in creating the models is fed back to the models, and the displacement response of the system is compared to the available measurements. During the validation stage, different earthquake data is used (i.e., ones that have not been used in modeling the equivalent-linear part or the nonlinear residual part) to see how well these computational models generalize when unknown datasets are introduced. Just like the testing stage, the displacement responses obtained from the computational models are compared to the corresponding measurements.

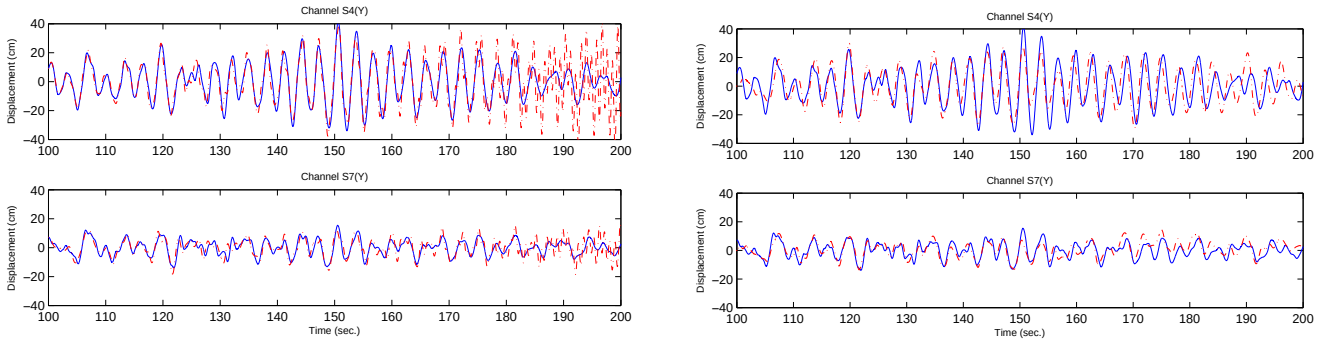


(a) Linear model.

(b) Nonlinear model.

Figure 1.9: Displacement time history estimates from the computational model (dotted line) superposed on the corresponding displacements from the measured data (solid line). The rows correspond to channels S4(Y) and S7(Y), respectively. The computational model is created using EQ1 and is tested using EQ1. A segment of 100 sec. is shown from the strong motion part of the records.

### Testing

Figures 1.9(a) and 1.9(b) show the results from the linear and the nonlinear models, respectively. Both figures show the results from two representative channels; $S4(Y)$ and $S7(Y)$, respectively. In each subfigure, 100 sec. segment of the displacement response estimate is superposed on the corresponding response from the measured data. It is seen from Fig. 1.9(a) that the results from the linear model show an excellent match with the target displacement for about 70 sec. However, after 70 seconds some instabilities are observed in both channels. Similar results were obtained from the rest of the channels as well. Figure 1.9(b) shows the results from the nonlinear model. It is seen that the estimates match the target displacements fairly well. Furthermore, as opposed to the linear model, no instabilities are observed throughout the record. Similar results were observed in the other channels.

### Validation and Generalization

Figures 1.10(a) and 1.10(b) show the validation results, where new earthquake data (unknown to the models) are fed to the computational models. The results shown are from dataset (EQ2). Similar trends are observed as in the testing stage. The estimates from the linear model are good for about 20 seconds, then instabilities are observed in most of the channels. While the results from the nonlinear model are stable throughout the entire record, and match the main oscillations of the target displacement records fairly well. Similar trends were observed when feeding other earthquake data (EQ3 through EQ10) to the computational models.

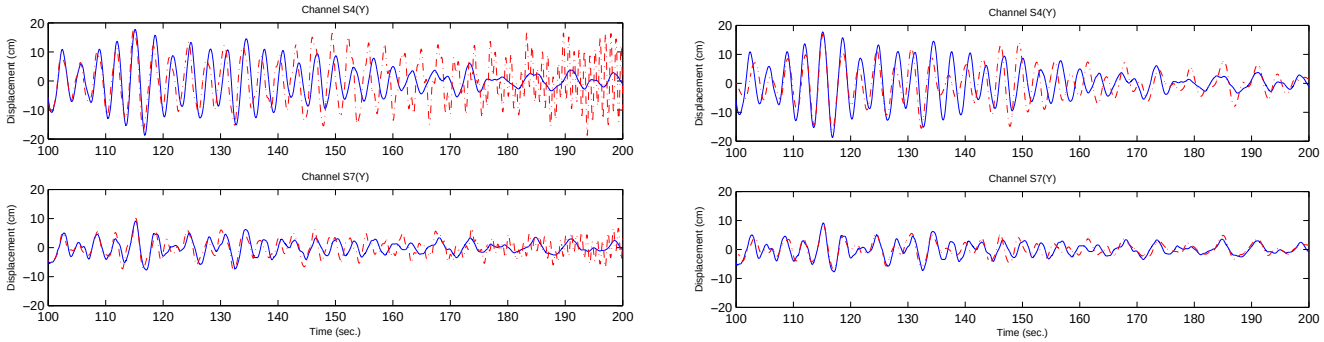


(a) Linear model. (b) Nonlinear model.

Figure 1.10: Displacement time history estimates from the computational model (dotted line) superposed on the corresponding displacements from the measured data (solid line). The rows correspond to channels S4(Y) and S7(Y), respectively. The computational model is created using EQ1 and is validated using EQ2. A segment of 100 sec. is shown from the strong motion part of the records.

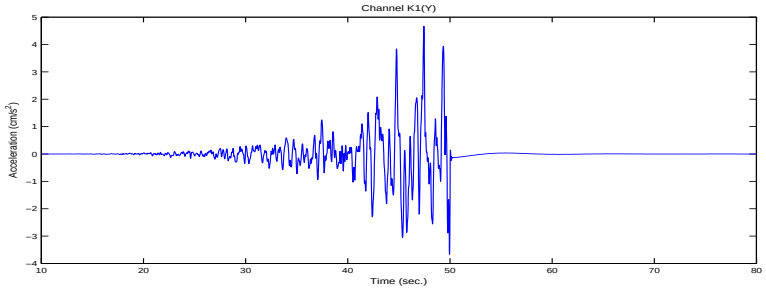


Figure 1.11: A segment of the base excitation used for the identification of the damping ratio.

### 1.6.3 Dependance of Bridge Damping Parameters on Nature of Computational Model

In order to identify the fundamental natural frequency ($\omega_1$) and the corresponding damping ratio ($\zeta_1$) using the developed linear and nonlinear computational models, new synthetic base excitations were generated. The first 50 seconds of the new records are identical to the ones recorded during the main shock (EQ1), then for the rest of the record, the excitation is artificially set to be zero. A sample excitation is shown in Fig. 1.11. Tracking the free-vibration of the superstructure during zero-excitation period (i.e., after the initial 50 seconds), one can observe the fundamental natural frequency and can compute the damping ratio using the logarithmic decrement approach using $\delta = \ln x_1/x_2$ and $\zeta = \delta/\sqrt{(2\pi)^2 + \delta^2}$, where $x_1$ and $x_2$ are two consecutive peaks in the free-vibration response, and $\zeta$ is the desired damping ratio.

The displacement response estimates from channel $S5R(Y)$ (located at the mid-span of the

bridge-deck) are shown in figures 1.12(a) and 1.12(b). Fig. 1.12(a) shows the displacement estimate from the linear model, and Fig. 1.12(b) shows the estimate from the nonlinear model. The time between two consecutive peaks ($\Delta t_i$) is calculated for four cycles during the free-vibration part of the record (i.e., after $t = 50sec.$). Then, the inverse of the average is calculated to obtain an estimate of the fundamental natural frequency $\hat{f} = 4/(\Delta t_1 + \Delta t_2 + \Delta t_3 + \Delta t_4)$. The natural frequency results obtained from the linear and the nonlinear models are consistent with each other and are $\hat{f}_{ln} = 0.328$ (Hz) and $\hat{f}_{nln} = 0.326$ (Hz), where $\hat{f}_{ln}$ represents the result from the linear model and $\hat{f}_{nln}$ represents the result from the nonlinear model. These results also match previously reported results that are calculated using different system identification techniques.

The damping ratio is calculated for four consecutive cycles, then the average is calculated. The damping ratio obtained for the linear model is $\hat{\zeta}_{ln} = 1.63\%$ and for the nonlinear model is $\hat{\zeta}_{nln} = 4.26\%$. This difference in the damping ratio between the linear and the nonlinear model can also be observed by looking at figures 1.12(a) and 1.12(b). The decay in the response from the linear model (Fig. 1.12(a)) is not clearly visible (i.e., $\hat{\zeta}_{ln} = 1.63\%$), while the decay in the response from the nonlinear model (Fig. 1.12(b)) can be seen clearly (i.e., $\hat{\zeta}_{nln} = 4.26\%$).

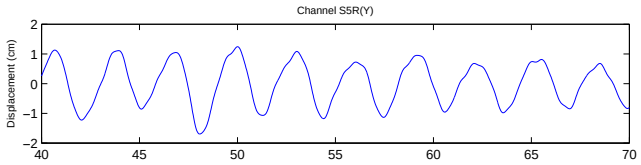


(a) Linear model.

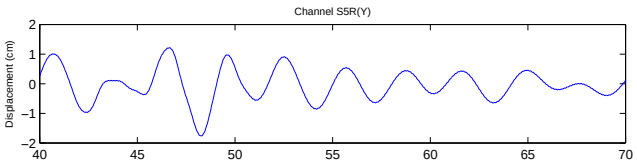


(b) Nonlinear model.

Figure 1.12: A segment of the displacement time history estimate corresponding to channel S5R(Y).

Although the results from the linear computational model agrees with the least-square identification result (i.e., $\zeta = 1.5\%$), both values only represent the equivalent linear part of the system and do not take into account the nonlinear part of the response. The addition of the nonlinear residual in the nonlinear computational model is reflected in the obtained corresponding damping ratio (i.e., $\hat{\zeta}_{nln} = 4.26\%$). Although both computational models provide an accurate estimate of the natural frequency, the nonlinear computational model is a better representative of the complex nonlinear system under investigation. When the bridge undergoes significant nonlinear forces, an equivalent linear model might not capture the full system dynamic characteristics (especially, damping ratio). The inclusion of the nonlinear residual term can provide a more accurate estimate of the damping ratio. The results further emphasize the importance of having an accurate approach for quantifying the damping due to variety of nonlinear features in the YBB response. Furthermore, the demonstrated approach is useful as a general methodology for other structures (not necessarily bridges).

## 1.7 DISCUSSION

In the first part of this study, measurements from 10 earthquakes and the corresponding 66 channels were organized in an efficient dataset to be used for various types of analyses in the context of structural health monitoring, system identification, and damage detection. During this process, the acceleration measurements were first band-pass filtered, then integrated to obtain the corresponding velocity and displacement signals.

The initial analysis involved using state-of-the-art system identification methodologies to identify the modal parameters of the system including the natural frequencies and equivalent viscous damping ratios. Both input-output and output-only methods were used. The three methods were MNExT-ERA, SRIM, and LSID. All three methods are based on linear system theory and are therefore associated with both modeling and estimation errors. It was found that the identified natural frequencies are comparable to each other and are in a range consistent with previously reported results in the literature. However, the identified damping ratios from the three methods were not consistent. This is mainly due to the fact that the identified damping ratios represent the linear viscous damping and do not take into account other sources of energy dissipation. In a complex system, such as the Yokohama Bay bridge, there are multiple sources of energy dissipation, such as local geometric nonlinearities, tower-to-deck connections, nonlinearities associated with the cables, etc. Therefore, it is seen that modeling the bridge as a linear system, is not an adequate approach for the purposes of damping ratio estimation.

As a result, there was a need to develop a reduced-order computational model that not only accurately represents the bridge, but also takes into account the contribution of the associated severe nonlinear forces that occur during major earthquakes, such as the ones being analyzed in this study. A hybrid modeling approach is proposed in this study, where the equivalent linear part is modeled using a well-known parametric least-square identification approach, while the identified nonlinear forces are modeled using the nonparametric neural network approach. The combined contributions are then integrated into an ODE solver to dynamically predict the response of the system to various non-stationary excitations. It is shown that the proposed nonlinear mathematical models are able to predict natural frequencies as well as damping ratios that take into account not only the linear viscous damping, but also the contribution from the other energy dissipation sources. For example, the damping ratio associated with mode 1 from EQ1 was estimated for both linear and nonlinear computational models and are given as $\hat{\zeta}_{ln} = 1.63\%$ and $\hat{\zeta}_{nln} = 4.26\%$, respectively. Further analyses were performed to show the importance of including the nonlinear forces in these models. The nonlinear mathematical models prove to be robust and stable when used for response prediction, while the linear models accurately estimate the system response for short duration but

suffer from numerical instabilities after a certain time. It is shown throughout the analysis, that the nonlinear forces are a very important part of such complex systems and should not be ignored. Estimating accurate damping ratios is crucial from the engineering design perspective, and in this study it is shown that relying on linear models only is not sufficient for accurate damping estimation.

While the results presented in this study show the importance of including the nonlinear effects in the proposed mathematical models, the authors are aware that these results can be further improved. This can be done by performing sensitivity analysis on the parameters of the neural networks as well as trying different nonparametric nonlinear modeling approaches such as function fitting, machine learning, amongst others. These approaches are currently under investigation by the authors.

## 1.8 SUMMARY AND CONCLUSIONS

System identification approaches have a significant role in extracting dominant features from structural measurements. There is a need to construct robust mathematical models for computational purposes to augment experimental studies. Furthermore, it is important to have models that capture the correct physics of the underlying system and allow the proper characterization of the system's nonlinear behavior. Given the lack of suitable data sets for full-scale structures under extreme loads, the strong shaking of the 2011 Great East Japan earthquake and its several strong aftershocks provide a unique opportunity to develop, test, and validate such mathematical models. In this study, the recorded response of Yokohama Bay Bridge (a large flexible bridge), driven into nonlinear response range, was used to develop mathematical models for computational purposes. The extensive multi-component measurements from relatively dense sensor array were also analyzed for system identification purposes. In the first part of the study, three well-established linear system identification methods (i.e., MNExT-ERA, SRIM, and LSID) were used to identify the modal characteristics of the system (i.e., natural frequencies and damping ratios). It was seen that the natural frequency estimates matched the expectations, while the damping ratio estimates were not consistent. The inconsistent damping estimates were mainly due to the fact that all three identification methods were based on linear system theory that takes into account only the linear viscous damping, while the available measurements were mostly from the strong shaking of the bridge driven to its nonlinear range. The analysis emphasized the importance of having mathematical models that accurately takes into account the nonlinear characteristics of the system that can be used for response prediction as well as damping estimation. In the second part of the study both linear and nonlinear mathematical models were developed, validated, and compared. The nonlinear mathematical model was developed using a combination of parametric (least-square) and

non-parametric (neural network) approaches along with time-marching (Runge-Kutta) techniques for dynamic response calculations. It was shown that the nonlinear mathematical models are more accurate and reliable from the linear models both in response prediction as well as damping estimation. The demonstrated approach is a general methodology and can be used for various other structural systems (not necessarily bridges).

## 1.9 ACKNOWLEDGMENT

This study was supported in part by a contract from the California Department of Transportation (Caltrans). The assistance of Dr Charles Sikorsky of Caltrans is appreciated.

# Bibliography


[1] Andrew W. Smyth, Jin-Song Pei, and Sami F. Masri. System identification of the Vincent Thomas suspension bridge using earthquake records. *Earthquake Engineering & Structural Dynamics*, 32(3):339–367, March 2003.

[2] Dionysius M. Siringoringo and Yozo Fujino. Observed Dynamic Performance of the Yokohama-Bay Bridge from System identification Using Seismic Records. *Structural Control and Health Monitoring*, 13(1):226–244, January 2006.

[3] Dionysius M. Siringoringo and Yozo Fujino. Dynamic Characteristics of a Curved Cable-Stayed Bridge Identified From Strong Motion Records. *Engineering Structures*, 29(8):2001–2017, August 2007.

[4] Dionysius M Siringoringo and Yozo Fujino. System Identification Applied to Long-Span Cable-Supported Bridges Using Seismic Records. *Earthquake Engineering & Structural Dynamics*, 37(3):361–386, 2008.

[5] Dionysius M. Siringoringo and Yozo Fujino. System Identification of Suspension Bridge From Ambient Vibration Response. *Engineering Structures*, 30(2):462–477, February 2008.

[6] Dionysius M. Siringoringo, Yozo Fujino, and Tomonori Nagayama. Dynamic Characteristics of an Overpass Bridge in a Full-Scale Destructive Test. *Journal of Engineering Mechanics*, 10:268, September 2011.

[7] WH Hu, Carlos Moutinho, and Elsa Caetano. Continuous Dynamic Monitoring of a Lively Footbridge for Serviceability Assessment and Damage Detection. *Mechanical Systems and Signal Processing*, 33(November):38–55, 2012.

[8] DM Siringoringo and Y Fujino. Response Analysis of Yokohama Bay Bridge under the 2011 Great East-Japan Earthquake. *Proc. 15th World Conf. Earthquake Engineering*, 2012.

[9] Dionysius M. Siringoringo, Yozo Fujino, and Kenji Namikawa. Seismic Responses Analyses of the Yokohama-Bay Cable-Stayed Bridge in the 2011 Great East Japan (Tohoku) Earthquake. *Journal of Bridge Engineering*, 10.1061, May 2013.

[10] AM Abdel-Ghaffar and RH Scanlan. Ambient Vibration Studies of Golden Gate Bridge: I. Suspended Structure. *Journal of Engineering Mechanics*, 111(4):463–482, 1985.

[11] AM Abdel-Ghaffar and RH Scanlan. Ambient Vibration Studies of Golden Gate Bridge: II. Pier-Tower Structure. *Journal of Engineering Mechanics*, 111(4):483–499, 1985.

[12] Tomonori Nagayama, Masato Abe, Yozo Fujino, and Kenji Ikeda. Structural Identification of a Nonproportionally Damped System and Its Application to a Full-Scale Suspension Bridge. *Journal of Structural Engineering*, 131(10):1536–1545, 2005.

[13] Rosario Ceravolo and Nicola Tondini. Dynamic characterization of complex bridge structures with passive control systems. *Structural Control and Health Monitoring*, 19(4):511–534, 2012.

[14] HF Zhou, YQ Ni, and JM Ko. Eliminating temperature effect in vibration-based structural damage detection. *Journal of Engineering Mechanics*, 137(12):785–796, 2012.

[15] K Y Koo, J M W Brownjohn, D I List, and R Cole. Structural health monitoring of the Tamar suspension bridge. *Structural Control and Health Monitoring*, 20(4):609–625, 2013.

[16] G.H. Ill James, Thomas G Carrie, and James P Lauffer. The Natural Excitation Technique ( NExT ) for Modal Parameter Extraction From Operating Wind Turbines. *Sandia National Labs., Albuquerque, NM (United States)*, 1993.

[17] JN Juang and RS Pappa. An Eigensystem Realization Algorithm For Modal Parameter Identification And Model Reduction. *Journal of guidance, control, and dynamics*, 1985.

[18] Xianfei He, Babak Moaveni, Joel P Conte, Ahmed Elgamal, and Sami F Masri. System Identification of Alfred Zampa Memorial Bridge Using Dynamic Field Test Data. *Journal of structural Engineering*, 135(1):54–66, 2009.

[19] Jer-Nan Juang. System Realization Using Information Matrix. *Journal of Guidance, Control, and Dynamics*, 20(3):492–500, May 1997.

[20] S.F. Masri, R. K. Miller, a. F. Saud, and T. K. Caughey. Identification of Nonlinear Vibrating Structures: Part I- Formulation. *Journal of Applied Mechanics*, 54(4):918 – 922, 1987.

[21] S.F. Masri, R. K. Miller, a. F. Saud, and T. K. Caughey. Identification of Nonlinear Vibrating Structures: Part II- Applications. *Journal of Applied Mechanics*, 54(4):923 – 929, 1987.

[22] S.F. Masri and G A Bekey. A Global Optimization Search Using Adaptive Random Search. *Applied Mathematics and Computation*, 7(4):353–375, 1980.

[23] S.F. Masri, A.W. Smyth, A.G. Chassiakos, M. Nakamura, and T.K. Caughey. Training neural networks by adaptive random search techniques. *Journal of Engineering Mechanics*, 125(February):123, 1999.

[24] Shilei Zhang, Huanding Wang, Wei Wang, and Shaofeng Chen. Damage Detection in Structures Using Artificial Neural Networks. *2010 International Conference on Artificial Intelligence and Computational Intelligence*, pages 207–210, October 2010.

[25] Goh Lyn Dee, Norhisham Bakhary, Azlan Abdul Rahman, and Baderul Hisham Ahmad. A Comparison of Artificial Neural Network Learning Algorithms for Vibration-Based Damage Detection. *Advanced Materials Research*, 163-167:2756–2760, December 2010.

# Chapter 2

# UCSD FINAL REPORT

## 2.1 YOKOHAMA BRIDGE ANALYSIS - DAMAGE ASSESSMENT BASED ON MARCH 11, 2011 RECORDED DATA.

## 2.2 LEVEL III DAMAGE IDENTIFICATION OF A BRIDGE MODEL.

# UCSD REPORT:

# YOKOHAMA BRIDGE ANALYSIS - DAMAGE ASSESSMENT BASED ON MARCH 11, 2011 RECORDED DATA.

**By G. Benzoni - G. Lomiento - N. Bonessio**

La Jolla, August 2013

# List of Figures

**Figure 12**. Transfer functions of the vertical displacements of the deck during the main shock event. **A**: Sensor locations on the deck. **B**: Transfer functions of the vertical displacements. The plots follow the sequence of the sensors displayed in the sensor map.

**Figure 13**. Transfer functions of the longitudinal displacements of the deck during the main shock event. **A**: Sensor locations on the deck. **B**: Transfer functions of the longitudinal displacement. The plots follow the sequence of the sensors displayed in the sensor map.

**Figure 14**. Transfer functions of the longitudinal displacements of the towers during the main shock event. **A**: Sensor locations on the Tower #1 (Homoku side). **B**: Transfer functions of the longitudinal displacements of Tower #1. **C**: Sensor locations on the Tower #2 (Oguru side). **D**: Transfer functions of the longitudinal displacements of Tower #1.

**Figure 15**. Transfer functions of the lateral displacements of the deck during the main shock event. **A**: Sensor locations on the deck. **B**: Transfer functions of the lateral displacement. The plots follow the sequence of the sensors displayed in the sensor map.

**Figure 16**. Transfer functions of the lateral displacements of the towers during the main shock event. **A**: Sensor locations on the Tower #1 (Homoku side). **B**: Transfer functions of the lateral displacements of Tower #1. **C**: Sensor locations on the Tower #2 (Oguru side). **D**: Transfer functions of the longitudinal displacements of Tower

**Figure 17**. Front page of the DIIB software. The interpretative scheme geometry of the Yokohama Bay Bridge is uploaded and shown in the figure panel. The nodes on the scheme correspond to available acquisition channels.

**Figure 18**. Vibration frequency of the principal modes of the bridge in longitudinal, lateral and vertical direction as identified from main shock and after shocks data.

**Figure 19**. Mode shapes and frequencies identified from the main shock acceleration data set. Top figure: first longitudinal mode. Middle figure: first vertical mode. Bottom figure: first lateral mode (view from the top).

**Figure 20**. Mode shapes and frequencies identified from the first 20 seconds of the main shock. Top figure: first longitudinal mode. Middle figure: first vertical mode. Bottom figure: first lateral mode (view from the top).

**Figure 21**. Mode shapes and frequencies identified from the after shock #3 acceleration data set. Top figure: first longitudinal mode. Middle figure: first vertical mode. Bottom figure: first lateral mode (view from the top).

**Figure 22**. Damage locations on the bridge identified for the main shock. Reference condition: first 20 seconds of the main shock.

**Figure 23**. Damage localization normalized index Z and damage severity index $\alpha$ along the deck and the tower structures for the main shock. Reference condition: first 20 seconds of the main shock.

**Figure 24**. Damage locations on the bridge identified for the after shock #3. Reference condition: first 20 seconds of the main shock.

**Figure 25**. Damage localization normalized index Z and damage severity index a along the deck and the tower structures.

# List of Tables

# Introduction

This report presents the application of the damage detection procedure defined in Bonessio et al. (2011) and Benzoni et al. (2012) to the Yokohama Bay Bridge, a 2,821 ft (860 m) long, 93 ft (28.5 m) wide cable stayed bridge in Yokohama, Japan (**Fig. 1**). Opened September 27, 1989, the bridge crosses the Tokyo Bay with a 3-span continuous deck plate (main span 1,510 ft or 460 m) and is part of the Bayshore Route of the Shuto Expressway. The main girder consists of double-deck steel truss-box with six lanes upper deck and two lanes lower deck. The bridge has two H-shaped towers welded as monolithic section with the height of 565 ft (172m) and width of 96 ft (29.25m). Earthquake resistance is one of the main concerns in the bridge design. To reduce accelerations on the deck, the girder is suspended from towers and end piers by means of link-bearing connections in such a way that the effect of superstructure inertia force on the substructure is reduced during an earthquake by maintaining a longitudinal fundamental period of about 7.7 sec, i.e. a frequency of about 0.13 Hz (Siringorino and Fujino 2012). Details of these connections are shown in **Fig. 2**. These connections are composed by a double-head steel pendulum, with length of 10m and 2 m for the end-link and the tower-link respectively, and steel-PTFE sliding bearings. In transverse direction, the girder movement is restricted by wind shoes at all piers and towers. Transverse gaps exist between wind shoe and girder to allow for tower-girder transverse relative motion. The Yokohama Bay Bridge experienced significant oscillations during the main shock and after shocks of the 2011 earthquake off the Pacific coast of Tōhoku.

**Figure 1**. Yokohama Bay Bridge (source: www.yokogawa-bridge.co.jp/).

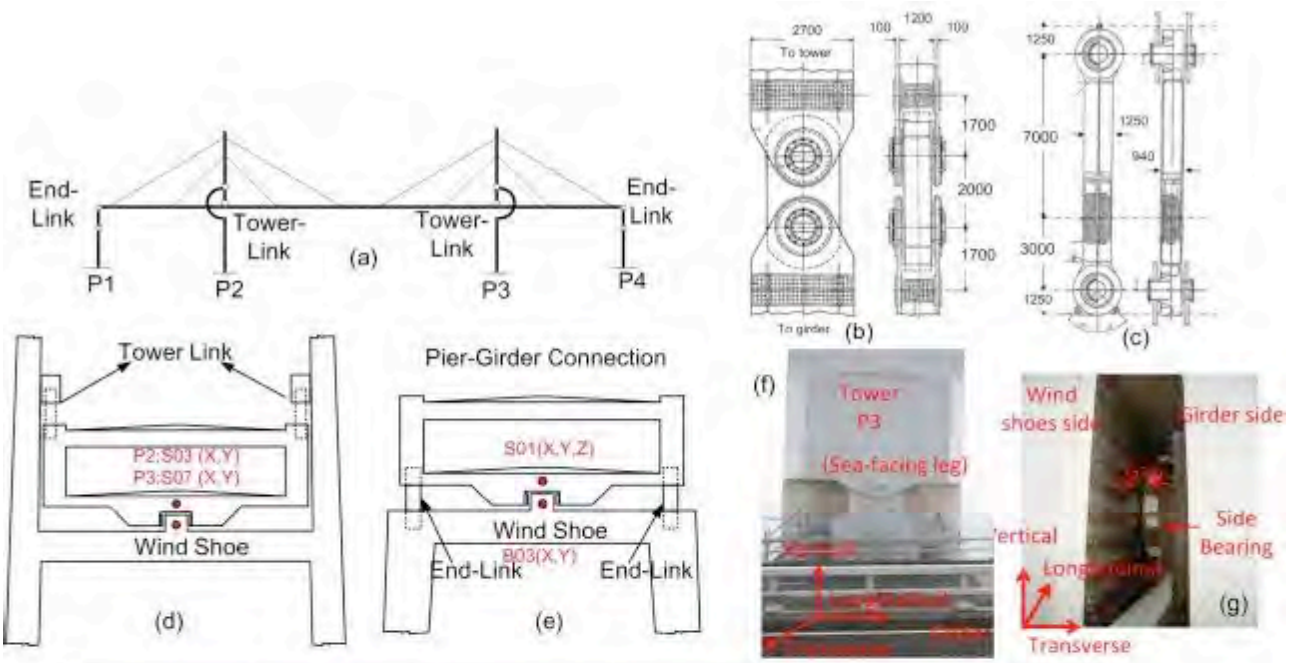


**Figure 2**. (a) Characteristics of pier-to-girder and tower-to-girder connections, (b) detail figure of tower-link, (c)detail figure of end-link, (d) Schematic figure of tower-to-girder connection, (e) Schematic figure of pier-to-girder connection, (f) photo of tower link and (g) snapshot photo of wind shoe transverse gap between tower/pierand girder (source: Siringorino and Fujino 2012).

This undersea megathrust earthquake off the coast of Japan had a main shock of magnitude 9.0 (Mw) that occurred on the March 11$^{th}$ 2011 with the epicenter approximately 70 kilometers (43 mi) east of the Oshika Peninsula of Tōhoku and the hypocenter at an underwater depth of approximately 30 km (19 mi). Many aftershocks occurred between March 11$^{th}$ and 15$^{th}$. In **Fig. 3** the epicenters of the main shock and all the ground shakings recognized as after shocks of the Tohoku earthquake are reported. It should be noted that, due to the significant distance from the epicenter, ground accelerations were strongly attenuated at the bridge location, which is indicated by the white circle on the map. The application of the above mentioned damage detection procedure, which requires only-output data recorded by the accelerometer network installed on the bridge, is particularly meaningful when compared with the input-output neural network approach that use ODE solvers to form a reduced-order computational model to predict the response of the bridge to various ground motion time histories. This output-only procedure, which has been extensively validated through ambient vibration data from the Vincent Thomas Bridge (Benzoni et al., 2013) and used also for a limited number of acceleration sets recorded during ground shaking events, is here applied to an extensive set of earthquake data. A total of 10 sets of acceleration data are used to identify modal characteristics and possible damages on the bridge.

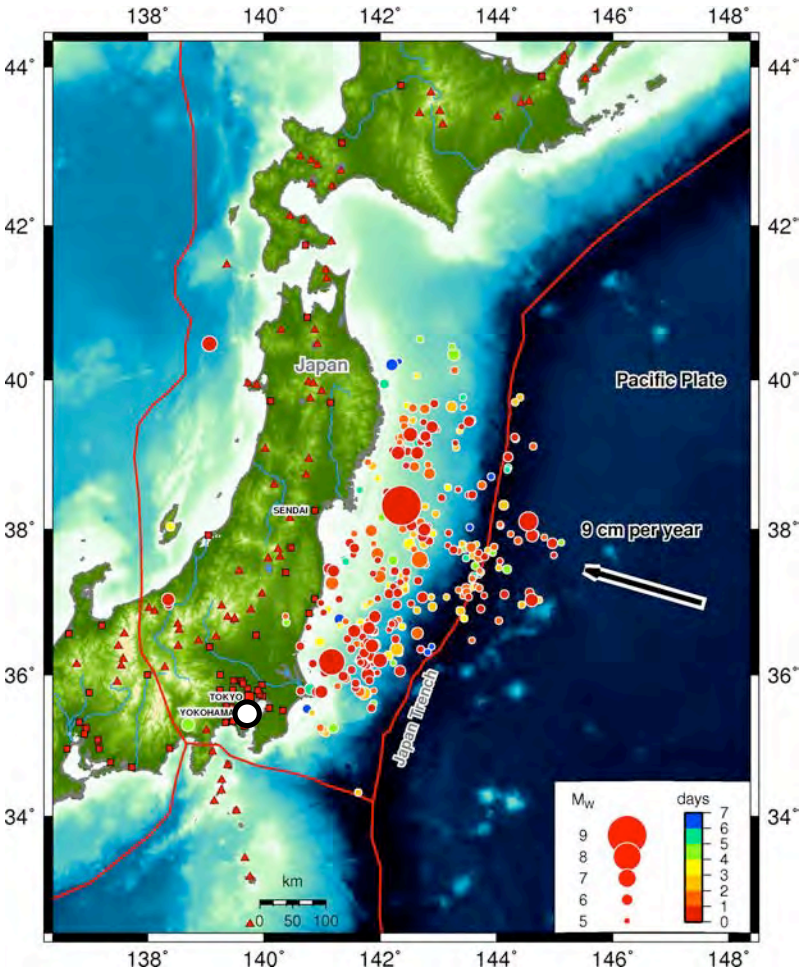


**Figure 3**. Map showing the Yokohama Bay Bridge (white spot) and the epicenters of main shocks and aftershocks of the Tohoku Earthquake (source: http://comet.nerc.ac.uk/).

Acceleration histories were recorded by a network of 36 accelerometers, which is installed on the Yokohama Bay Bridge:

- 12 accelerometers on the deck (S1-S9)
- 7x2 accelerometers on the 2 towers (T1-T8)
- 8 accelerometers on the piles (K1-K8)
- 2 accelerometers on the shoulders (B1,B2)

for a total of 93 recording channels in X (longitudinal), Y (lateral), and Z (vertical) directions, as shown in **Fig. 4**. Additional accelerometers recorded the free-field acceleration on the ground in X, Y, and Z directions (G1).

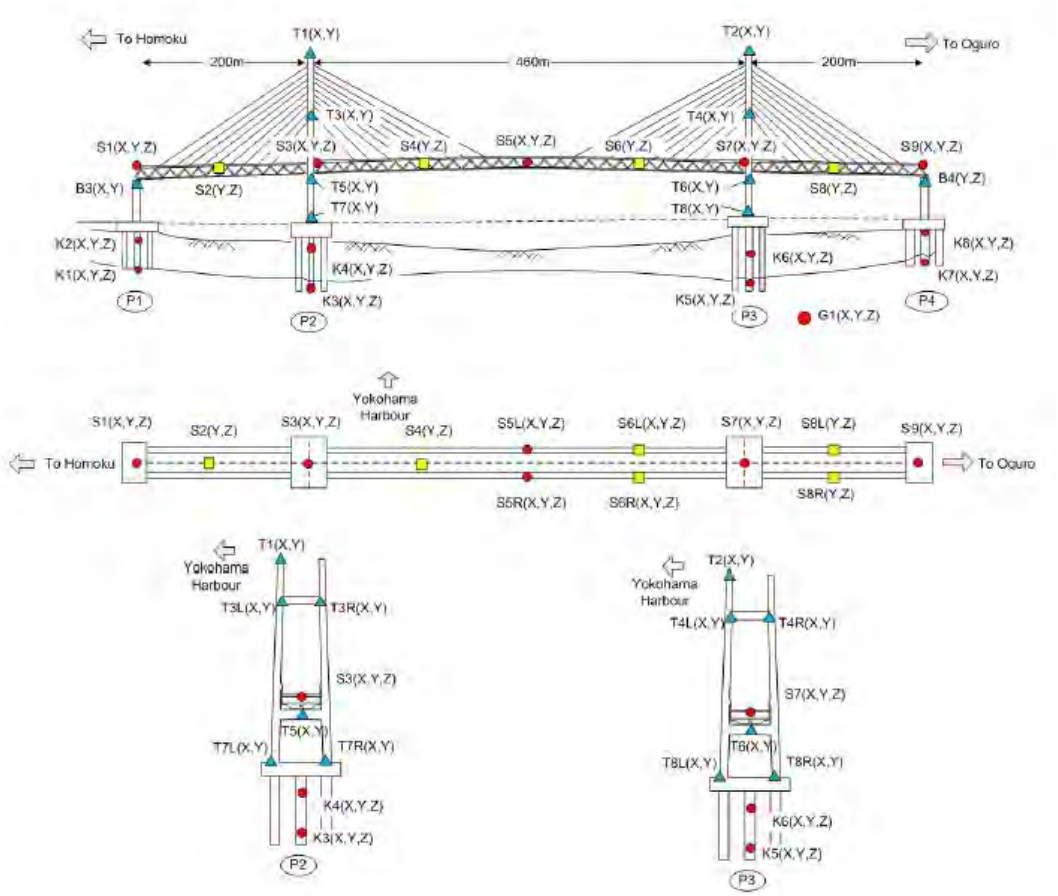


**Figure 4**. Sensor network on the Yokohama Bay Bridge. Squares identify bi-directional accelerometers in lateral (Y) and vertical (Z) direction. Triangles identify bi-directional accelerometers in longitudinal (X) and vertical (Z) direction. Circles identify tri-directional accelerometers (X, Y, Z).

The acceleration histories have been sampled at 100Hz. Trigger time, length, moment Magnitude Mw, and epicenter to bridge distance of the events under investigation are reported in **Table 1**.

All the available seismic events occurred in the first 5 days after the main shock, with the first five aftershocks (AS) within a 24 hour time window. Only for aftershock AS#8 the epicenter was less than 50 miles (~80 km) away from the Yokohama Bay Bridge.

In **Fig. 5**, the peak acceleration values recorded on the bridge deck and towers are presented for each input in longitudinal, lateral, and vertical direction.

**Table 1.** Acceleration data sets.

| Event name | Files name | Trigger time (JST) | Length (s) | Mw | Distance (mi) [km] |
|---|---|---|---|---|---|
| MS (main shock) | M/S03111447.45w | 2011/03/11 14:47:45.00 | 600.00 | 9.0 | 247 [398] |
| AS #1 | M/S03111516.16w | 2011/03/11 15:16:16.00 | 480.00 | 7.7 | 119 [192] |
| AS #2 | M/S03111527.20w | 2011/03/11 15:27:20.00 | 240.00 | 7.5 | 352 [567] |
| AS #3 | M/S03111629.33w | 2011/03/11 16:29:33.00 | 60.00 | 6.5 | 375 [603] |
| AS #4 | M/S03111720.14w | 2011/03/11 17:20:14.00 | 180.00 | 6.1 | 183 [295] |
| AS #5 | M/S03120400.21w | 2011/03/12 04:00:21.00 | 120.00 | 6.7 | 127 [205] |
| AS #6 | M/S03131027.11w | 2011/03/13 10:27:11.00 | 120.00 | 6.4 | 144 [233] |
| AS #7 | M/S03141003.33w | 2011/03/14 10:03:33.00 | 60.00 | 6.2 | 126 [204] |
| AS #8 | M/S03152232.08w | 2011/03/15 22:32:08.00 | 120.00 | 6.4 | 40 [64] |
| AS #9 | M/S03161252.41w | 2011/03/16 12:52:41.00 | 120.00 | 6.1 | 92 [148] |

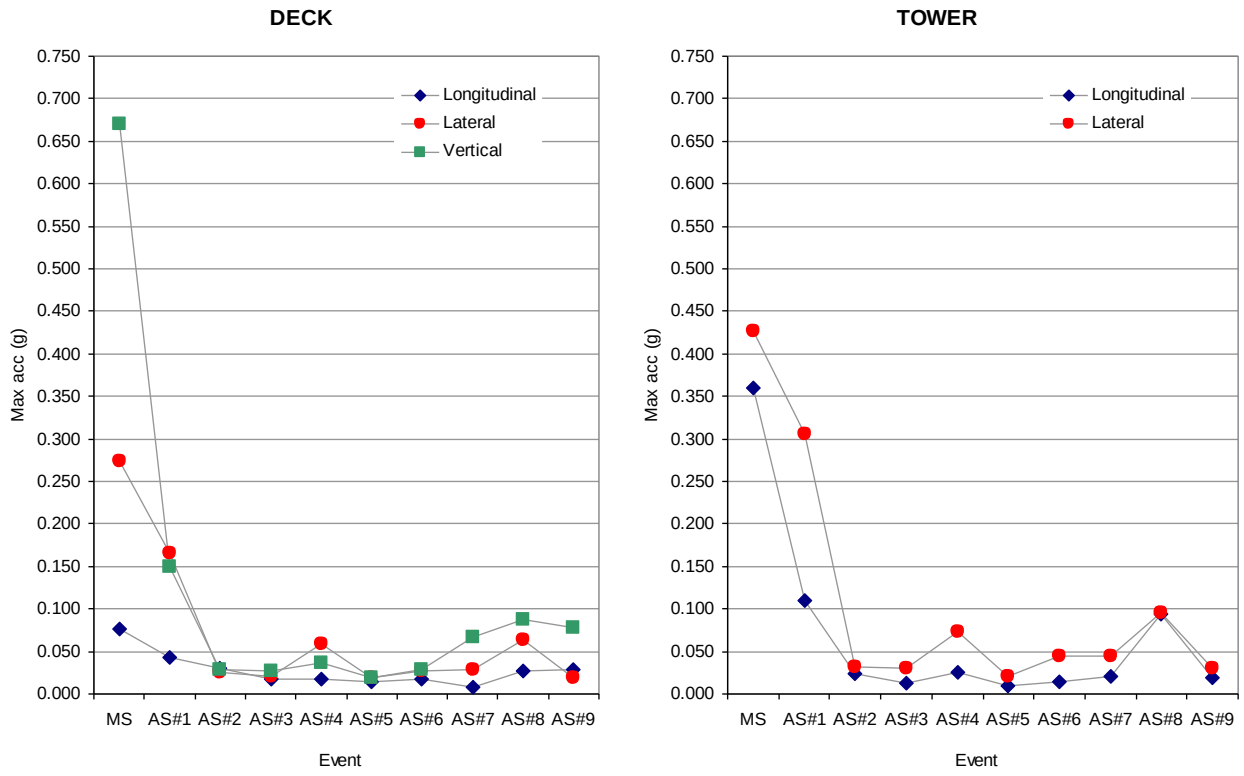


**Figure 5**. Peak acceleration values recorded in longitudinal, lateral and vertical direction on the bridge deck and on the towers during the shaking events.

With the exception of the main shock and the 1st after shock, the maximum acceleration recorded on the bridge did not exceed 0.10g in any direction. For the deck, highest acceleration values are found for vertical and lateral vibration of the bridge. Very low acceleration values were detected on the deck in longitudinal direction, showing that the above mentioned link-bearing connections were effective. For the towers, the lateral acceleration always exceeded the longitudinal acceleration. All the data from the main shock and the nine after shocks are used for the damage detection on the suspension bridge.

Many sources of uncertainties could affect the final results of the damage identification procedure. Differences in environmental conditions and in excitation intensities are important aspects that need to be acknowledged while analyzing results. In fact, for long cable suspended bridges these aspects can both induce significant changes of the dynamic properties of the structural system. Even daily changes originated by variations in environmental variables such as temperature, precise hour of measurements, speed of wind, etc. were found to be potentially larger than the modal variations due to damage (Raghavendrachar and Aktan 1992; Farrar and Jauregui 1999; Fu and De Wolf 2001; Mevel et al. 2003). Vibration frequencies were recognized to be more sensitive to these aspects than mode shapes (Brincker et al. 2001). These variations could be source of false positives in the damage detection procedure, which is based on the comparison between modal characteristics in a reference undamaged condition and in a supposedly damaged condition. With this in mind, the accuracy of the procedure will be evaluated through the comparison with the evidence from visual inspections, which were conducted after the main shock and several times during the aftershock activity (Siringorino and Fujino 2012).

## Preliminary Data Analysis

A preliminary analysis of the data recorded on the Yokohama Bay Bridge during the March 11, 2011 earthquake main shock was performed in order to check the quality of the recorded data in each acquisition channel and to detect basic vibration characteristics of the bridge.

Plots of the acceleration histories are reported for the deck in **Fig. 6** to **Fig. 8**. From these plots, several malfunctioning channels are clearly identified. The malfunctioning sensors of the deck are all on the Oguro's side of the bridge. Specifically, bi-directional sensors S8L, S8R (lateral Y and vertical Z direction) and tri-directional sensor S9 (X, Y and Z directions) are affected by significant errors. Data from these channels were excluded from the damage detection procedure.

Similar plots are presented for the longitudinal and lateral acceleration histories recorded on the towers in **Fig. 9** and **Fig. 10**. Two malfunctioning channels are identified on the towers. The malfunctioning sensors are located at the bottom of the Tower #1 (Homoku side). Bi-directional sensor T7L is not properly working in longitudinal X direction, while bi-directional sensor T7R is malfunctioning in later al Y direction.

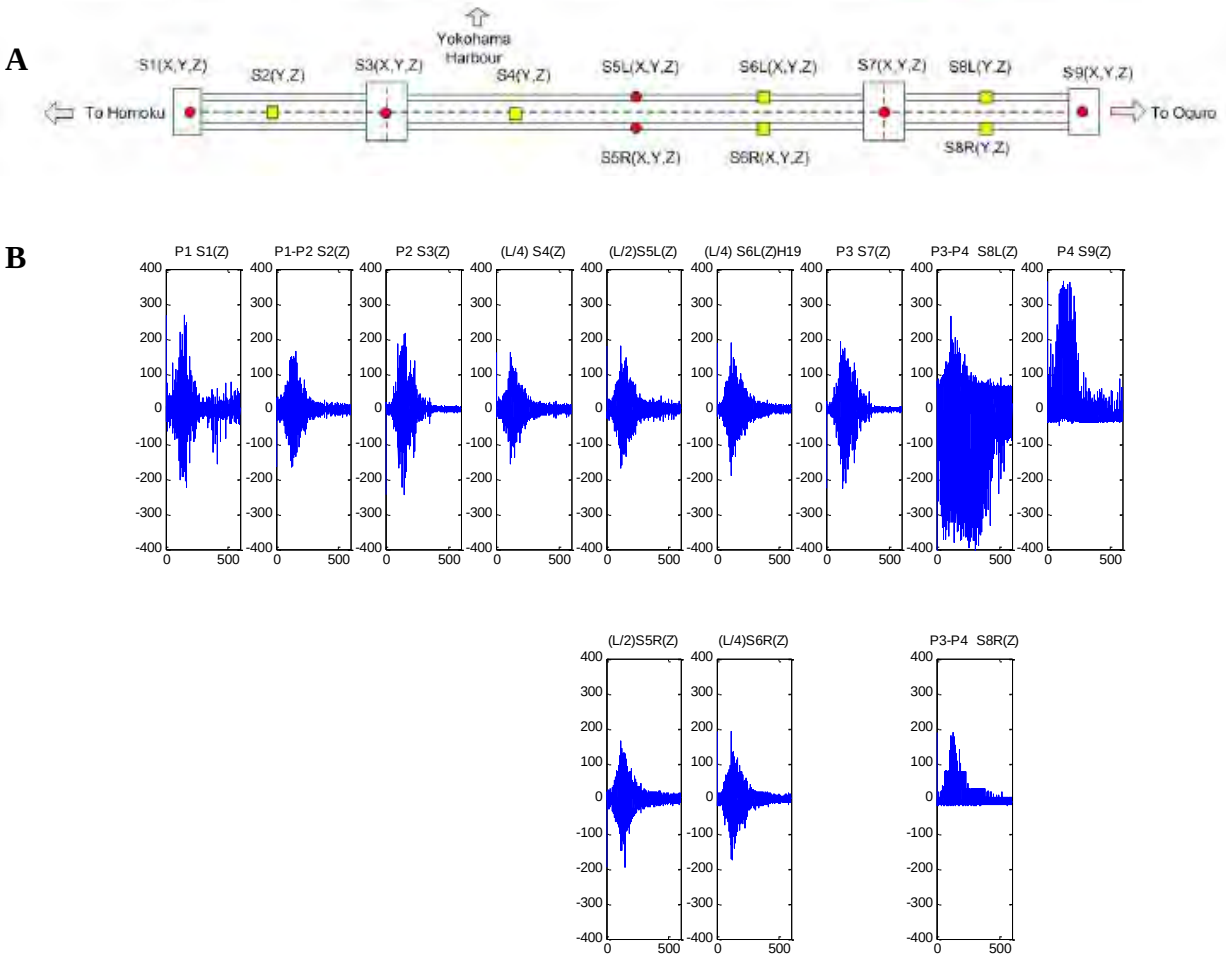


**Figure 6**. Vertical accelerations on the deck during the main shock event. **A**: Sensor locations on the deck. **B**: Vertical acceleration (cm/S$^2$) in each sensor. The plots follow the sequence of the sensors displayed in the sensor map. First row: sensor in the center and at the left side of the bridge (direction Yokohama Harbor). Second row: sensors at the right side of the bridge.

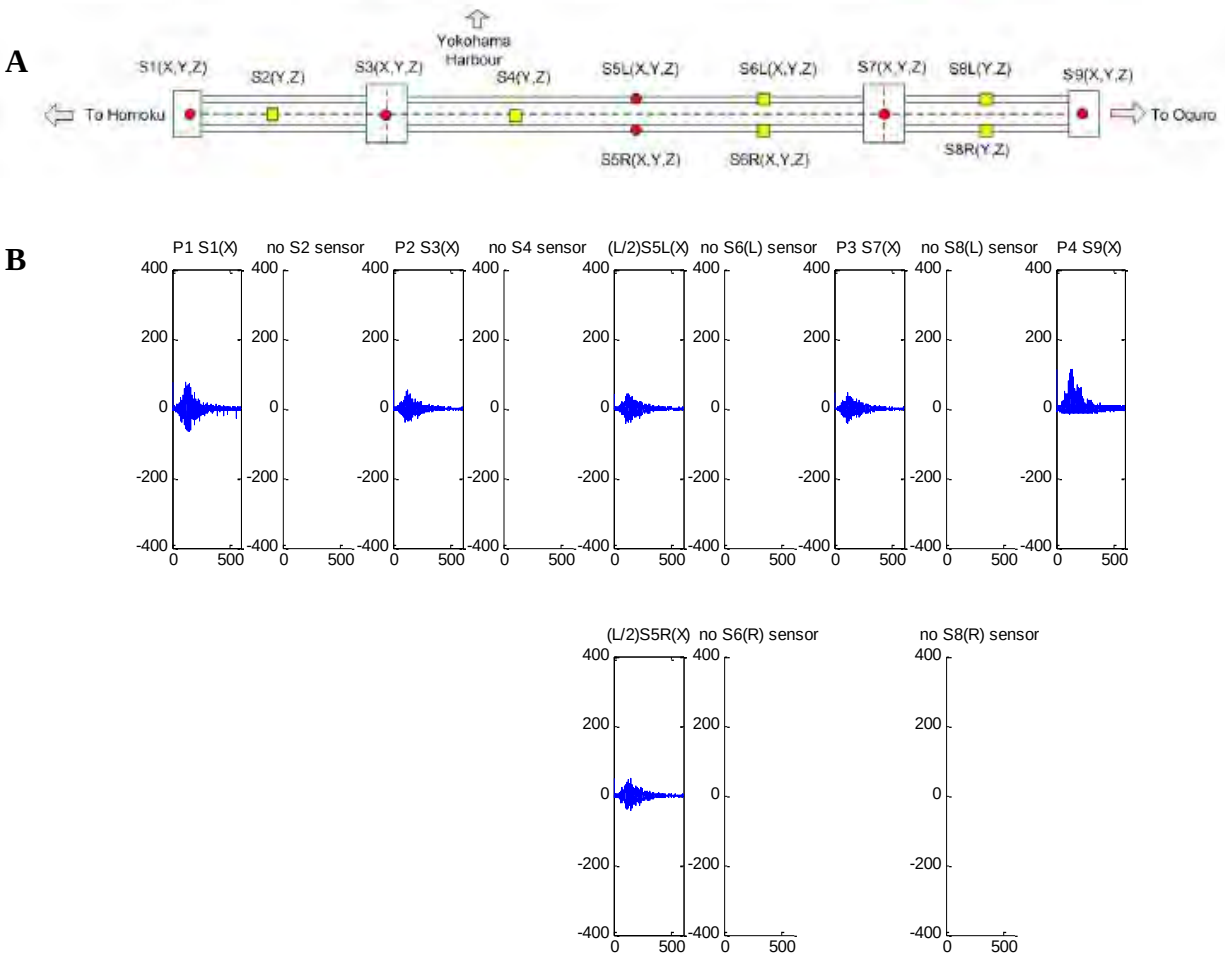


**Figure 7**. Longitudinal accelerations on the deck during the main shock event. **A**: Sensor locations on the deck. **B**: Longitudinal acceleration ($cm/S^2$) in each sensor. The plots follow the sequence of the sensors displayed in the sensor map. First row: sensor in the center and at the left side of the bridge (direction Yokohama Harbor). Second row: sensors at the right side of the bridge.

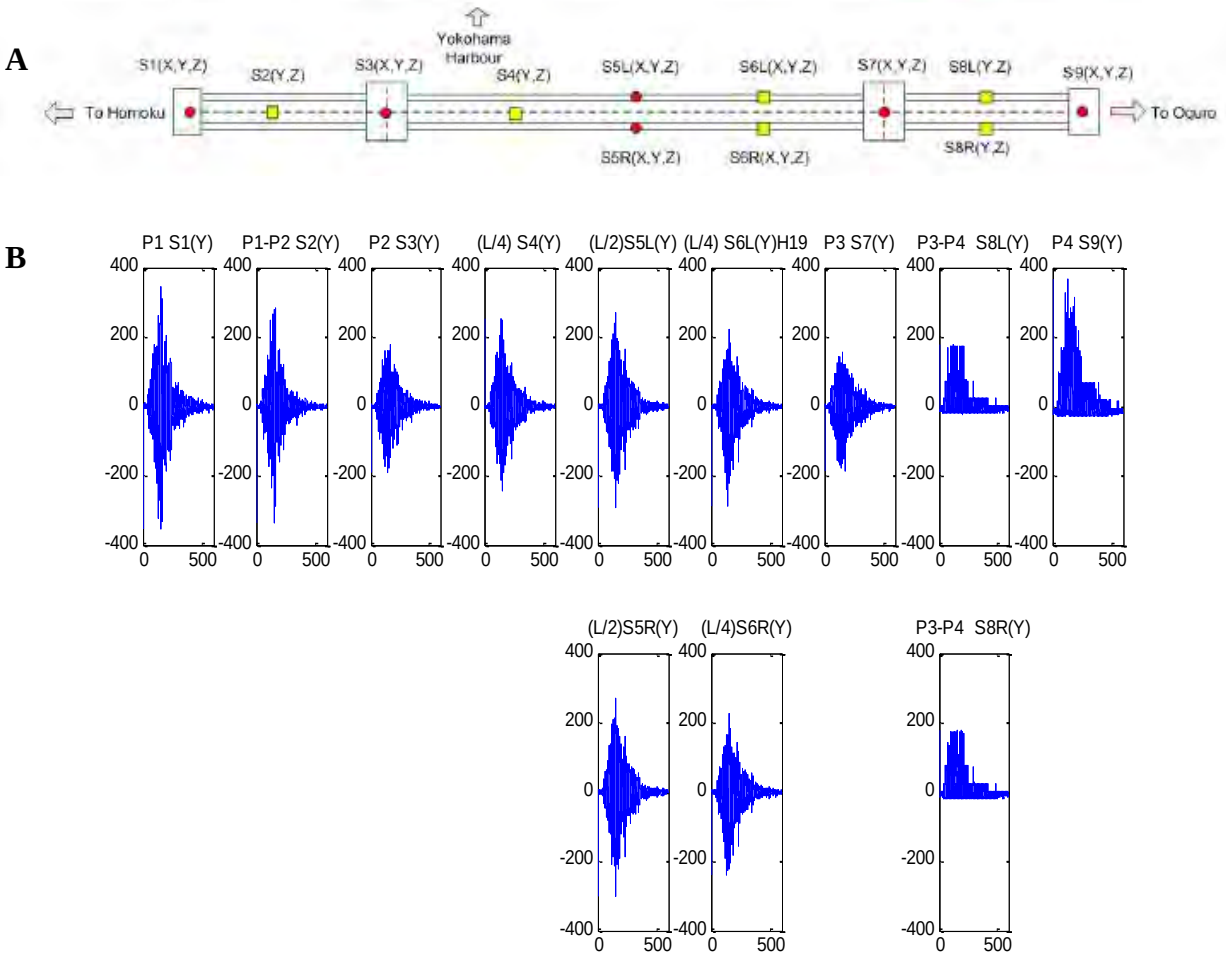


**Figure 8**. Lateral accelerations on the deck during the main shock event. **A**: Sensor locations on the deck. **B**: Lateral acceleration (cm/$S^2$) in each sensor. The plots follow the sequence of the sensors displayed in the sensor map. First row: sensor in the center and at the left side of the bridge (direction Yokohama Harbor). Second row: sensors at the right side of the bridge.

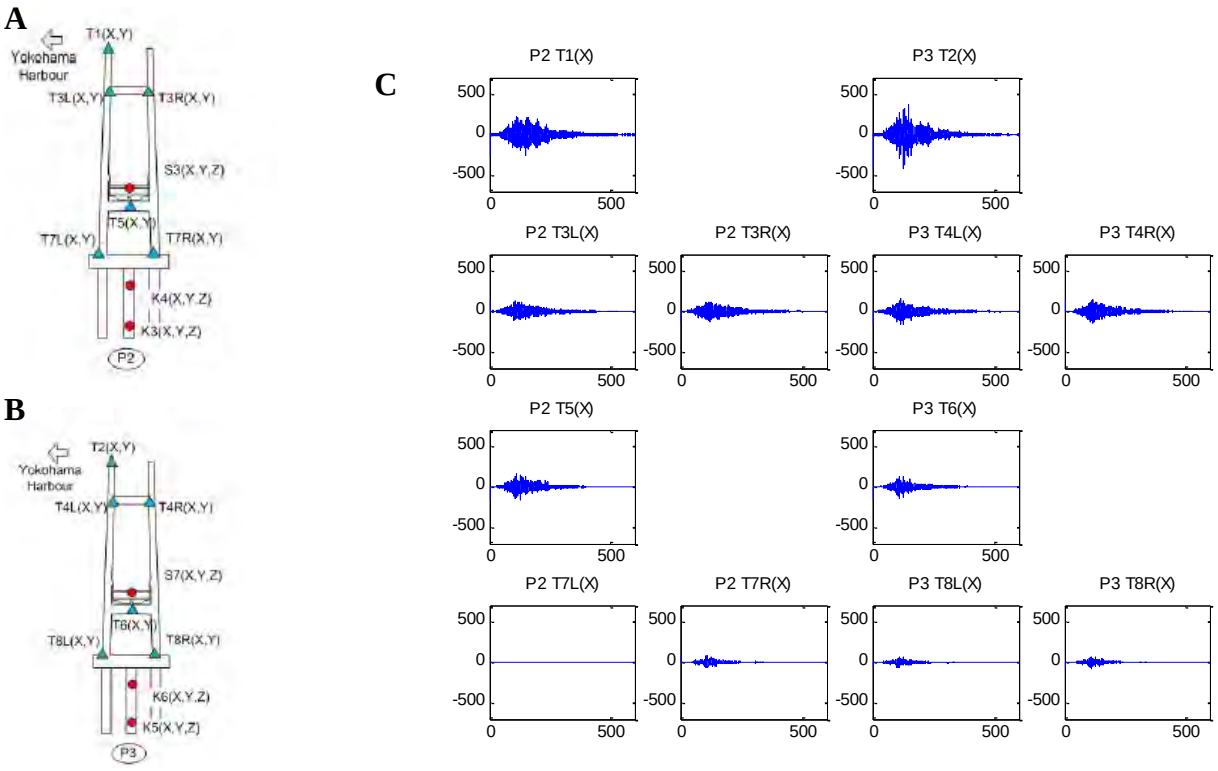


**Figure 9**. Longitudinal accelerations on the towers during the main shock event. **A**: Sensor locations on the Tower #1 (Homoku side). **B**: Sensor locations on the Tower #2 (Oguru side). **C**: Longitudinal acceleration ($cm/S^2$) in each sensor. Plots in the first two columns refer to Tower #1. Plots in the last two columns refer to Tower #2.

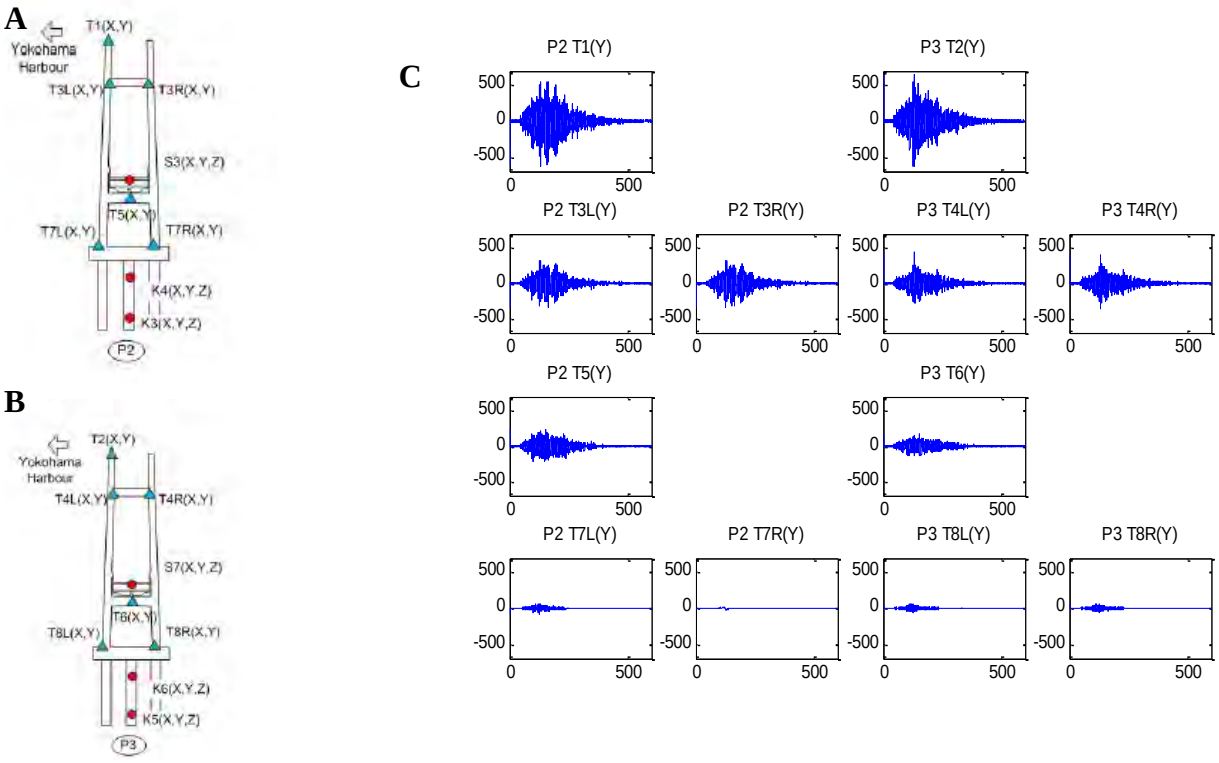


**Figure 10**. Lateral accelerations on the towers during the main shock event. **A**: Sensor locations on the Tower #1 (Homoku side). **B**: Sensor locations on the Tower #2 (Oguru side). **C**: Lateral acceleration (cm/$S^2$) in each sensor. Plots in the first two columns refer to Tower #1. Plots in the last two columns refer to Tower #2.

Displacements were obtained from the acceleration histories through double integration. The baseline correction played a crucial role in the conversion of acceleration data to displacement data. Recent developments in digital strong-motion accelerographs have made great improvements in data quality. Some of the errors found in analog data do not exist in digital strong-motion data, for example, the warping of records and the digitization errors. Other errors, such as the uncertainty of the initial baseline, have been significantly reduced as well. However, a large offset still exists in high-resolution and high-sampling-rate digital data despite the improved data quality. Hence, baseline correction is still an important issue in the processing of digital data.

A variety of baseline errors can be produced by various combinations of the initial velocity and the background noise. The displacement evaluated from accelerations recorded on the deck and the towers are affected by significant baseline errors. Exemplificative errors are shown in **Fig. 11B**, where the vertical displacement histories affected by baseline errors are plotted at the deck sensor locations shown in **Fig. 11A**. The displacements are here evaluated as the double integral of the vertical acceleration data, and are additionally corrected by removing a linear trend and applying a band pass filter 0.05Hz-20Hz. This simple baseline correction is evidently not sufficient. All the baselines of the displacement histories have different shapes, and even the components in different directions recorded at the same acquisition channel may have different shapes. The major baseline errors found in these digital data can be attributed to a variety of factors, including constant drift in the acceleration, low-frequency instrument noise, low-frequency background noise, small initial values for acceleration and velocity, and possibly manipulation errors. In this data analysis, a three-step algorithm was chosen to correct these errors.

This three-step algorithm includes:

1. fitting the baseline of acceleration by the least squares,
2. applying a band-pass filter in acceleration
3. fitting the baseline of velocity by the least squares.

Least-squares fit of a straight line before filtering is used to remove the baseline drift in acceleration. Then, the filtering removes high and low-frequency background noise errors that exist in the acceleration. Finally, subtracting a series of continuous, piecewise linear trends from the velocity history removes the baseline trend of the displacement history.

A demonstration of this three-step baseline correction is shown in **Fig. 11C** where corrected vertical displacement histories are plotted at the same locations of **Fig. 11B**. No baseline errors are visible in the corrected displacement waveforms.

The anomalous displacement values at the Oguro side of the bridge are due to the above mentioned malfunctioning of the accelerometers S8L, S8R and S9. A peak vertical displacement of 12.5 cm was found at the center at the deck, while in the lateral and longitudinal direction the peak displacements were about 50 cm and 20 cm, respectively.

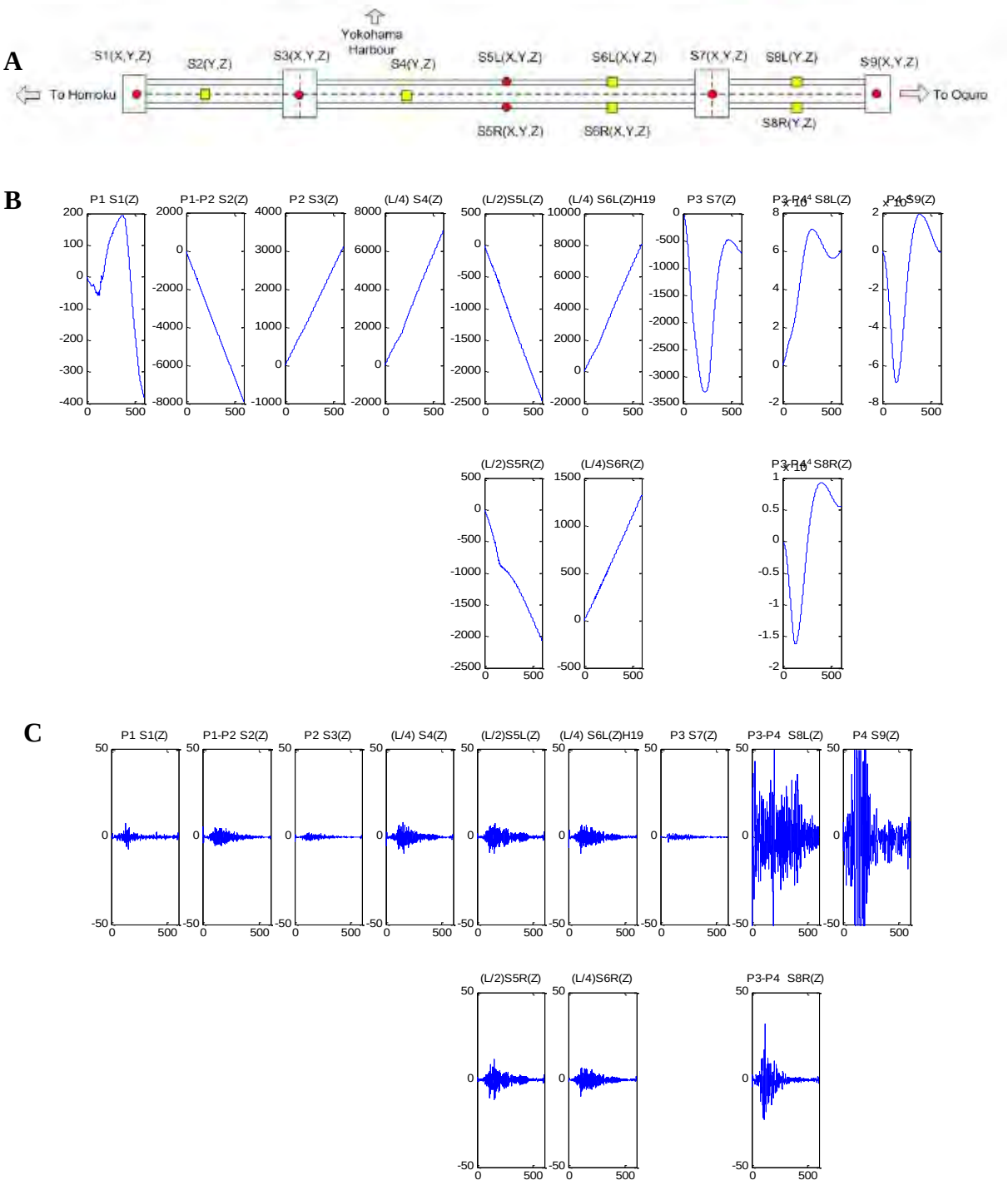


**Figure 11**. Vertical displacements on the deck during the main shock event. **A**: Sensor locations on the deck. **B**: Vertical displacement (cm) history affected by baseline errors. **C**: Vertical displacement (cm) history after the three step baseline correction. The plots follow the sequence of the sensors displayed in the sensor map.

In order to identify the main vibration frequencies of the bridge, transfer functions were computed at all the sensor locations of the bridge. Ground acceleration time histories from the free-field sensors were used as input for the transfer functions. An example of the computed transfer function for the vertical displacement is shown in **Fig. 12B**, at the sensor deck locations of **Fig. 12A**.

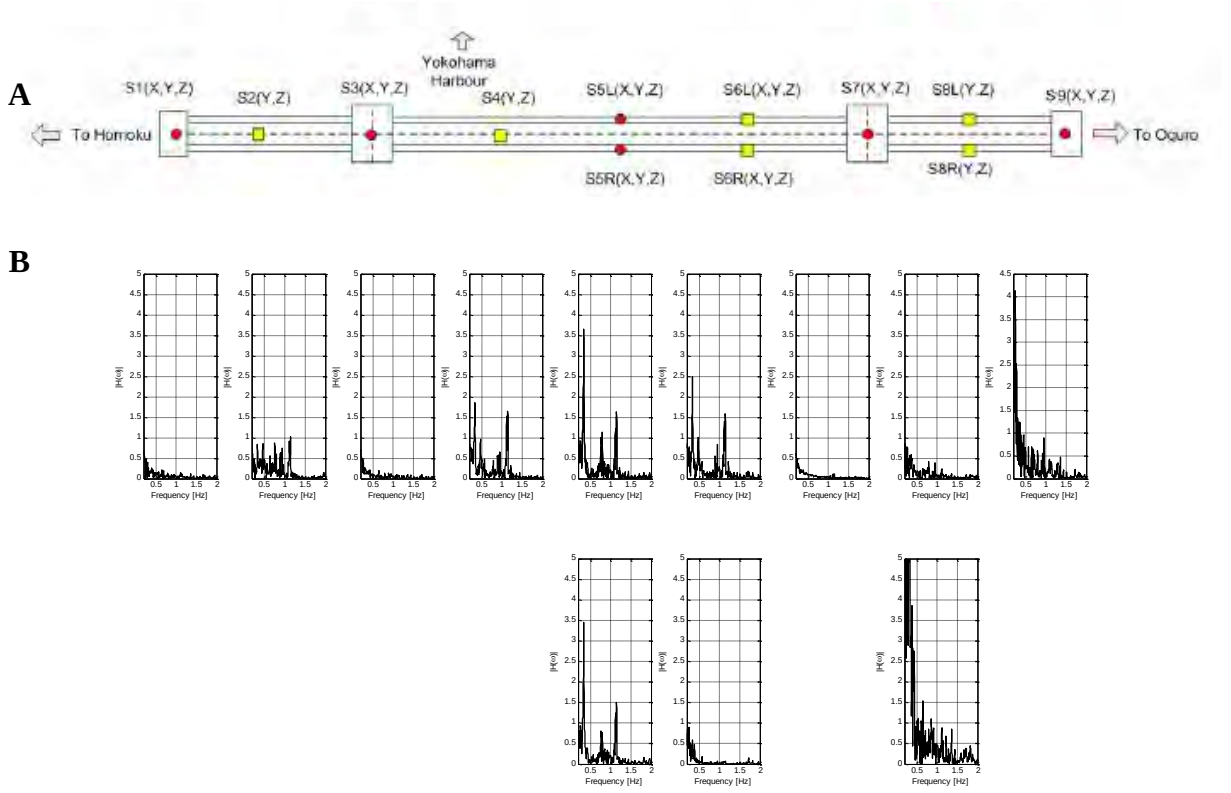


**Figure 12**. Transfer functions of the vertical displacements of the deck during the main shock event. **A**: Sensor locations on the deck. **B**: Transfer functions of the vertical displacements. The plots follow the sequence of the sensors displayed in the sensor map.

The preliminary frequency content analysis performed through these transfer functions allowed identifying several dominant frequencies associated with natural vibration modes of the bridge. An example is given by the transfer functions plotted in **Fig. 12B**. Peaks at frequency values of 0.34 Hz, 0.79 Hz for the sensors S2 (mid side-span), S4 (1/4 main-span), S5L/R (mid main-span), and S6L/R (3/4 main-span) suggest symmetric vertical modes of the deck. Peaks at frequency values of 0.47 Hz, 0.95 Hz for the sensors S2 (mid side-span), S4 (1/4 main-span), and S6L/R (3/4 main-span) suggest asymmetric vertical mode shapes.

For the longitudinal motion of the deck, three frequencies are identified from the analysis of the transfer function plots of **Fig. 13**: 0.12 Hz 1.6Hz, 1.75Hz. Peak values at the first frequency of 0.12Hz appear higher than all the other peak values. The amplitude of the transfer function peaks is practically

constant along the bridge. This frequency is associated with a swing mode of the deck, and is in good agreement with the expected frequency of 0.13 Hz. This mode involves slippage of the above mentioned hinge link-bearing connections.

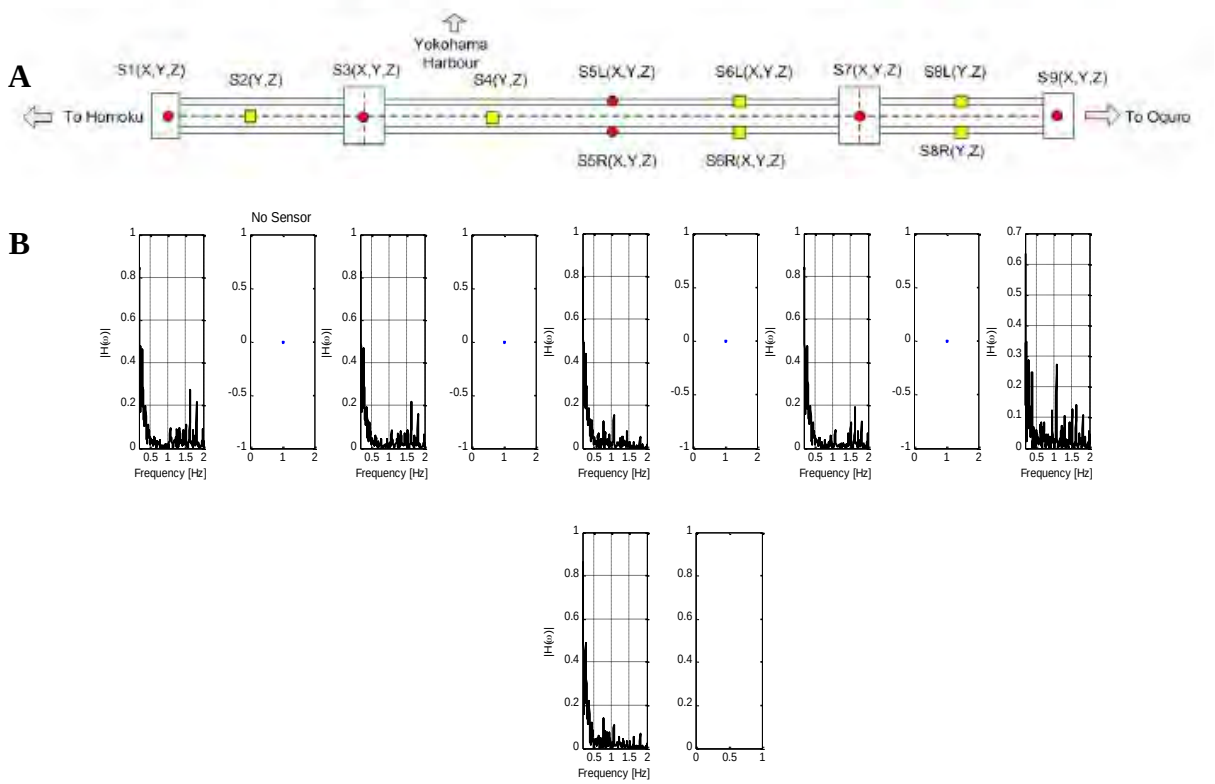


**Figure 13**. Transfer functions of the longitudinal displacements of the deck during the main shock event. **A**: Sensor locations on the deck. **B**: Transfer functions of the longitudinal displacement. The plots follow the sequence of the sensors displayed in the sensor map.

In **Fig. 14**, transfer functions of the longitudinal displacements are plotted for both the towers of the bridge. The analysis of these transfer functions confirms the presence of significant longitudinal oscillations at a frequency of about 0.12 Hz.

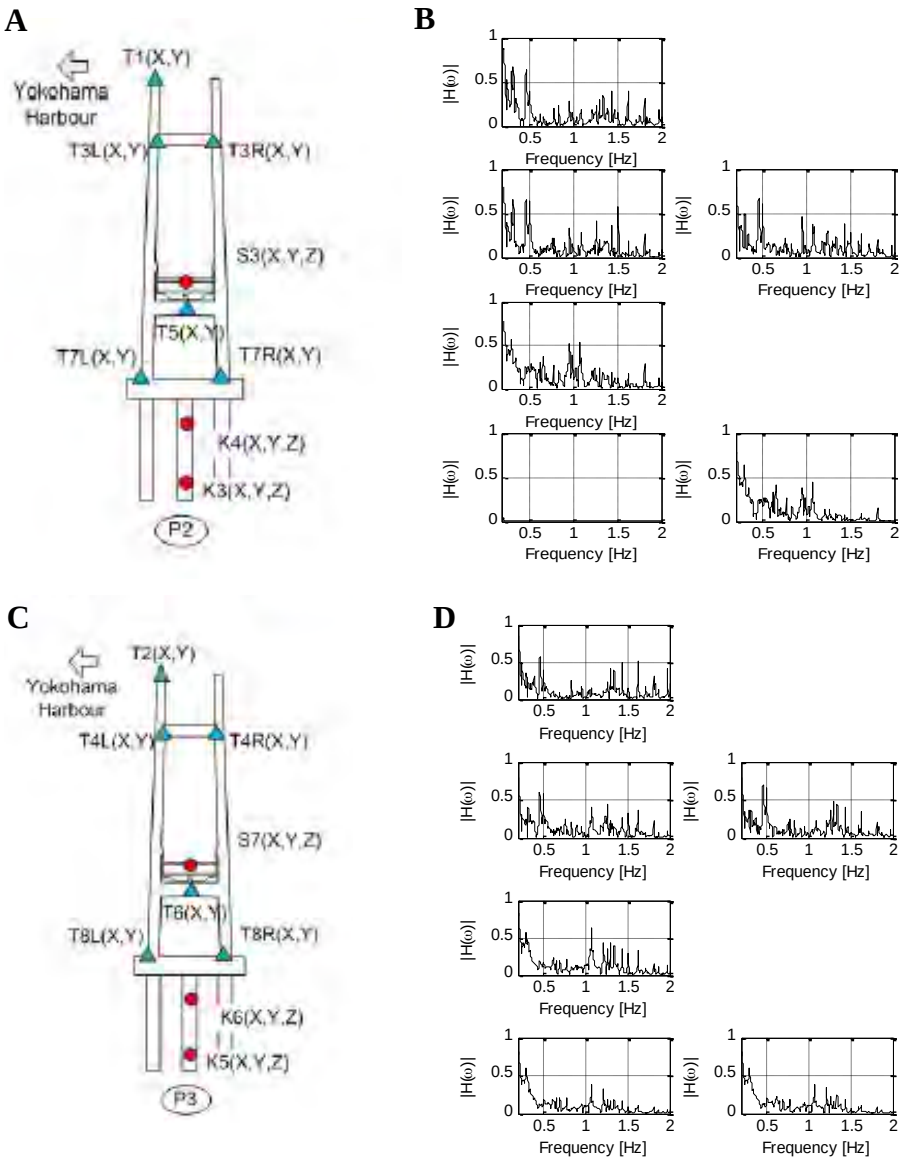


**Figure 14**. Transfer functions of the longitudinal displacements of the towers during the main shock event. **A**: Sensor locations on the Tower #1 (Homoku side). **B**: Transfer functions of the longitudinal displacements of Tower #1. **C**: Sensor locations on the Tower #2 (Oguru side). **D**: Transfer functions of the longitudinal displacements of Tower #1.

Three frequencies are identified from the transfer functions of the lateral displacements: 0.32 Hz, 0.42Hz, and 0.54Hz (**Fig. 15**). The first frequency 0.32 Hz is associated with increasing displacement amplitude along the deck towards the midspan of the bridge at both the Homoku and the Oguro sides. The displacement pattern associated with the 0.42 Hz frequency suggests a sinusoidal shape, with displacement in the side span in opposition with the displacement in the midspan.

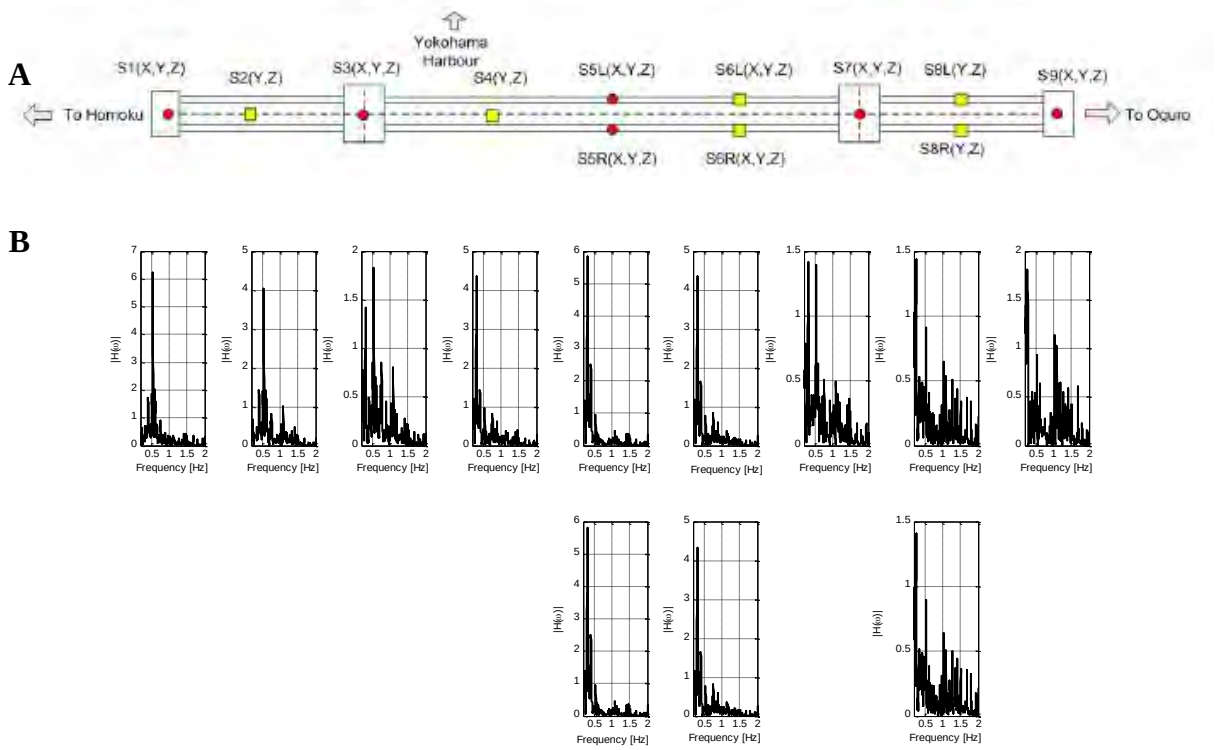


**Figure 15**. Transfer functions of the lateral displacements of the deck during the main shock event. **A**: Sensor locations on the deck. **B**: Transfer functions of the lateral displacement. The plots follow the sequence of the sensors displayed in the sensor map.

From the analysis of the lateral transfer functions of the towers (**Fig. 16**), main peaks are identified at frequency values of 0.31 Hz, 0.42, Hz, and 0.56 Hz, which are very close to the values identified for the deck's lateral displacement.

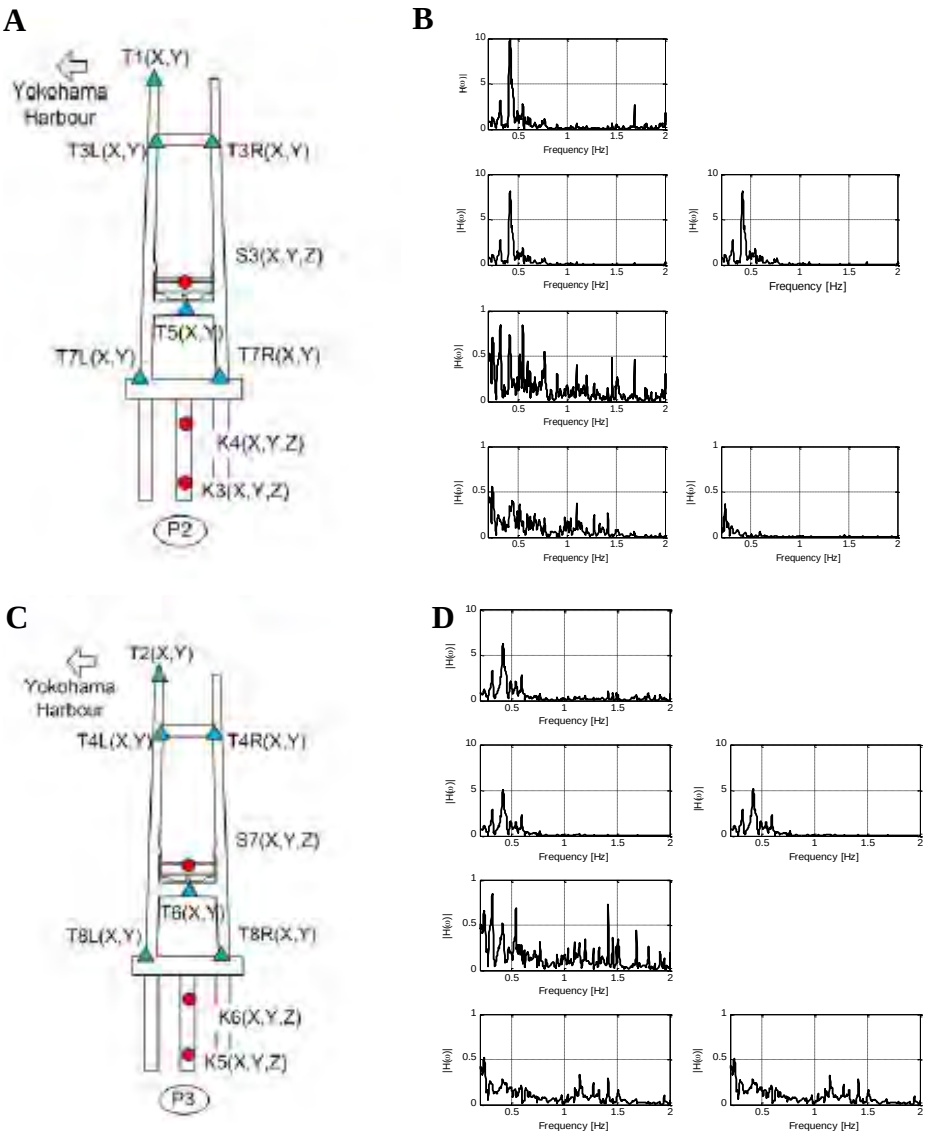


**Figure 16**. Transfer functions of the lateral displacements of the towers during the main shock event. **A**: Sensor locations on the Tower #1 (Homoku side). **B**: Transfer functions of the lateral displacements of Tower #1. **C**: Sensor locations on the Tower #2 (Oguru side). **D**: Transfer functions of the longitudinal displacements of Tower #1.

In summary, the preliminary analysis of the frequency response of the bridge led to the following considerations.

1. All the sensors between the tower and the end piers at the Oguro side of the bridge appear malfunctioning. These sensors are not be included in the damage analysis. This missing information does not allow a reliable identification of non-symmetric modes of the bridge. For this reason only symmetric modes are considered in the analysis. In order to assess the mode shapes of the whole deck, the acceleration time histories from the Homoku side of the bridge are mirrored to substitute missing acceleration histories at the Oguro side.
2. After a three step baseline correction, the displacement histories were converted to transfer functions and used to identify the main oscillation frequencies of the bridge. The principal mode frequencies identified in the longitudinal, lateral, and vertical direction are 0.12 Hz, 0.32 Hz, and 0.34 Hz, respectively. The first longitudinal mode appears as a swinging mode of the deck. The vertical and lateral modes have very similar frequencies and are likely to be coupled.

## Damage detection on the Yokohama Bay Bridge

In order to detect possible damage states in the bridge components, the SHM algorithm presented in Bonessio et al. (2011) and Benzoni et al. (2012) has been used. The proposed approach use acceleration records from a dispersed set of sensors to obtain information about the condition of the entire structure. The SHM procedure detects damages based on the changes of the modal characteristics of the bridge between a reference “undamaged” condition and a “possible damage” condition. The procedure was developed specifically to allow identifying damages at a local level (in bearings, restraints and seismic devices) as well as at a global level. The “local” detection of performance changes is of paramount importance. All the devices installed on a bridge, in fact, tend to concentrate a significant contribution to the performance of the structure and are a possible candidate for degradation during the service life as well as during seismic events. However, this information becomes relevant only if related to the “global” structural conditions. The variability of the device performance characteristics is, in fact, not immediately reflected in a critical change of the structural performance but should be identified through changes of the structural parameters.

The implemented algorithm of the procedure make it suitable for automation and the subsequent incorporation into specific computer codes. The DIIB (Damage Identification on Isolated Bridges) software is a program developed to identify early stages of degradation in monitored bridges by using the above mentioned procedure (Benzoni et al, 2013). Possible degraded conditions are detected in structural elements as well as in bearings and anti-seismic devices. The Yokohama Bridge was implemented into the DIIB software (**Fig. 17**) which provides graphical representation of the damage localization index Z and the damage quantification index $\alpha$ along the elements of the bridge.


**Figure 17**. Front page of the DIIB software. The interpretative scheme geometry of the Yokohama Bay Bridge is uploaded and shown in the figure panel. The nodes on the scheme correspond to available acquisition channels.

## *Identification of modal characteristics*

The software performs the structural identification of the bridge by means of an output only SSI-Cov (Peeters, 2000) analysis of the acceleration data at the sensor locations.

The SSI-Cov method is as an output-only response approach, i.e. the structure is treated as excited by an unknown input and only output measurements (e.g. accelerations) are available. This condition closely represents the reality of a complex structure under a program of monitoring for structural health assessment purposes. For the SSI-Cov method the deterministic knowledge of the input is replaced by the assumption that the input is a realization of a stochastic process (white noise).

In the evaluation of the mode shapes, the malfunctioning channels on the Oguru side of the bridge were substituted with the symmetric channels on the Homoku side. Due to this approximation, only symmetric modes can be identified and mode shapes can not be used for the damage identification on the Oguro side of the bridge.

Slight changes in the modal characteristics of the bridge have been identified for different ground motions. Three principal modes, one in each of the three response directions (longitudinal, lateral, and

vertical), were identified. Average values and standard deviation of the vibration frequencies of the three modes are:

1st Longitudinal mode - frequency: 0.118 ± 0.017 Hz (Coefficient Of Variation COV = 0.144)

1st Lateral mode - frequency: 0.295 ± 0.011 Hz (COV = 0.037)

1st Vertical mode - frequency: 0.372 ± 0.022 Hz (COV = 0.059)

A plot of the vibration frequencies for different events is presented in **Fig. 18**.

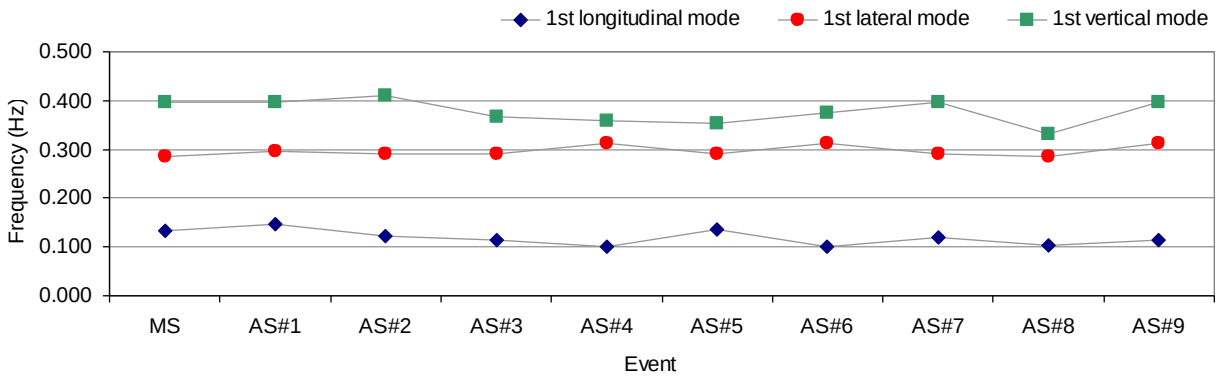


**Figure 18**. Vibration frequency of the principal modes of the bridge in longitudinal, lateral and vertical direction as identified from main shock and after shocks data.

The variation of the vibration frequency as identified from different data sets is limited and can be attributed to different sources. The change in natural frequencies may indicate non linearity of the bridge behavior. Several factors such as material nonlinearity, geometric nonlinearity due to large displacement in cable and behavior of pier-to-girder and tower-to-girder connections are known as common sources of nonlinearity in cable-stayed bridge seismic response. Environmental conditions can also affect the behavior of the bridge. The highest variation, expressed by the Coefficient Of Variation (COV), was found for the longitudinal mode, while the frequency of the lateral mode appeared the most stable. The magnitude of the frequency changes is in a typical range of variation for in field testing of bridges. Raghavendrachar and Aktan (1992) found nearly 10% changes in frequencies due to changes in ambient conditions for a multispan reinforced concrete bridge. Fu and De Wolf (2001) identified approximately the same range of frequency shift for a steel-girder bridge, as due only to temperature changes. Brincker et al. (2001) showed that mode shape information becomes more important in the damage detection since mode shapes are less sensitive to temperature changes than natural frequencies.

In **Fig. 19** the three principal mode shapes in longitudinal, vertical and lateral direction are presented, as identified from the main shock data set. The first longitudinal mode is a swing mode. This mode shows a relatively large modal displacement between the end-pier's cap and the girder, indicating a hinge mechanism between the pier-cap and girder during the earthquake. Girder motion in longitudinal

direction is accommodated by the link-bearing connections. These connections are expected to slide during an earthquake so that large vibration energy from the pier or tower would not be transferred to the girder and vice-versa (Maeda et al. 1991). In such condition, relative displacement between pier and girder and between tower and girder will be sufficiently large and the high frequency components of the pier and tower vibration will not be transferred to the deck. The second mode involves the vertical oscillation of the deck and longitudinal oscillation of the towers. The third plot represents a top view of the first lateral mode of the bridge.

In order to identify modes for a reference (undamaged) condition, the first 20 seconds of the main shock, characterized by low acceleration levels, were isolated and treated as an independent acceleration data set. Modes identified from this reference data set are presented in **Fig. 20**. Since there is no significant change in the environmental conditions, the differences between the modes of **Fig. 19** and **Fig. 20** may indicate that the bridge response has entered the non-linear region during the main shock due to the higher excitation amplitude. One difference is particularly remarkable in the first longitudinal modal shape. While during the main shock, the vibration of the bridge is characterized by slippage at both the bearing-link connections, during the first 20 seconds of the input, slippage occurred only at the tower #1, on the Homoku side of the bridge. This difference could be attributed to a non-linear behavior of the link-bearing connections. This connection is in fact affected by friction forces and for low excitation levels does not function as a fully hinged connection. Any difference in the friction force of the two connections could produce differential slippage.

As a comparison with the modes shapes of **Fig. 19** and **Fig. 20**, mode shapes identified from the after shock #3, which is characterized by a lower excitation level, are presented in **Fig. 21**. For the longitudinal mode identified from the after shock records, the relative displacement of the deck to the towers appears lower than in the main shock modes. As mentioned above, this difference could be attributed to frictional forces in the link-bearing connections. The greatest slippage appears again at the tower #1, on the Homoku side of the bridge, suggesting that a difference in friction between the two connections may be present.

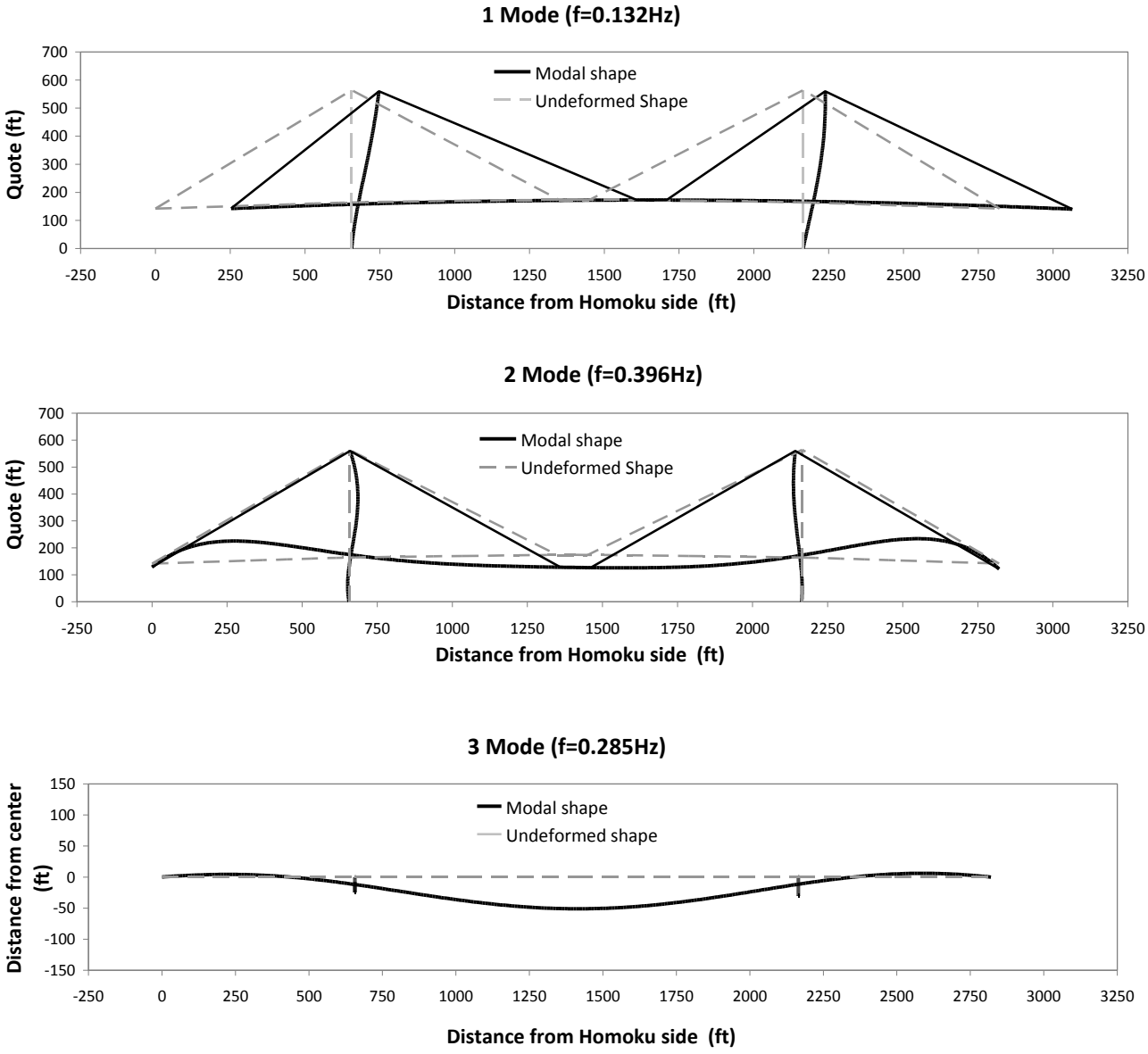


**Figure 19**. Mode shapes and frequencies identified from the main shock acceleration data set. Top figure: first longitudinal mode. Middle figure: first vertical mode. Bottom figure: first lateral mode (view from the top).

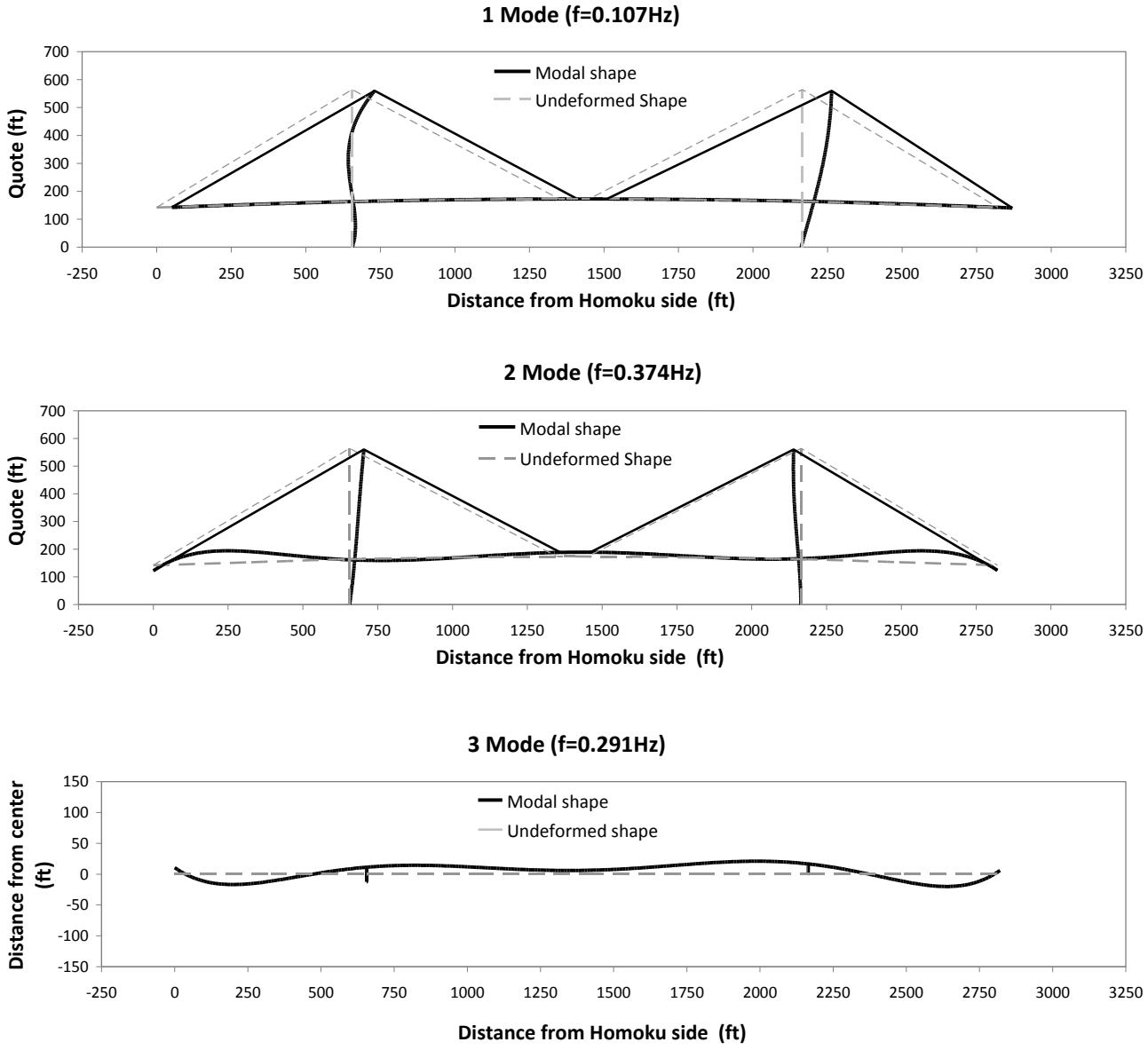


**Figure 20**. Mode shapes and frequencies identified from the first 20 seconds of the main shock. Top figure: first longitudinal mode. Middle figure: first vertical mode. Bottom figure: first lateral mode (view from the top).

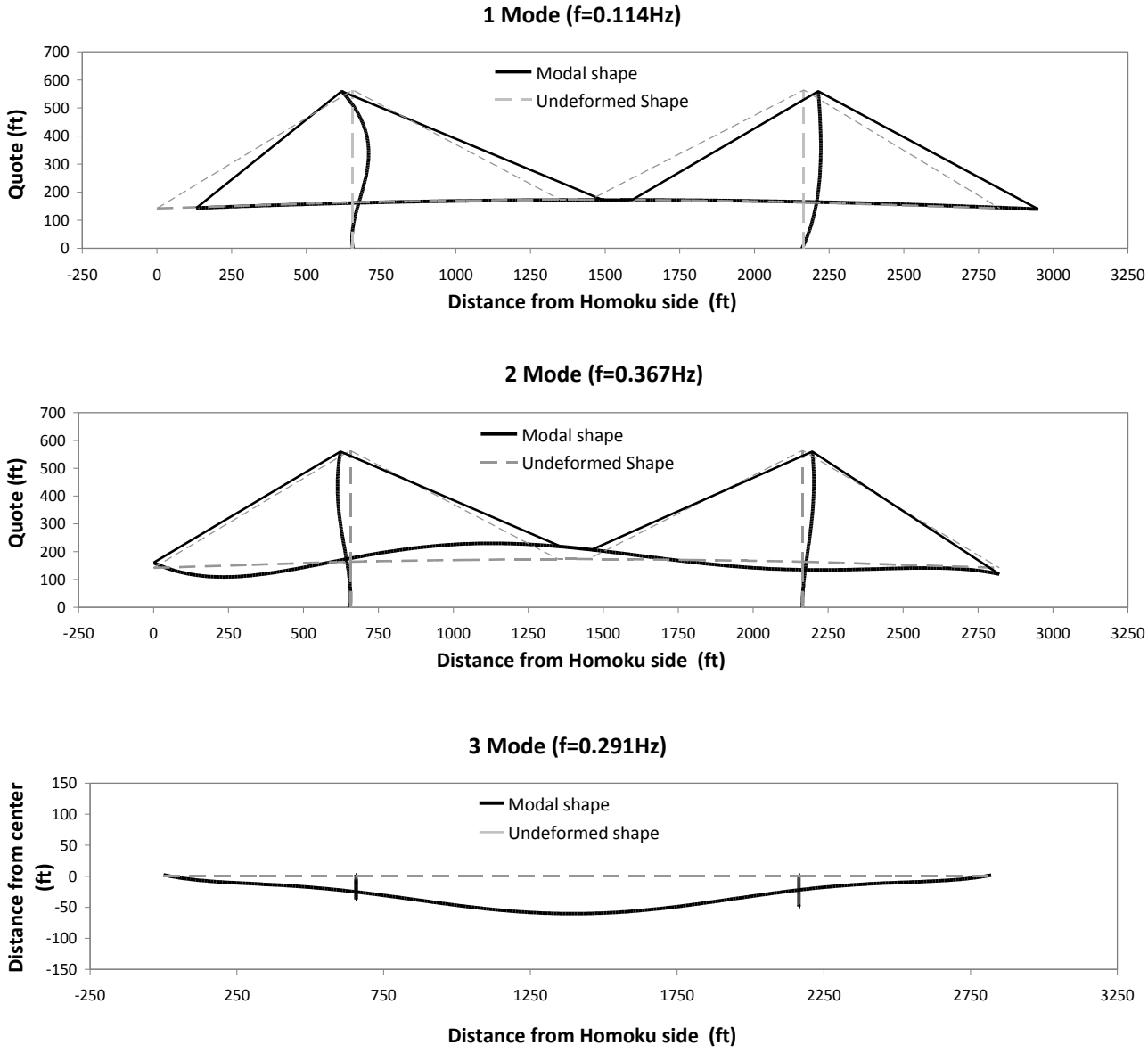


**Figure 21**. Mode shapes and frequencies identified from the after shock #3 acceleration data set. Top figure: first longitudinal mode. Middle figure: first vertical mode. Bottom figure: first lateral mode (view from the top).

### *Damage identification*

The proposed damage detection algorithm use changes in the modal strain energy to detect damages in deck to tower links, as well as in structural parts of the bridge. For the *i-th* vibration mode, the damage in the *j-th* element with respect to the reference *k-th* element is localized through the localization parameter:

$$\beta_{i,jk} = \frac{\int_{L_j} \varepsilon^{*2} dl}{\int_{L_j} \varepsilon^{2} dl} \cdot \frac{\int_{L_k} \varepsilon^{2} dl}{\int_{L_k} \varepsilon^{*2} dl} \qquad (1).$$

A normalized term, for the generic *j-th* term and *i-th* mode is defined as

$$\beta_{i,j} = \frac{\beta_{i,jk}}{\beta_{i,k_{\min}}} \qquad (2).$$

The multi-modal localization term for the *j-th* element was defined by combination of the modal components:

$$\beta_j = \sum_{i=1}^{n} \gamma_i \beta_{i,j} \qquad (3)$$

with the reliability parameter for each mode defined as:

$$\gamma_i = \frac{(1/q_i)^2}{\sum_{i=1}^{n} (1/q_i)^2} \qquad (4)$$

The multi-modal localization term is used for the definition of a damage localization index calculated as:

$$Z_j = \left| \frac{\beta_j - \bar{\beta}}{\sigma_\beta} \right| \qquad (5)$$

where the parameters $\bar{\beta}$ and $\sigma_\beta$ represent the mean and the standard deviation of $\beta_j$, respectively. The damaged condition, for the *j-th* element, is indicated by a value of $Z_j \geq 2$ if a probability of 98% is required.

The proposed algorithm allows also the assessment of the severity level of the damage expressed through the index $\alpha_j$ that represents the fractional change in stiffness of the j-th element:

$$\alpha_j = (\beta_j)^{-0.5} - 1 \qquad \alpha_j \geq -1 \qquad (6).$$

The algorithm was applied to the bridge to detect damages with respect to a reference (undamaged) condition. The first 20 seconds of the main shock acceleration data were used as reference acceleration data set. In **Fig. 22**, the red circles identify damage location identified through the condition $Z_j \geq 2$ for the main shock.

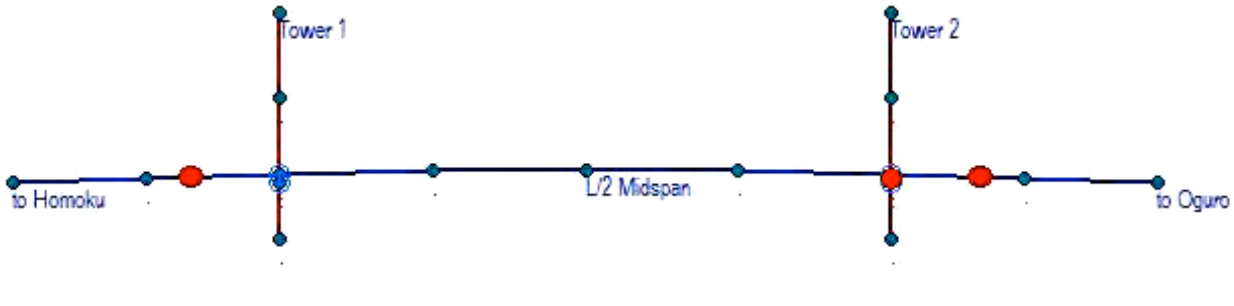


**Figure 22**. Damage locations on the bridge identified for the main shock. Reference condition: first 20 seconds of the main shock.

The damage detection algorithm identifies the side span of the bridge and the link between deck and tower at the Oguro side as possible damage locations. The damage localization index Z and the damage severity index $\alpha$ are plotted in **Fig. 23** for the deck, the devices and the towers. For the deck, the location is expressed as the distance (in ft) from the Homoku end, while for the towers, the location is given from the top of the foundation. Conventionally, the devices are concentrated in the schematic of the bridge at the end of the deck. The results for the two towers are consecutively plotted on the same graph.

Damages on the deck are identified where Z index exceeds the values +2 along the deck. Two spikes of the Z distribution along the deck exceed the threshold at 480 ft and 2390 ft from the Homoku side. These two occurrences appear as false positives numerically generated by close-to-zero values of the curvature of the deck in the vertical mode. In case of very small curvature values, in fact, even a small variation between the reference and the present condition corresponds to a high increment of the Z index. Using many vibration modes in vertical direction would reduce the occurrence of this type of false-positives. It should be noted that these high values of the Z index correspond to very limited values of the damage severity index $\alpha$ ($|\alpha| < 5\%$).

The damage in the connection links is identified by the last spike in the Z index plot, which significantly exceeds the threshold value of 2. The damage severity index $\alpha$ associated with this damage is about -0.8, which means that a reduction of stiffness of about 80% occurred during the main shock. As mentioned above, this reduction of stiffness could be attributed to transition between a predominantly stick behavior of the bearing-link connections to a predominantly slip behavior. From the visual inspection reported in (Siringorino and Fujino 2012), scratches were found on the wind shoes of the tower #2 suggesting that the girder had experienced large relative longitudinal movement. For this relative displacement to occur, the link-bearing connections between girder and tower must have slipped. This physical evidence supports the results of the response analysis and the type of longitudinal mode generated by the system identification procedure. In addition, since between the wind shoe and the deck a lateral gap was provided, the reported would only be possible if the deck came into contact with the wind shoes due to lateral movements.

For the low intensity after shock #3, a similar distribution of damages along the structure was identified. The localization of the damages for this earthquake is presented in **Fig. 24**. The damage locations identified on the Oguro side are not considered reliable due to the absence of acceleration data in that portion of the bridge. As shown in **Fig. 25**, the damage severity index $\alpha$ for the link deck-tower indicates a stiffness reduction of about -60% in the link-bearing connection, which suggests that the hinge connections were not functioning as fully hinged links.

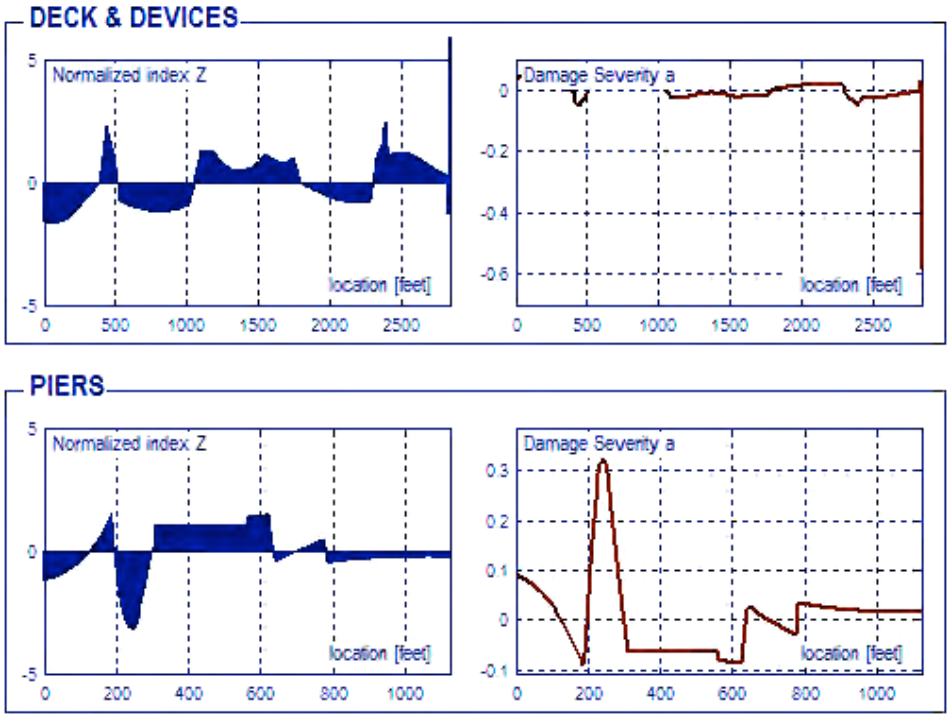


**Figure 23**. Damage localization normalized index Z and damage severity index α along the deck and the tower structures for the main shock. Reference condition: first 20 seconds of the main shock.

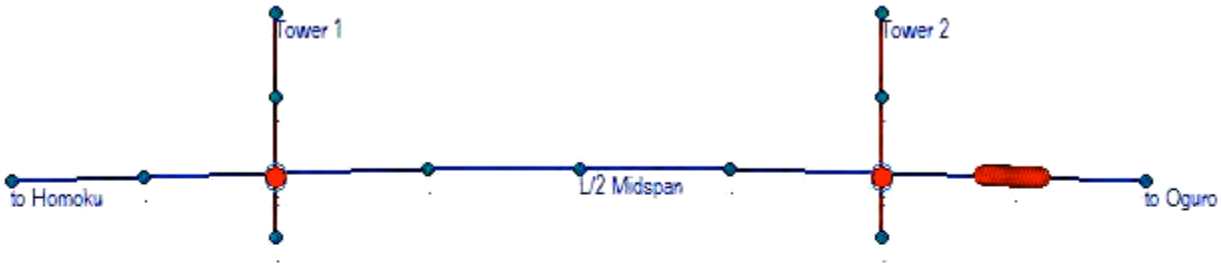


**Figure 24**. Damage locations on the bridge identified for the after shock #3. Reference condition: first 20 seconds of the main shock.

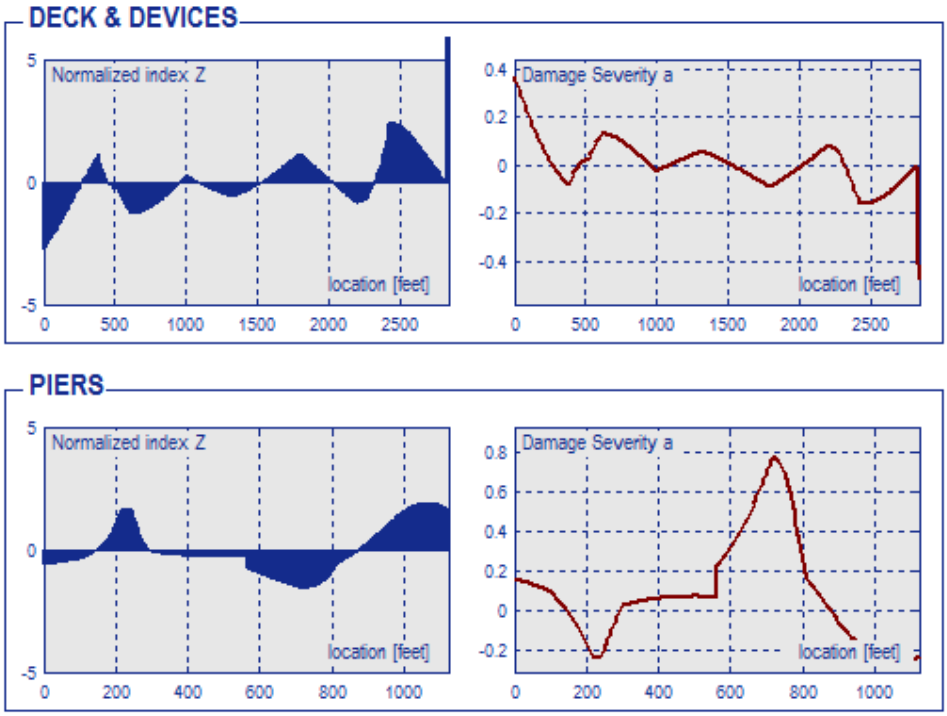


**Figure 25**. Damage localization normalized index Z and damage severity index a along the deck and the tower structures.

## Discussion of results

The response of the Yokohama Bay Bridge to the 2011 Great East Japan earthquake and following aftershocks is analyzed. Even if the analysis is conditioned by the absence of reliable acceleration data from the Oguro side of the bridge, based on the results of the damage detection procedure no structural damage to the Yokohama Bay Bridge was identified for the main shock excitations and the following after shocks. This is in agreement with the design expectations, since the excitations were considerably below the design and seismic-retrofit seismic loads (Maeda et al. 1991). The damage detection procedure identified changes in stiffness of the link-bearing connections between towers and deck, probably due to friction forces affecting the hinge mechanism. During the highest amplitude excitation, these connections appear effective in suspending the bridge deck to the towers and in reducing superstructure inertia force on the substructure. In locations characterized by close-to-zero curvature values from the first vertical mode, small absolute variations in curvature between the reference and the present condition introduced big increments of the Z parameter, i.e. false positives in the damage localization. Replacement of malfunctioning sensors, which would allow including further vibration modes, would certainly help in reducing these localization errors.

# References

Bonessio N., Lomiento G., Benzoni G., [2011] “Damage identification procedure for seismically isolated bridges”, Structural Control Health Monitoring, DOI:10.1002/stc448.

Benzoni G., Bonessio N., Lomiento G., [2011] “Structural Health Monitoring of Bridges with Anti-Seismic Devices” Proceedings of the 8th European Conference on Structural Dynamics (Eurodyn 2011), Leuven, Belgium 4-6 July 2011.

Benzoni G., Bonessio N., Lomiento G., [2013] “Structural Health Monitoring of Bridges with Seismic Response Modification Devices” Structural System Research Projects, Department of Structural Engineering, University of California San Diego, Report SSRP-13/02, May.

Raghavendrachar, M. and A. E. Aktan (1992) "Flexibility by Multireference Impact Testing for Bridge Diagnostics," ASCE Journal of Structural Engineering, 118, 2 186-2203.

Benzoni, G. and Seible, F. [1998] “Design of The Caltrans Seismic Response Modification Device (SRMD) Test Facility,” Proc. of the USA – ITALY Workshop on Protective Systems, Report No. MCEER-98-0015, Multidisciplinary Center for Earthquake Engineering Research, Buffalo, New York City.

CSI Analysis Reference Manual for SAP200®, ETABS®, and SAFE™, 2007, Computers and Structures, Inc, Berkley, California.

Mevel, L., Goursat, M., and Basseville, M. (2003). "Stochastic subspace-based structural identification and damage detection and localisation—application to the Z24 bridge benchmark." Mechanical Systems and Signal Processing 17.1: 143-151.

Fu, Y., and DeWolf, J. T. (2001) "Monitoring and analysis of a bridge with partially restrained bearings." Journal of Bridge Engineering 6.1: 23-29.

Farrar, C. R., and Jauregui D.A. (1999a) "Comparative study of damage identification algorithms applied to a bridge: I. Experiment." Smart Materials and Structures 7.5: 704.

Maeda, K. Otsuka, A. Takano, H. (1991), “The design and construction of Yokohama Bay Bridge, Cable-Stayed Bridges Recent Developments and their Futures”. M.Ito et.al. (Editors). Elsevier Science Publisher B.V.377-395.

Siringorino, D. M., Fujino, Y, (2012) “Response Analysis of Yokohama Bay Bridge under the 2011 Great East Japan Earthquake”, Proc. 15th World Conference of Earthquake Enineering, Lisbon, Portugal.

# Level III damage identification of a bridge model

By Gianmario Benzoni, Giuseppe Lomiento, Noemi Bonessio

## Disclaimer

The opinions, recommendations and conclusions contained within this report are solely those of the authors, and do not necessarily reflect the views or policies of the project sponsors. This report does not constitute a standard, specification, or regulation.

## Summary

## List of figures

## List of tables

## Abstract

Aimed at evaluating the efficacy of ambient vibration based damage identification procedures for bridges equipped with sparse sensor networks, shake table tests were conducted on a two-columns one-span model bridge in which damages were simulated through steel parts removal from different portions of the structure. The damage identification capability of a multi-modal strain-based method (Bonessio et al. 2012) was investigated for low-amplitude mono- and tri-dimensional vibration conditions. The experimental tests were performed at the Caltrans Seismic Response Modification Devices (SRMD) facility at the University of California San Diego. Vibration data collected through wired accelerometers, widely used in existing sensor network installations on bridge infrastructure, were processed to identify modal dynamic characteristics of the bridge model in un-damaged and damaged conditions. A minimum number of sensors strictly necessary for proper description of the curvature distribution along damaged structural elements were used. The identified modal characteristics were subsequently used for a level III damage identification (damage detection, localization and severity estimation).

The procedure appeared able to identify presence of local damages in different portions of the bridge even for complex scenarios, involving simultaneous damages in the columns and the longitudinal beams of the deck. Damages were localized and quantified in terms of stiffness reduction with an acceptable level of precision. Errors in the assessment of the damage extension and severity was mainly attributed to lack of robustness in the evaluation of modal vectors from the system identification and can be reduced by a more dense sensors distribution. Compared to single-mode damage detection, the use of multiple vibration modes allowed a more stable localization of the damage. However, since damages have different effects depending on the direction of deflection of the damaged elements, it was easier to interpret single-mode than multi-modal severity indices, which provide average measures of damages from vibration modes in different directions.

Data collected from the experimental campaign on the model bridge constitutes a valuable base for further benchmark investigations of damage identification procedures. An extension of the test campaign is proposed to complete the already available dataset with additional damage scenarios, which represent bottom to top damage propagation in bridge columns and degradation of seismic isolators installed right below the deck.

## Introduction

Since the earliest applications, downscaled models in which controlled damages were simulated in a lab environment have been used to evaluate the effectiveness of Structural Health Monitoring (SHM) techniques for bridge structures. Even if mainly focused on simplified damage scenarios involving deck elements and bearings, these experimental studies provided remarkable results which contributed to understanding of critical aspects of system identification and damage detection procedures applied to bridge structures. Support failures and crack propagation were investigated on a two-span aluminum plate-girder deck by Mazurek and De Wolf (1990). Results of this study highlighted how mode shapes are heavily influenced by crack propagation, with the greatest changes in the proximity of the defect. Test beams designed to respond similarly to actual bridges with different damage scenarios (type, location, degree) were subjected to low-level free vibration tests by Spyrakos, et al. (1990). The study suggested that mode shapes may be used to locate damage based on input-output system identification. In (Spillman and Williams, 1993), an instrumented scale model bridge was investigated to check the feasibility of neural processing applied to structural damage detection. The bridge element under investigation was a flexible steel beam 4.58 meters in length. The beam was modified so that various states of damage could be introduced by the removal or addition of gusset plates over damaged cross sections. Following these studies, which were focused specifically on deck elements of bridges, Liang et al. (1997) tested a 1:6 down-scaled model of a single span highway bridge. Also in this study, however, all the simulated damage conditions were introduced into the deck and the bearings, by cutting the girder at the middle span and removing one of the bearings of the bridge. Results showed that the location of the damage can be determined by using changes of the modal energy transfer ratio. In more recent studies, system identification and statistical pattern recognition approaches were applied to vibration data from model bridge decks. In (Haritos and Owen, 2004), three scale model reinforced-concrete flat slab bridge configurations were used to verify the ability of recognition approached in providing information about the location and severity of damage. Further studies that investigate the feasibility of the detection of damages occurring simultaneously in different portions of bridge structures, including deck, columns and seismic devices, are now compelling.

The object of this report is the application of damage detection procedure to a steel bridge model, which is specifically designed to simulate simultaneous damages with different levels of severity at different locations of columns, deck and bearings, from low amplitude shake table tests. A comprehensive study of the bridge model was conducted to verify the applicability of a damage detection algorithm initially developed for seismic response modification devices of bridges (Bonessio et al. 2012) to complex damage scenarios in bridge structures. The data collected from the experimental test program constitutes an

unique database that can be used for future evaluation of the damage detection capability of different SHM algorithms.

## Experimental test program

The experimental test program consisted of low amplitude shake table tests, simulating ambient vibration in three orthogonal directions, namely longitudinal, lateral, and vertical direction, on a small scale steel specimen of a two-column bridge. The tests have the principal objective to verify the capability of methods for the detection of a given damage scenario simulated on the columns and deck of the bridge. The investigation consists of a system identification phase where data from accelerometric records are used to determine the dynamic characteristics of the bridge, and of a damage detection phase where a procedure is applied to localize and quantify damages based on changes of the identified dynamic characteristics with respect to a baseline undamaged condition.

For the damage assessment a series of five damage scenarios were simulated by extracting specifically designed removable steel flanges from the columns and the beam elements, as described in details in the next paragraph. The identification of the modal characteristics was performed through mono- and multi-directional excitations and thus information about improvements in the damage detection due to use of multiple modes in different direction is available. The bridge model and test setup, the prediction of its dynamic behavior, and tests results are summarized in the following.

### Bridge model and test setup

The one-span steel bridge model was conceived to allow removing parts on columns and deck elements and to accommodate viscous dampers and friction isolators. The model is composed by two identical columns and one single-span deck structure, realized by two longitudinal beam elements connected by transversal secondary beams. The column section is made of four flanged vertical portions, each one constituted by a central hollow rectangular section HSS8x4x1/4 and four peripheral C4x7.25 sections, and a cap beam for the connection with the deck. The total column height is 82”, while the width of the cap beam is 51”. The deck is made by two steel boxes, realized with ½” thick plates, connected by two tri-parted longitudinal W6x15 beams, with additional bottom and top ¼” plates to augment flanges thickness. The deck structure is 126” length by 64” wide. A total of 44 structural parts (16 in each column and 12 in the deck) are removable to simulate local damages in the structural bridge components. The use of removable parts to simulated damages is justified by the experimental program objective of not exceeding the elastic range in all the structural components, while at the same time reducing their stiffness in a controlled way. After damages are simulated, the previous undamaged condition can be restored by placing back the removed parts and the model can be used for further tests. The bridge model was

designed to allow connecting deck to the cap beams of the columns directly or through small scale friction concave isolators. Viscous dampers can also be installed between the column and the deck to improve the energy dissipation capacity of the bridge. Additional mass is provided through steel plates located over the deck structure (3,600 lb) to rise the vibration period of the system. Selected schematic drawings of the column are presented in **Fig. 1** and **Fig. 2**. In **Fig. 3** and **Fig. 4**, a plan view and two section views of the deck are presented, respectively. Removable parts are identified through orange patches. The additional steel plates are visible on top of the shake table installation of the bridge model shown in **Fig. 5**.

The present investigation deals with the bridge configuration without isolators and dissipating devices, for which the deck is directly connected to the columns through bolted connections able to transfer flexural moments. The bridge model was subjected to shake table tests in the Caltrans Seismic Response Modification Devices laboratory at the University of California, San Diego. The test installation consisted in (1) the placement of the bridge columns on the shake table with the orientation shown in Fig. 5, (2) the connection of the columns bottom 2" thick steel plates through 8 bolts each (moment resisting connection) to the table, (3) the placement of the deck structure (with clamped steel plates for additional mass) over the columns, (4) the connection of the deck to the columns cap beams through 8 bolts each (moment resisting connection), (5) the instrumentation with displacement transducers and wired accelerometers. In details, the sensor system was composed by:

- 5 displacement transducers (**Fig. 6**),
- 9 tri-ax wired accelerometers, labeled #1to9 (cyan colored in **Fig. 7**), and
- 8 mono-ax wired accelerometers (4 in Y dir + 2 in X dir + 2 in Z dir), labeled #10to17 (green colored in **Fig. 7**).

Additional feedback was provided by the 6 mono-ax accelerometers of the shake table.

Prior the shaking tests execution, a Finite Element Model (FEM) was implemented to analyze dynamic characteristics of the bridge model and calibrate the excitation input.

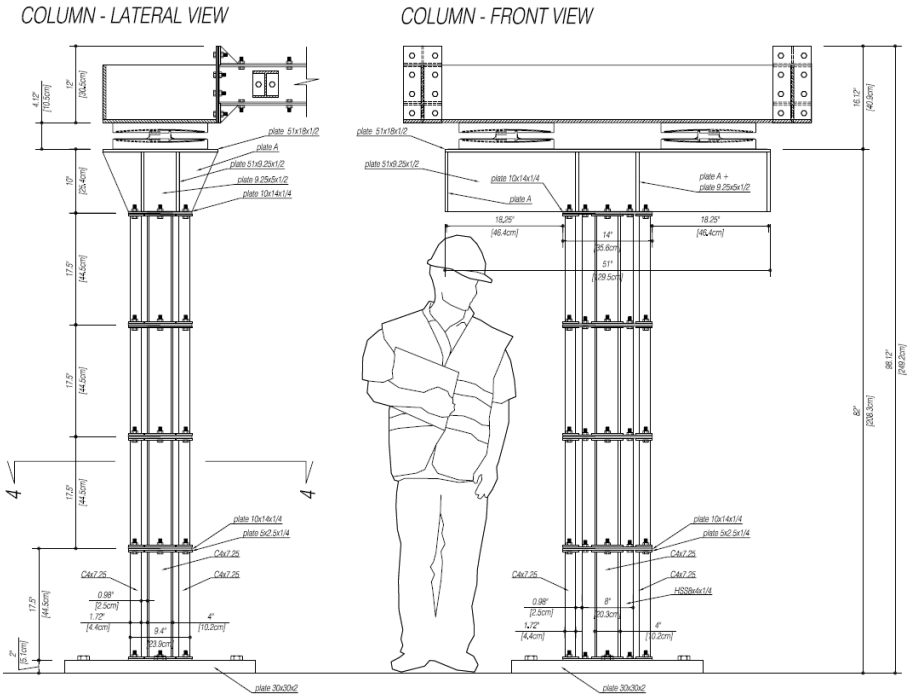


**Fig. 1.** Bridge column model. Lateral and front view of the steel column. Each column is composed by four segments and a cap beam.

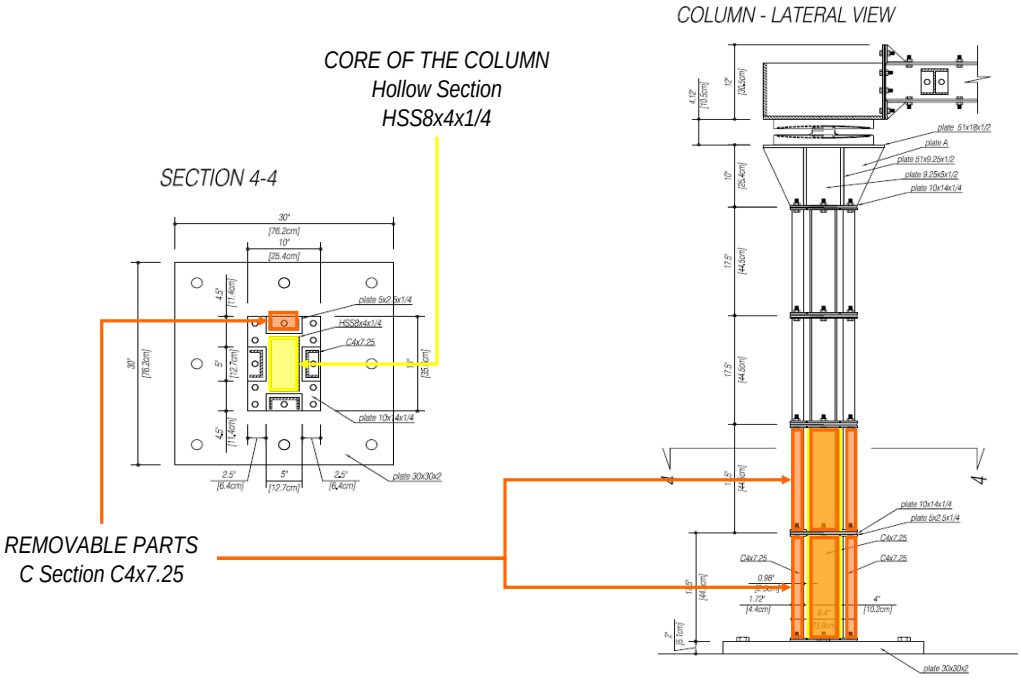


**Fig. 2.** Bridge model column. Four removable parts (orange) are provided in all the four structural segments of the columns. The fix part (yellow) of each structural element is a rectangular hollow section.

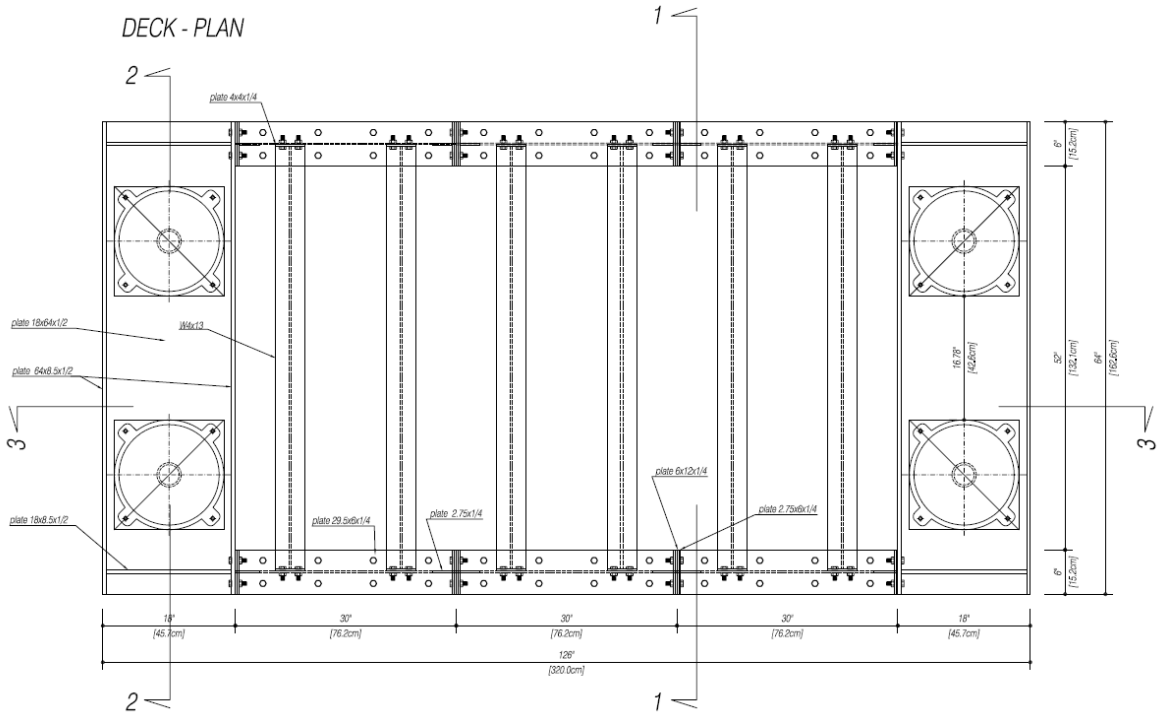


**Fig. 3.** Bridge deck model. Plan view of the steel deck. The deck is composed by two longitudinal primary beams, connected by six transversal secondary beams. Each longitudinal beam is divided into three segments. Two lateral steel boxes allow connecting the deck to the isolators or directly to the columns.

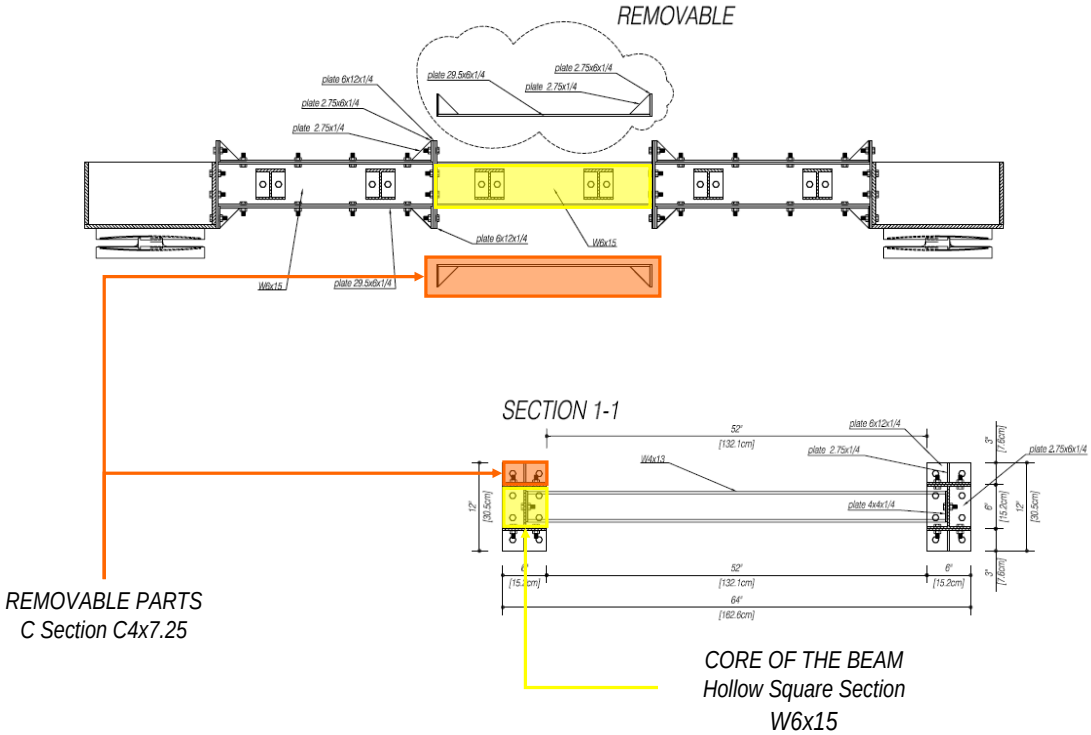


**Fig. 4.** Bridge model deck. Two removable flanges (orange) are provided in all the three structural segments of the longitudinal beams. The fix part (yellow) of each structural element is a I section.

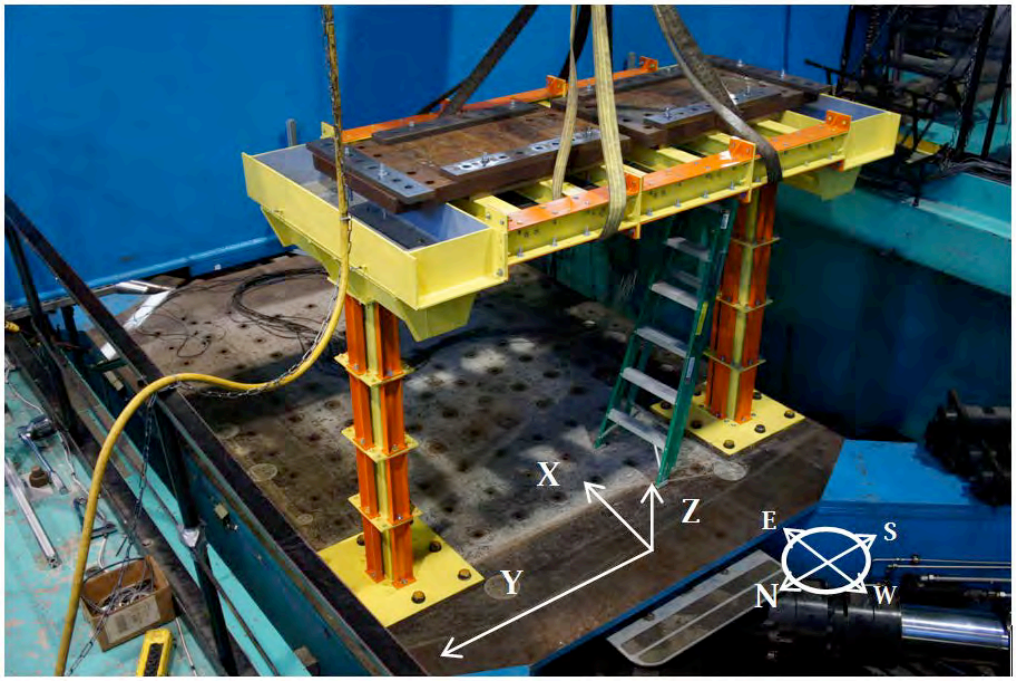


**Fig. 5.** Shake-table bridge model setup. Steel plates clamped to the secondary beams of the deck are added to increase the mass of the model. The deck is directly connected to the cap beams, without interposition of seismic isolators.

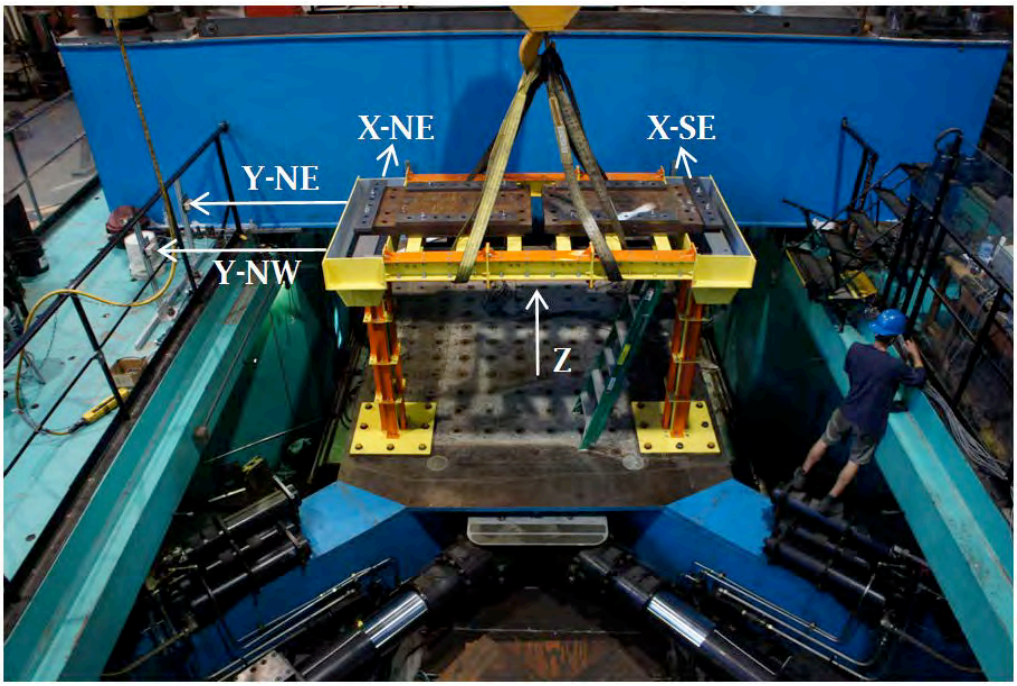


**Fig. 6.** Location and direction of the displacement transducers installed on the bridge. Y-dir transducers connect the deck to an external aluminum frame. X-dir transducers connect the deck to the transverse beam of the shake table. The Z-dir transducers connect the center of the deck to the shake table.

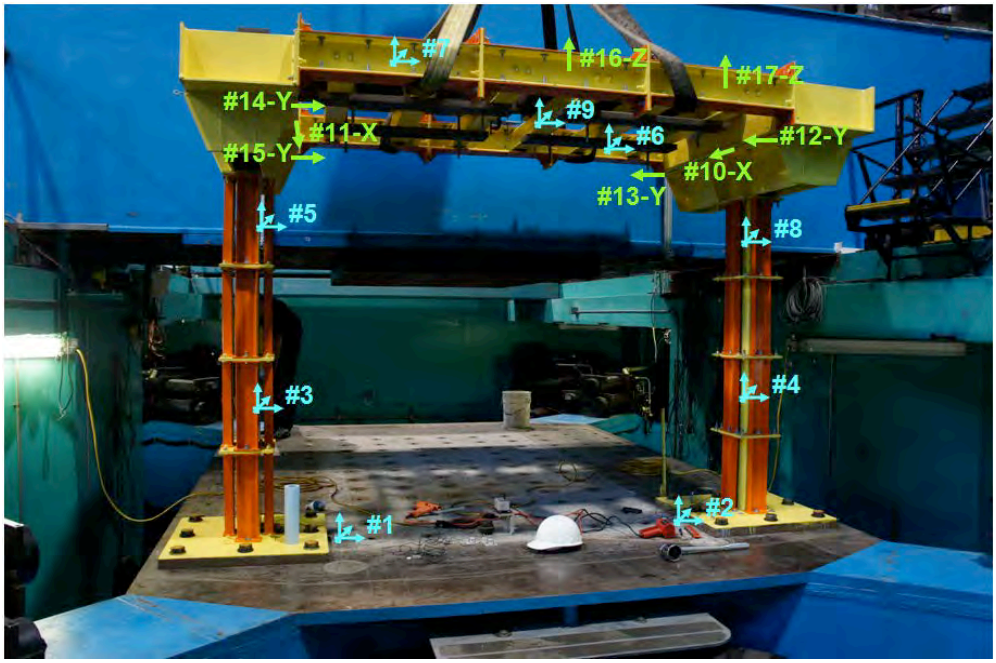


**Fig. 7.** Location and direction of the accelerometers installed on the bridge model: tri-ax accelerometers #1 to 9 (cyan) are installed on the columns and the deck structure; uni-ax accelerometers #10 to 15 (green) are installed on the cap beams of the columns; two additional uni-ax accelerometers #16 and 17 (green) are installed on the W beam of the deck.

## Finite Element Model

The elastic FEM of the bridge model was implemented in the structural analysis software SAP2000 ©. Shell elements, with plate and membrane behavior, were used to model the cap beams of the columns, the terminal portions of the deck, anchoring plates, and connecting flanges between beams and columns segments. Mono-dimensional frame elements were adopted for the single components of each segment of beams and columns and for the secondary transverse beams of the deck. A 3D view of the FEM model is displayed in **Fig. 8**.

Natural mode shapes and frequencies of the bridge model were evaluated through Finite Element modal Analysis. As expected, the first two modes results in a prevalent longitudinal and lateral motion, with a vibration frequency of 5.10 Hz and 6.21 Hz, respectively. The third natural mode involves a torsional motion of the deck, associated with an 8.70 Hz vibration frequency. The shapes of the first longitudinal (Y direction), lateral (X direction), torsional (about Z axis), and vertical (Z direction) modes are shown in **Fig. 9**, **Fig. 10**, **Fig. 11** and **Fig. 12**, respectively.

The model has been used to calibrate the input excitation of the preliminary dynamic tests and to predict the dynamic response of the model bridge. Band-pass filters were used to reduce the energy content of the random noise acceleration histories used as excitation during the shake table tests. The filter range is

chosen to include in the input frequency content the natural frequencies associated with the principal vibration modes shown in **Figs. 9** to **12**. If properly excited by the input, all these modes can be used for the multi-modal detection of the induced damages scenarios.

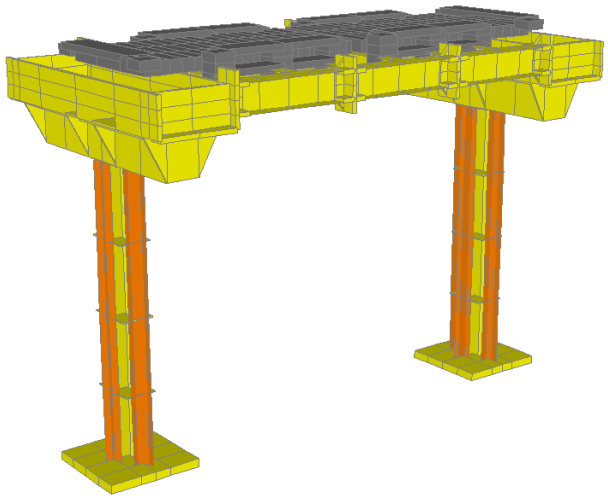

**Fig. 8.** Finite Element Model of the bridge model, including additional mass clamped to the deck structure.

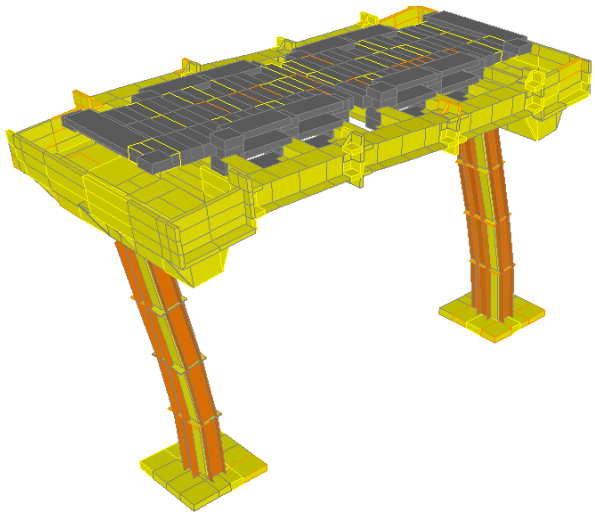

**Fig. 9.** First longitudinal natural vibration mode from the FEM analysis. Period T = 0.196 s (f = 5.10 Hz).

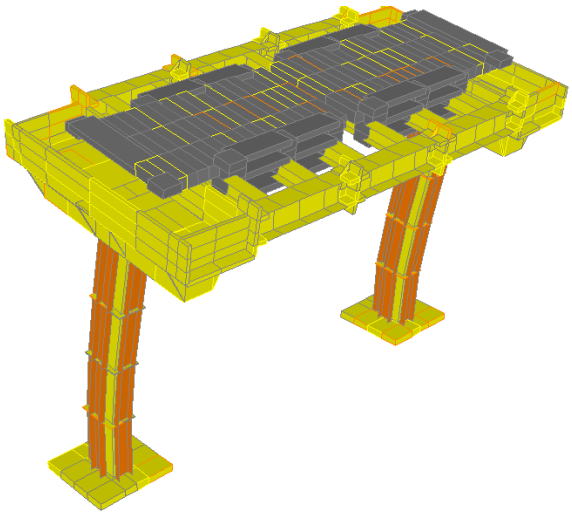

**Fig. 10.** First lateral natural vibration mode from the FEM analysis. Period T = 0.161 s (f = 6.21 Hz).

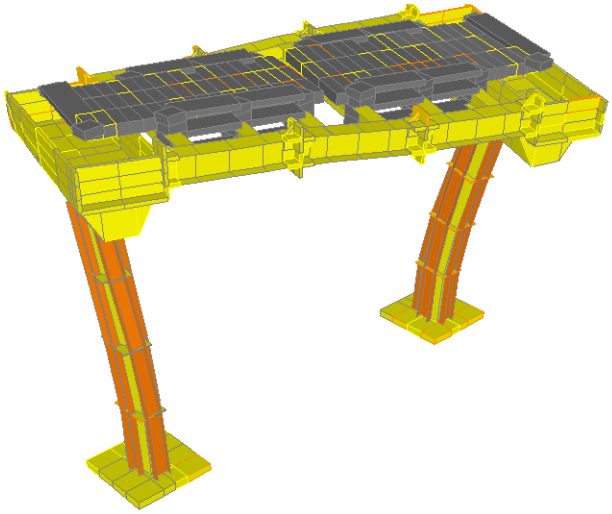

**Fig. 11.** First torsional natural vibration mode from the FEM analysis. Period T = 0.115 s (f = 8.70 Hz).

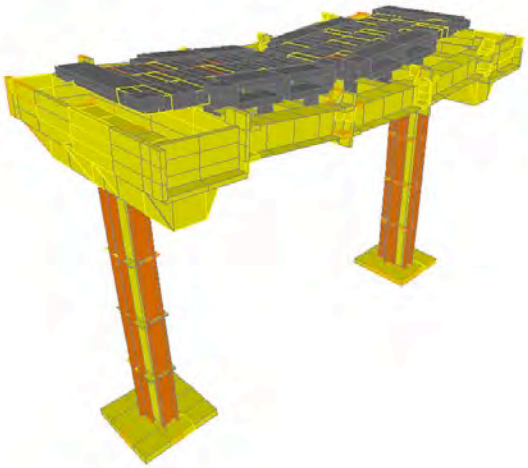

**Fig. 12.** First vertical natural vibration mode from the FEM analysis. Period T = 0.081 s (f = 12.32 Hz).

## Dynamic tests

The model has been tested in the “undamaged” and in 5 “damaged” conditions (obtained by removal of one or more removable parts). A total of 19 dynamic tests were performed (Oct 05-08, 2012) with three types of white noise input excitations with a flat (constant) power spectral density over a fixed frequency range obtained through a random generation algorithm specifically developed in Matlab®. This type of input was chosen as representative of ambient vibrations that can be recorded on a road bridge structure during normal operation. Each input is represented by an acceleration time history which was imposed in displacement control to the shake table. Type A and B inputs, with a flat (constant) power spectral density over the frequency range 1-10Hz, were used for the horizontal motion of the table. Input A was used in all the mono-directional tests, while input B was used as lateral horizontal input in multi-directional tests when input A was used in longitudinal direction. Time histories and Fast Fourier Transform (FFT) functions of acceleration, velocity and displacement for the input type A are reported in **Fig. 13**. The amplitude of the input function was chosen as the maximum amplitude the bridge model could withstand while still in the elastic range, with no plastic hinge formation and no damage in the bolted connections.

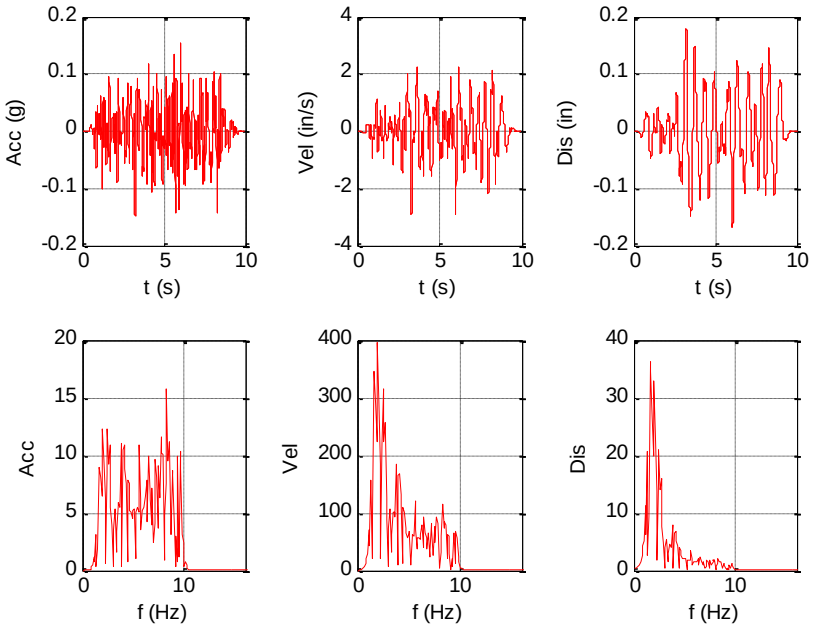


**Fig. 13.** Acceleration, velocity and displacement of the horizontal input (Y dir). First row: time histories. Second row: Fast Fourier Transform functions.

The peak acceleration for input A is 0.154g, which produces a higher acceleration on the deck structure due to dynamic amplification. The peak acceleration at the top of the bridge model evaluated through the FEM analysis by assuming the input A applied in longitudinal direction is 0.659g, which is about 4.3 times the peak acceleration of the table. Similar values are found for input B, which has a peak acceleration of 0.146g and produces lateral acceleration on the deck as high as 0.795g, with a dynamic

amplification factor of about 5.4. Peak acceleration, velocity and displacement values of the input A and B are reported in **Table 1** and **Table 2**, respectively. Maximum horizontal displacement and acceleration of the deck and maximum moment at the base of the column, as evaluated from the FEM model, are also reported.

**Table 1.** Type A (horizontal) input motion characteristics and expected bridge response values.

| **INPUT** | | | | | |
|---|---|---|---|---|---|
| $D_{max}$ base | 0.180 | in | = | 4.6 | mm |
| $V_{max}$ base | 2.264 | in/s | = | 57.5 | mm/s |
| $A_{max}$ base | 0.154 | g | | | |
| RMS displacement | 0.063 | in | = | 1.6 | mm |
| **BRIDGE RESPONSE** | | | | | |
| $A_{max}$ deck | 0.659 | g | | | |
| Dynamic amplification | 4.272 | - | | | |
| $D_{max}$ deck | 0.244 | in | = | 6.2 | mm |
| $M_{max}$ column | 5.9 | kip-ft | = | 7.97 | kNm |

**Table 2.** Type B (horizontal) input motion characteristics and expected bridge response values.

| **INPUT** | | | | | |
|---|---|---|---|---|---|
| $D_{max}$ base | 0.177 | in | = | 4.5 | mm |
| $V_{max}$ base | 2.504 | in/s | = | 63.6 | mm/s |
| $A_{max}$ base | 0.146 | g | | | |
| RMS displacement | 0.035 | in | = | 0.9 | mm |
| **BRIDGE RESPONSE** | | | | | |
| $A_{max}$ deck | 0.795 | g | | | |
| Dynamic amplification | 5.426 | - | | | |
| $D_{max}$ deck | 0.202 | in | = | 5.1 | mm |
| $M_{max}$ column | 12.0 | kip-ft | = | 16.25 | kNm |

The type C input was used as vertical input and has a higher frequency content ranging from 5 to 15Hz. The peak acceleration imposed in vertical direction is 0.230g, which is approximately 50% higher that in the horizontal directions, and produces vertical acceleration at the center of the deck up to 1.738g (dynamic amplification factor equal to 7.56). In **Fig. 14**, acceleration, velocity and displacement time histories and FFT functions of the vertical input are represented. A synthesis of the peak values of the vertical input and of the expected bridge response is reported in **Table 3**.

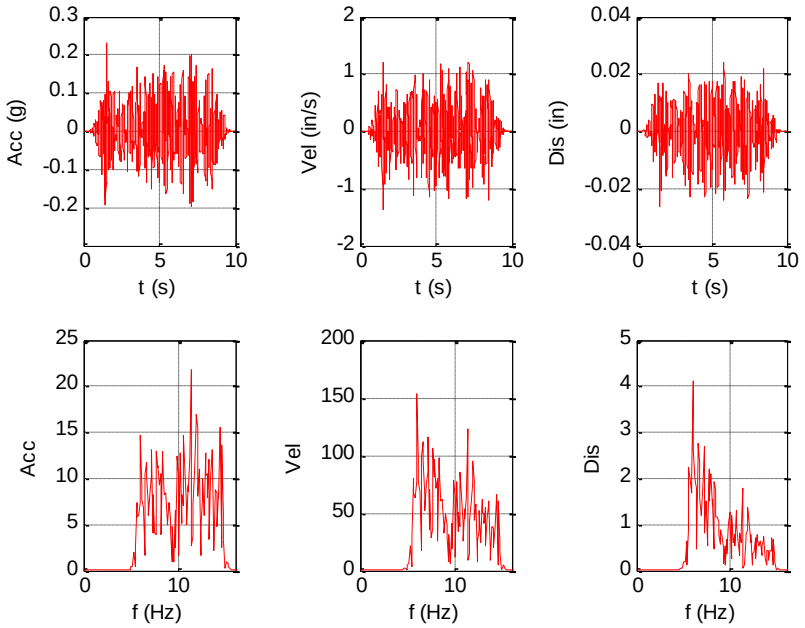


**Fig. 14.** Acceleration, velocity and displacement of the vertical input (Z dir). First row: time histories. Second row: Fast Fourier Transform functions.

**Table 3.** Vertical input motion characteristics and expected bridge response values.

| | | | | | |
|---|---|---|---|---|---|
| **INPUT** | | | | | |
| $D_{max}$ base | 0.024 | in | = | 0.6 | mm |
| $V_{max}$ base | 1.206 | in/s | = | 30.6 | mm/s |
| $A_{max}$ base | 0.230 | g | | | |
| RMS displacement | 0.009 | in | = | 0.2 | mm |
| **BRIDGE RESPONSE** | | | | | |
| $A_{max}$ deck | 1.738 | g | | | |
| Dynamic amplification | 7.56 | - | | | |
| $D_{max}$ deck | 0.112 | in | = | 2.8 | mm |
| $M_{max}$ deck | 3.16 | kip-ft | = | 4.26 | kNm |

Three levels of input intensity were used, specifically 10%, 25%, and 50% of the reference input. The acceleration values associated with the 25% input intensity represent commonly encountered values due to ambient vibration of common bridges in service. Label, date/time of completion, type/intensity of the input in each direction, and simulated damage of each test are reported in **Table 4**.

The damage scenarios are identified with labels from #1 to #5. The damage in the North Column was simulated by removal of the bottom C section on the South side of the column, and affects primarily the stiffness of the column for oscillations in longitudinal direction (see **Fig. 5** for the orientation of the bridge model). The bottom C section on the West side of the column was removed to simulate a lateral

damage in the South Column. The middle upper plate of the West side beam was removed to simulate damage in the deck. All the single damages are visible in **Fig. 15**, in which the shaking-table test setup of the model bridge in the damage #3 configuration (damages in the North Column, the South Column and the West longitudinal deck beam) is shown.

**Table 4.** Summary of the dynamic tests.

| | | Input Type-Intensity[1,2] | | | |
|---|---|---|---|---|---|
| **Test #** | **Date-time** | **Dir-X** | **Dir-Y** | **Dir-Z** | **Simulated damage[3]** |
| 01 | Oct 5, 2012 – 3:29PM | A-10% | - | - | - |
| 02 | Oct 5, 2012 – 3:35PM | - | A-10% | - | - |
| 03 | Oct 5, 2012 – 3:47PM | A-25% | - | - | - |
| 04 | Oct 5, 2012 – 3:56PM | - | A-25% | - | - |
| 05 | Oct 8, 2012 – 10:29AM | - | - | C-10% | - |
| 06 | Oct 8, 2012 – 10:34AM | - | - | C-25% | - |
| 07 | Oct 8, 2012 – 10:44AM | A-50% | - | - | - |
| 08 | Oct 8, 2012 – 10:50AM | - | A-50% | - | - |
| 09 | Oct 8, 2012 – 10:55AM | - | - | C-50% | - |
| 10 | Oct 8, 2012 – 12:27PM | A-25% | B-25% | C-25% | - |
| 11 | Oct 8, 2012 – 1:33PM | A-25% | - | - | - |
| 12 | Oct 8, 2012 – 1:37PM | - | A-25% | - | - |
| 13 | Oct 8, 2012 – 1:44PM | - | - | C-25% | - |
| 14 | Oct 8, 2012 – 2:21PM | - | A-25% | - | Damage #1 |
| 15 | Oct 8, 2012 – 2:25PM | A-25% | B-25% | C-25% | Damage #1 |
| 16 | Oct 8, 2012 – 3:56PM | A-25% | B-25% | C-25% | Damage #2 |
| 17 | Oct 8, 2012 – 4:36PM | A-25% | B-25% | C-25% | Damage #3 |
| 18 | Oct 8, 2012 – 4:44PM | A-25% | - | - | Damage #4 |
| 19 | Oct 8, 2012 – 5:12PM | - | - | C-25% | Damage #5 |

**Notes**

[1] Input type A = reference input for horizontal direction (frequency band 1-10Hz).
Input type B = input for Y direction in 3D shaking (frequency band 1-10Hz).
Input type C = reference input for Z direction (frequency band 5-20Hz).

[2] Input intensity is expressed as percentage of a reference input, for which the bridge model reaches the estimated ultimate capacity.

[3] Damage #1 = North Column.
Damage #2 = North Column + South Column.
Damage #3 = North Column + South Column + Deck.
Damage #4 = South Column + Deck.
Damage #5 = Deck.

**Fig. 15.** Damage #3 shake-table model bridge setup. Simulated damages through steel parts removal are visible in the North Column, the South Column and the West longitudinal deck beam.

## Dynamic response of the bridge

Acceleration and displacement data were collected and analyzed to assess the dynamic characteristics of the bridge. General observations from the dynamic response of the bridge model can be summarized as follows.

**1.** The noise floor in the tri-axial sensors is higher than in the uni-axial accelerometers. The noise floor of the uni-axial sensor is approximately 15dB lower that the noise floor in the tria-xial sensors. Differences are mainly due to the different measurement range of the accelerometers, which is ±10g for the triax and ±5g for the uniax sensors. A 0.05-20 Hz Band Pass (BP) filter was applied to reduce the effects of the floor noise on the recorded data. The effects of the filter on the acceleration histories are shown in **Fig. 16a** and **b**, in which raw data and corrected data from triax sensor #9X (center of the deck) and uniax sensor #10X (top of the North column) are reported for test 07.

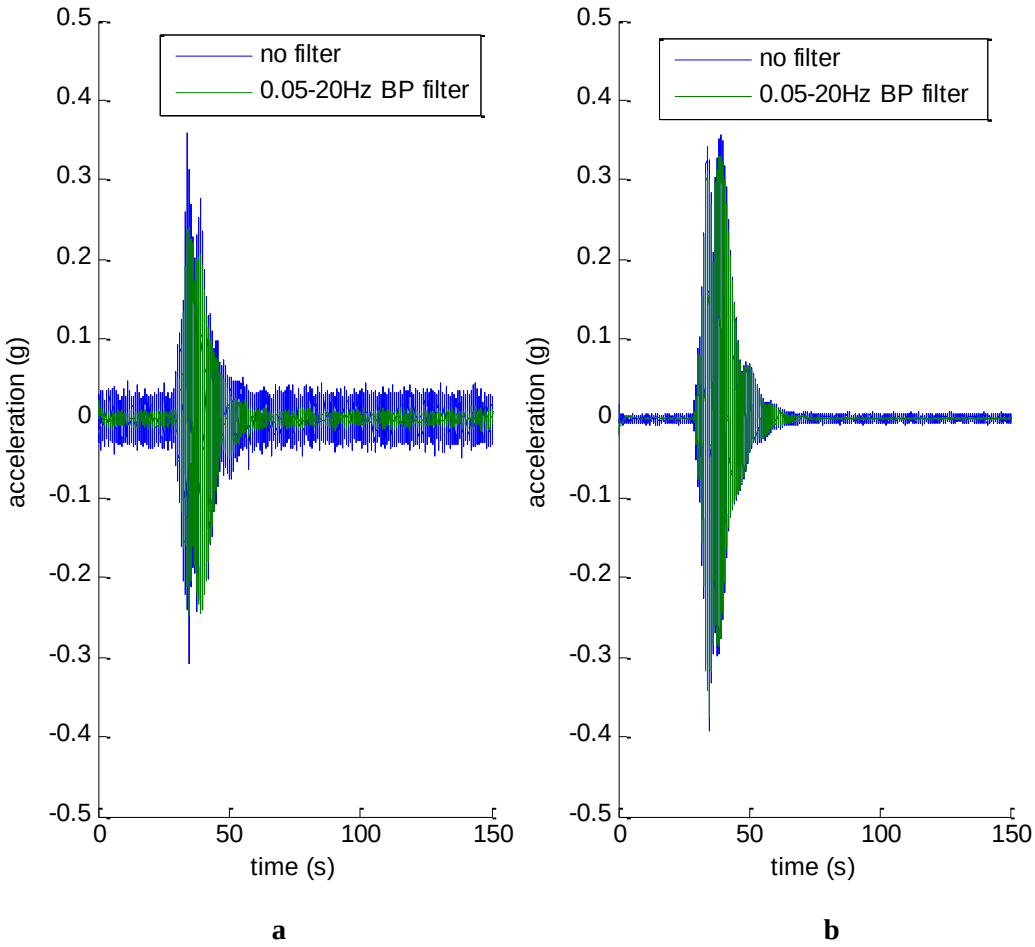


**Fig. 16.** Test 07 raw (no filter) and corrected (0.05-20 Hz Band Pass filter) acceleration histories from **a**) sensors #9X (center of the deck) and **b**) sensor #10X (top of the North column).

**2.** Peak acceleration values from tests appear not consistent with values predicted through FEM analysis. For mono-directional tests, peak acceleration values on the bridge are lower than FEM values in X direction, and higher in Y and Z directions. For the tri-directional test #10, experimental peak accelerations are higher than predicted values. Maximum acceleration values were experienced during the 50% input intensity tests. For these tests, the peak acceleration values expected from the FEM analysis in X (lateral direction of the bridge), Y (longitudinal direction of the bridge), and Z direction (vertical direction) were 50% x 0.795g (see $A_{max}$ deck in **Table 2**) = **0.398g**, 50% x 0.659g (see $A_{max}$ deck in **Table 1**) = **0.330g**, and 50% x 1.738g (see $A_{max}$ deck in **Table 3**) = **0.869g**, respectively. The corresponding values from tests #7, 8 and 9 were instead **0.353g** (-11%), **0.579g** (+75%) and **1.521g** (+75%). Apart from noise errors in the data acquisition, this inconsistency is attributed to differences between the as-built specimen and the FEM model that can be consequence of a number of causes including construction defects, installation defects, modeling approximations for stiffness and damping properties. Significant amplification effects occurred in the tri-directional tests #10. For this test, while expected peak accelerations in X, Y, and Z direction were 25% x 0.795g = **0.199g**, 50% x 0.659g = **0.165g**, and 50% x 1.738g = **0.435g**, respectively, experimental peak acceleration values resulted as high as **0.303g** (+52%), **0.337g** (+104%), and **1.13g** (+159%). In **Fig. 16**, peak acceleration values from all the tests on the undamaged bridge model (tests #1 to 13) are compared with values predicted through FEM analyses. Each plot refers to acceleration one specific direction (X, Y, Z), and arrows identify mono-directional tests with excitation in the same direction. Black triangles identify the tri-directional test #10. As expected, maximum acceleration values were recorded for the vertical oscillations of the model bridge, which are associated with a fundamental vibration mode characterized by a higher frequency with respect to the fundamental modes in longitudinal and lateral direction. Due to the observed inconsistency between experimental and predicted values, input excitations for tests on the damaged model (tests #14 to 19) were limited to 25% intensity to prevent unexpectedly high stresses in the specimen.

**3.** The bridge model exhibits dynamic coupling between longitudinal and lateral modes in mono-directional tests. The coupling is evidenced by both acceleration and displacement histories. Vertical excitations appeared to have small effects on the motion in other directions.

In **Fig. 18** and **19**, the acceleration histories recorded by the accelerometer #9 (center of the deck) are reported for the test 04, 03, and 06 respectively. In all these mono-directional tests, the 25% intensity input was used as the excitation on the undamaged bridge model. In the test 04 the excitation was in Y direction (longitudinal direction of the bridge), while in the test 03 the excitation was in X direction (lateral direction of the bridge), and in test 06 the bridge was subjected to a vertical excitation.

As visible in **Fig. 18**, the excitation in longitudinal direction induced a limited motion in lateral direction (X dir) of the model bridge. Vertical motion is negligible. Peak values of the recorded accelerations are 0.253 g in Y dir (6.66 times the maximum acceleration = 0.038 g of the shake table) and 0.103 g in X dir.

The X dir excitation (test 03) induced a proportionally higher longitudinal motion of the model bridge (Y dir), as evidenced by plots of **Fig. 19**. The peak values of the accelerations are 0.127 g in X dir (3.34 times the maximum acceleration = 0.038 g of the shake table) and 0.056 g in Y dir.

Acceleration histories of **Fig. 20** for test 06, in which the bridge was subjected to a vertical excitation with 25% intensity showed vibrations only in vertical direction with a peak acceleration value of 0.106 g (1.84 times the maximum acceleration = 0.0575 g of the shake table).

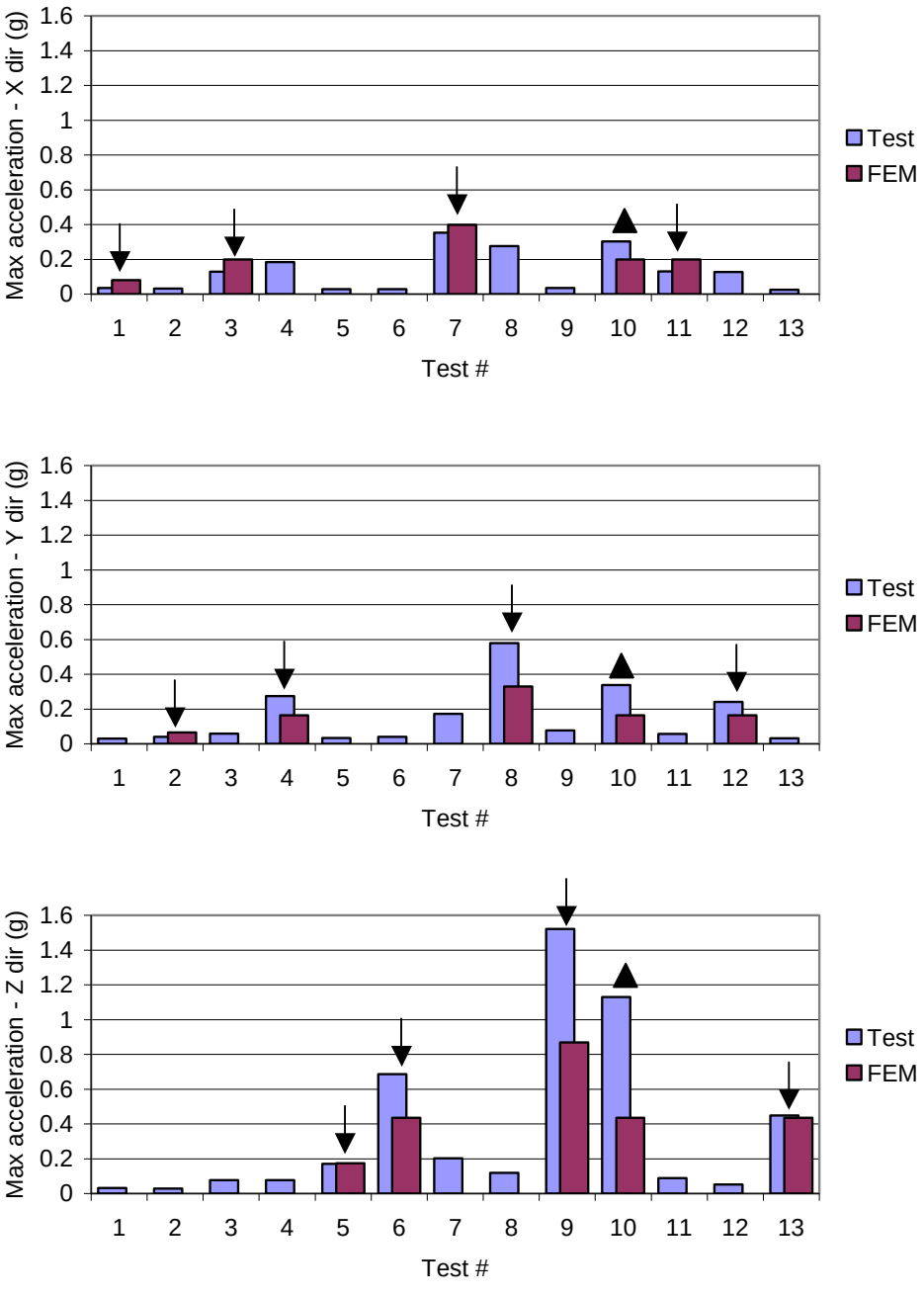


**Fig. 17.** Comparison between peak acceleration values from the tests and the FEM analysis. In each plot, arrows identify mono-directional tests with input in the same direction of the transducers. Triangles identify tri-directional tests.

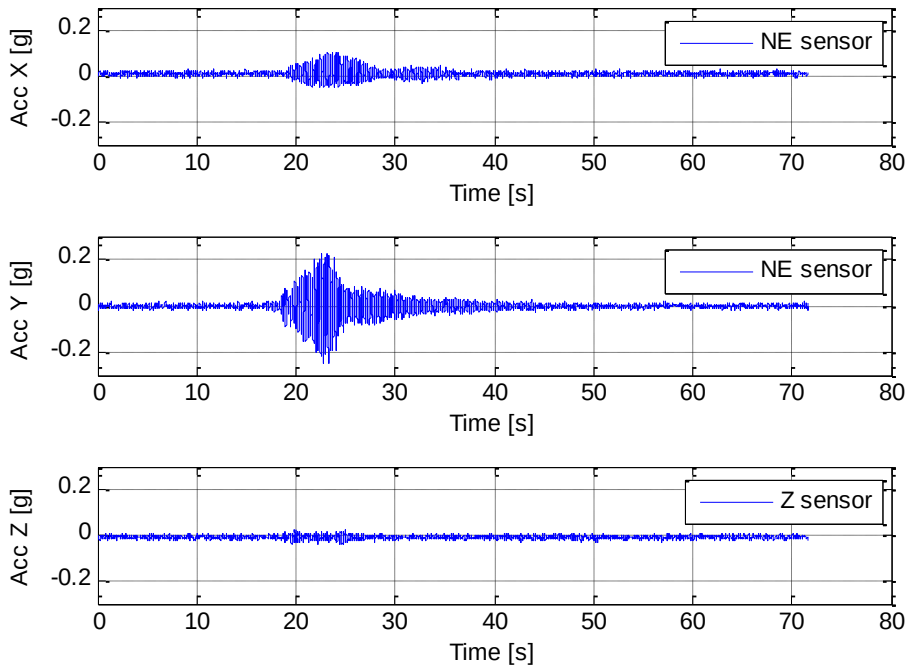


**Fig. 18.** Input Y direction – intensity 25% (test 04). Acceleration histories from the accelerometer #9 in X (top of the figure), Y (middle) and Z direction (bottom).

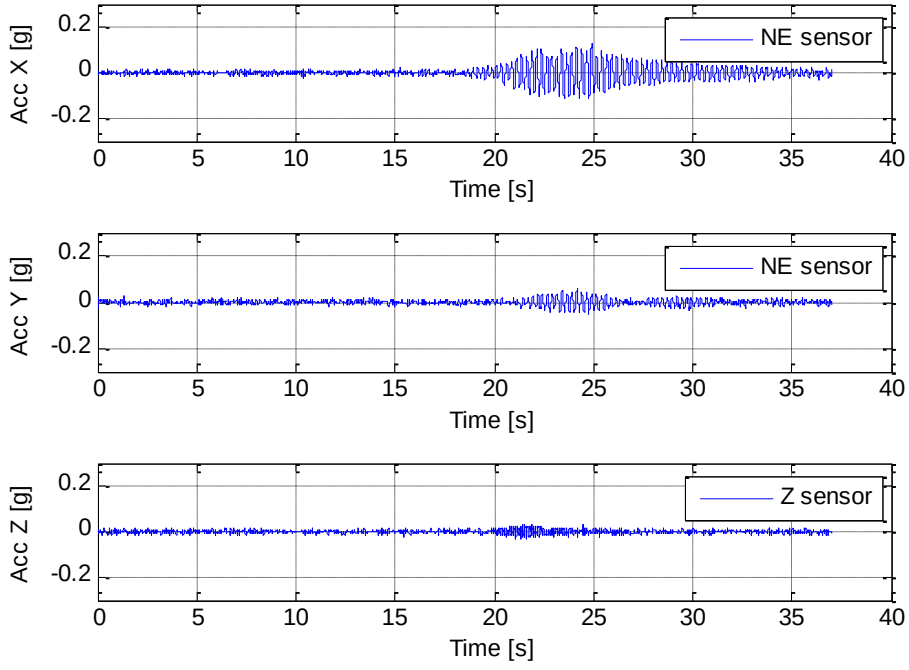


**Fig. 19.** Input X direction – intensity 25% (test 03). Acceleration histories from the accelerometer #9 in X (top of the figure), Y (middle) and Z direction (bottom).

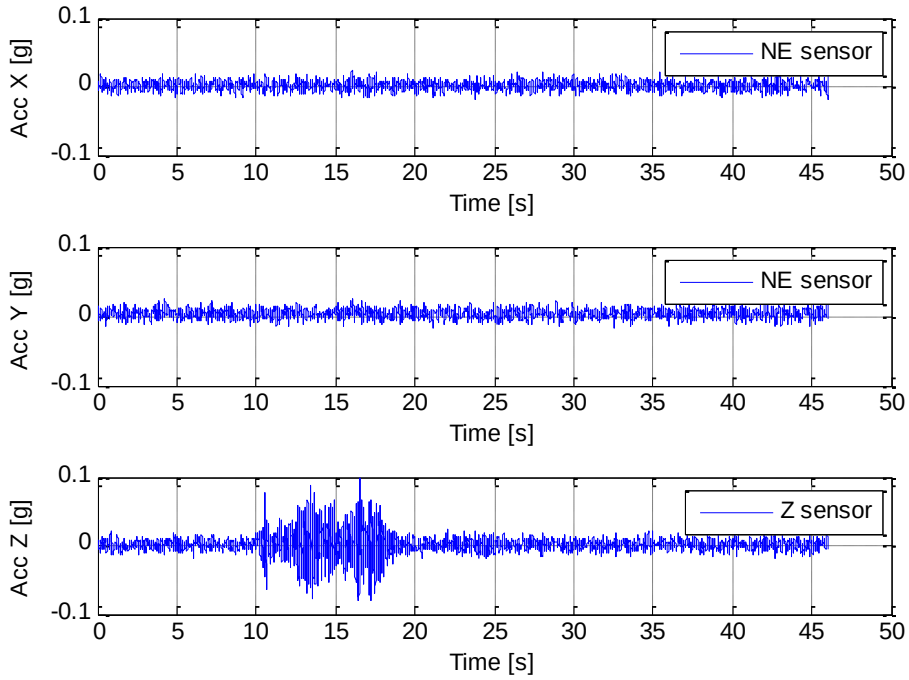


**Fig. 20.** Input Z direction – intensity 25% (test 06). Acceleration histories from the accelerometer #9 in X (top of the figure), Y (middle) and Z direction (bottom).

Similar results are confirmed by displacement histories recorded by the five transducers installed on the deck. During mono-directional tests in longitudinal and lateral direction, the transducers recorded low-to medium displacements in the direction orthogonal to the direction of excitation. During the 50% intensity test #7 in X direction (lateral direction of the bridge model), the deck had lateral displacements as high as 0.191", and longitudinal displacement up to 0.055" (29% of the lateral displacement). During test #8, in which the 50% intensity excitation was applied in Y direction, the peak longitudinal displacement of the deck resulted 0.296", while a 0.099" displacement was recorded in lateral direction (33% of the longitudinal displacement). For the 50% intensity excitation in vertical direction of test #9, a peak vertical displacement of 0.046" was recorded in the center of the deck, while displacement in longitudinal and lateral direction did not exceed 0.012" and 0.06", respectively, which are comparable with the precision of the instrument. The presence of coupled oscillations during mono-directional tests is mainly attributed to limited asymmetry in the structural configuration and small mass eccentricities due to positioning errors of the additional mass on the model bridge.

Small difference in the displacement recorded by parallel sensors (see **Fig. 6** for the map of the displacement transducers) both in longitudinal (NW and NE transducers) and lateral direction (NE and SE transducers) evidences modest torsional motion during the tests.

Peak displacement values from all the tests are represented in **Fig. 21**.

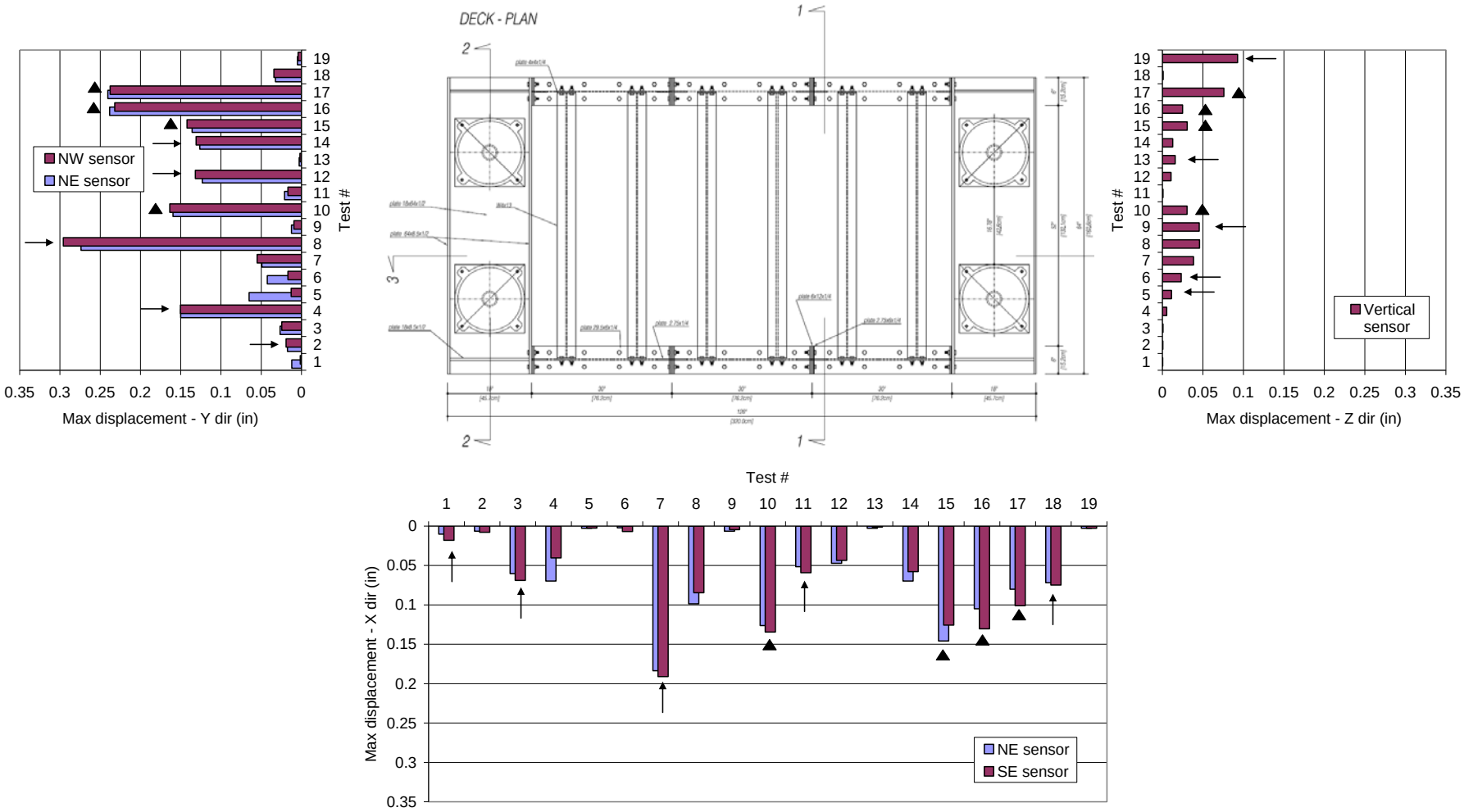


**Fig. 21.** Peak relative displacement values from the displacement transducers. In each plot, arrows identify mono-directional tests with input in the same direction of the transducers. Triangles identify tri-directional tests. For the localization of the sensors, see **Fig. 6**.

Each plot refers to transducers in the same direction. Arrows identify mono-directional tests with input in the same direction of the transducers. Black triangles identify tri-directional tests. Longitudinal displacements (Y direction) are plotted on the left side of the figure, lateral displacements (X direction) are represented in the bottom plot, and vertical displacement values (Z direction) are reported on the right side. It should be noted that tests from #14 to #19 refer to simulated damage scenarios and are characterized by higher displacement with respect to the correspondent tests on the undamaged bridge model. These increments in the peak displacement values are consequence of the reduction of stiffness induced by the simulated damages.

**4.** As evidenced by the transfer functions of the acceleration histories, main vibration frequencies associated with longitudinal, lateral, and torsional motion are lower than the values predicted through FEM analysis of the bridge model. This difference suggests a higher flexibility of the bridge model compared with the numerical model. In vertical direction, instead, a higher frequency is detected, suggesting a stiffening effect of the additional mass, which is clamped to the secondary beams of the deck, as shown in **Fig. 5**.

In **Fig. 22**, exemplificative transfer functions of acceleration histories from all the accelerometers in longitudinal (Y) direction are shown for test 04. In the left plot, the transfer functions are represented on the frequency range 0-25Hz. Two peaks are clearly identified, associated with longitudinal and torsional vibrations of the deck. The highest peak, with a frequency of 4.13 Hz, corresponds to the fundamental longitudinal vibration mode of the bridge model. A detailed representation of this peak is provided in the right plot of **Fig. 22**. In this representation, it is possible to distinguish between accelerations recorded on the second segment (bottom) of the columns (accelerometers #3, 4), on the top segment of the columns (accelerometers #5, 9), and on the cap-beams and deck structures (accelerometers #6, 7, 9, 12, 13, 14, 15). See **Fig. 7** for the map of the accelerometers.

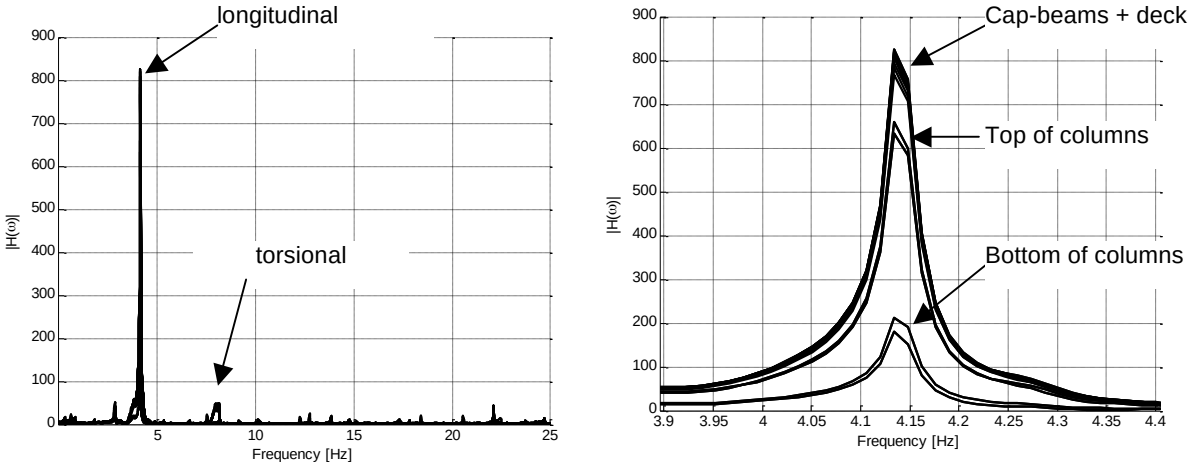


**Fig. 22.** Input Y direction – intensity 25% (test 04). Transfer functions of the accelerations (band-pass filter 0.05-20 Hz). Left: frequency range = 0-25 Hz. Right: frequency range = 3.9-4.4 Hz.

If the peak values of the transfer functions are used for a preliminary description of the vibration mode in longitudinal direction, the mode shape in the right plot of **Fig. 23** is obtained. The mode shape appears consistent with the longitudinal fundamental mode shape obtained through FEM analysis, represented on the left side of **Fig. 23**. Despite the good agreement of the mode, vibration frequency values significantly differ. Experimental data evidence a frequency of 4.13 Hz, which is 19% lower than the FEM frequency of 5.10 Hz (see **Fig. 9**). This discrepancy is mainly attributed to defects in the assembly of the bridge model that results in a higher flexibility compared with the numerical model.

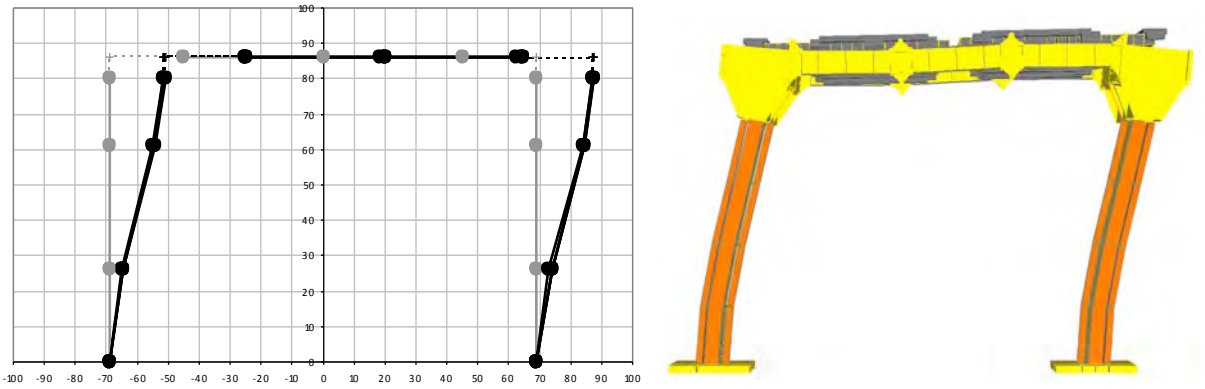


**Fig. 23.** First longitudinal mode of the bridge model. Preliminary identification of the modal characteristics. Right: from transfer functions of acceleration data - f = 4.13 Hz. Left: FEM analysis - f = 5.10 Hz.

Similar considerations are valid for the fundamental vibration mode in lateral (X) direction. Transfer function of the lateral acceleration histories from test 03 are represented in **Fig. 24**. In the left side plot, over the frequency range 0-25Hz, peak values associated with lateral and torsional motion of the model bridge are clearly evidenced. From the detailed representation of the transfer functions in the right plot, a vibration frequency of 3.95 Hz is recognized, which is 36% lower than the frequency (6.21 Hz, as shown in **Fig. 10**) expected from the FEM analysis.

In both tests #03 and #04, torsional motion played a secondary role during the model bridge oscillations. Peaks of the transfer functions associated with the torsional motion are already evidenced in **Fig. 22** and **23**. In **Fig. 25**, a detailed representation of the longitudinal transfer functions of from test #04 (left) and lateral transfer functions from #03 (right) is presented over the frequency range 7-9 Hz. For both tests, peak values corresponds to a frequency value of 7.98 Hz, which is 8% lower than the frequency associated with the torsional vibration mode of the model bridge predicted through FEM analysis (8.70 Hz, as shown in **Fig. 11**).

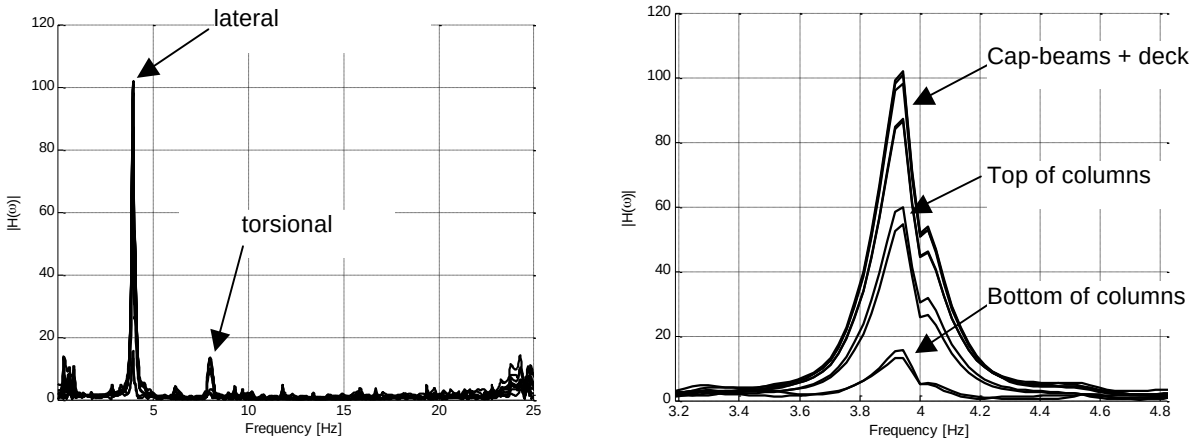


**Fig. 24.** Input X direction – intensity 25%. Transfer functions of the accelerations (band-pass filter 0.05-20 Hz).

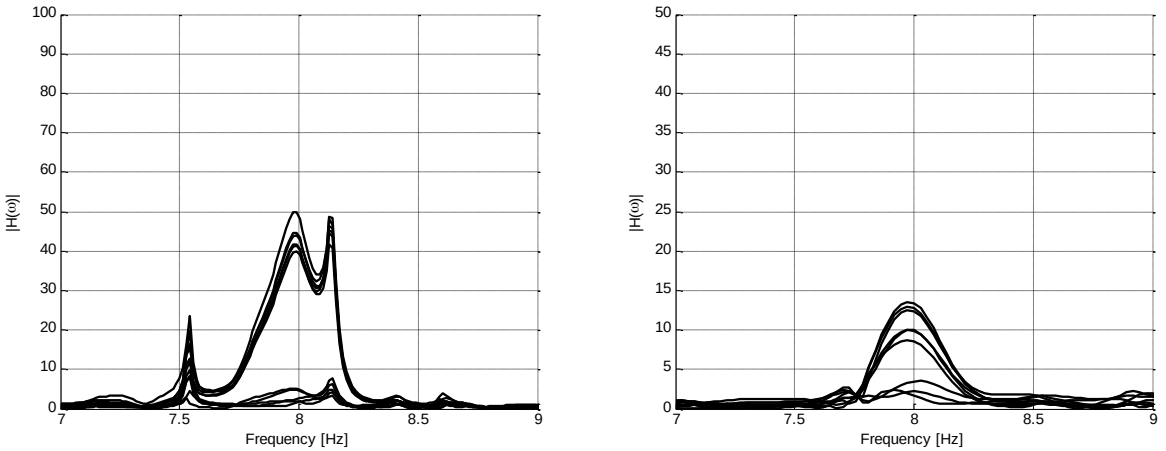


**Fig. 25.** Peak of the acceleration transfer functions associated with torsional motion of the model bridge (band-pass filter 0.05-20 Hz). **a**) Input Y direction (test #04) – intensity 25%. **b**) Input X direction (test #03) – intensity 25%.

From the analysis of the transfer functions of vertical acceleration data from test #06 (**Fig. 26**), one fundamental frequency is identified, which is associated with the peak at 18.2 Hz. This frequency is 48% higher than the frequency associate with the fundamental vertical mode from the FEM model, which is 12.32Hz (see **Fig. 12**). The increment of the vibration frequency indicates a higher stiffness for the model bridge compared to the FEM mode, which is mainly attributed to the stiffening effects of the steel plates clamped to the deck to add vibrating mass.

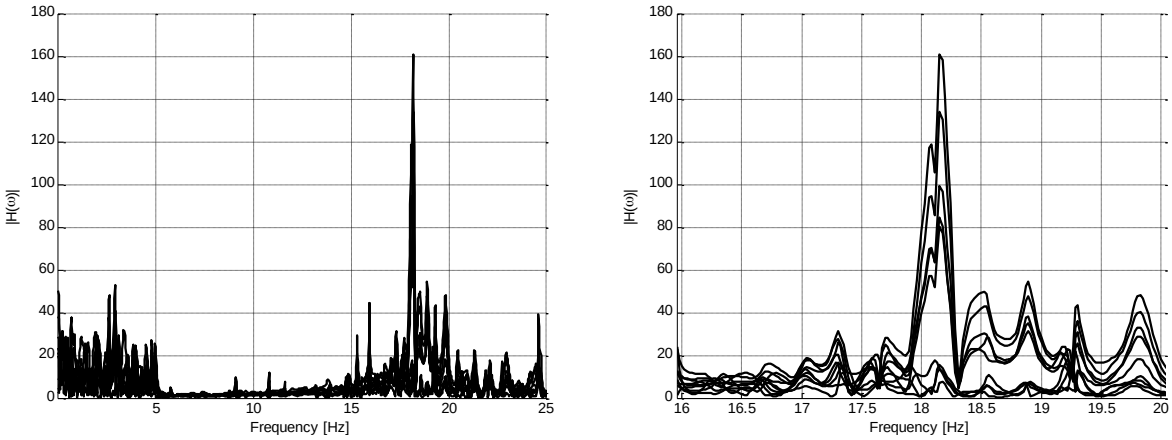


**Fig. 26.** Input Z direction – intensity 25%. Transfer functions of the accelerations (band-pass filter 0.05-20 Hz). Left: frequency range = 0-25 Hz. Right: frequency range = 16-20 Hz.

Frequency values identified through peak picking on the transfer functions of the acceleration data are reported in Table 5 for all the tests. Low intensity (10%) tests #1 and #2 show higher values of vibration frequency compared to all the other tests. After bolt connections settled in these tests, values appear stable for both medium (25%) and high (50%) intensity tests. The average ± standard deviation frequency values for tests #1 to 13 on the undamaged bridge configuration are:

- lateral vibration (X direction): 3.92 ± 0.11 Hz (-23% with respect to FEM = 5.10 Hz)
- longitudinal vibration (Y direction): 4.04 ± 0.16 Hz (-35% with respect to FEM = 6.21 Hz)
- torsional vibration (about Z axis): 7.99 ± 0.18 Hz (-9% with respect to FEM = 8.70 Hz)
- vertical vibration (Z direction): 18.04 ± 0.25 Hz (+46% with respect to FEM = 12.32 Hz)

The closeness between vibration frequencies in lateral and longitudinal direction supports the idea that the above mentioned coupling of the fundamental modes in these directions can result even for small asymmetries in the structural system and limited eccentricities of the center of mass of the bridge.

**5.** Simulated damages have small but noticeable effects on the fundamental vibration frequencies of the bridge. These effects are visible on the data of **Table 5**, in which gray shades are used to identify the directions mostly affected by the simulated damages. The different damages appear to affect in different ways the vibration frequencies of the model bridge. When damage in longitudinal direction is simulated on the North column (tests #14, 15, 16, 17), a 3 % reduction of the longitudinal vibration frequency, from 3.98 Hz for the undamaged bridge, to 3.91 ± 0.06 Hz is detected. For a damage in lateral direction in the South column (tests #16, 17, 18), the lateral vibration frequency decreases from 3.92 Hz to 3.56 ± 0.12 Hz (8% reduction). This confirms the expectations about the different sensitivity of the bridge model to lateral and longitudinal damages in the columns. The C profile removal from the lateral side of the South column has higher effects since affects the direction with higher stiffness. The lateral damage in the South column (tests #16, 17, 18) appears to affect primarily the torsional vibration frequency of the model, which decreases from 7.99 Hz to 7.50 ± 0.09 Hz (6% reduction). The simulated damage on the middle

portion of one of the primary beams of the deck (tests #17, 18, 19) produces a 3% reduction of the vertical vibration frequency from 18.04 Hz to 17.57 ± 0.01 Hz.

**Table 5.** Fundamental vibration frequencies from peak picking on transfer functions.

| | | Fundamental vibration frequency (Hz) | | | |
|---|---|---|---|---|---|
| | Test # | Lateral (X dir) | Longitudinal (Y dir) | Torsional (Z axis) | Vertical (Z dir) |
| undamaged | 1 | 4.10 | - | 8.27 | - |
| | 2 | - | 4.25 | 8.27 | - |
| | 3 | 3.87 | - | 8.03 | - |
| | 4 | - | 4.05 | 7.96 | - |
| | 5 | - | - | - | 18.32 |
| | 6 | - | - | - | 18.26 |
| | 7 | 3.84 | - | 8.06 | - |
| | 8 | - | 3.82 | 7.90 | - |
| | 9 | - | - | - | 17.88 |
| | 10 | 3.84 | 4.10 | 7.76 | 17.74 |
| | 11 | 3.94 | - | 7.94 | - |
| | 12 | - | 4.00 | 7.76 | - |
| | 13 | - | - | - | 17.98 |
| damaged | 14 | - | 3.92 | 7.94 | |
| | 15 | 3.90 | 3.94 | 7.89 | 18.06 |
| | 16 | 3.56 | 3.82 | 7.40 | 17.58 |
| | 17 | 3.44 | 3.94 | 7.51 | 17.58 |
| | 18 | 3.68 | - | 7.58 | - |
| | 19 | - | - | - | 17.56 |

## Damage identification

The damage detection algorithm that has been used on the model bridge is described in details in (Bonessio et al. 2012; Benzoni et al. 2011) and was specifically developed to localize and quantify damages in structural components and devices of bridge structures. In synthesis, the approach is based on acceleration records from a dispersed set of sensors to obtain information about the global and local behavior of the bridge. After a system identification phase is completed, the SHM procedure detects damages based on the changes of the modal characteristics of the bridge between a reference "undamaged" condition, used as a baseline, and a "damaged" condition. The indices used to localize and estimate the severity of damages are defined upon mutual variation of modal deformations in all the portions the structure is subdivided in. Results of the system identification and the damage detection procedure are presented in what follows.

## System identification

For the identification of the modal characteristics, the output-only Subspace Stochastic Identification Covariance (SSI-Cov) (Peeters 2000) method was used, since tests were performed to simulate ambient-like vibrations with unknown input. This condition closely represents the reality of a complex structure subjected to a monitoring program for structural health assessment purposes.

For the SSI-Cov method the deterministic knowledge of the input is replaced by the assumption that the input is a realization of a stochastic process (white noise). Prior to applying the SSI-Cov method, acceleration records from all the 19 channels shown in **Fig. 7** were converted to displacement histories. Signals were processed through band-pass 0-20 Hz zero-phase digital filtering (Oppenheim and Schafer 1989) and linear de-trending, before numerical integration via the trapezoidal method. Results from the application of the SSI-Cov method were organized in stabilizations charts to allow separating physical poles, which correspond to actual modes of the system and tend to stabilize as the order of the model increases, from numerical ones. Common tolerances values of 1%, 5%, and 2% for frequency, damping ratio, and the Modal Assurance Criterion on the mode shape, respectively, were used to identify stable poles from a 200 order model.

Different modal characteristics were identified from the tests, depending on the directions in which the input was applied: lateral and torsional vibration modes from mono-directional tests in X direction (lateral tests # 01, 03, 07, 11, and 18); longitudinal and torsional vibration modes from mono-directional tests in Y direction (longitudinal tests # 02, 04, 08, 12, and 14); vertical modes from Z direction tests # 05, 06, 09, 13, and 19; the whole set of modes from 3D tests #10, 15, 16, and 17. Mono-ax accelerometers #10 and 12 were used as reference sensors for the lateral and longitudinal modes, respectively, while tri-ax accelerometers #6 on the south-west side and #9 in the center of the deck were used as references for torsional and vertical modes. A typical stabilization diagram from X direction tests is shown in **Fig. 27**, which refers to test #03. The envelope of the Power Spectral Density functions evaluated for all the records is added to the plot to highlight the presence of peaks for frequency values associated with physical poles. In the plot, poles that respect all the stability conditions are represented with blue markers, while red markers identify poles that are stable in terms of at least one among frequency, damping ratio, and mode shape. For this mono-directional test, only the lateral and torsional modes are identified. A similar chart is represented in **Fig. 28** for the 3D test #10, in which instead modes in all directions are visible. As indicated by the arrows, the lateral and the longitudinal mode are very close in frequency, and can be subjected to coupling during the vibration.

Summaries of vibration frequencies and damping ratios from all the case studies are provided in **Table 6** and **Table 7**, respectively. Damaged scenarios were separated from un-damaged conditions of the bridge model. Damage shades indicate the direction of vibration mostly affected by the simulated damage. The most noticeable effect of damages is the shift of the vibration frequencies to lower values compared to un-

damaged values. Small differences with the frequency values identified through peak picking from the transfer functions (**Table 5**) were detected. Very low (< 4%) values of damping ratios emerged from the analysis, confirming that the model behaved in its elastic range during all the tests. However, no clear trend is recognizable for the damping ratios as a consequence of the damages. All these aspects about frequencies and damping ratios are clearly visible in terms of average values and standard deviations for damaged and damaged scenarios, reported in **Table 8**. In terms of average values, simulated damages determined a reduction of the frequency values for the lateral and longitudinal modes from 3.87 Hz and 4.10 Hz to 3.59 Hz (-7%) and 3.96 Hz (-3%), respectively. Similar entities of reduction were detected also for the torsional and vertical modes, which showed frequency shifts from 7.95 Hz and 17.88 Hz to 7.49 (-6%) Hz and 16.95 Hz (-5%). Average damping ratios instead increased for the longitudinal mode (from 0.43% to 2.22%), while decreased for all the other vibration modes (lateral = from 1.48% to 0.68%l; torsional = from 0.84% to 0.44%; vertical = from 0.80% to 0.28%).

The following aspects were observed on the mode shapes: (a) lateral and longitudinal modes are not perfectly mono-directional vibration modes, with noticeable but small motion components orthogonal to the predominant direction of oscillation; (b) the torsional vibration mode is characterized by mainly lateral deflection of the columns, and both lateral and vertical deflection of the deck's beams due to the concordant rotations and discordant lateral displacement at the top of the columns; (c) in the vertical mode, deflection of the columns appear negligible compared to deflection of the primary beams of the deck. All these aspects are visible in the average mode shapes represented in Figs. **29** to **32**, which refer to tests on the undamaged model bridge. The blue edges represent the undeformed configuration, while the black edges represent the mode shape at the levels where accelerometers are installed. All the mode shapes identified from the tests are instead reported in **Appendix 1**. Average and standard deviation values of the modes identified from tests on the undamaged bridge model are reported in **Tables 9** to **12**. The gray shade in the tables identifies the directions of the principal motion components for each mode. Each row corresponds to one sensor, the number of which is specified on the left side of each table.

A comparison between each mode shape and the average mode shapes of the bridge model was made through the Modal Assurance Criterion (Allemang and Brown, 1982), which is a scalar constant relating the degree of consistency (linearity) between one modal and another reference modal vector as follows:

$$MAC_i = \frac{\left|\psi_i^T \cdot \psi_{ref}\right|^2}{\left(\psi_i^T \cdot \psi_i\right) \cdot \left(\psi_{ref}^T \cdot \psi_{ref}\right)} \qquad (1)$$

where $\psi_i$ is the *i-th* modal vector and $\psi_{ref}$ is the reference modal vector. The modal assurance criterion takes on values from zero, representing no consistent correspondence, to one, representing a perfect correspondence. In this manner, if the modal vectors under consideration truly exhibit a consistent, linear

relationship, the modal assurance criterion should approach unity and the value of the modal scale factor can be considered to be reasonable. According to this criterion, all the undamaged modes appeared highly consistent with the average modal vectors, as only in one case each the lateral, torsional and vertical modes showed MAC values <0.90. When modal shapes from damaged scenarios were compared with the average undamaged modal shapes, MAC values significantly lower than unity were found only for the vertical modes, which showed MAC values as lower as 0.676 and appeared more affected by damages than all the other mode shapes in terms of modal displacements. MAC values for all the modal vectors are synthesized in **Table 13**. Locations of the sensors from the bottom center of the bridge model are synthesized in **Table 14**.

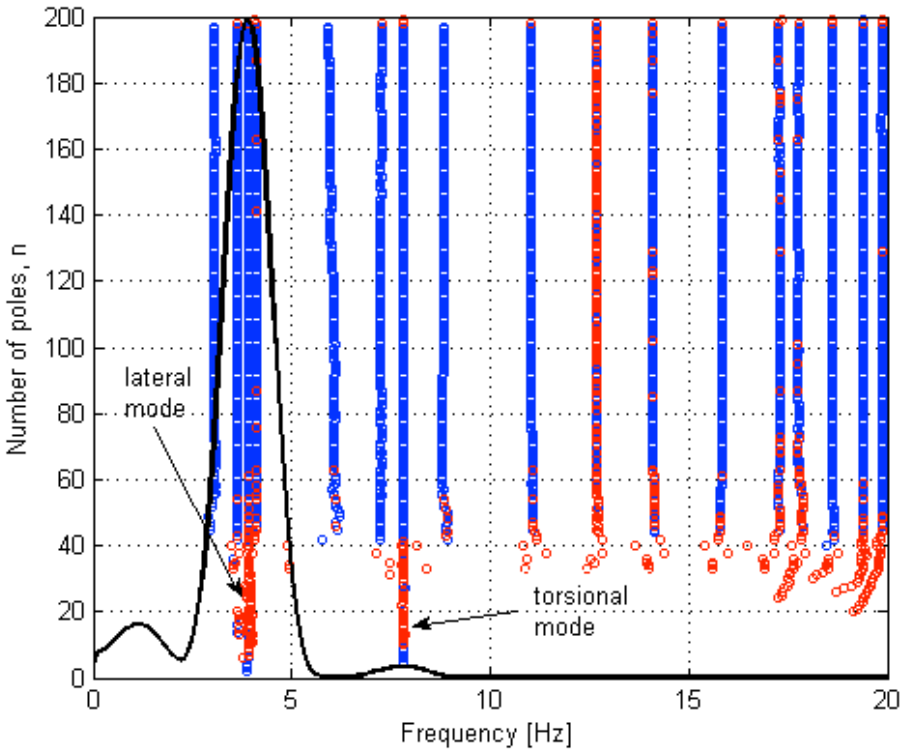


**Fig. 27.** Stabilization chart for test #07 (X direction). Red markers: stable poles for at least one among frequency, damping and mode shape. Blue markers: stable poles for frequency, damping and mode shape. Black line: envelope of PSD functions from all the accelerometric records.

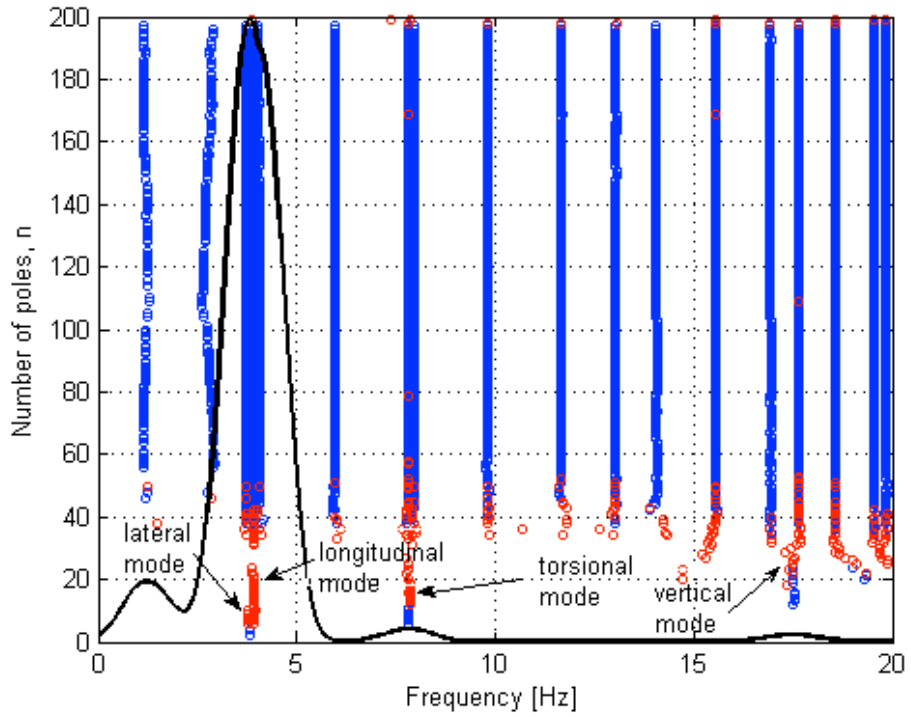


**Fig. 28.** Stabilization chart for test #10 (3D test). Red markers: stable poles for at least one among frequency, damping and mode shape. Blue markers: stable poles for frequency, damping and mode shape. Black line: envelope of PSD functions from all the accelerometric records.

**Table 6.** Fundamental vibration frequencies from SSI-Cov system identification.

| | | Fundamental vibration frequency (Hz) | | | |
|---|---|---|---|---|---|
| | Test # | Lateral (X dir) | Longitudinal (Y dir) | Torsional (Z axis) | Vertical (Z dir) |
| undamaged | 1 | 4.02 | - | 8.33 | - |
| | 2 | - | 4.24 | 8.17 | - |
| | 3 | 3.94 | - | 8.03 | - |
| | 4 | - | 4.06 | 7.95 | - |
| | 5 | - | - | - | 18.40 |
| | 6 | - | - | - | 18.36 |
| | 7 | 3.90 | - | 7.83 | - |
| | 8 | - | 4.03 | 7.86 | - |
| | 9 | - | - | - | 17.73 |
| | 10 | 3.79 | 4.13 | 7.92 | 17.65 |
| | 11 | 3.86 | - | 7.90 | - |
| | 12 | - | 4.03 | 7.89 | - |
| | 13 | - | - | - | 17.79 |
| damaged | 14 | - | 4.04 | 7.82 | |
| | 15 | 3.68 | 4.00 | 7.79 | 17.61 |
| | 16 | 3.59 | 3.92 | 7.47 | 17.62 |
| | 17 | 3.58 | 3.87 | 7.45 | 16.91 |
| | 18 | 3.60 | - | 7.55 | - |
| | 19 | - | - | - | 16.99 |

**Table 7.** Modal damping ratios from SSI-Cov system identification.

| | | Modal damping ratio (%) | | | |
|---|---|---|---|---|---|
| | Test # | Lateral (X dir) | Longitudinal (Y dir) | Torsional (Z axis) | Vertical (Z dir) |
| undamaged | 1 | 1.62 | - | 0.68 | - |
| | 2 | - | 0.74 | 1.77 | - |
| | 3 | 0.74 | - | 0.15 | - |
| | 4 | - | 0.45 | 0.65 | - |
| | 5 | - | - | - | 0.55 |
| | 6 | - | - | - | 0.67 |
| | 7 | 0.11 | - | 0.93 | - |
| | 8 | - | 0.63 | 0.22 | - |
| | 9 | - | - | - | 0.71 |
| | 10 | 1.69 | 0.13 | 3.06 | 0.47 |
| | 11 | 2.30 | - | 0.90 | - |
| | 12 | - | 0.21 | 0.36 | - |
| | 13 | - | - | - | 0.91 |
| damaged | 14 | - | 1.34 | 0.40 | |
| | 15 | 2.40 | 2.97 | 0.14 | 1.90 |
| | 16 | 0.82 | 3.94 | 0.49 | 0.40 |
| | 17 | 0.88 | 0.63 | 0.09 | 0.37 |
| | 18 | 0.34 | - | 0.74 | - |
| | 19 | - | - | - | 0.19 |

**Table 8.** Average value ± standard deviation of frequencies and damping ratios.

| | | Vibration mode | | | |
|---|---|---|---|---|---|
| | | Lateral (X dir) | Longitudinal (Y dir) | Torsional (Z axis) | Vertical (Z dir) |
| undamaged | frequency (Hz) | 3.87 ± 0.12 | 4.10 ± 0.09 | 7.95 ± 0.16 | 17.88 ± 0.80 |
| | damping ratio (%) | 1.48 ± 0.90 | 0.43 ± 0.26 | 0.84 ± 0.87 | 0.80 ± 0.51 |
| damaged | frequency (Hz) | 3.59 ± 0.01 | 3.96 ± 0.08 | 7.49 ± 0.05 | 16.95 ± 0.06 |
| | damping ratio (%) | 0.68 ± 0.29 | 2.22 ± 1.51 | 0.44 ± 0.33 | 0.28 ± 0.13 |

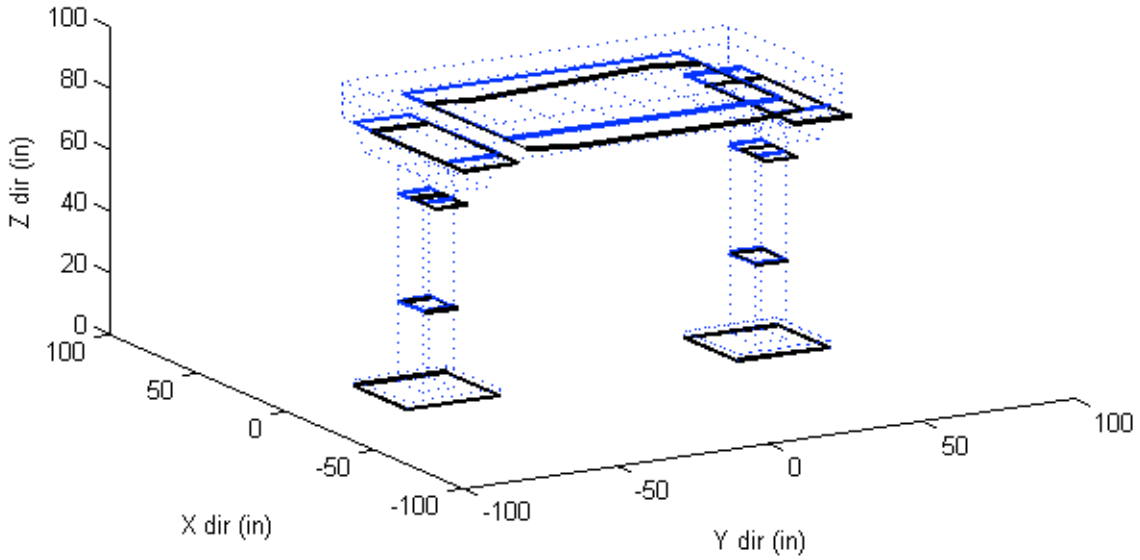


**Fig. 29.** Average lateral (X dir) mode shape for the undamaged model bridge.

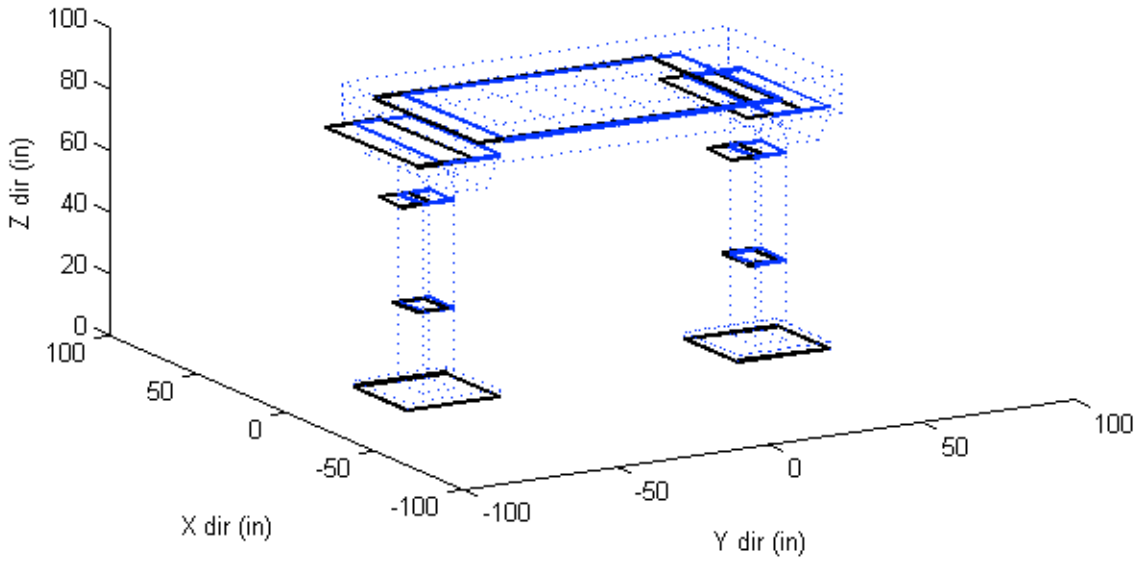


**Fig. 30.** Average longitudinal (Y dir) mode shape for the undamaged model bridge.

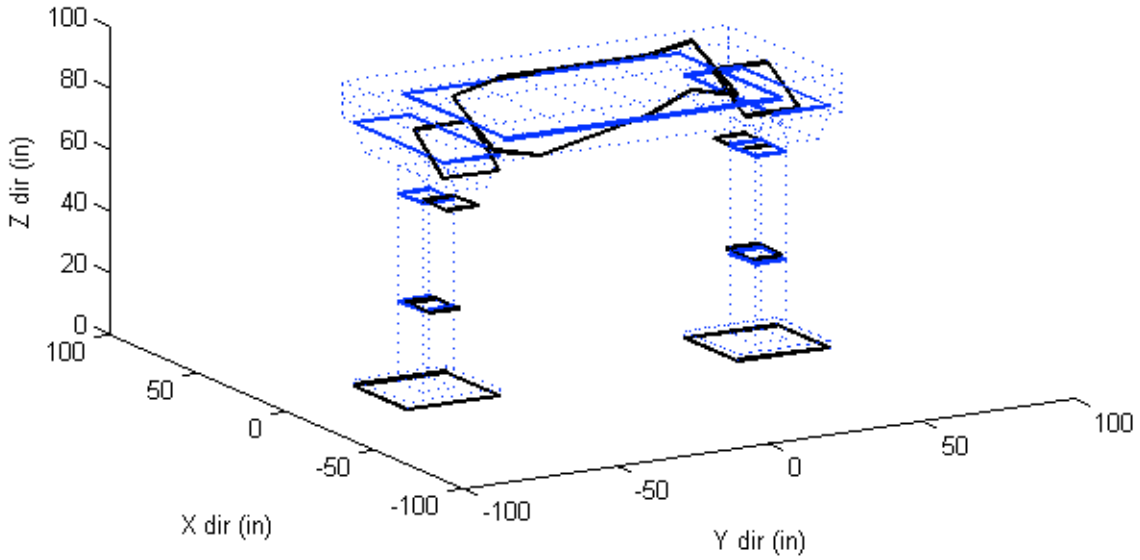


**Fig. 31.** Average torsional (about Z axis) mode shape for the undamaged model bridge.

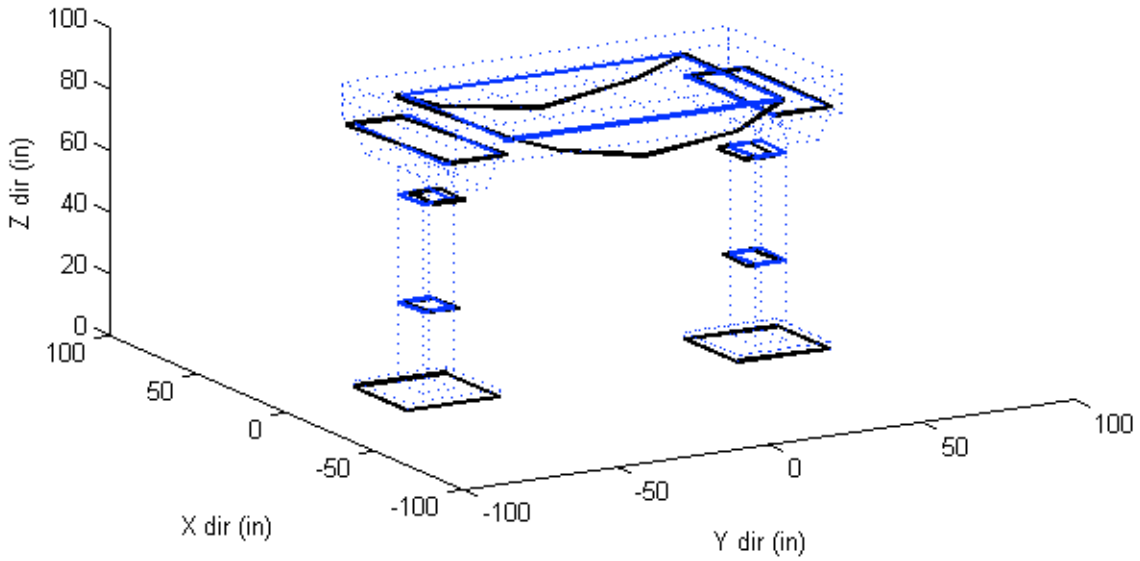


**Fig. 32.** Average vertical (Z dir) mode shape for the undamaged model bridge.

**Table 9.** Lateral mode: average and standard deviation values of the modal displacement.

| | Sensor # W → E | | Average values X | Y | Z | Standard deviation X | Y | Z |
|---|---|---|---|---|---|---|---|---|
| Top ← Bottom | 1 | North Column | 0 | 0 | 0 | - | - | - |
| | 3 | | -0.210 | -0.019 | 0.006 | ±0.026 | ±0.023 | ±0.004 |
| | 5 | | -0.764 | -0.066 | 0.014 | ±0.037 | ±0.055 | ±0.005 |
| | 14 | | - | -0.083 | - | - | ±0.054 | - |
| | 11 | | -1.072 | - | - | ±0.025 | - | - |
| | 15 | | - | -0.075 | - | - | ±0.064 | - |
| Top ← Bottom | 2 | South Column | 0 | 0 | 0 | - | - | - |
| | 4 | | -0.162 | -0.012 | 0.012 | ±0.074 | ±0.022 | ±0.019 |
| | 8 | | -0.691 | -0.063 | 0.015 | ±0.071 | ±0.051 | ±0.012 |
| | 12 | | - | -0.086 | - | - | ±0.066 | - |
| | 10 | | -1.308 | - | - | ±0.016 | - | - |
| | 13 | | - | -0.082 | - | - | ±0.054 | - |
| N ← S | 17 | Deck | - | - | -0.135 | - | - | ±0.008 |
| | 6 | | -1.274 | -0.074 | 0.134 | ±0.047 | ±0.075 | ±0.010 |
| | 16 | | - | - | -0.135 | - | - | ±0.010 |
| | 9 | | -1.308 | -0.091 | -0.002 | ±0.016 | ±0.065 | ±0.011 |
| | 7 | | -1.301 | -0.086 | -0.143 | ±0.044 | ±0.066 | ±0.017 |

**Table 10.** Longitudinal mode: average and standard deviation values of the modal displacement.

| | Sensor # W → E | | Average values X | Y | Z | Standard deviation X | Y | Z |
|---|---|---|---|---|---|---|---|---|
| Top ← Bottom | 1 | North Column | 0 | 0 | 0 | - | - | - |
| | 3 | | 0.020 | -0.188 | 0.008 | ±0.030 | ±0.053 | ±0.020 |
| | 5 | | 0.061 | -0.656 | 0.001 | ±0.100 | ±0.074 | ±0.016 |
| | 14 | | - | -0.862 | - | - | ±0.028 | - |
| | 11 | | 0.107 | - | - | ±0.162 | - | - |
| | 15 | | - | -0.928 | - | - | ±0.139 | - |
| Top ← Bottom | 2 | South Column | 0 | 0 | 0 | - | - | - |
| | 4 | | 0.022 | -0.215 | 0.017 | ±0.030 | ±0.041 | ±0.028 |
| | 8 | | 0.071 | -0.674 | 0.001 | ±0.099 | ±0.081 | ±0.015 |
| | 12 | | - | -0.846 | - | - | ±0.079 | - |
| | 10 | | 0.112 | - | - | ±0.175 | - | - |
| | 13 | | - | -0.827 | - | - | ±0.011 | - |
| N ← S | 17 | Deck | - | - | 0.049 | - | - | ±0.091 |
| | 6 | | 0.123 | -0.820 | -0.051 | ±0.178 | ±0.079 | ±0.091 |
| | 16 | | - | - | 0.049 | - | - | ±0.092 |
| | 9 | | 0.112 | -0.837 | -0.002 | ±0.175 | ±0.115 | ±0.001 |
| | 7 | | 0.114 | -0.846 | 0.036 | ±0.175 | ±0.079 | ±0.086 |

**Table 11.** Torsional mode: average and standard deviation values of the modal displacement.

| Sensor # | | | Average values | | | Standard deviation | | |
|---|---|---|---|---|---|---|---|---|
| W → E | | | X | Y | Z | X | Y | Z |
| Top ← Bottom | 1 | North Column | 0 | 0 | 0 | - | - | - |
| | 3 | | -0.342 | -0.008 | 0.033 | ±0.078 | ±0.079 | ±0.081 |
| | 5 | | -1.307 | 0.030 | 0.107 | ±0.285 | ±0.152 | ±0.065 |
| | 14 | | - | -0.906 | - | - | ±0.144 | - |
| | 11 | | -1.501 | - | - | ±0.139 | - | - |
| | 15 | | - | 1.107 | - | - | ±0.122 | - |
| Top ← Bottom | 2 | South Column | 0 | 0 | 0 | - | - | - |
| | 4 | | 0.287 | 0.074 | 0.040 | ±0.093 | ±0.158 | ±0.145 |
| | 8 | | 1.129 | 0.163 | -0.083 | ±0.135 | ±0.198 | ±0.135 |
| | 12 | | - | -0.869 | - | - | ±0.132 | - |
| | 10 | | 0.187 | - | - | ±0.191 | - | - |
| | 13 | | - | 1.013 | - | - | ±0.095 | - |
| N ← S | 17 | Deck | - | - | 0.384 | - | - | ±0.116 |
| | 6 | | 1.017 | 1.109 | -0.279 | ±0.246 | ±0.125 | ±0.143 |
| | 16 | | - | - | -0.018 | - | - | ±0.103 |
| | 9 | | 0.187 | 0.102 | - | ±0.191 | ±0.170 | ±0.153 |
| | 7 | | -0.949 | -0.869 | -0.392 | ±0.144 | ±0.132 | ±0.152 |

**Table 12.** Vertical mode: average and standard deviation values of the modal displacement.

| Sensor # | | | Average values | | | Standard deviation | | |
|---|---|---|---|---|---|---|---|---|
| W → E | | | X | Y | Z | X | Y | Z |
| Top ← Bottom | 1 | North Column | 0 | 0 | 0 | - | - | - |
| | 3 | | 0.031 | 0.185 | -0.018 | ±0.069 | ±0.019 | ±0.056 |
| | 5 | | -0.063 | 0.340 | -0.044 | ±0.081 | ±0.073 | ±0.014 |
| | 14 | | - | 0.187 | - | - | ±0.113 | - |
| | 11 | | 0.041 | - | - | ±0.123 | - | - |
| | 15 | | - | -0.156 | - | - | ±0.191 | - |
| Top ← Bottom | 2 | South Column | 0 | 0 | 0 | - | - | - |
| | 4 | | 0.117 | -0.178 | -0.017 | ±0.211 | ±0.075 | ±0.032 |
| | 8 | | 0.088 | -0.324 | -0.122 | ±0.063 | ±0.091 | ±0.156 |
| | 12 | | - | 0.050 | - | - | ±0.008 | - |
| | 10 | | 0.040 | - | - | ±0.097 | - | - |
| | 13 | | - | 0.179 | - | - | ±0.100 | - |
| N ← S | 17 | Deck | - | - | -0.488 | - | - | ±0.651 |
| | 6 | | 0.050 | 0.037 | -0.658 | ±0.060 | ±0.117 | ±0.085 |
| | 16 | | - | - | -0.673 | - | - | ±0.907 |
| | 9 | | 0.040 | 0.058 | -1.234 | ±0.097 | ±0.009 | ±0.083 |
| | 7 | | 0.019 | 0.050 | -0.585 | ±0.037 | ±0.008 | ±0.071 |

**Table 13.** Modal Assurance Criterion (MAC) values for each mode with respect to the average mode shapes of the undamaged bridge model.

| | | MAC values | | | |
|---|---|---|---|---|---|
| | Test # | Lateral (X dir) | Longitudinal (Y dir) | Torsional (Z axis) | Vertical (Z dir) |
| Undamaged | 1 | 0.994 | - | 0.881 | - |
| | 2 | - | 0.994 | 0.971 | - |
| | 3 | 0.994 | - | 0.979 | - |
| | 4 | - | 0.995 | 0.995 | - |
| | 5 | - | - | - | 0.863 |
| | 6 | - | - | - | 0.912 |
| | 7 | 0.998 | - | 0.967 | - |
| | 8 | - | 0.871 | 0.981 | - |
| | 9 | - | - | - | 0.940 |
| | 10 | 0.997 | 0.988 | 0.989 | 0.965 |
| | 11 | 0.996 | - | 0.952 | - |
| | 12 | - | 0.993 | 0.991 | - |
| | 13 | - | - | - | 0.962 |
| damaged | 14 | - | 0.962 | 0.994 | |
| | 15 | 0.993 | 0.990 | 0.853 | 0.982 |
| | 16 | 0.868 | 0.987 | 0.973 | 0.779 |
| | 17 | 0.978 | 0.988 | 0.924 | 0.845 |
| | 18 | 0.989 | - | 0.944 | - |
| | 19 | - | - | - | 0.676 |

**Table 14.** Location of the sensors.

| | Sensor # (W → E) | | Location (in) | | |
|---|---|---|---|---|---|
| | | | X | Y | Z |
| Top ← Bottom | 1 | North Column | -49 | 0 | 0 |
| | 3 | | -49 | 4 | 28.25 |
| | 5 | | -49 | 4 | 63.25 |
| | 14 | | -45 | -24.5 | 81 |
| | 11 | | -45 | 0 | 81 |
| | 15 | | -45 | 24.5 | 81 |
| Top ← Bottom | 2 | South Column | 49 | 0 | 0 |
| | 4 | | 49 | 4 | 28.25 |
| | 8 | | 49 | 4 | 63.25 |
| | 12 | | 45 | -24.5 | 81 |
| | 10 | | 45 | 0 | 81 |
| | 13 | | 45 | 24.5 | 81 |
| N ← S | 17 | Deck | 30 | -29 | 88 |
| | 6 | | 30 | 29 | 88 |
| | 16 | | 0 | -29 | 88 |
| | 9 | | 0 | 0 | 88 |
| | 7 | | -30 | -29 | 88 |

## Damage detection results

Based on mode shapes identified through the SSI-Cov method, the modal strain-energy based algorithm described in (Bonessio et al. 2012) was used to localize and quantify the entity of simulated damages in the model bridge elements.

The algorithm was developed to allow combinations of damage indices from a number of vibration modes into a multi-modal damage index in order to reduce false positives in the damage detection, which are generally due to singular points in the strain distribution along the elements that characterize each mode shape. For the *i-th* vibration mode, the damage is localized through the localization parameter:

$$\beta_{i,jk} = \frac{\int_{L_j} \varepsilon^{*2} dl}{\int_{L_j} \varepsilon^{2} dl} \cdot \frac{\int_{L_k} \varepsilon^{2} dl}{\int_{L_k} \varepsilon^{*2} dl} \qquad (2)$$

where $\varepsilon$ is the generic strain term, in two of the sub-elements in which the model bridge elements are subdivided, indicated with *j* and *k*. A normalized damage localization term, for the generic *j-th* sub-element and the *i-th* mode is defined as

$$\beta_{i,j} = \frac{\beta_{i,jk}}{\beta_{i,k_{\min}}} \qquad (3)$$

simply through division of the index evaluated in Eq. 1 by $\beta_{i,k_{\min}}$, which is the minimum value of the index $\beta_{i,jk}$ once a generic *k* element is chosen as a reference. The multi-modal localization term for the *j-th* element is then defined as a combination of the single modal terms:

$$\beta_j = \sum_{i=1}^{n} \gamma_i \beta_{i,j} \qquad (4)$$

with the reliability parameter for each mode defined in terms of $q_i$, i.e. the average values of the deviation of the normalized terms $\beta_{i,j}$ from the value 1, as:

$$\gamma_i = \frac{(1/q_i)^6}{\sum_{i=1}^{n} (1/q_i)^6} \qquad (5).$$

A statistical significance criterion is then used to identify locations of damage through the definition of the damage localization index:

$$Z_j = \left| \frac{\beta_j - \overline{\beta}}{\sigma_\beta} \right| \qquad (6)$$

where the parameters $\overline{\beta}$ and $\sigma_\beta$ represent the mean and the standard deviation of $\beta_j$, respectively. The damaged condition, for the *j-th* element, is indicated by a value of $Z_j \geq 1.645$ which identifies a 90% confidence level.

The proposed algorithm allows also the assessment of the severity level of the damage expressed through the index $\alpha_j$ that represents the fractional change in stiffness of the *j-th* element:

$$\alpha_j = (\beta_j)^{-0.5} - 1 \qquad \alpha_j \geq -1 \qquad (7).$$

The algorithm was applied to mode shapes identified from tests #14 to 19, in which different damage scenarios were simulated, with respect to the reference (undamaged) condition represented by the average mode shapes identified in tests #1 to13. Modal displacements were interpolated through polynomial 3$^{rd}$ order functions for the columns and 4$^{th}$ order functions for the deck beams of the model bridge to allow evaluation of strain values as analytical derivatives in order to be entered in Eq. (2). Since flexural deformations are predominant in both the columns and the deck elements, the generic strain term $\varepsilon$ was expressed in terms of curvature, evaluated analytically through double derivative of the polynomial functions.

In order to integrate curvature values as in Eq. (2), the four portions of the columns and the three portions of the primary beams were further subdivided into four sub-elements each. Damage indices were evaluated for each one of these sub-elements to allow a more detailed damage assessment along the structural elements. Each damage case scenario has been analyzed separately and results are presented in the following, specifically for the North and South columns and the West beam of the deck, into which singular damages were actually simulated.

**Damage in the North Column**

This specific damage consists of a longitudinal damage in the South-bottom portion of the North Column (see **Fig. 15**). This damage is simulated by its own in tests #14 and 15, and in conjunction with damages in the South Column and the West beam of the deck in tests #16 and 17, respectively. The steel part removal from the bottom of the North Column is expected to generate different entities of stiffness reduction, depending on the direction in which the column deflects. The highest stiffness reduction is theoretically associated with longitudinal deformation of the column, as the steel part was removed in this direction. Assuming a perfect bending behavior, the stiffness variation is given by the reduction of the moment of inertia of the column section, which is 21% in longitudinal direction and 1% in lateral direction. The torsional stiffness variation is instead given by the 6% reduction of the polar moment of inertia. These values are considered as upper limits, as imperfections of the columns will cause the actual stiffness reduction to be lower. Damage detection results for the scenarios associated with damage in the North Column are presented in the following.

**1**. Single-mode damage detection was able to identify and localize the damage at the bottom of the column in all the tests (#14 to 17). The only longitudinal vibration mode was used for the single-mode damage detection procedure, since highest stiffness variation was expected for longitudinal deflection of the column. Compared with the 19" actual damage extension, only the lowest 10" to 15" of the North column were identified as effectively damaged through the statistical localization criterion $Z_j \geq 1.645$, even if significant variations of stiffness were identified in the lowest 20" of the column by the quantification index $\alpha_j$. The stiffness reduction was found to be as high as 24% in test #16, while it appeared as 16%, 9% and 21% from tests #14, 15 and #17 respectively, as can be seen from **Fig. 33** to **36**. In each of these figures, the $\beta_j$ localization term, the localization index $Z_j$ and the quantification index $\alpha_j$ are represented. The dispersion in the estimation of the extension and the severity of the damage is manly attributed to the limited number of sensors available for the identification of the column mode shape. Apart from the accelerometer at the base, three accelerometers were used to collect vibration data along the column. With such a small number of accelerometers, any defect in the system identification could result in significant errors in the estimation of the modal shape and the consequent deformations. Improvement in the estimation of the damage severity could be obtained by using redundant accelerometers along the structural element.

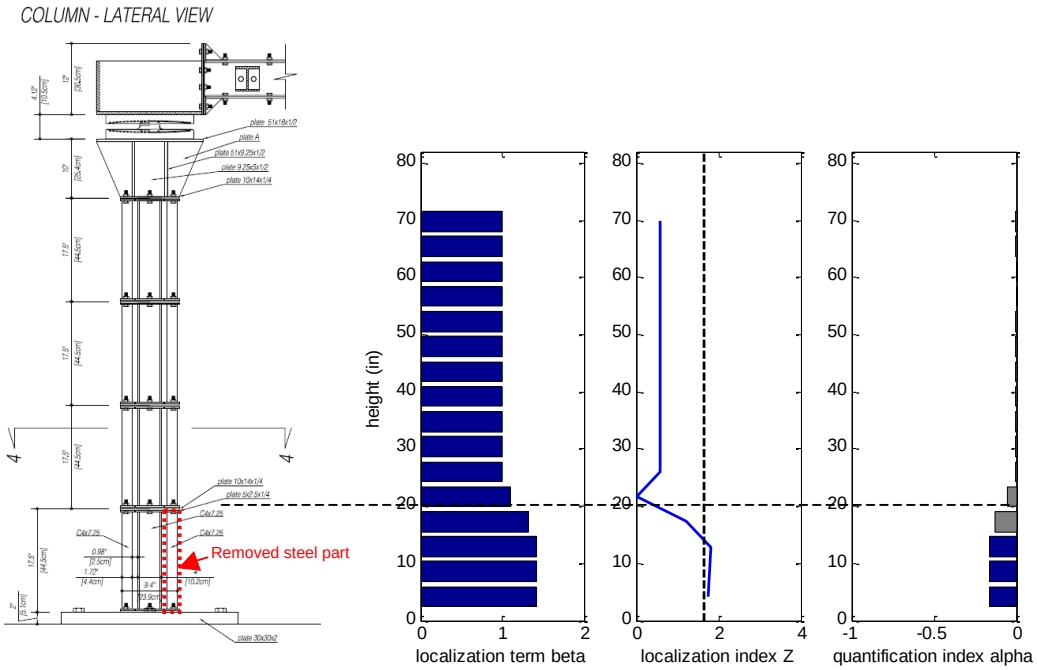


**Fig. 33.** Single-mode damage assessment in the North-Column – test #14. Localization term, localization index, and quantification index.

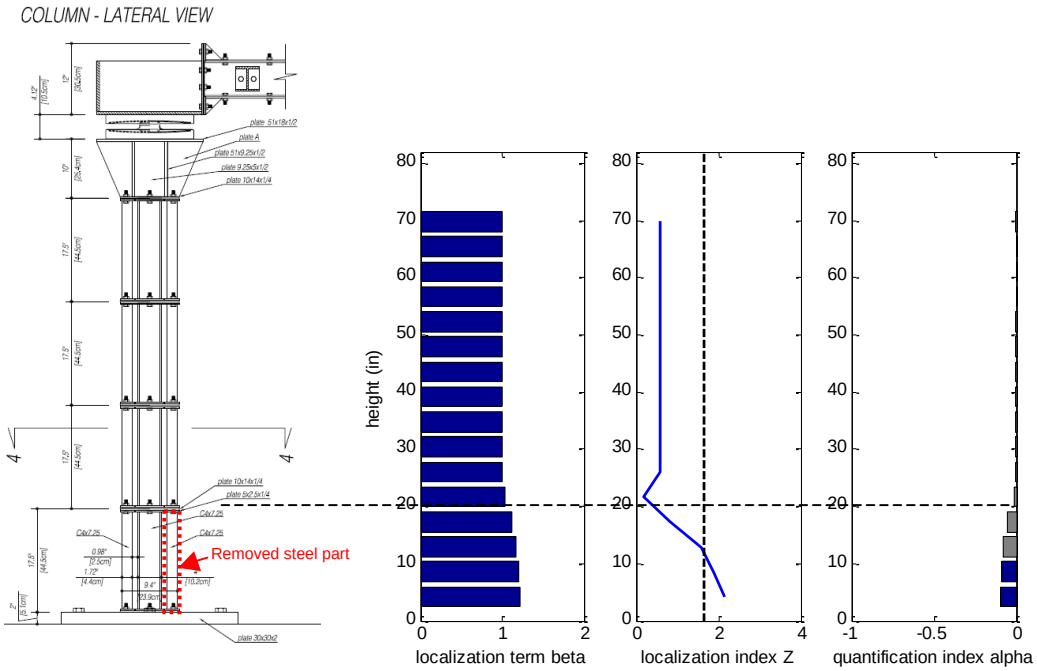


**Fig. 34.** Single-mode damage assessment in the North-Column – test #15. Localization term, localization index, and quantification index.

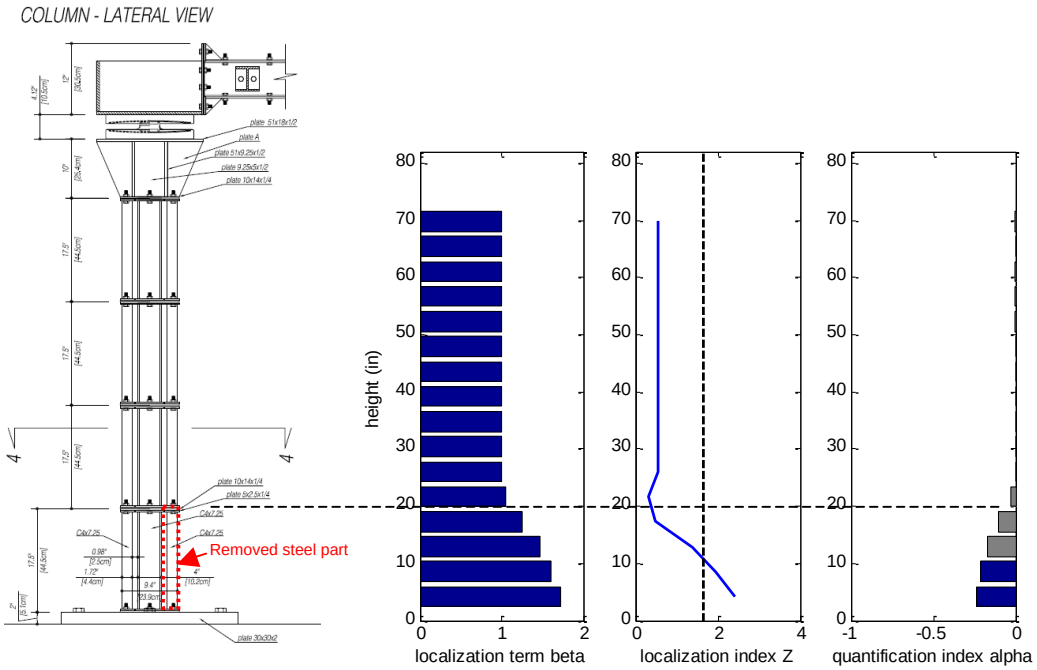


**Fig. 35.** Single-mode damage assessment in the North-Column – test #16. Localization term, localization index, and quantification index.

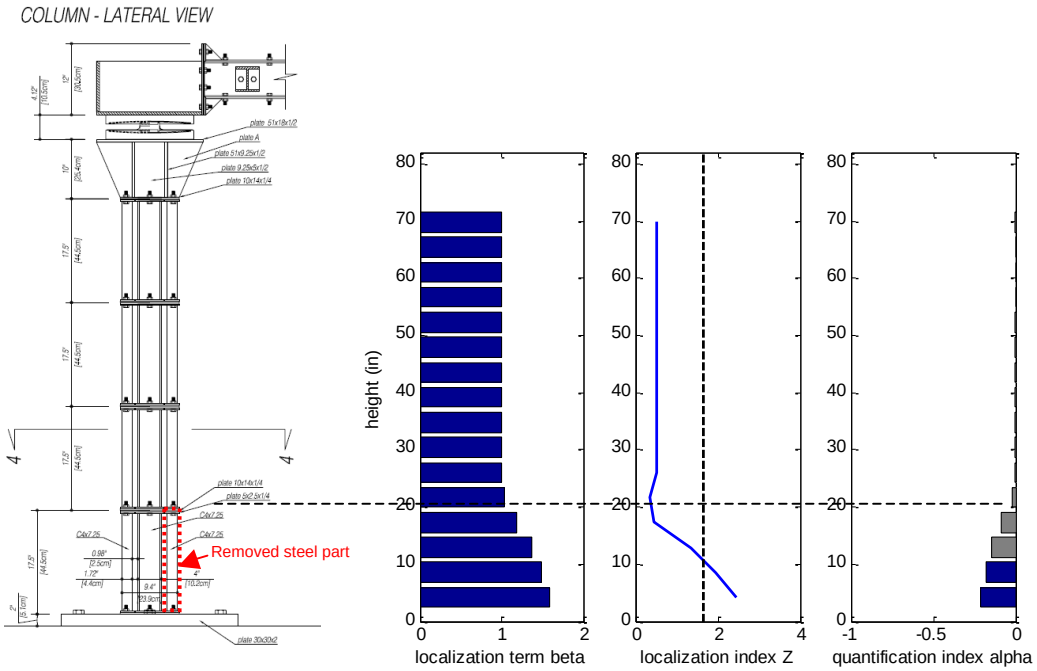


**Fig. 36.** Single-mode damage assessment in the North-Column – test #17. Localization term, localization index, and quantification index.

**2**. The multi-mode damage detection procedure localized the damage at the bottom of the column in all the tests (#15 to 17). Out of the four modes used in the analysis, the longitudinal vibration mode was recognized as the most significant one based on the reliability index $\gamma_i$, and always contributed for more than 50% to the multi-modal damage localization term. Single and multi-modal localization terms $\beta_{i,j}$ and $\beta_j$ are plotted in **Figs. 37** to **39**, with indication of the mode reliability index $\gamma_i$ for each mode. From the values of the $\gamma_i$ index, only the column deformations associated with the torsional and vertical modes appeared to contribute to the damage detection, while lateral modes appeared ineffective for the damage identification ($\gamma_i$ <1). The lateral mode was expected to have no contribution to the damage detection, since the simulated damage has practically no effects on the stiffness in lateral direction. The vertical and torsional mode, instead, contributed up to 40% and 26% to the multi-modal localization term. In **Figs. 40** to **42**, the multi-modal localization term $\beta_j$, the localization index $Z_j$ and the severity index $\alpha_j$ are represented for each damage scenario. The statistical criterion $Z_j \geq 1.645$ allowed locating the damage in the lowest 10" of the North column, with significant variation of stiffness evidenced in the lowest 20" by the quantification index $\alpha_j$. As already noted for the single-mode detection procedure, also for the multi-modal procedure a significant variability is associated with the quantification of the damage. However, the use of multiple modes allowed reducing this variability that is mainly associated with errors affecting modal curvatures evaluated from a limited number of sensors. Stiffness variations from the multi-modal procedure are lower than the correspondent values previously identified from the longitudinal mode only, and specifically -9%, -13% and -15% for tests #15, #16 and #17, respectively. This is due to the fact that the multi-modal procedure provides a global measure of the damage, by combining maximum effects of the damage in longitudinal direction with minor effects in other directions. This evidence suggests that while the damage identification and localization benefit from the robustness of a damage detection procedure based on vibration modes in multiple directions, vibration modes in each specific direction should be considered separately to have a clear interpretation of the damage severity information.

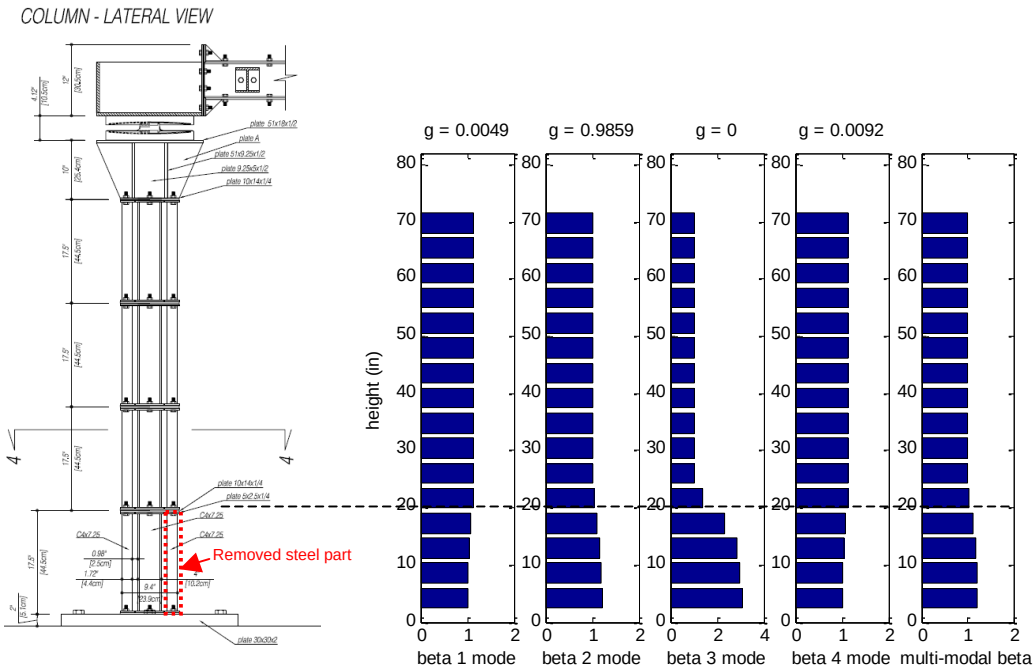


**Fig. 37.** Multi-modal damage assessment in the North-Column – test #15. Single modal localization terms $\beta_{i,j}$ and reliability indices $\gamma_i$, combined multi-modal localization term $\beta_j$.

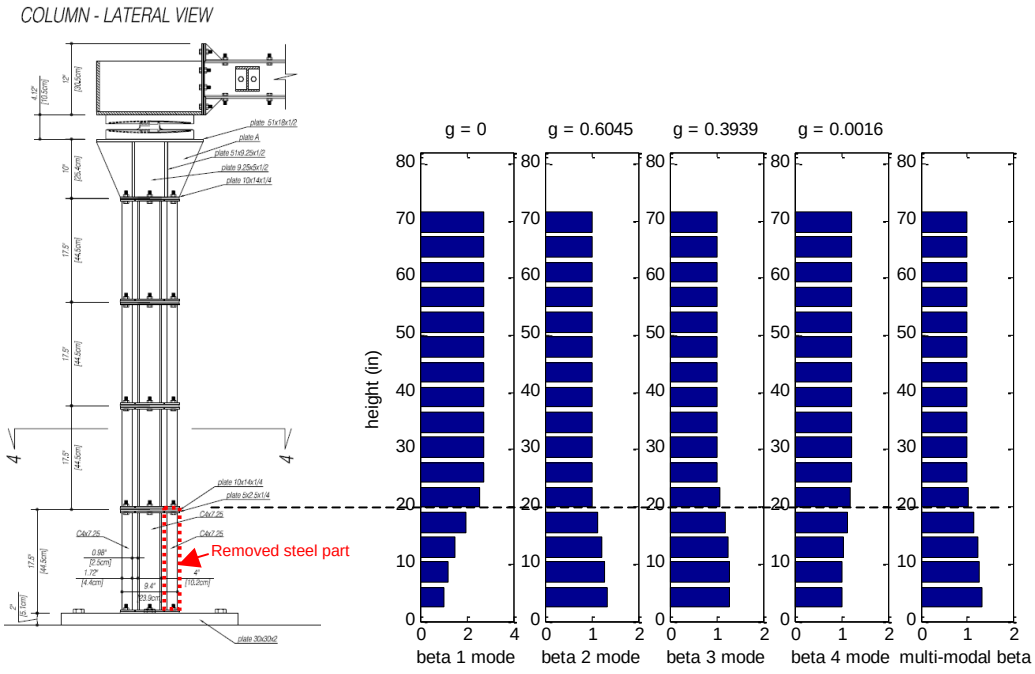


**Fig. 38.** Multi-modal damage assessment in the North-Column – test #16. Single modal localization terms $\beta_{i,j}$ and reliability indices $\gamma_i$, combined multi-modal localization term $\beta_j$.

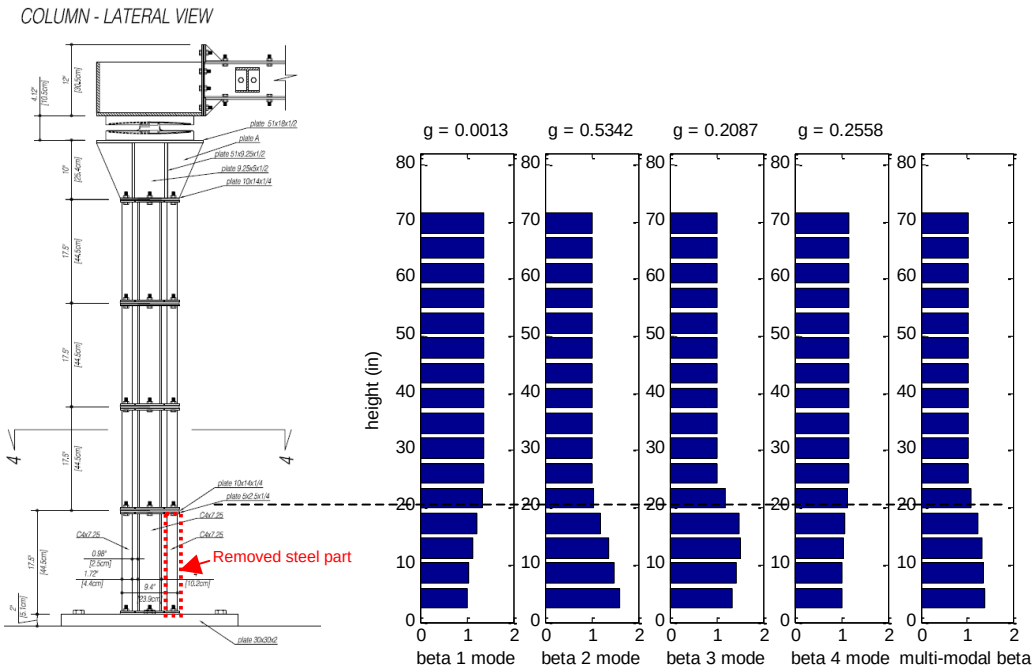


**Fig. 39.** Multi-modal damage assessment in the North-Column – test #17. Single modal localization terms $\beta_{i,j}$ and reliability indices $\gamma_i$, combined multi-modal localization term $\beta_j$.

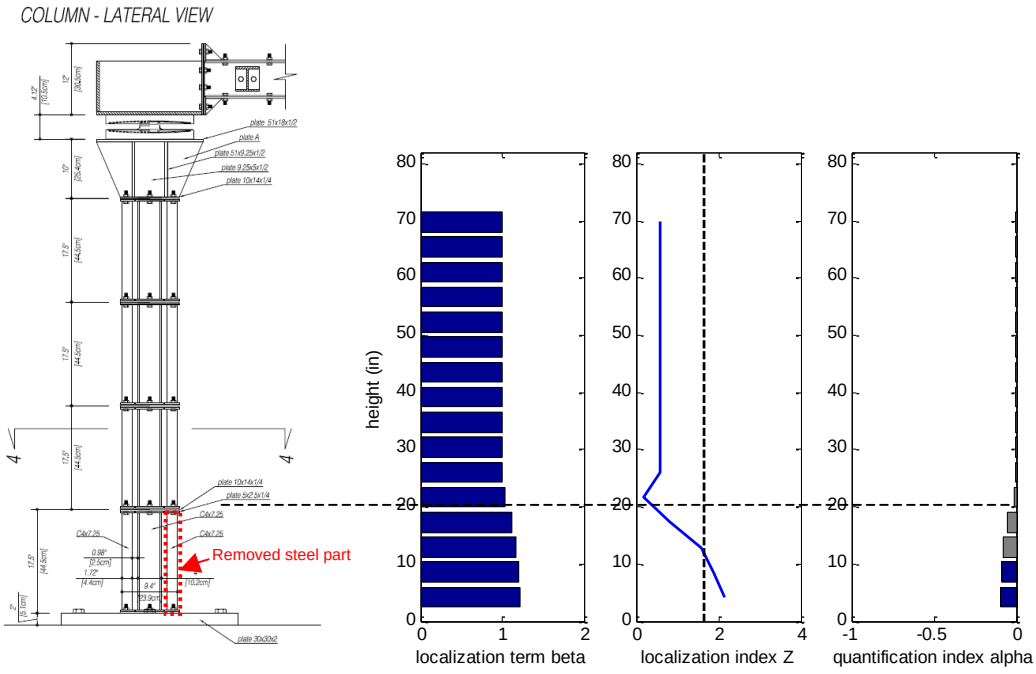


**Fig. 40.** Multi-modal damage assessment in the North-Column – test #15. Localization term, localization index, and quantification index.

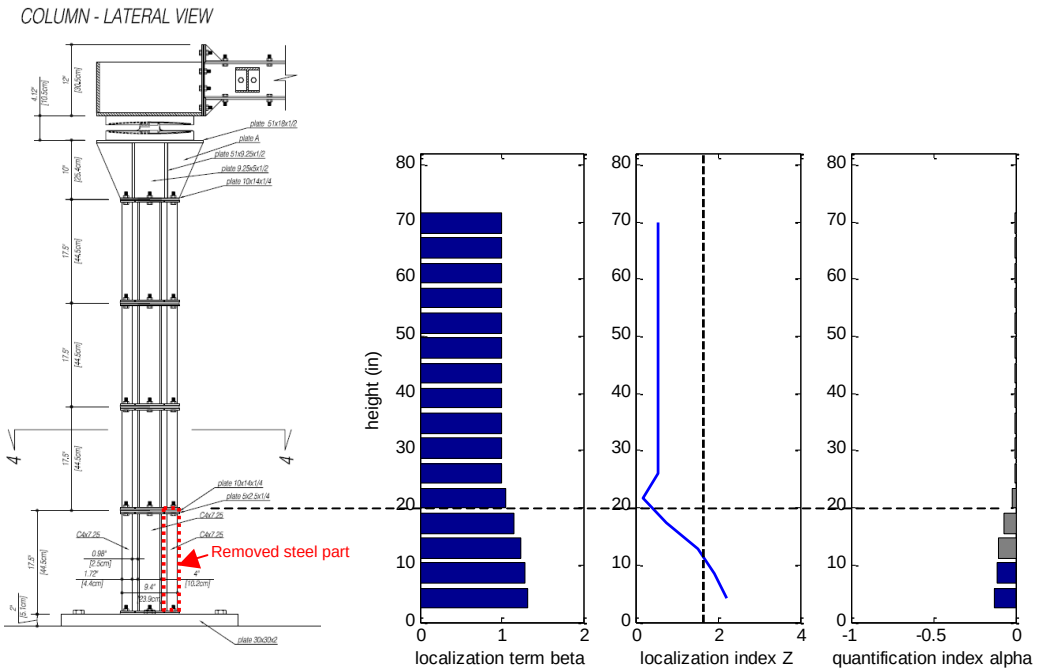


**Fig. 41.** Multi-modal damage assessment in the North-Column – test #16. Localization term, localization index, and quantification index.

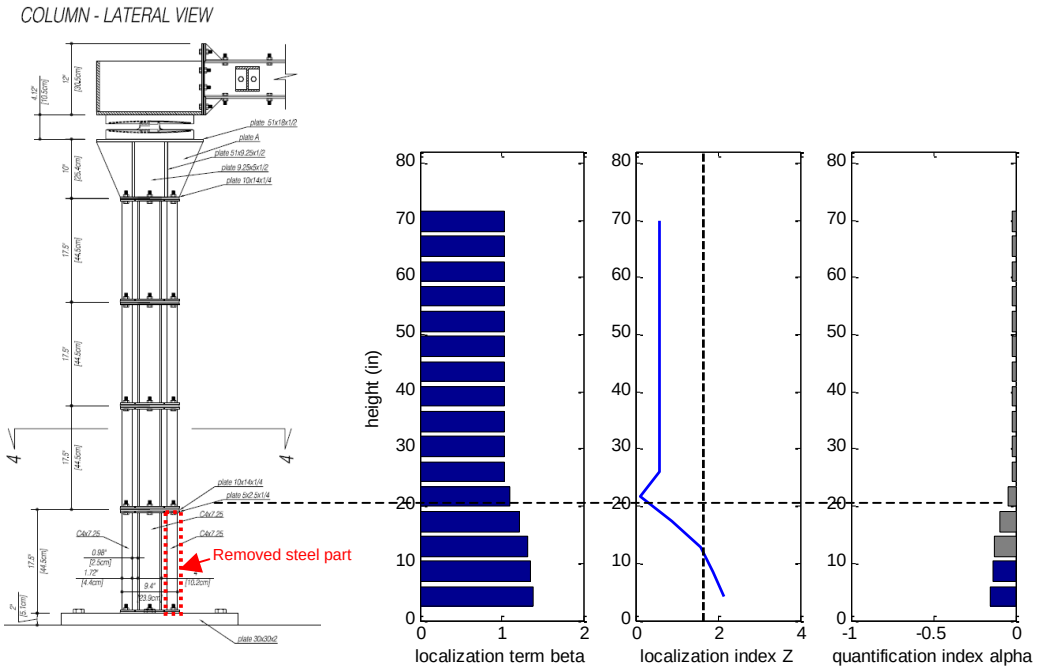


**Fig. 42.** Multi-modal damage assessment in the North-Column – test #17. Localization term, localization index, and quantification index.

**Damage in the South Column**

The bottom C4x7.25 West profile was removed to simulate a lateral damage in the South Column (see **Fig. 15**). If a perfect flexural behavior is assumed, this part removal is expected to produce a stiffness variation given by the reduction of the moment of inertia of the column section, which is 15% in lateral direction and 3% in longitudinal direction. The torsional stiffness variation is instead attributed to the 13% reduction of the polar moment of inertia. Compared to the North Column, similar results were found when the identification procedure was applied to detect damages in the South Column.

**1**. Single-mode damage detection was able to identify and localize the lateral damage at the bottom of the South Column in all the tests (#16, 17 and 18). Based on the lateral vibration mode only, the lowest 10" of the South column were identified as effectively damaged through the statistical localization criterion $Z_j \geq 1.645$. Stiffness reduction of 15%, 9% and 33% was identified for tests #16, 17 and #18 respectively, as shown in **Fig. 43** to **45**. As already discussed for the North Columns, the dispersion affecting the severity values is manly attributed to the limited number of sensors available for the identification of the column modal deformations.

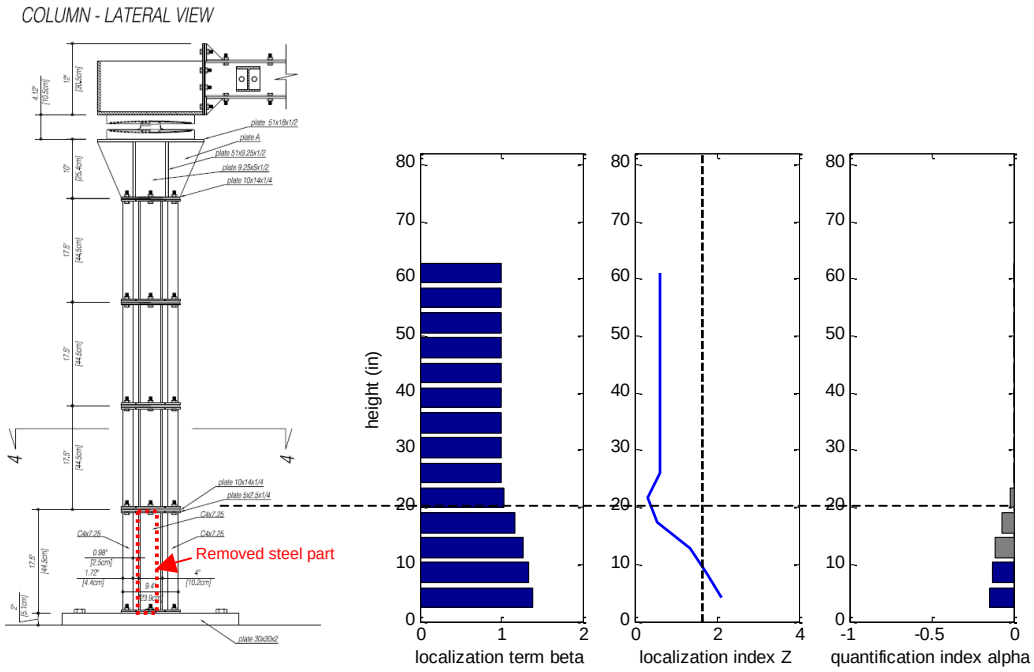


**Fig. 43.** Single-mode damage assessment in the South-Column – test #16. Localization term, localization index, and quantification index.

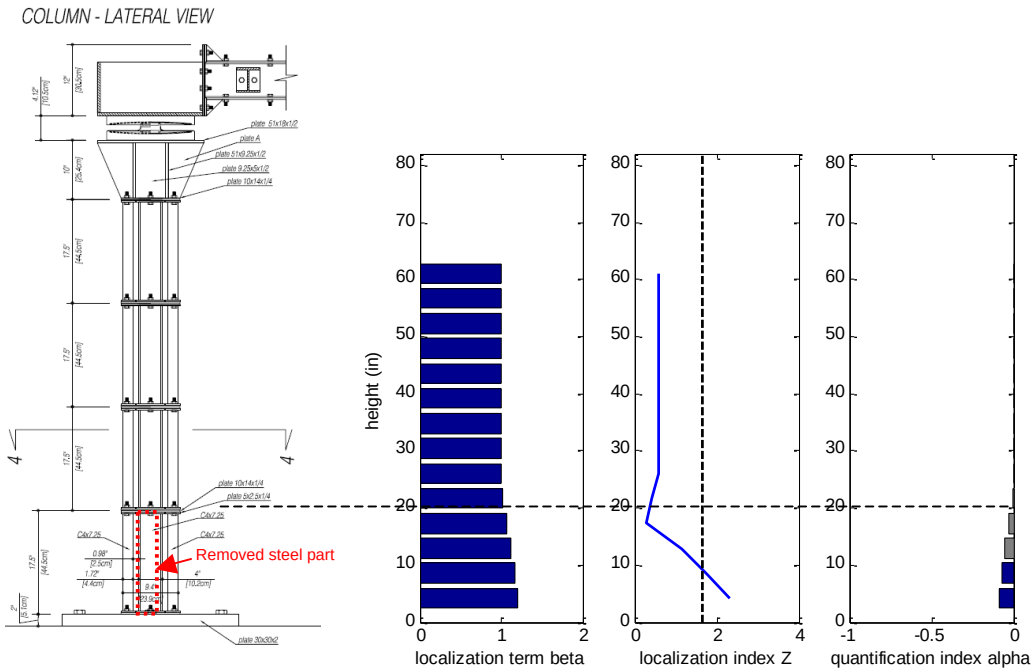


**Fig. 44.** Single-mode damage assessment in the South-Column – test #17. Localization term, localization index, and quantification index.

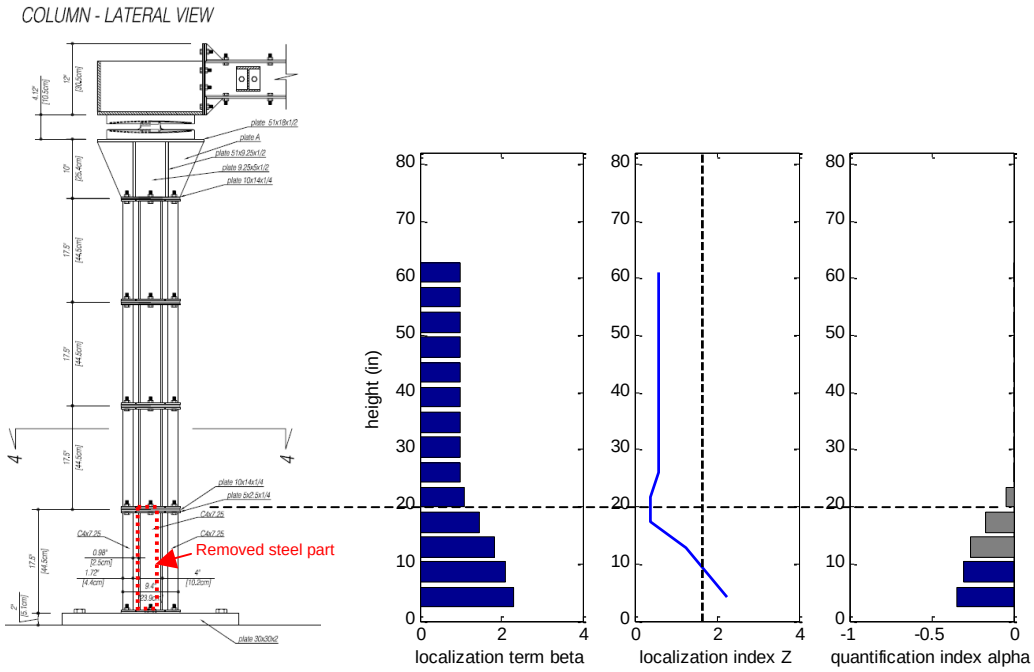


**Fig. 45.** Single-mode damage assessment in the South-Column – test #18. Localization term, localization index, and quantification index.

**2**. The multi-mode damage detection procedure allowed identifying and locating the damage at the bottom of the South Column in all the tri-dimensional tests (#16 and 17). For test #16 the longitudinal mode provided the higher contribution to the multi-modal localization term, while for test #17 the lateral mode contributed most, as shown in **Figs. 46** and **47**. For test #16, a damage extension of 15" was identified through the multi-modal localization index, which is closer to the real extension (19") compared to the one found by the single-mode procedure (10"). As already noted for the damage at the bottom of the North Column, stiffness variation values obtained through the multi-modal procedure are less dispersed and lower than the correspondent values previously identified from the single-mode procedure based on the lateral mode only, which suffer more from errors in the evaluation of the single modal vector used in the analysis. Stiffness reduction as high as 5% and 9% were identified for tests #16 and 17, as visible from the quantification index represented in Figs. **48** and **49**.

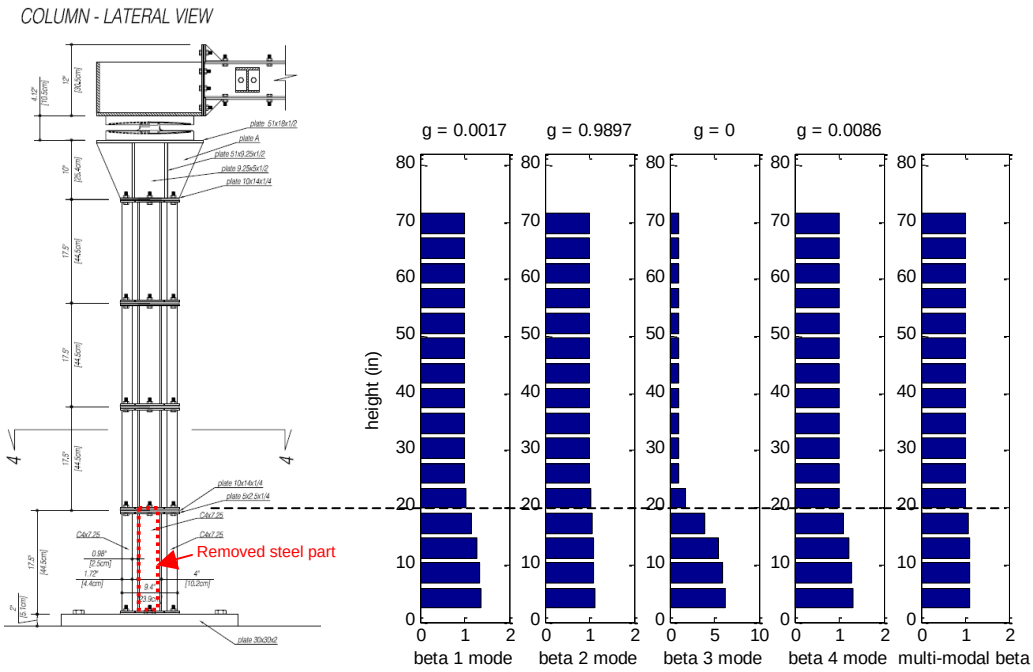


**Fig. 46.** Multi-modal damage assessment in the South-Column – test #16. Single modal localization terms $\beta_{i,j}$ and reliability indices $\gamma_i$, combined multi-modal localization term $\beta_j$.

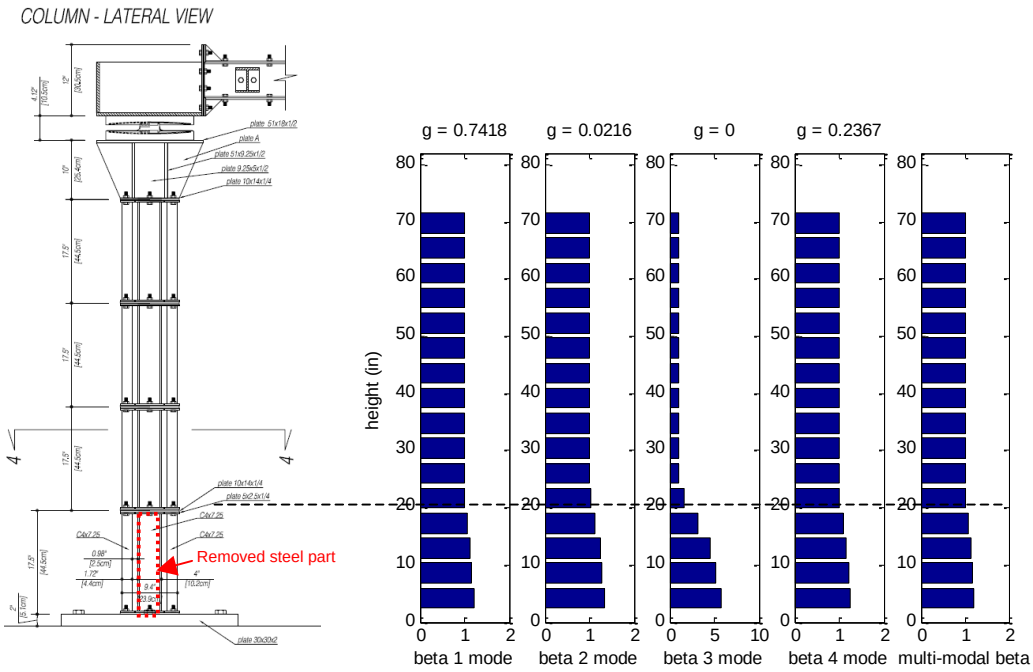


**Fig. 47.** Multi-modal damage assessment in the South-Column – test #17. Single modal localization terms $\beta_{i,j}$ and reliability indices $\gamma_i$, combined multi-modal localization term $\beta_j$.

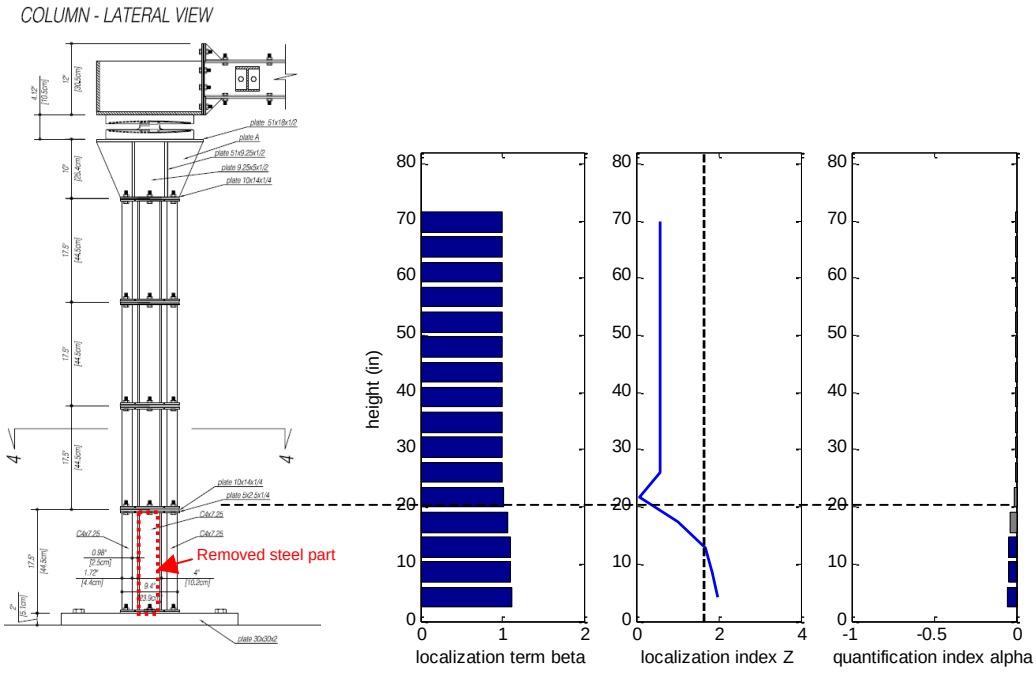


**Fig. 48.** Multi-modal damage assessment in the South-Column – test #16. Localization term, localization index, and quantification index.

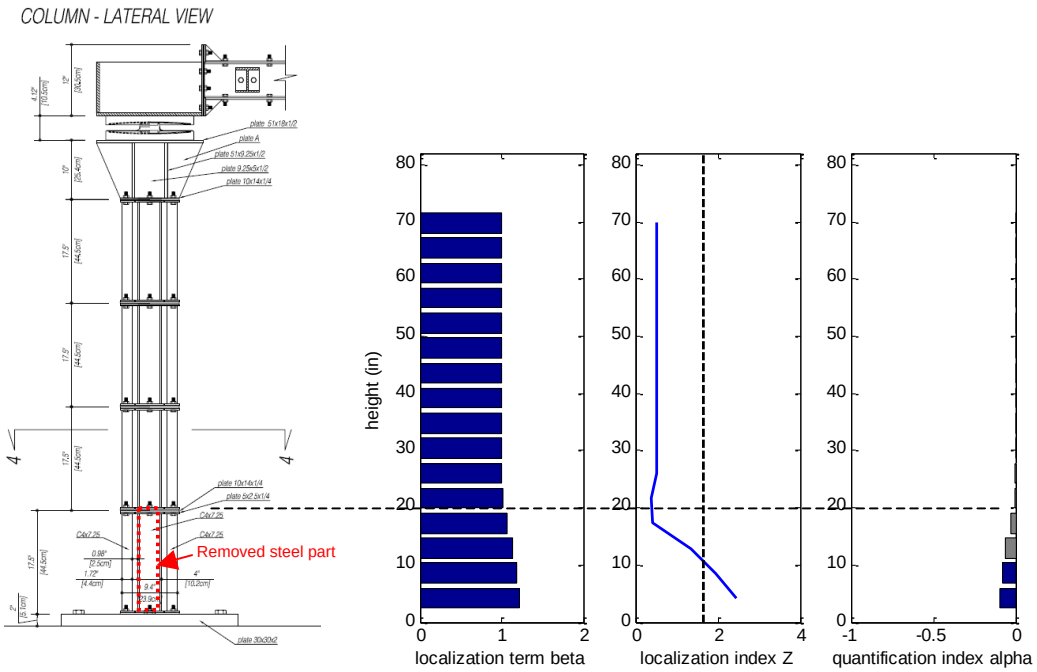


**Fig. 49.** Multi-modal damage assessment in the South-Column – test #17. Localization term, localization index, and quantification index.

**Damage in the West longitudinal deck beam**

The bottom ¼" thick plate was removed from the middle portion of the West longitudinal beam to simulate damage in the deck structure. This part removal produces a 32% and 25% reduction of the moment of inertia about the horizontal axis (associated with bending in the vertical plane) and the vertical axis (associated with bending in the horizontal plane), respectively. Results from the application of the damage identification procedure are synthesized in the following.

**1**. Single-mode damage detection was able to identify and localize the damage from all the available vertical mode shapes (tests #16, and 19). Based on the vertical mode only, damage was localized in the ±10" from the center of the deck, versus the actual damage extension of ±15". With only three vertical acceleration measurements along the damaged beam, additional modal displacements at the beam ends were evaluated through extrapolation from the columns displacements. The deflected shape of the beam was described with 5 displacement values, which is the minimum number of data needed for the evaluation of a 2$^{nd}$ order polynomial distribution of the curvature. Mainly due to lack of redundant data, which determined a distribution highly sensitive to any variation in the available data, the single-mode detection algorithm overestimated the damage effects in terms of stiffness variation and predicted a stiffness reduction of -49% and -56% for tests #17 and 19, respectively, as shown in **Figs. 50** and **51**, where the multi-modal localization term $\beta_j$, the localization index $Z_j$ and the severity index $\alpha_j$ are represented.

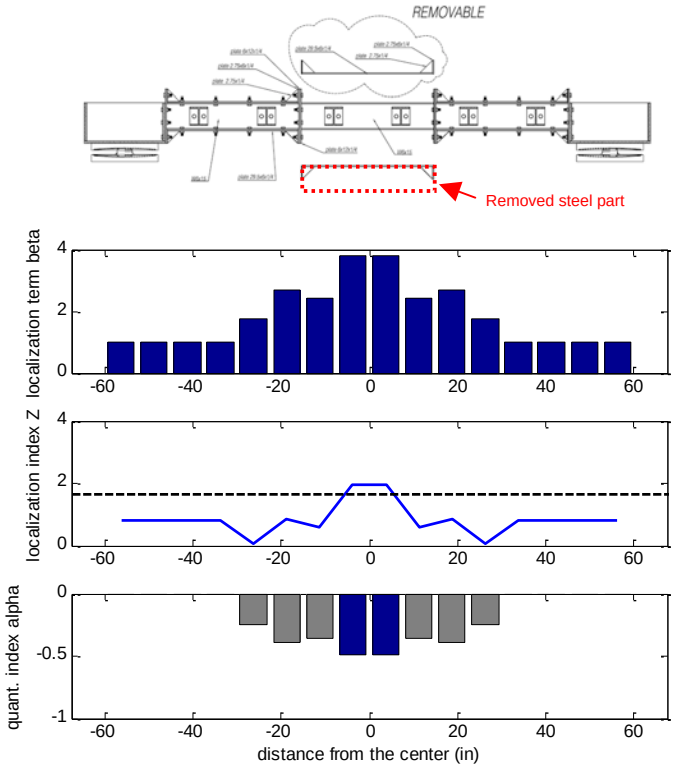


**Fig. 50.** Single-mode damage assessment in the West deck beam – test #17. Localization term, localization index, and quantification index.

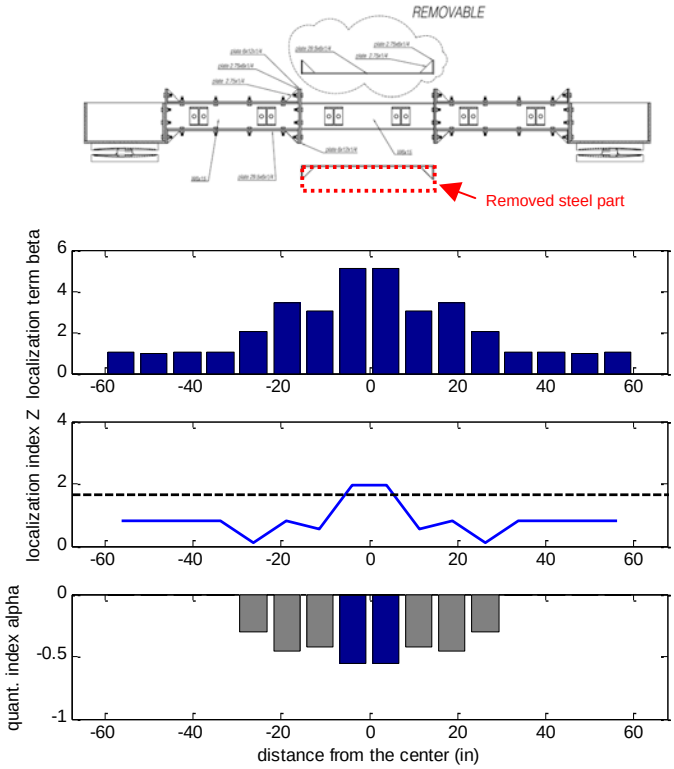


**Fig. 51.** Single-mode damage assessment in the West deck beam – test #19. Localization term, localization index, and quantification index.

**2**. The multi-mode damage detection procedure allowed identifying and locating the damage for the tri-dimensional test #17, in a damage scenario with damages simulated also in both the columns. Based on the higher number of available sensors, the lateral vibration mode provided the greatest contribution to the multi-modal localization term. For lateral deflections a stiffness reduction of 25% was expected. However, since sensors distributed all around the deck and not specifically on the damaged beam were used, the identified deflection referred to both the longitudinal beams and allowed evaluating an average stiffness reduction of 17% for the couple of beams as a whole. The localization terms are shown in **Fig. 52**, while the localization index and the severity index are represented in **Fig. 53**.

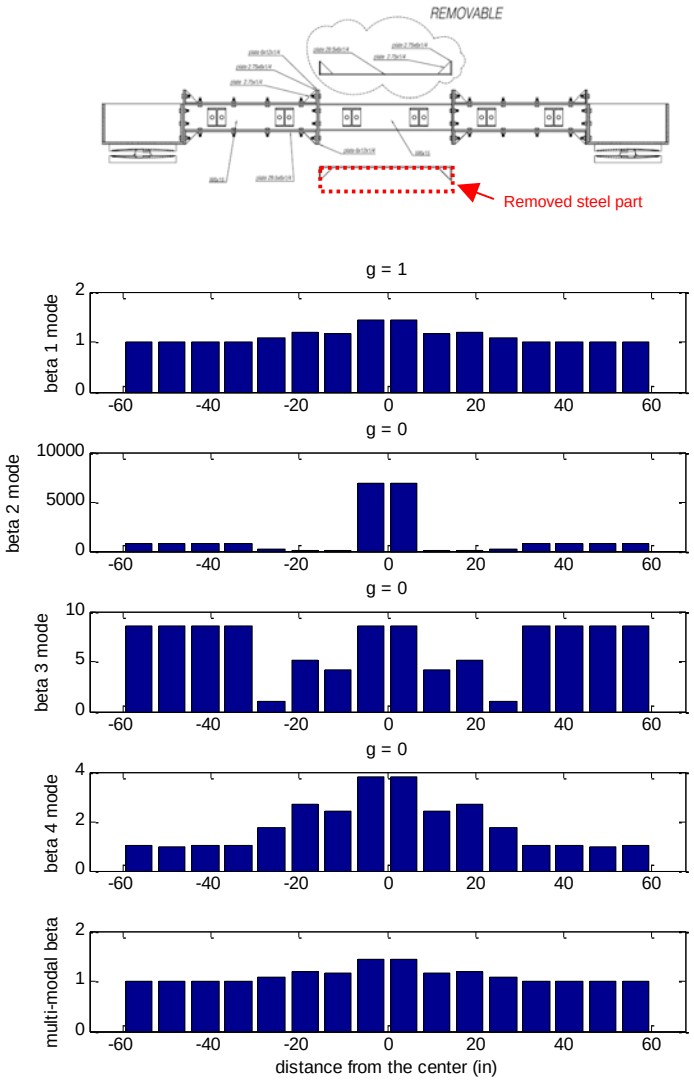


**Fig. 52.** Multi-modal damage assessment in the West deck beam – test #17. Single modal localization terms $\beta_{i,j}$ and reliability indices $\gamma_i$, combined multi-modal localization term $\beta_j$.

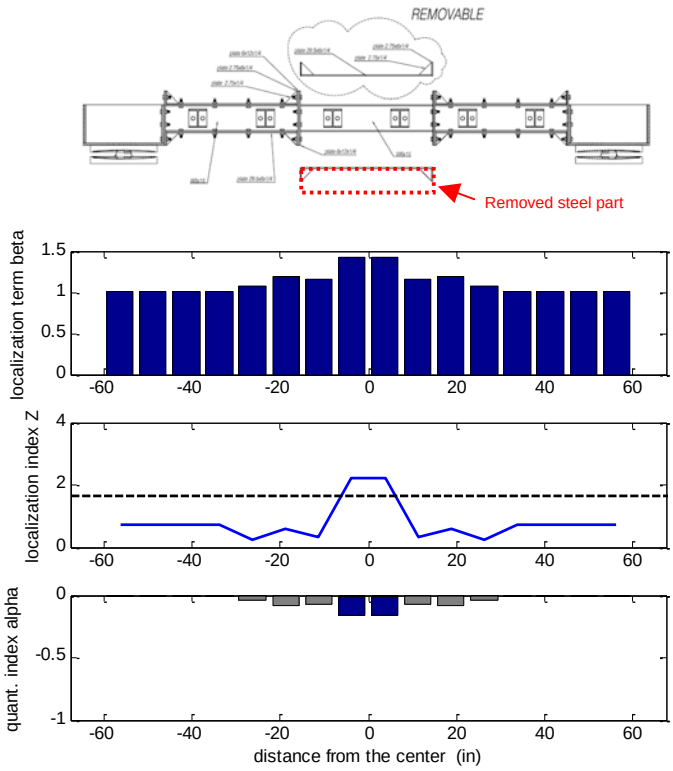


**Fig. 53.** Multi-modal damage assessment in the West deck beam – test #17. Localization term, localization index, and quantification index.

## Further experimental testing campaign

Further experimental tests are proposed to extend the assessment of the damage identification procedures capability for Level III identification of damages in complex scenarios. Proposed tests will focus on damages on columns and isolators, as summarized in **Table 15**. Two levels of input intensity (25% and 50%) will be used. The following test protocol is proposed. Test #1 and #2 will be performed on the undamaged bridge model. After these tests, damages will be simulated in the first 3 lower segments of the North column (N column, for the orientation see **Fig. 5**). Different damages can be simulated in each column segment by removing 4 steel C sections (see **Fig. 2**). In the proposed tests, only C sections in longitudinal directions will be removed. Initially, the North and South C sections of the first segment (parts 1N and 1S) will be removed to simulated two different levels of damage at the bottom of the column (test #3 to #6). Additional damages will be simulated on the upper portions of the N column by removing North C sections from the second and third segment (test #7 to #10). In tests #11 and #12, damages will be only at the North side of the N column (segments 1, 2 and 3). In tests #13 and #14, the isolators on the North column will be damaged. In these tests, the north column and the isolator will be

simultaneously damaged (increment of friction). In tests #15 to #17 damages in the columns will be reduced. Tests # 21 and #22 will be a repetition of tests #1 and #2.

**Table 15.** Proposed test protocol.

| | Input Type-Intensity[1,2] | | | |
|---|---|---|---|---|
| **Test #** | **Dir-X** | **Dir-Y** | **Dir-Z** | **Simulated damage: part removed** |
| 01 | - | A-25% | - | - |
| 02 | - | A-50% | - | - |
| 03 | - | A-25% | - | N Column segments: 1N, |
| 04 | - | A-50% | - | N Column segments: 1N, |
| 05 | - | A-25% | - | N Column segments: 1N, 1S |
| 06 | - | A-50% | - | N Column segments: 1N, 1S |
| 07 | - | A-25% | - | N Column segments: 1N, 1S, 2N |
| 08 | - | A-50% | - | N Column segments: 1N, 1S, 2N |
| 09 | - | A-25% | - | N Column segments: 1N, 1S, 2N, 3N |
| 10 | - | A-25% | - | N Column segments: 1N, 1S, 2N, 3N |
| 11 | - | A-25% | - | N Column segments: 1N, 2N, 3N |
| 12 | - | A-50% | - | N Column segments: 1N, 2N, 3N |
| 13 | - | A-50% | - | N Column segments: 1N, 2N, 3N + NE Isolator |
| 14 | - | A-50% | - | N Column segments: 1N, 2N, 3N+ NE,NW Isolators |
| 15 | - | A-50% | - | N Column segments: 1N, 2N+ NE,NW Isolator |
| 16 | - | A-50% | - | N Column segments: 1N + NE,NW Isolators |
| 17 | - | A-25% | - | NE,NW Isolators |
| 18 | - | A-50% | - | NE,NW Isolators |
| 19 | - | A-25% | - | NE Isolator |
| 20 | - | A-50% | - | NE Isolator |
| 21 | - | A-25% | - | - |
| 22 | - | A-50% | - | - |

## Summary and conclusion

Aimed at evaluating the efficacy of ambient vibration based damage identification procedures for bridges, the capability of a Level III method (damage detection, localization and severity estimation) was investigated through shake table tests on a bridge model equipped with a sparse sensor network.

The two-columns one-span bridge model allows simulating simultaneous damages in different positions through steel part removal. The modal deformation based damage identification procedure described in (Bonessio et al. 2012) was used to identify damages in five different scenarios, in which damages in both columns and the longitudinal beams of the deck were combined in different ways. A minimum number of accelerometers required to determine a proper distribution of curvature along the damaged elements was installed on the bridge model.

The input only SSI-Cov system identification procedure was used to identify modal characteristics in un-damaged and damaged conditions. Based on the identified modal characteristics, single- and multi-modal indices were used to detect, localize, and quantify the severity and the extension of the damage. Results from the experimental campaign showed that, even from a non-redundant sparse network of accelerometers, the damage identification procedure was able to detect damages in all the simulated scenarios. The localization and severity estimation of the damage was acceptable but suffered by lack of redundant data, which made each modal vector highly sensible to any variations from one test to another one. Thus, an improvement both in terms of localization and quantification are expected from more dense sensor networks. The multi-modal indices provided higher stability in the damage identification results than indices based on singular modes. However, as the damages result in different changes of the element stiffness depending on the direction of deflection, multi-modal methods only allow a global average estimation of the damage severity from modal displacement in longitudinal, lateral and vertical direction. A clear interpretation of the damage severity in terms of stiffness variation appears possible only by considering modes with predominant displacements in a given direction.

Acceleration and displacement data collected from tests on the model bridge constitute an important database that can be used for further evaluation of the efficacy of a number of damage identification methods. Complimentary tests aimed at simulating propagation of the damage from the bottom to the top of the columns and in seismic isolators installed between the deck and the columns are proposed for a possible extension of the existing dataset.

## References


Allemang, R. J., Brown, D. L., (1982). “A correlation coefficient for modal vector analysis”, *Proceedings of International Modal Analysis Conference*, pp. 110–116.

Benzoni, G., Bonessio, N., Lomiento, G. (2011). “Structural Health Monitoring of Bridges with Anti-Seismic Devices” *Proceedings of the 8th European Conference on Structural Dynamics* (Eurodyn 2011), Leuven, Belgium 4-6 jul 2011.

Bonessio, N., Lomiento, G., Benzoni, G., (2012). “Damage identification procedure for seismically isolated bridges”, *Structural Control and Health Monitoring*, 19(5), 565-578.

Haritos, N., and Owen., J. S., (2004). "The use of vibration data for damage detection in bridges: a comparison of system identification and pattern recognition approaches." *Structural Health Monitoring* 3.2: 141-163.

Liang, Z., Lee, G. C. and Kong., F., (1997) "On detection of damage location of bridges." *Proceedings of SPIE, the International Society for Optical Engineering*. Vol. 3089.

Mazurek, D. F., and DeWolf, J. T. (1990). “Experimental study of bridge monitoring technique.” *J. Struct. Engrg., ASCE*, 116 (9 ), 2532–2549.

Oppenheim, A.V., and R.W. Schafer, *Discrete-Time Signal Processing*, Prentice-Hall, 1989, pp.284–285.

Peeters, B., (2000). “System Identification and damage detection in civil engineering.” *Ph.D. thesis Department of Civil Engineering*. K.U. Leuven Belgium.

Spillman Jr, W. B., Huston, D. R., Fuhr, P. L., & Lord, J. R. (1993). “Neural network damage detection in a bridge element.” *Proceedings of the 1993 North American Conference on Smart Structures and Materials* (pp. 288-299). International Society for Optics and Photonics.

Spyrakos, C., Chen, H.L., Stephens, J. and Govindaraj,V., (1990). “Evaluating Structural Deterioration Using Dynamic Response Characterization,” *Proceedings of The International Workshop on Intelligent Structures*, Taipei, Taiwan, pp. 137-153.

# Appendix I – Identified vibration modes

Test 01 – Lateral vibration mode

| Sensor # | | | Modal displacement | | |
|---|---|---|---|---|---|
| | W → E | | X | Y | Z |
| Top ← Bottom | 1 | North Column | 0 | 0 | 0 |
| | 3 | | -0.241 | 0.003 | 0.004 |
| | 5 | | -0.805 | -0.008 | 0.009 |
| | 14 | | - | -0.039 | - |
| | 11 | | -1.088 | - | - |
| | 15 | | - | -0.014 | - |
| Top ← Bottom | 2 | South Column | 0 | 0 | 0 |
| | 4 | | -0.059 | 0.022 | -0.014 |
| | 8 | | -0.594 | -0.010 | 0.017 |
| | 12 | | - | -0.024 | - |
| | 10 | | -1.324 | - | - |
| | 13 | | - | -0.034 | - |
| N ← S | 17 | Deck | - | - | -0.145 |
| | 6 | | -1.212 | 0.023 | 0.147 |
| | 16 | | - | - | -0.148 |
| | 9 | | -1.324 | -0.036 | -0.013 |
| | 7 | | -1.293 | -0.024 | -0.139 |

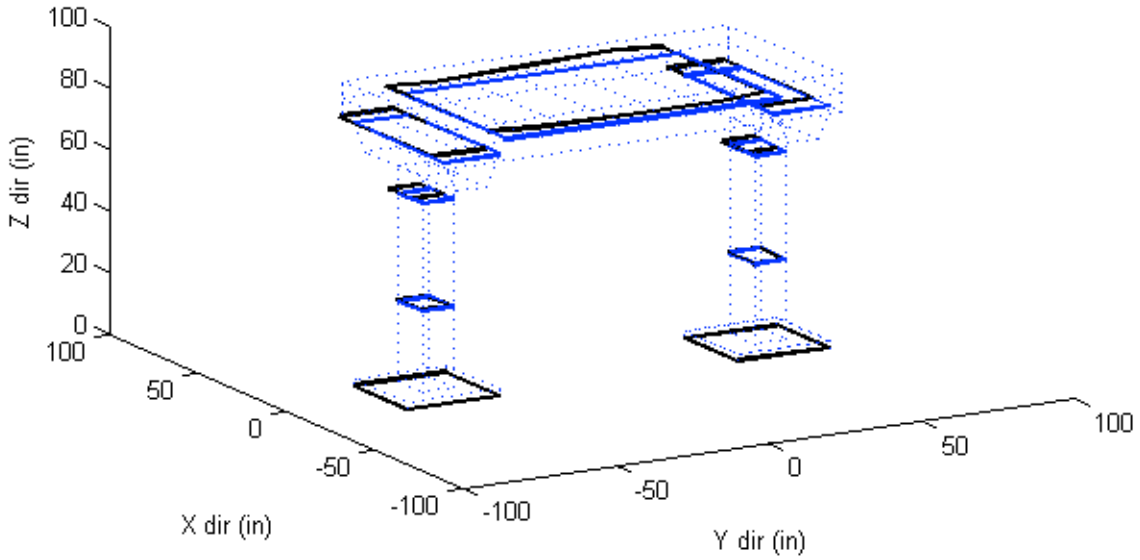

Test 01 – Torsional vibration mode

| Sensor # | | | | Modal displacement | | |
|---|---|---|---|---|---|---|
| | W → E | | | X | Y | Z |
| Top ← Bottom | 1 | | North Column | 0 | 0 | 0 |
| | 3 | | | -0.239 | -0.033 | 0.226 |
| | 5 | | | -1.971 | -0.342 | 0.143 |
| | 14 | | | - | -0.550 | - |
| | 11 | | | -1.301 | - | - |
| | | 15 | | - | 0.896 | - |
| Top ← Bottom | 2 | | South Column | 0 | 0 | 0 |
| | 4 | | | 0.477 | 0.481 | 0.377 |
| | 8 | | | 1.270 | 0.697 | -0.100 |
| | 12 | | | - | -0.815 | - |
| | 10 | | | -0.190 | - | - |
| | | 13 | | - | 1.181 | - |
| N ← S | 17 | | Deck | - | - | 0.185 |
| | | 6 | | 1.568 | 1.442 | -0.157 |
| | 16 | | | - | - | -0.128 |
| | 9 | | | -0.190 | 0.521 | -0.366 |
| | 7 | | | -0.936 | -0.815 | -0.199 |

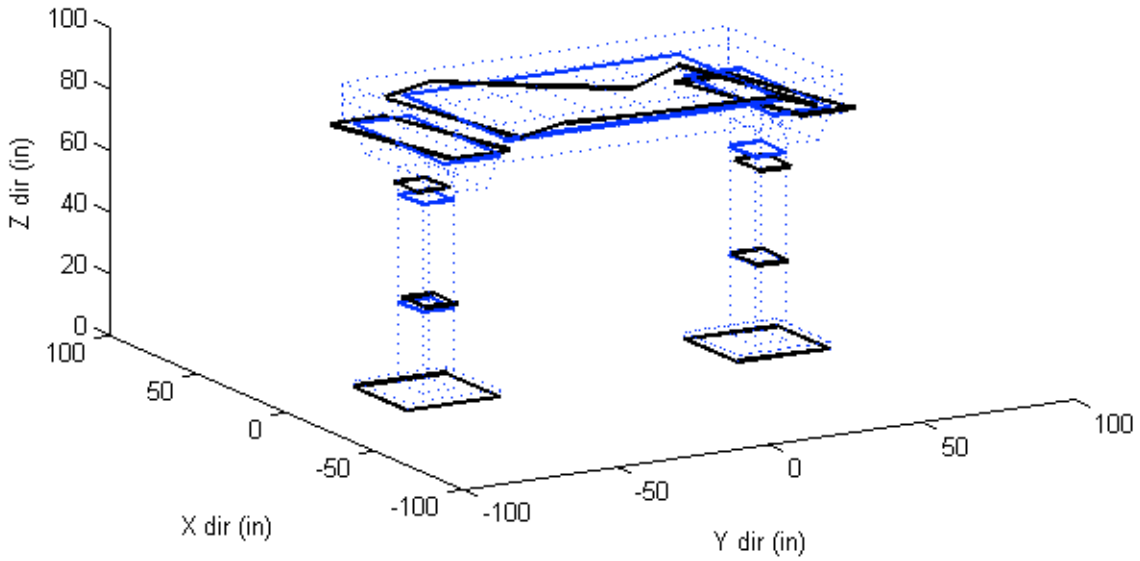

Test 02 – Longitudinal vibration mode

| Sensor # | | | | Modal displacement | | |
|---|---|---|---|---|---|---|
| | W → E | | | X | Y | Z |
| Top ← Bottom | 1 | | North Column | 0 | 0 | 0 |
| | 3 | | | 0.020 | -0.179 | 0.039 |
| | 5 | | | 0.027 | -0.708 | 0.011 |
| | 14 | | | - | -0.849 | - |
| | 11 | | | 0.046 | - | - |
| | | 15 | | - | -0.894 | - |
| Top ← Bottom | 2 | | South Column | 0 | 0 | 0 |
| | 4 | | | 0.015 | -0.196 | 0.005 |
| | 8 | | | 0.035 | -0.709 | 0.016 |
| | 12 | | | - | -0.864 | - |
| | 10 | | | 0.045 | - | - |
| | | 13 | | - | -0.813 | - |
| N ← S | 17 | | Deck | - | - | 0.017 |
| | | 6 | | 0.060 | -0.811 | -0.012 |
| | 16 | | | - | - | 0.017 |
| | 9 | | | 0.045 | -0.885 | -0.002 |
| | 7 | | | 0.052 | -0.864 | 0.010 |

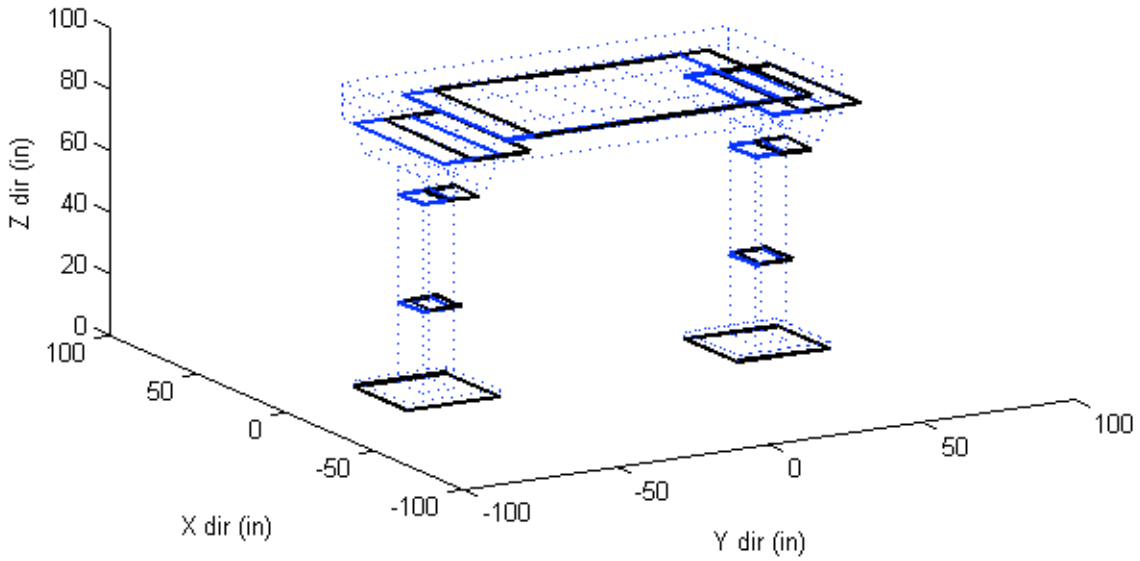

Test 02 – Torsional vibration mode

| Sensor # | | | Modal displacement | | |
|---|---|---|---|---|---|
| W → E | | | X | Y | Z |
| Top ← Bottom | 1 | North Column | 0 | 0 | 0 |
| | 3 | | -0.187 | 0.036 | 0.043 |
| | 5 | | -1.342 | -0.031 | 0.143 |
| | 14 | | - | -1.074 | - |
| | 11 | | -1.433 | - | - |
| | 15 | | - | 0.950 | - |
| Top ← Bottom | 2 | South Column | 0 | 0 | 0 |
| | 4 | | 0.402 | -0.110 | -0.115 |
| | 8 | | 1.313 | 0.067 | -0.136 |
| | 12 | | - | -1.084 | - |
| | 10 | | 0.368 | - | - |
| | 13 | | - | 0.865 | - |
| N ← S | 17 | Deck | - | - | 0.391 |
| | 6 | | 1.197 | 0.991 | -0.487 |
| | 16 | | - | - | -0.012 |
| | 9 | | 0.368 | -0.065 | -0.055 |
| | 7 | | -1.024 | -1.084 | -0.628 |

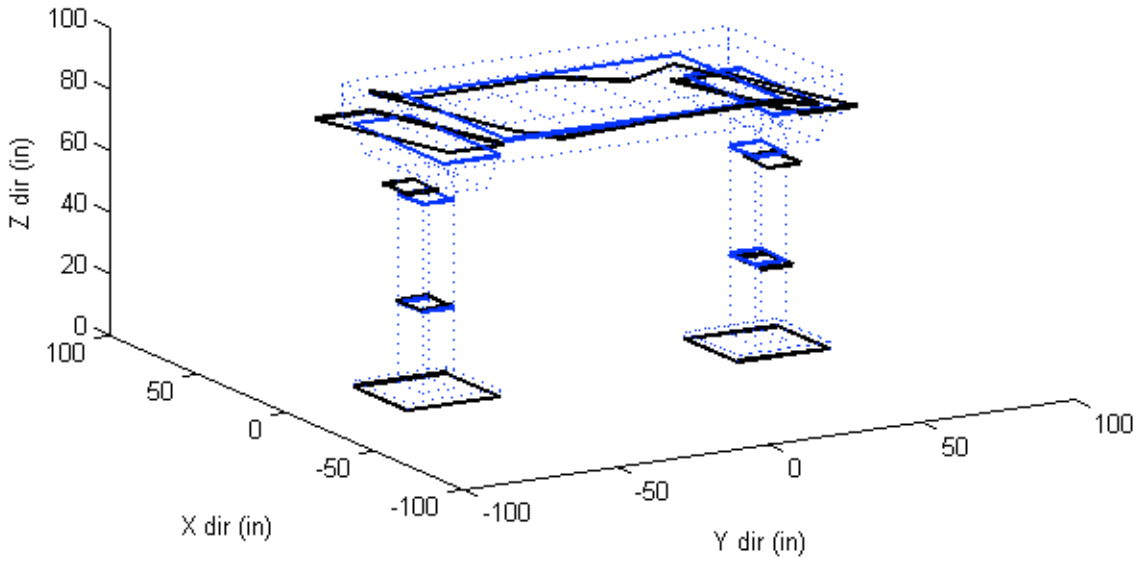

Test 03 – Lateral vibration mode

| Sensor # | | | Modal displacement | | |
|---|---|---|---|---|---|
| | W → E | | X | Y | Z |
| Top ← Bottom | 1 | North Column | 0 | 0 | 0 |
| | 3 | | -0.233 | -0.051 | -0.001 |
| | 5 | | -0.785 | -0.135 | 0.010 |
| | 14 | | - | -0.147 | - |
| | 11 | | -1.055 | - | - |
| | 15 | | - | -0.152 | - |
| Top ← Bottom | 2 | South Column | 0 | 0 | 0 |
| | 4 | | -0.183 | -0.033 | 0.022 |
| | 8 | | -0.673 | -0.122 | 0.024 |
| | 12 | | - | -0.176 | - |
| | 10 | | -1.315 | - | - |
| | 13 | | - | -0.145 | - |
| N ← S | 17 | Deck | - | - | -0.132 |
| | 6 | | -1.340 | -0.165 | 0.132 |
| | 16 | | - | - | -0.131 |
| | 9 | | -1.315 | -0.179 | -0.009 |
| | 7 | | -1.376 | -0.176 | -0.172 |

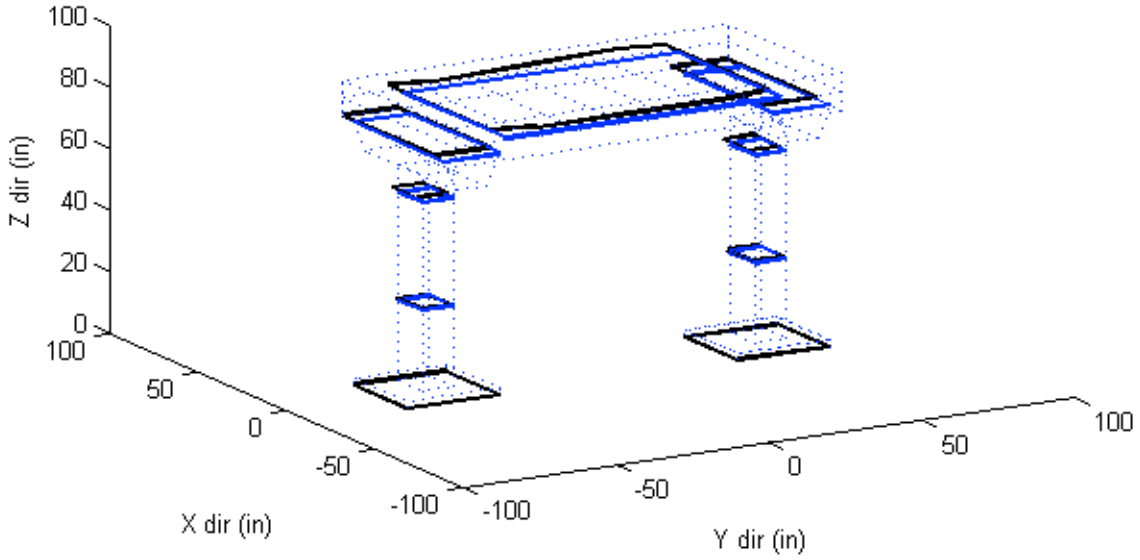

Test 03 – Torsional vibration mode

| Sensor # | | | Modal displacement | | |
|---|---|---|---|---|---|
| W → E | | | X | Y | Z |
| Top ← Bottom | 1 | North Column | 0 | 0 | 0 |
| | 3 | | -0.382 | -0.037 | -0.067 |
| | 5 | | -1.356 | 0.131 | 0.038 |
| | 14 | | - | -1.007 | - |
| | 11 | | -1.337 | - | - |
| | 15 | | - | 1.082 | - |
| Top ← Bottom | 2 | South Column | 0 | 0 | 0 |
| | 4 | | 0.268 | -0.035 | -0.126 |
| | 8 | | 1.321 | 0.006 | -0.153 |
| | 12 | | - | -0.983 | - |
| | 10 | | 0.383 | - | - |
| | 13 | | - | 0.911 | - |
| N ← S | 17 | Deck | - | - | 0.436 |
| | 6 | | 1.126 | 1.136 | -0.517 |
| | 16 | | - | - | 0.020 |
| | 9 | | 0.383 | 0.046 | 0.028 |
| | 7 | | -0.921 | -0.983 | -0.448 |

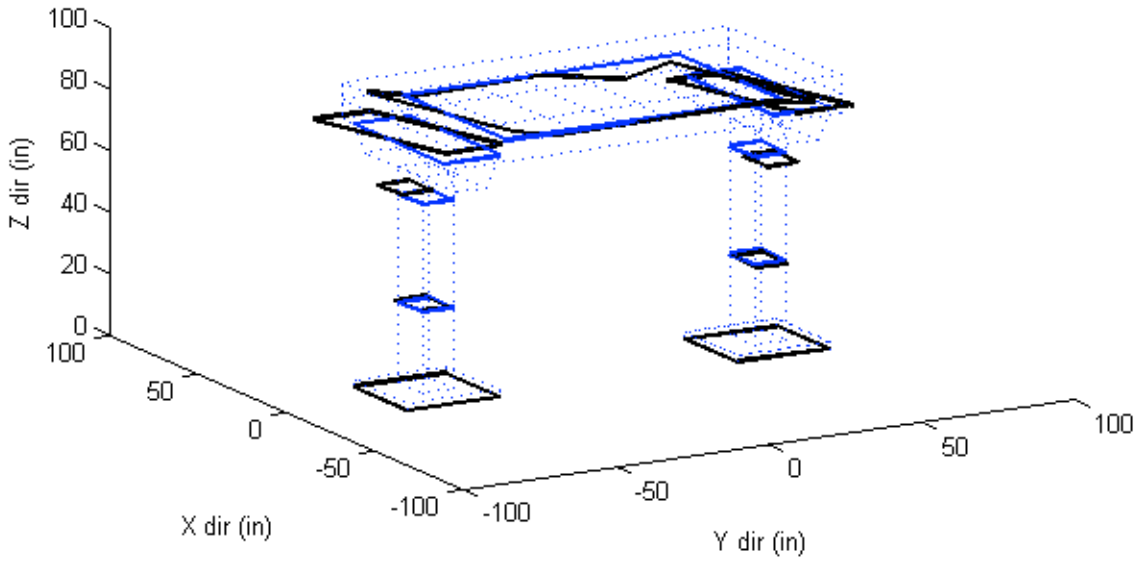

Test 04 – Longitudinal vibration mode

| Sensor # | | | | Modal displacement | | |
|---|---|---|---|---|---|---|
| | W → E | | | X | Y | Z |
| Top ← Bottom | 1 | | North Column | 0 | 0 | 0 |
| | 3 | | | 0.007 | -0.215 | 0.007 |
| | 5 | | | 0.030 | -0.681 | 0.007 |
| | 14 | | | - | -0.846 | - |
| | 11 | | | 0.057 | - | - |
| | | 15 | | - | -0.864 | - |
| Top ← Bottom | 2 | | South Column | 0 | 0 | 0 |
| | 4 | | | 0.009 | -0.240 | 0.006 |
| | 8 | | | 0.040 | -0.709 | 0.002 |
| | 12 | | | - | -0.891 | - |
| | 10 | | | 0.060 | - | - |
| | | 13 | | - | -0.821 | - |
| N ← S | 17 | | Deck | - | - | 0.023 |
| | | 6 | | 0.070 | -0.861 | -0.024 |
| | 16 | | | - | - | 0.022 |
| | 9 | | | 0.060 | -0.885 | -0.003 |
| | 7 | | | 0.063 | -0.891 | 0.011 |

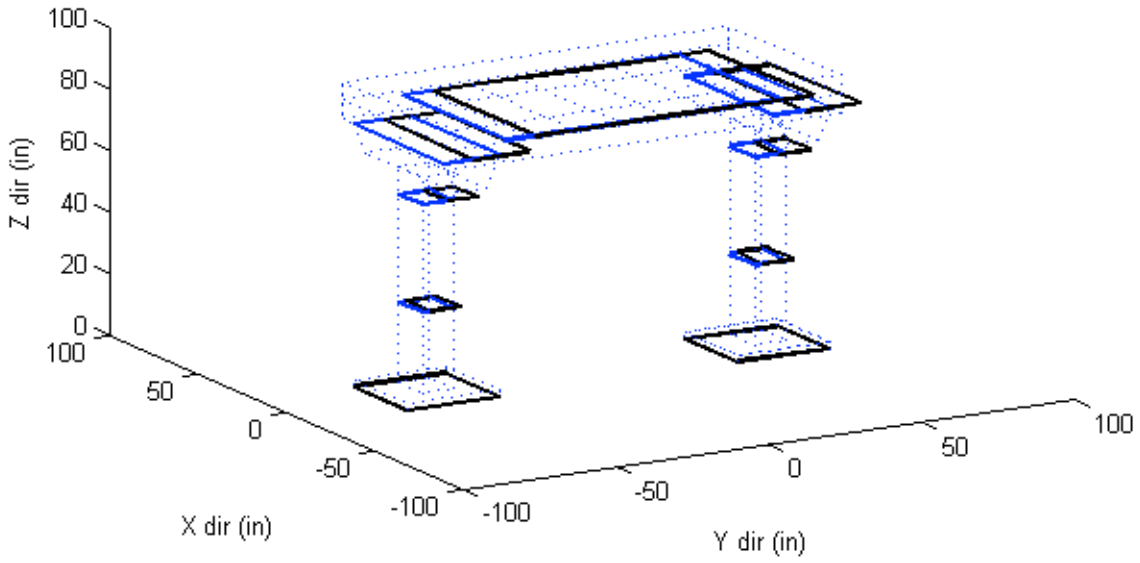

Test 04 – Torsional vibration mode

| Sensor # | | | Modal displacement | | |
|---|---|---|---|---|---|
| W → E | | | X | Y | Z |
| Top ← Bottom | 1 | North Column | 0 | 0 | 0 |
| | 3 | | -0.345 | -0.029 | -0.027 |
| | 5 | | -1.255 | 0.126 | 0.128 |
| | 14 | | - | -0.897 | - |
| | 11 | | -1.606 | - | - |
| | 15 | | - | 1.132 | - |
| Top ← Bottom | 2 | South Column | 0 | 0 | 0 |
| | 4 | | 0.292 | 0.049 | 0.142 |
| | 8 | | 1.076 | 0.180 | -0.162 |
| | 12 | | - | -0.823 | - |
| | 10 | | 0.219 | - | - |
| | 13 | | - | 1.088 | - |
| N ← S | 17 | Deck | - | - | 0.384 |
| | 6 | | 0.910 | 1.113 | -0.252 |
| | 16 | | - | - | -0.057 |
| | 9 | | 0.219 | 0.062 | -0.027 |
| | 7 | | -0.937 | -0.823 | -0.387 |

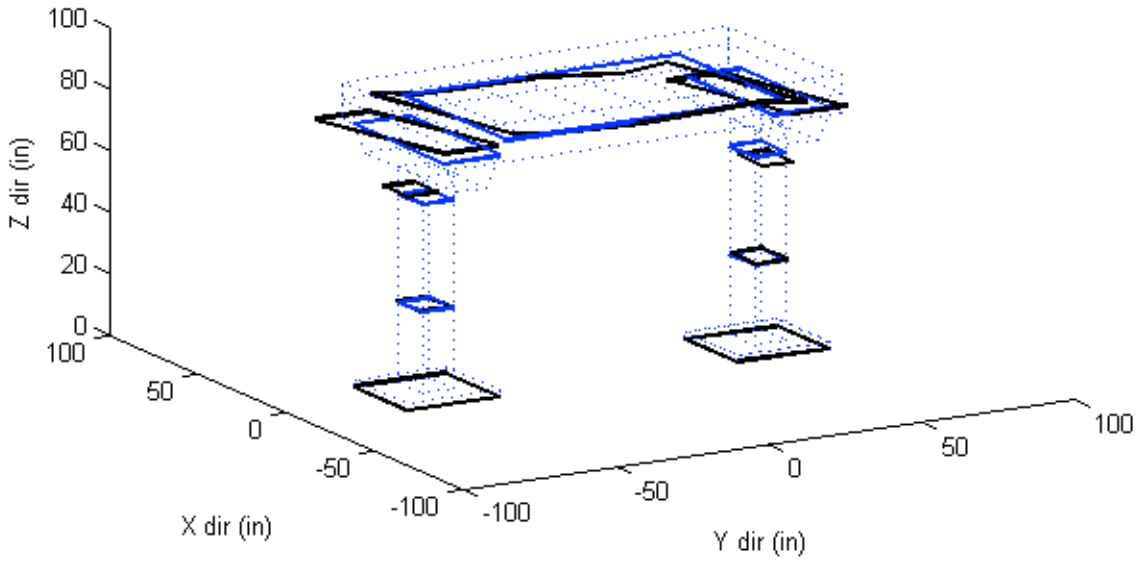

Test 05 – Vertical vibration mode

| Sensor # | | | Modal displacement | | |
|---|---|---|---|---|---|
| W → E | | | X | Y | Z |
| Top ← Bottom | 1 | North Column | 0 | 0 | 0 |
| | 3 | | 0.153 | 0.162 | 0.082 |
| | 5 | | -0.206 | 0.216 | -0.069 |
| | 14 | | - | -0.015 | - |
| | 11 | | 0.262 | - | - |
| | 15 | | - | 0.184 | - |
| Top ← Bottom | 2 | South Column | 0 | 0 | 0 |
| | 4 | | 0.494 | -0.044 | -0.045 |
| | 8 | | 0.200 | -0.164 | -0.400 |
| | 12 | | - | 0.050 | - |
| | 10 | | 0.212 | - | - |
| | 13 | | - | 0.001 | - |
| N ← S | 17 | Deck | - | - | 0.673 |
| | 6 | | 0.156 | 0.245 | -0.780 |
| | 16 | | - | - | 0.946 |
| | 9 | | 0.212 | 0.046 | -1.353 |
| | 7 | | 0.084 | 0.050 | -0.461 |

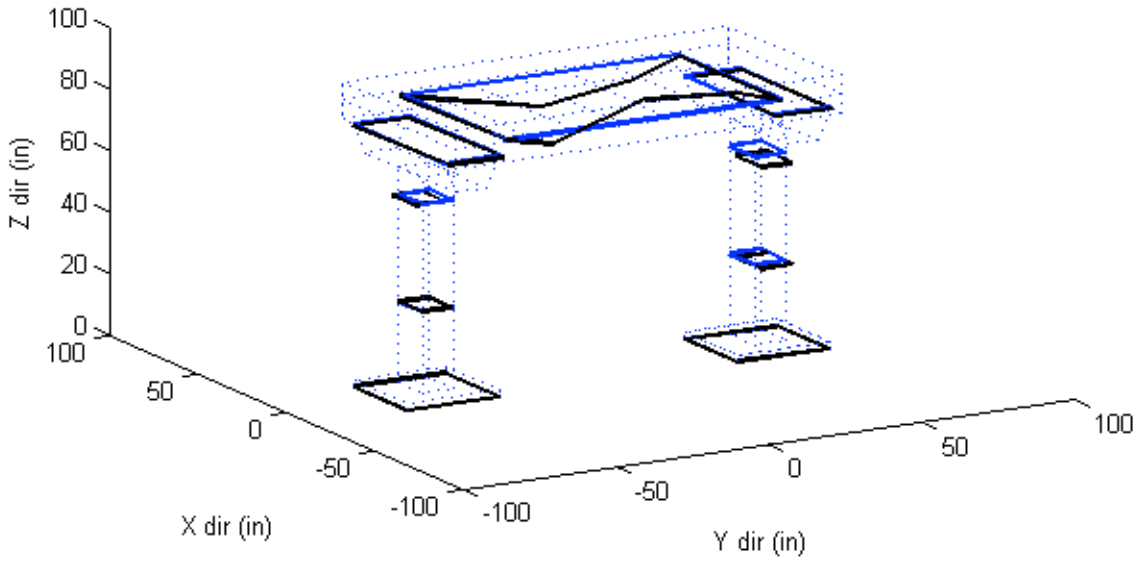

Test 06 – Vertical vibration mode

| Sensor # | | | Modal displacement | | |
|---|---|---|---|---|---|
| W → E | | | X | Y | Z |
| Top ← Bottom | 1 | North Column | 0 | 0 | 0 |
| | 3 | | 0.015 | 0.170 | -0.047 |
| | 5 | | -0.016 | 0.335 | -0.044 |
| | 14 | | - | 0.236 | - |
| | 11 | | -0.017 | - | - |
| | 15 | | - | -0.254 | - |
| Top ← Bottom | 2 | South Column | 0 | 0 | 0 |
| | 4 | | 0.021 | -0.197 | 0.036 |
| | 8 | | 0.065 | -0.344 | -0.040 |
| | 12 | | - | 0.037 | - |
| | 10 | | -0.013 | - | - |
| | 13 | | - | 0.218 | - |
| N ← S | 17 | Deck | - | - | -0.841 |
| | 6 | | 0.017 | -0.017 | -0.547 |
| | 16 | | - | - | -1.162 |
| | 9 | | -0.013 | 0.055 | -1.133 |
| | 7 | | -0.003 | 0.037 | -0.599 |

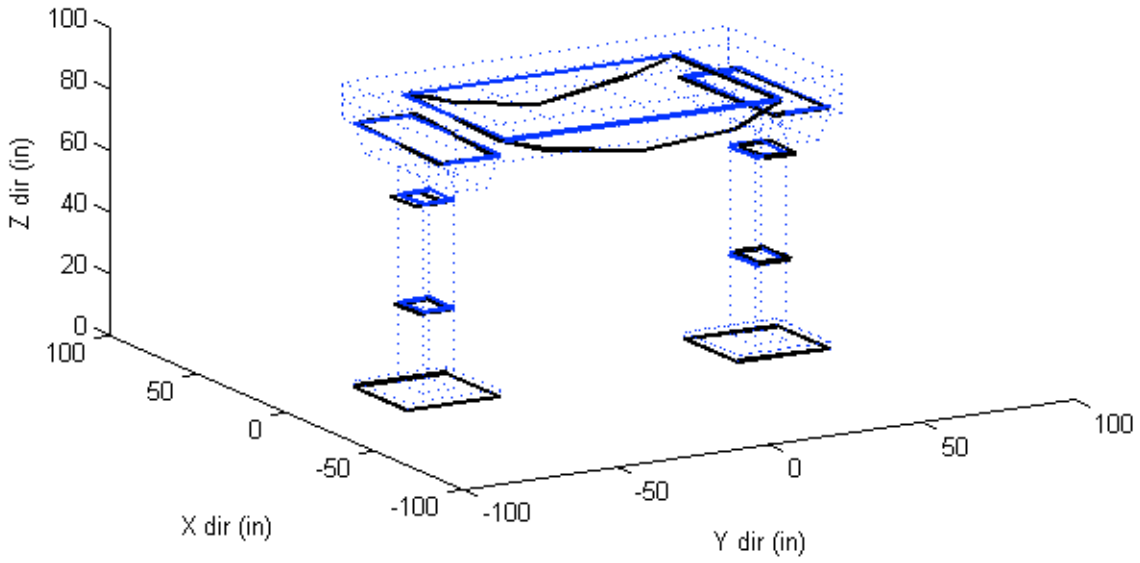

Test 07 – Lateral vibration mode

| Sensor # | | | Modal displacement | | |
|---|---|---|---|---|---|
| W → E | | | X | Y | Z |
| Top ← Bottom | 1 | North Column | 0 | 0 | 0 |
| | 3 | | -0.182 | -0.008 | 0.006 |
| | 5 | | -0.750 | -0.028 | 0.015 |
| | 14 | | - | -0.042 | - |
| | 11 | | -1.106 | - | - |
| | 15 | | - | -0.034 | - |
| Top ← Bottom | 2 | South Column | 0 | 0 | 0 |
| | 4 | | -0.169 | -0.009 | 0.004 |
| | 8 | | -0.699 | -0.028 | 0.014 |
| | 12 | | - | -0.039 | - |
| | 10 | | -1.290 | - | - |
| | 13 | | - | -0.042 | - |
| N ← S | 17 | Deck | - | - | -0.133 |
| | 6 | | -1.288 | -0.036 | 0.133 |
| | 16 | | - | - | -0.133 |
| | 9 | | -1.290 | -0.039 | 0.001 |
| | 7 | | -1.292 | -0.039 | -0.134 |

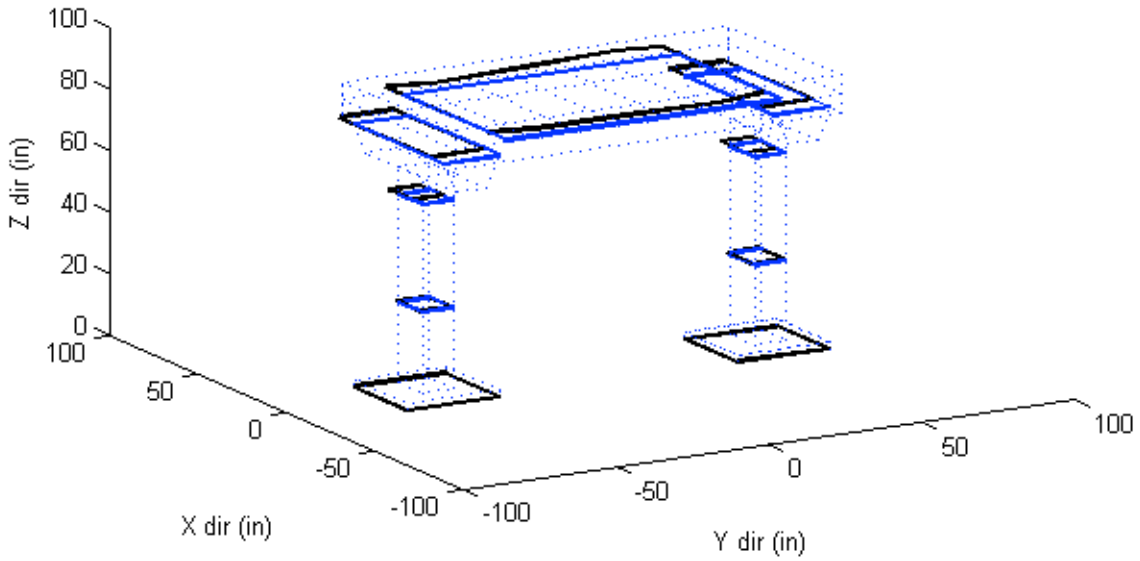

Test 03 – Torsional vibration mode

| Sensor # | | | Modal displacement | | |
|---|---|---|---|---|---|
| W → E | | | X | Y | Z |
| Top ← Bottom | 1 | North Column | 0 | 0 | 0 |
| | 3 | | -0.431 | -0.170 | 0.039 |
| | 5 | | -1.391 | 0.048 | 0.163 |
| | 14 | | - | -0.966 | - |
| | 11 | | -1.755 | - | - |
| | 15 | | - | 1.129 | - |
| Top ← Bottom | 2 | South Column | 0 | 0 | 0 |
| | 4 | | 0.190 | 0.084 | 0.068 |
| | 8 | | 0.999 | 0.095 | 0.016 |
| | 12 | | - | -0.889 | - |
| | 10 | | -0.099 | - | - |
| | 13 | | - | 0.977 | - |
| N ← S | 17 | Deck | - | - | 0.290 |
| | 6 | | 0.660 | 1.038 | -0.054 |
| | 16 | | - | - | -0.118 |
| | 9 | | -0.099 | 0.057 | 0.124 |
| | 7 | | -1.226 | -0.889 | -0.520 |

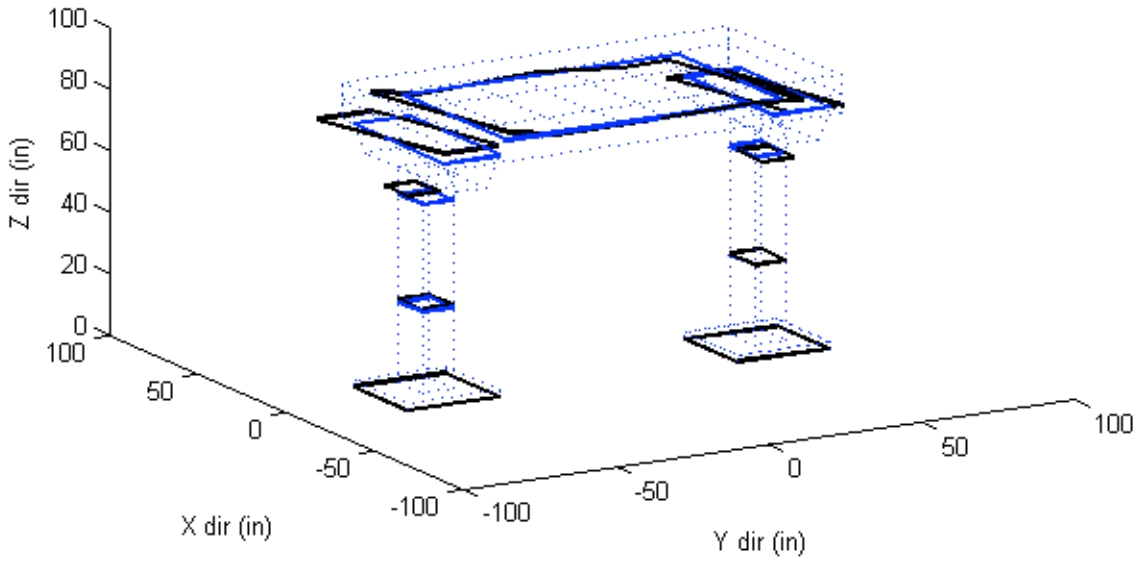

Test 08 – Longitudinal vibration mode

| Sensor # W → E | | | Modal displacement X | Y | Z |
|---|---|---|---|---|---|
| Top ← Bottom | 1 | North Column | 0 | 0 | 0 |
| | 3 | | 0.072 | -0.089 | -0.018 |
| | 5 | | 0.237 | -0.524 | -0.026 |
| | 14 | | - | -0.912 | - |
| | 11 | | 0.394 | - | - |
| | 15 | | - | -1.175 | - |
| Top ← Bottom | 2 | South Column | 0 | 0 | 0 |
| | 4 | | 0.075 | -0.152 | 0.066 |
| | 8 | | 0.247 | -0.529 | -0.025 |
| | 12 | | - | -0.705 | - |
| | 10 | | 0.419 | - | - |
| | 13 | | - | -0.840 | - |
| N ← S | 17 | Deck | - | - | 0.209 |
| | 6 | | 0.436 | -0.686 | -0.211 |
| | 16 | | - | - | 0.211 |
| | 9 | | 0.419 | -0.631 | - |
| | 7 | | 0.422 | -0.705 | 0.188 |

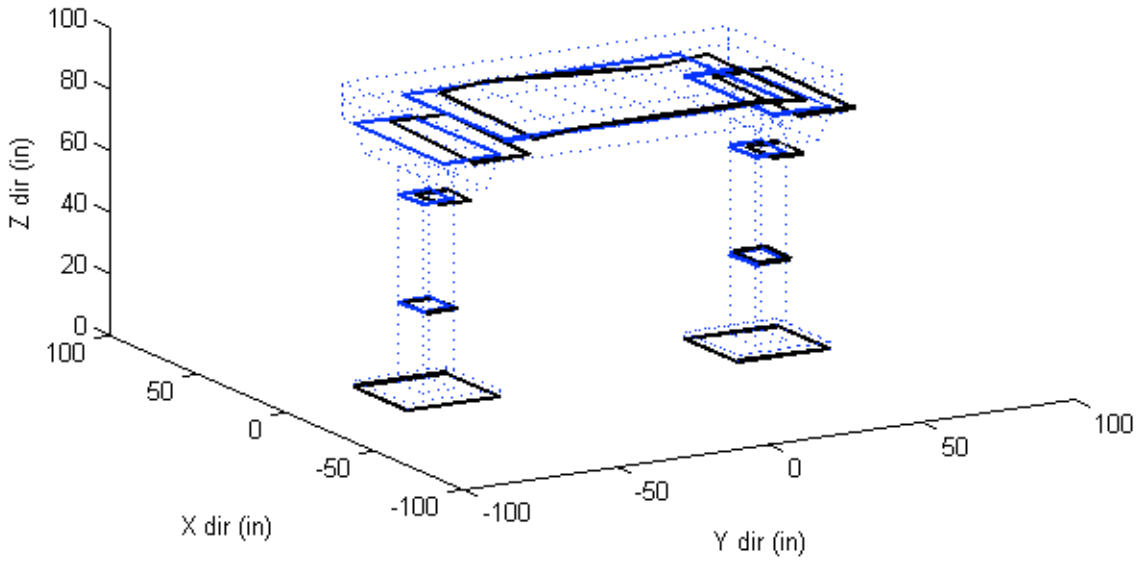

Test 04 – Torsional vibration mode

| Sensor # | | | Modal displacement | | |
|---|---|---|---|---|---|
| W → E | | | X | Y | Z |
| Top ← Bottom | 1 | North Column | 0 | 0 | 0 |
| | 3 | | -0.339 | -0.023 | 0.017 |
| | 5 | | -1.150 | 0.151 | 0.070 |
| | 14 | | - | -0.839 | - |
| | 11 | | -1.545 | - | - |
| | 15 | | - | 1.274 | - |
| Top ← Bottom | 2 | South Column | 0 | 0 | 0 |
| | 4 | | 0.182 | 0.116 | 0.056 |
| | 8 | | 1.013 | 0.215 | -0.092 |
| | 12 | | - | -0.668 | - |
| | 10 | | 0.234 | - | - |
| | 13 | | - | 1.070 | - |
| N ← S | 17 | Deck | - | - | 0.394 |
| | 6 | | 0.828 | 1.109 | -0.205 |
| | 16 | | - | - | - |
| | 9 | | 0.234 | 0.233 | 0.071 |
| | 7 | | -0.854 | -0.668 | -0.304 |

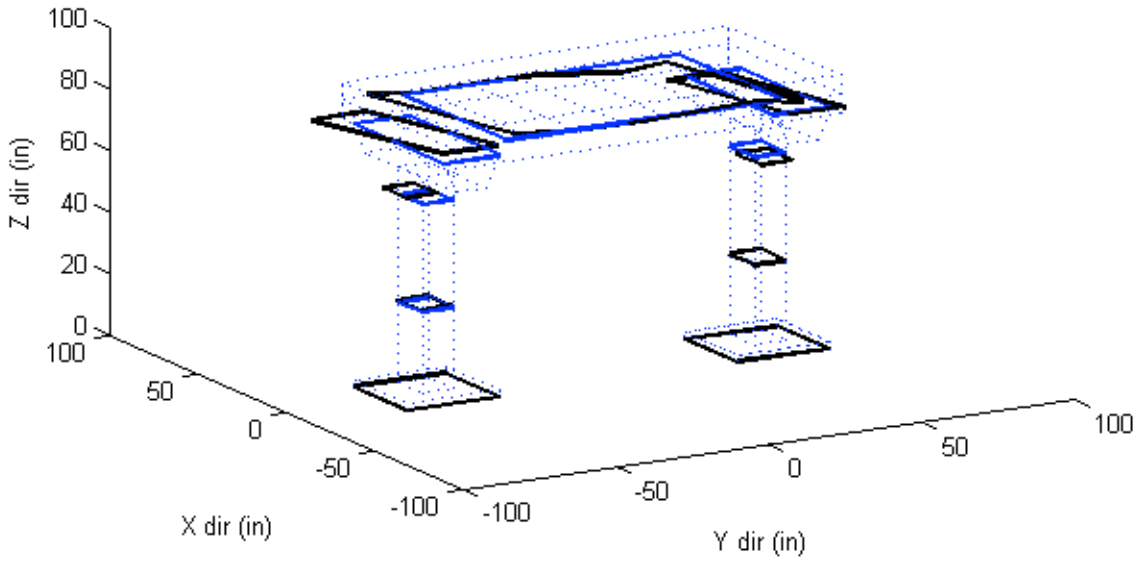

Test 09 – Vertical vibration mode

| Sensor # | | | Modal displacement | | |
|---|---|---|---|---|---|
| W → E | | | X | Y | Z |
| Top ← Bottom | 1 | North Column | 0 | 0 | 0 |
| | 3 | | -0.005 | 0.189 | -0.044 |
| | 5 | | -0.028 | 0.374 | -0.036 |
| | 14 | | - | 0.243 | - |
| | 11 | | -0.019 | - | - |
| | 15 | | - | -0.242 | - |
| Top ← Bottom | 2 | South Column | 0 | 0 | 0 |
| | 4 | | 0.022 | -0.207 | -0.013 |
| | 8 | | 0.052 | -0.352 | -0.056 |
| | 12 | | - | 0.056 | - |
| | 10 | | -0.008 | - | - |
| | 13 | | - | 0.230 | - |
| N ← S | 17 | Deck | - | - | -0.794 |
| | 6 | | 0.015 | -0.011 | -0.627 |
| | 16 | | - | - | -1.100 |
| | 9 | | -0.008 | 0.064 | -1.184 |
| | 7 | | -0.001 | 0.056 | -0.604 |

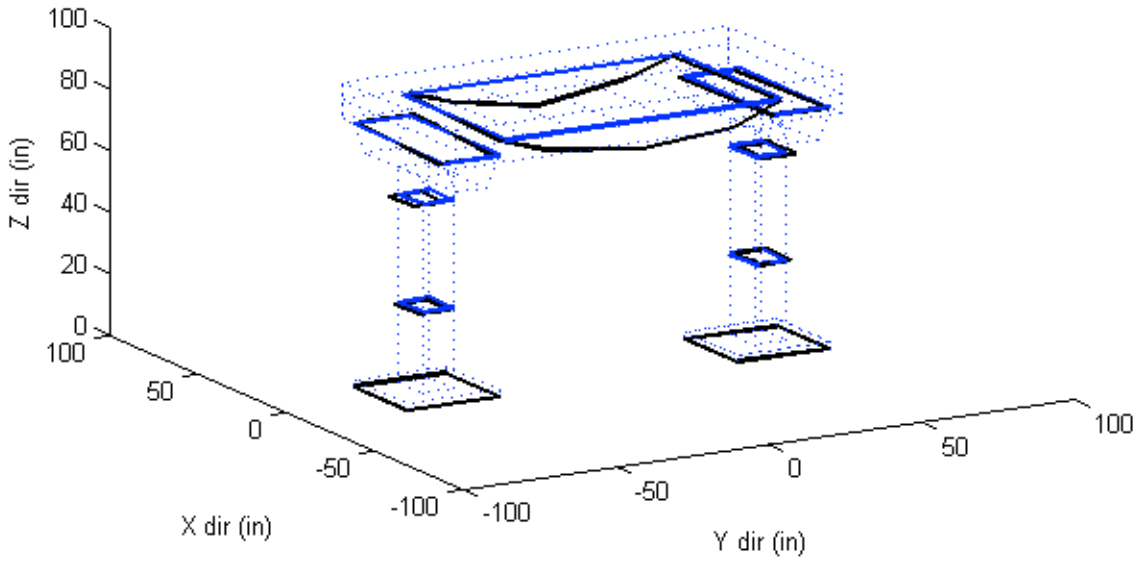

Test 10 – Lateral vibration mode

| Sensor # | | | Modal displacement | | |
|---|---|---|---|---|---|
| W → E | | | X | Y | Z |
| Top ← Bottom | 1 | North Column | 0 | 0 | 0 |
| | 3 | | -0.191 | -0.033 | 0.011 |
| | 5 | | -0.769 | -0.113 | 0.019 |
| | 14 | | - | -0.136 | - |
| | 11 | | -1.067 | - | - |
| | 15 | | - | -0.137 | - |
| Top ← Bottom | 2 | South Column | 0 | 0 | 0 |
| | 4 | | -0.137 | -0.032 | 0.035 |
| | 8 | | -0.693 | -0.111 | 0.025 |
| | 12 | | - | -0.133 | - |
| | 10 | | -1.317 | - | - |
| | 13 | | - | -0.136 | - |
| N ← S | 17 | Deck | - | - | -0.142 |
| | 6 | | -1.272 | -0.133 | 0.140 |
| | 16 | | - | - | -0.142 |
| | 9 | | -1.317 | -0.143 | -0.004 |
| | 7 | | -1.283 | -0.133 | -0.143 |

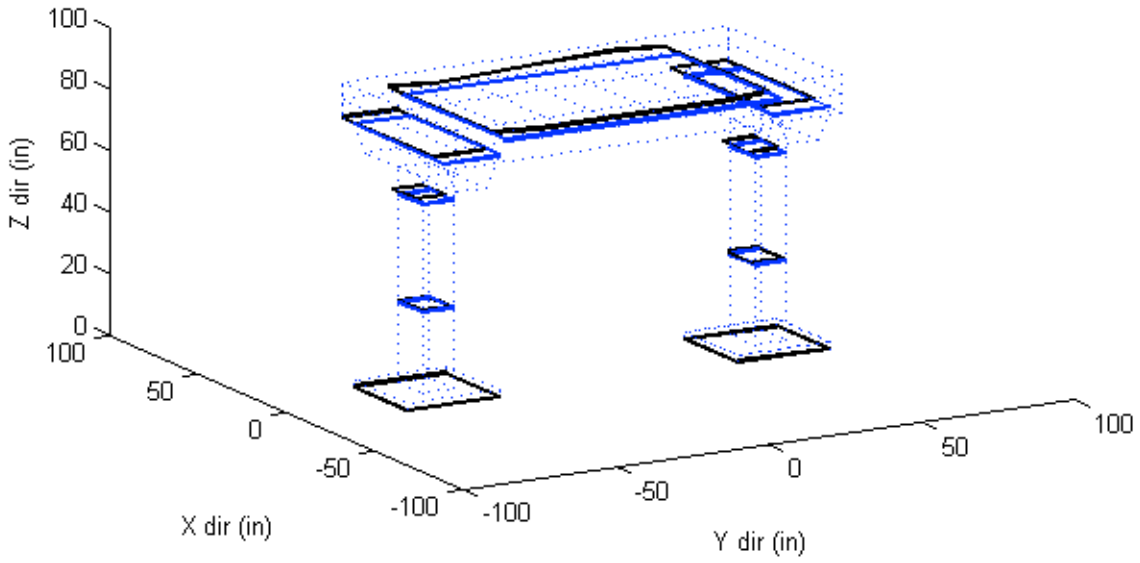

Test 10 – Longitudinal vibration mode

| Sensor # | | | Modal displacement | | |
|---|---|---|---|---|---|
| W → E | | | X | Y | Z |
| Top ← Bottom | 1 | North Column | 0 | 0 | 0 |
| | 3 | | -0.005 | -0.209 | 0.006 |
| | 5 | | -0.016 | -0.684 | 0.008 |
| | 14 | | - | -0.853 | - |
| | 11 | | -0.008 | - | - |
| | 15 | | - | -0.859 | - |
| Top ← Bottom | 2 | South Column | 0 | 0 | 0 |
| | 4 | | 0.001 | -0.237 | -0.001 |
| | 8 | | - | -0.703 | 0.006 |
| | 12 | | - | -0.881 | - |
| | 10 | | -0.017 | - | - |
| | 13 | | - | -0.834 | - |
| N ← S | 17 | Deck | - | - | -0.019 |
| | 6 | | -0.009 | -0.870 | 0.014 |
| | 16 | | - | - | -0.021 |
| | 9 | | -0.017 | -0.892 | -0.002 |
| | 7 | | -0.016 | -0.881 | -0.030 |

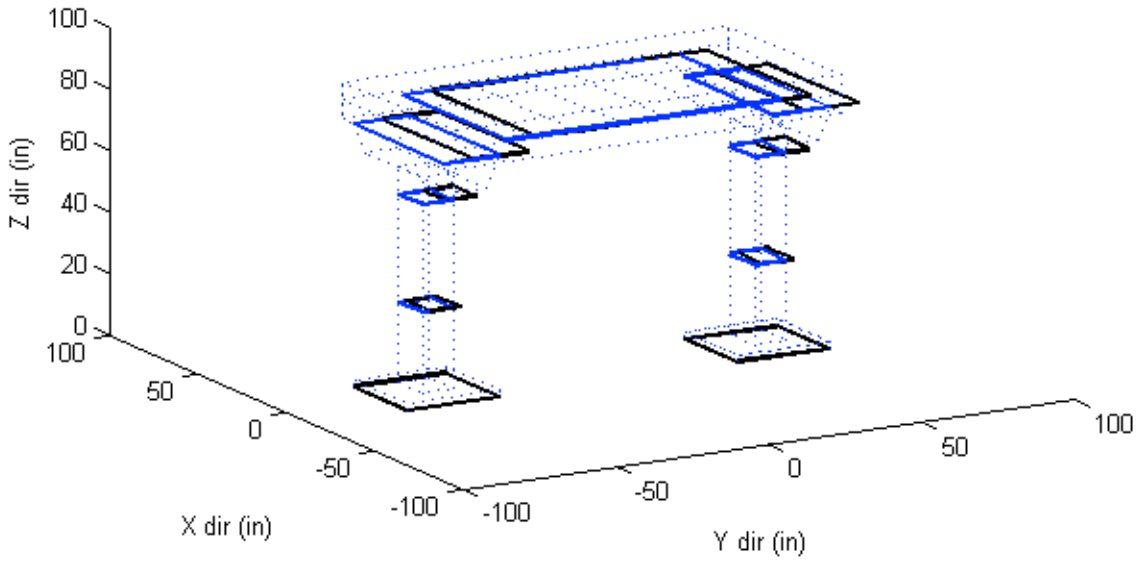

Test 10 – Torsional vibration mode

| Sensor # | | | Modal displacement | | |
|---|---|---|---|---|---|
| W → E | | | X | Y | Z |
| Top ← Bottom | 1 | North Column | 0 | 0 | 0 |
| | 3 | | -0.428 | -0.024 | 0.062 |
| | 5 | | -1.438 | 0.055 | 0.117 |
| | 14 | | - | -0.985 | - |
| | 11 | | -1.598 | - | - |
| | 15 | | - | 1.012 | - |
| Top ← Bottom | 2 | South Column | 0 | 0 | 0 |
| | 4 | | 0.280 | 0.063 | -0.033 |
| | 8 | | 1.133 | 0.094 | -0.128 |
| | 12 | | - | -1.053 | - |
| | 10 | | 0.149 | - | - |
| | 13 | | - | 0.938 | - |
| N ← S | 17 | Deck | - | - | 0.348 |
| | 6 | | 0.951 | 1.113 | -0.374 |
| | 16 | | - | - | -0.047 |
| | 9 | | 0.149 | 0.010 | 0.069 |
| | 7 | | -1.148 | -1.053 | -0.492 |

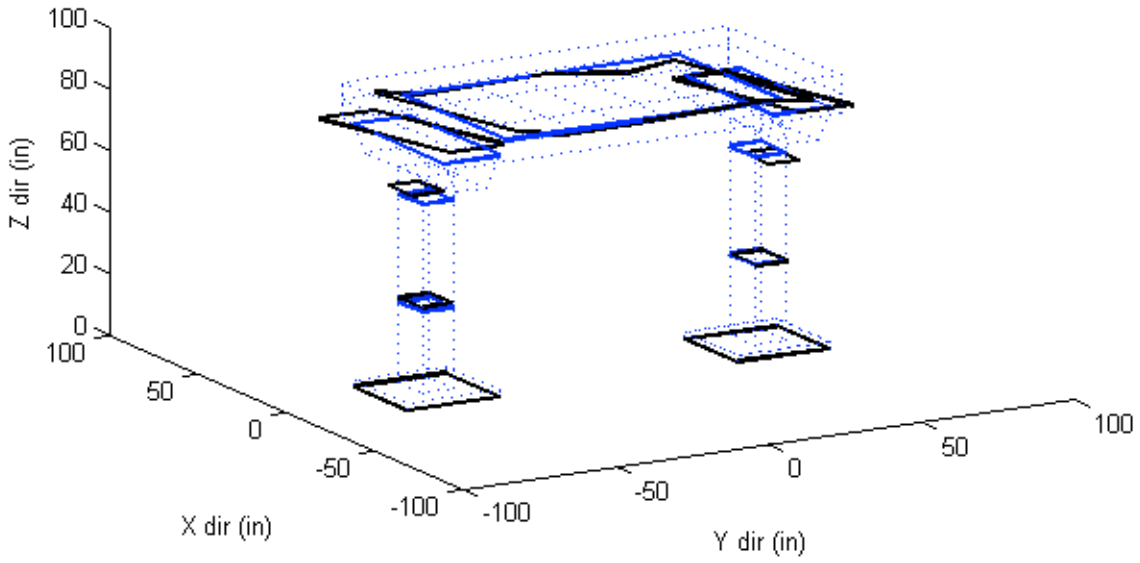

Test 10 – Vertical vibration mode

| Sensor # | | | Modal displacement | | |
|---|---|---|---|---|---|
| W → E | | | X | Y | Z |
| Top ← Bottom | 1 | North Column | 0 | 0 | 0 |
| | 3 | | -0.010 | 0.200 | -0.043 |
| | 5 | | -0.040 | 0.398 | -0.037 |
| | 14 | | - | 0.235 | - |
| | 11 | | -0.008 | - | - |
| | 15 | | - | -0.231 | - |
| Top ← Bottom | 2 | South Column | - | - | - |
| | 4 | | 0.025 | -0.221 | -0.033 |
| | 8 | | 0.056 | -0.376 | -0.053 |
| | 12 | | - | 0.058 | - |
| | 10 | | 0.004 | - | - |
| | 13 | | - | 0.228 | - |
| N ← S | 17 | Deck | - | - | -0.733 |
| | 6 | | 0.031 | -0.014 | -0.688 |
| | 16 | | - | - | -1.023 |
| | 9 | | 0.004 | 0.061 | -1.249 |
| | 7 | | 0.007 | 0.058 | -0.619 |

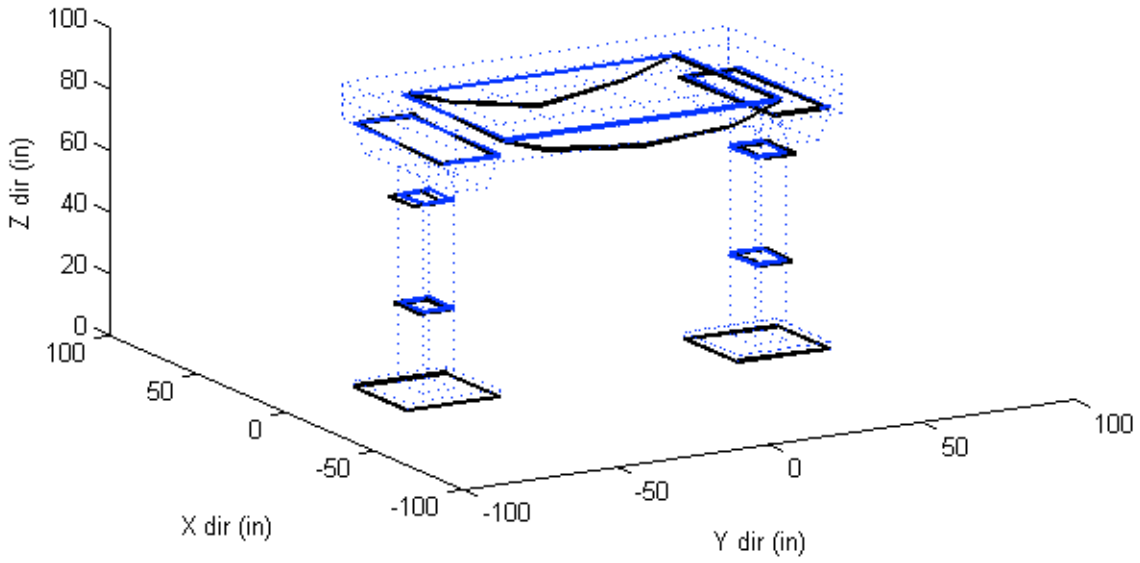

Test 11 – Lateral vibration mode

| Sensor # (W → E) | | | Modal displacement X | Y | Z |
|---|---|---|---|---|---|
| Top ← Bottom | 1 | North Column | 0 | 0 | 0 |
| | 3 | | -0.204 | -0.004 | 0.007 |
| | 5 | | -0.709 | -0.049 | 0.019 |
| | 14 | | - | -0.052 | - |
| | 11 | | -1.043 | - | - |
| | 15 | | - | -0.040 | - |
| Top ← Bottom | 2 | South Column | - | - | - |
| | 4 | | -0.263 | -0.006 | 0.013 |
| | 8 | | -0.794 | -0.045 | -0.004 |
| | 12 | | - | -0.057 | - |
| | 10 | | -1.291 | - | - |
| | 13 | | - | -0.054 | - |
| N ← S | 17 | Deck | - | - | -0.124 |
| | 6 | | -1.257 | -0.058 | 0.119 |
| | 16 | | - | - | -0.123 |
| | 9 | | -1.291 | -0.060 | 0.016 |
| | 7 | | -1.261 | -0.057 | -0.127 |

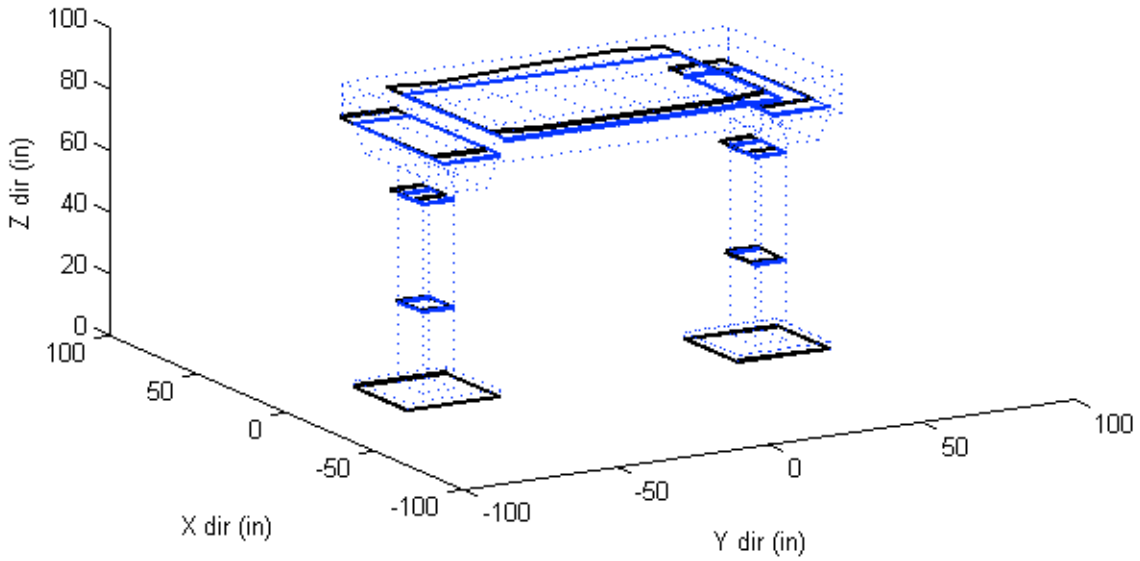

Test 11 – Torsional vibration mode

| Sensor # (W → E) | | | Modal displacement X | Y | Z |
|---|---|---|---|---|---|
| Top ← Bottom | 1 | North Column | 0 | 0 | 0 |
| | 3 | | -0.398 | 0.142 | -0.049 |
| | 5 | | -0.883 | -0.084 | -0.039 |
| | 14 | | - | -0.865 | - |
| | 11 | | -1.389 | - | - |
| | 15 | | - | 1.236 | - |
| Top ← Bottom | 2 | South Column | - | - | - |
| | 4 | | 0.206 | 0.093 | 0.051 |
| | 8 | | 0.930 | 0.059 | 0.262 |
| | 12 | | - | -0.767 | - |
| | 10 | | 0.341 | - | - |
| | 13 | | - | 1.047 | - |
| N ← S | 17 | Deck | - | - | 0.643 |
| | 6 | | 1.072 | 1.044 | -0.234 |
| | 16 | | - | - | 0.243 |
| | 9 | | 0.341 | -0.032 | 0.213 |
| | 7 | | -0.775 | -0.767 | -0.117 |

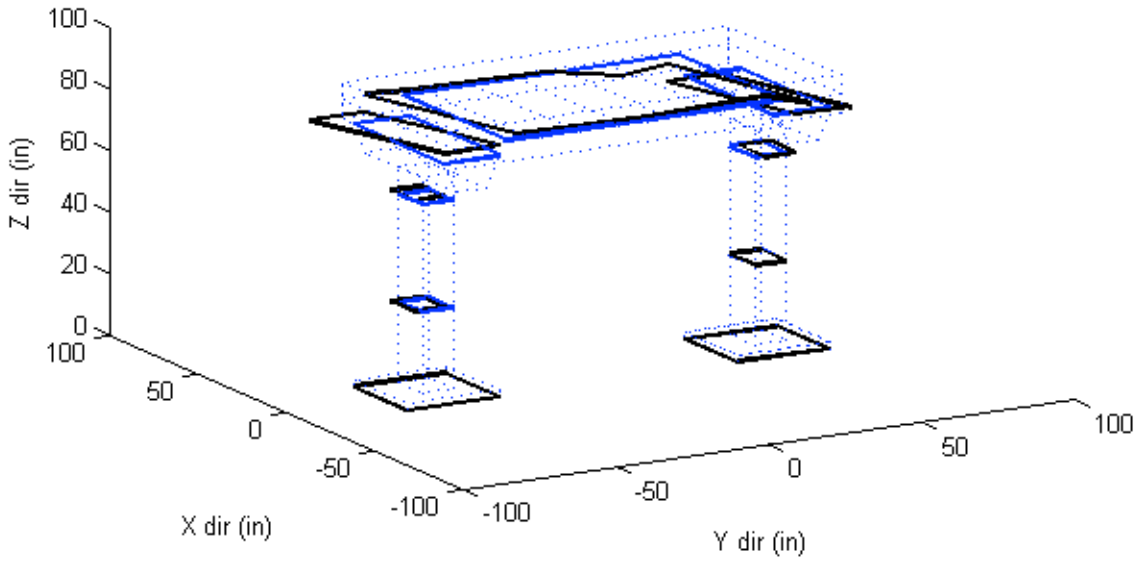

Test 12 – Longitudinal vibration mode

| Sensor # | | | Modal displacement | | |
|---|---|---|---|---|---|
| W → E | | | X | Y | Z |
| Top ← Bottom | 1 | North Column | 0 | 0 | 0 |
| | 3 | | 0.007 | -0.207 | 0.007 |
| | 5 | | 0.026 | -0.681 | 0.007 |
| | 14 | | - | -0.850 | - |
| | 11 | | 0.047 | - | - |
| | 15 | | - | -0.852 | - |
| Top ← Bottom | 2 | South Column | - | - | - |
| | 4 | | 0.009 | -0.250 | 0.008 |
| | 8 | | 0.035 | -0.717 | 0.006 |
| | 12 | | - | -0.888 | - |
| | 10 | | 0.050 | - | - |
| | 13 | | - | -0.825 | - |
| N ← S | 17 | Deck | - | - | 0.016 |
| | 6 | | 0.058 | -0.872 | -0.019 |
| | 16 | | - | - | 0.015 |
| | 9 | | 0.050 | -0.891 | -0.004 |
| | 7 | | 0.051 | -0.888 | 0.003 |

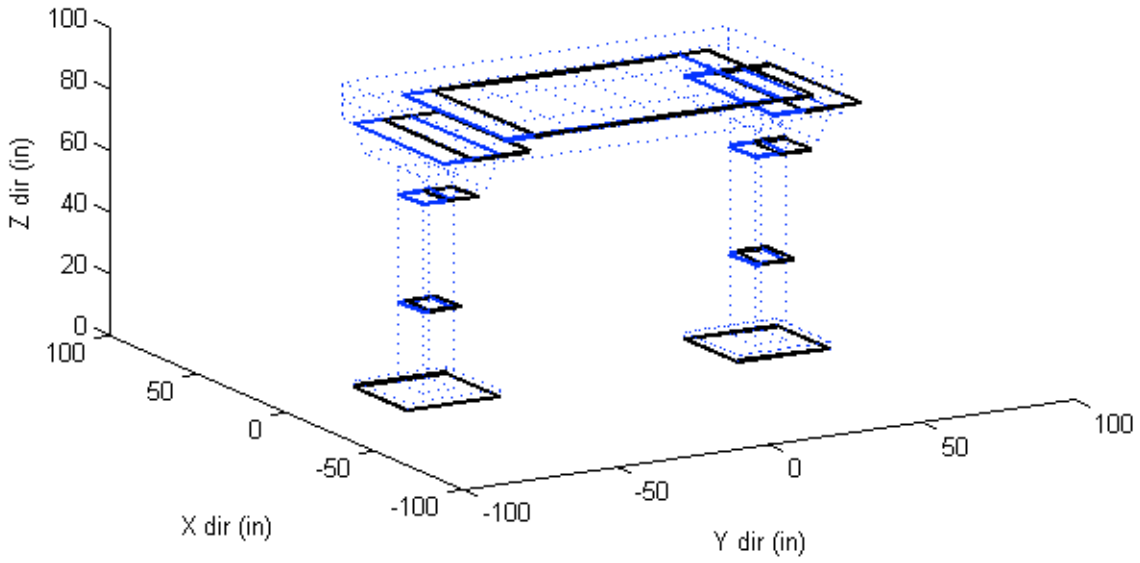

Test 12 – Torsional vibration mode

| Sensor # | | | | Modal displacement | | |
|---|---|---|---|---|---|---|
| | W → E | | | X | Y | Z |
| Top ← Bottom | 1 | | North Column | 0 | 0 | 0 |
| | 3 | | | -0.327 | 0.045 | 0.043 |
| | 5 | | | -1.106 | 0.116 | 0.167 |
| | 14 | | | - | -0.895 | - |
| | 11 | | | -1.491 | - | - |
| | | 15 | | - | 1.178 | - |
| Top ← Bottom | 2 | | South Column | - | - | - |
| | 4 | | | 0.313 | 0.020 | 0.018 |
| | 8 | | | 1.129 | 0.149 | -0.216 |
| | 12 | | | - | -0.794 | - |
| | 10 | | | 0.232 | - | - |
| | | 13 | | - | 1.069 | - |
| N ← S | 17 | | Deck | - | - | 0.370 |
| | | 6 | | 0.908 | 1.057 | -0.247 |
| | 16 | | | - | - | -0.052 |
| | 9 | | | 0.232 | 0.157 | -0.051 |
| | 7 | | | -0.821 | -0.794 | -0.430 |

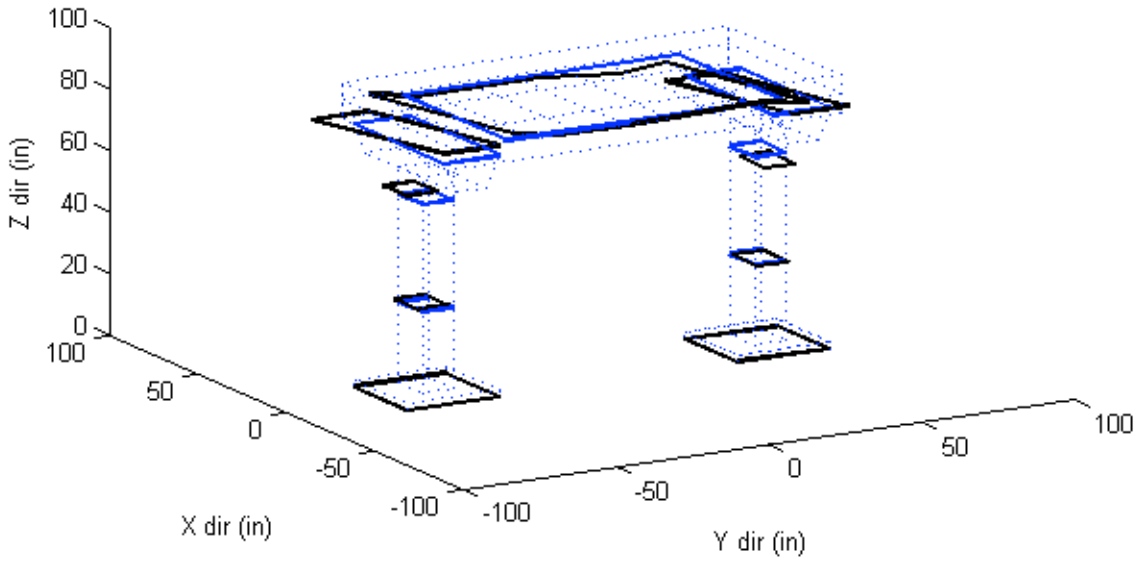

Test 13 – Vertical vibration mode

| Sensor # | | | Modal displacement | | |
|---|---|---|---|---|---|
| | W → E | | X | Y | Z |
| Top ← Bottom | 1 | North Column | 0 | 0 | 0 |
| | 3 | | 0.003 | 0.204 | -0.040 |
| | 5 | | -0.024 | 0.377 | -0.037 |
| | 14 | | - | 0.234 | - |
| | 11 | | -0.012 | - | - |
| | 15 | | - | -0.238 | - |
| Top ← Bottom | 2 | South Column | - | - | - |
| | 4 | | 0.021 | -0.219 | -0.030 |
| | 8 | | 0.066 | -0.385 | -0.059 |
| | 12 | | - | 0.049 | - |
| | 10 | | 0.005 | - | - |
| | 13 | | - | 0.220 | - |
| N ← S | 17 | Deck | - | - | -0.745 |
| | 6 | | 0.030 | -0.017 | -0.647 |
| | 16 | | - | - | -1.026 |
| | 9 | | 0.005 | 0.067 | -1.249 |
| | 7 | | 0.006 | 0.049 | -0.643 |

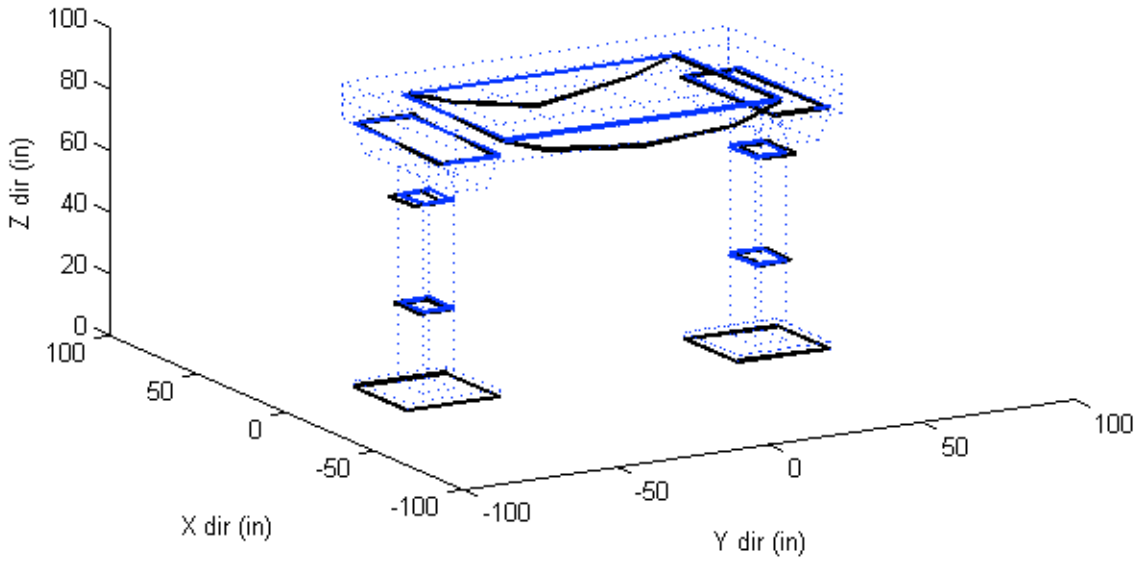

Test 14 – Longitudinal vibration mode

| Sensor # | | | Modal displacement | | |
|---|---|---|---|---|---|
| W → E | | | X | Y | Z |
| Top ← Bottom | 1 | North Column | 0 | 0 | 0 |
| | 3 | | -0.040 | -0.209 | 0.016 |
| | 5 | | -0.154 | -0.767 | 0.027 |
| | 14 | | - | -0.781 | - |
| | 11 | | -0.243 | - | - |
| | 15 | | - | -0.762 | - |
| Top ← Bottom | 2 | South Column | 0 | 0 | 0 |
| | 4 | | -0.038 | -0.204 | 0.004 |
| | 8 | | -0.150 | -0.745 | 0.030 |
| | 12 | | - | -0.954 | - |
| | 10 | | -0.282 | - | - |
| | 13 | | - | -0.818 | - |
| N ← S | 17 | Deck | - | - | -0.163 |
| | 6 | | -0.277 | -0.919 | 0.162 |
| | 16 | | - | - | -0.161 |
| | 9 | | -0.282 | -0.948 | -0.005 |
| | 7 | | -0.278 | -0.954 | -0.162 |

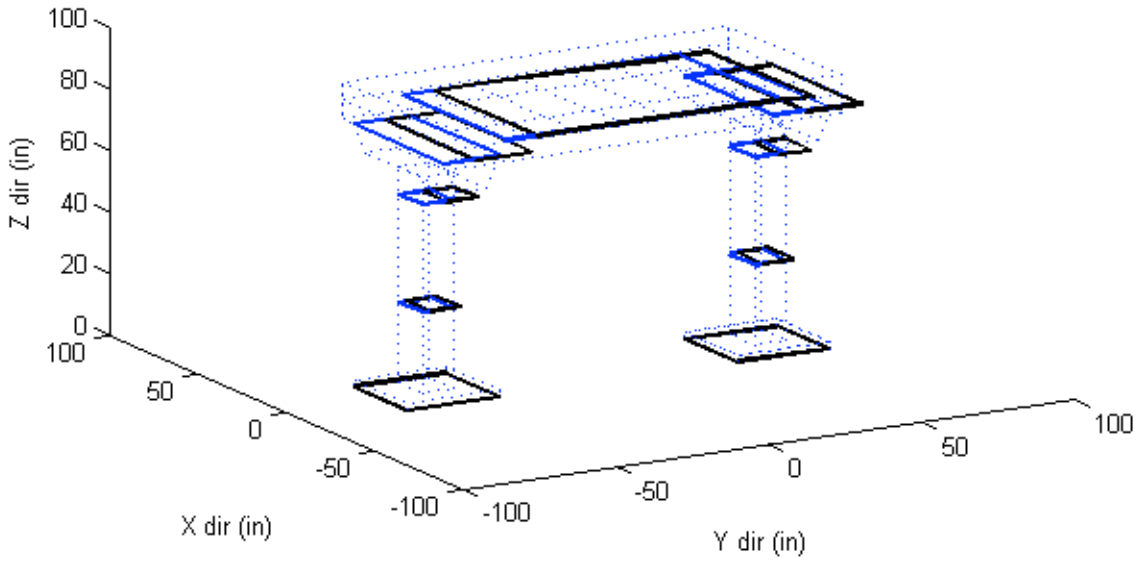

Test 14 – Torsional vibration mode

| Sensor # | | | Modal displacement | | |
|---|---|---|---|---|---|
| W → E | | | X | Y | Z |
| Top ← Bottom | 1 | North Column | 0 | 0 | 0 |
| | 3 | | -0.342 | 0.012 | 0.042 |
| | 5 | | -1.176 | 0.129 | 0.141 |
| | 14 | | - | -0.978 | - |
| | 11 | | -1.551 | - | - |
| | 15 | | - | 1.178 | - |
| Top ← Bottom | 2 | South Column | 0 | 0 | 0 |
| | 4 | | 0.261 | -0.021 | -0.039 |
| | 8 | | 1.102 | 0.070 | -0.124 |
| | 12 | | - | -0.815 | - |
| | 10 | | 0.235 | - | - |
| | 13 | | - | 0.985 | - |
| N ← S | 17 | Deck | - | - | 0.398 |
| | 6 | | 0.948 | 1.051 | -0.259 |
| | 16 | | - | - | -0.027 |
| | 9 | | 0.235 | 0.036 | -0.008 |
| | 7 | | -0.854 | -0.815 | -0.398 |

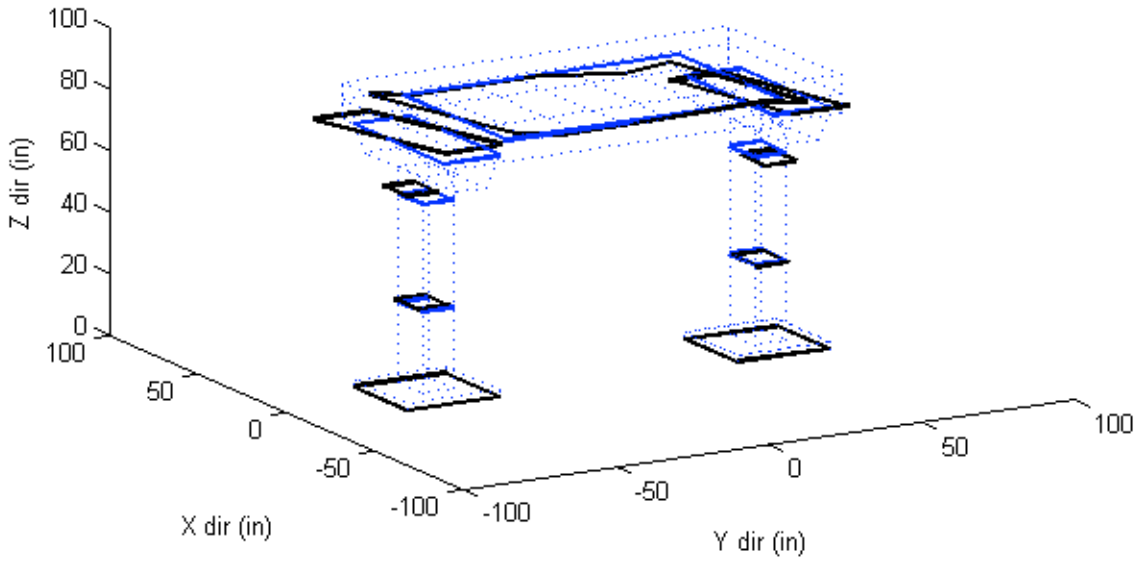

Test 15 – Lateral vibration mode

| Sensor # | | | | Modal displacement | | |
|---|---|---|---|---|---|---|
| | W → E | | | X | Y | Z |
| Top ← Bottom | 1 | | North Column | 0 | 0 | 0 |
| | 3 | | | -0.206 | -0.043 | 0.011 |
| | 5 | | | -0.775 | -0.128 | 0.028 |
| | 14 | | | - | -0.165 | - |
| | 11 | | | -1.124 | - | - |
| | | 15 | | - | -0.156 | - |
| Top ← Bottom | 2 | | South Column | 0 | 0 | 0 |
| | 4 | | | -0.158 | -0.038 | 0.024 |
| | 8 | | | -0.651 | -0.124 | 0.031 |
| | 12 | | | - | -0.166 | - |
| | 10 | | | -1.282 | - | - |
| | | 13 | | - | -0.158 | - |
| N ← S | 17 | | Deck | - | - | -0.133 |
| | | 6 | | -1.238 | -0.158 | 0.139 |
| | 16 | | | - | - | -0.133 |
| | 9 | | | -1.282 | -0.164 | 0.004 |
| | 7 | | | -1.287 | -0.166 | -0.139 |

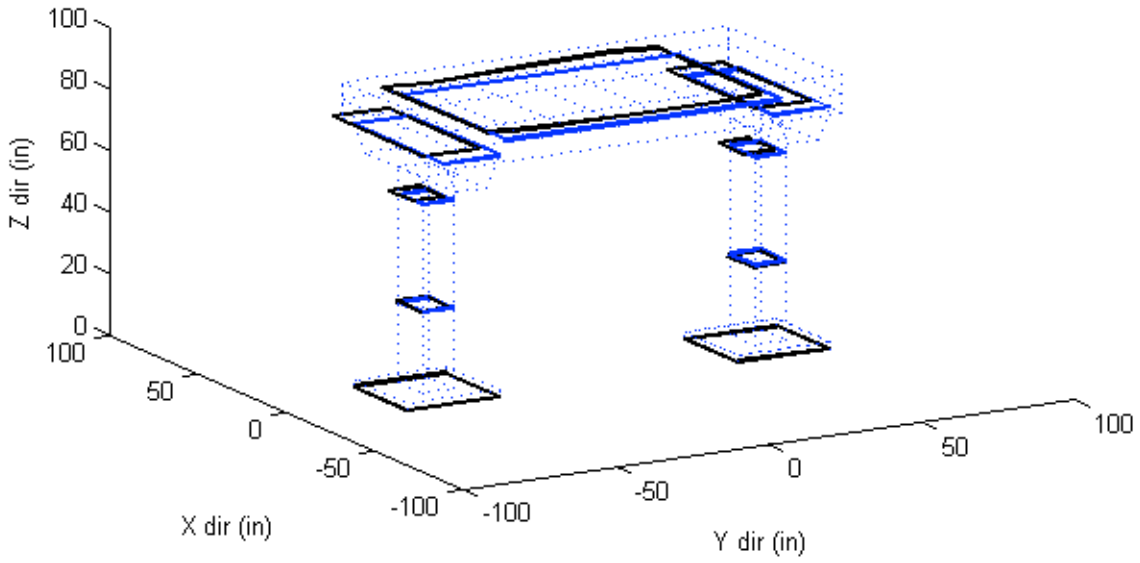

Test 15 – Longitudinal vibration mode

| Sensor # | | | Modal displacement | | |
|---|---|---|---|---|---|
| W → E | | | X | Y | Z |
| Top ← Bottom | 1 | North Column | 0 | 0 | 0 |
| | 3 | | -0.001 | -0.195 | 0.010 |
| | 5 | | -0.018 | -0.685 | 0.009 |
| | 14 | | - | -0.859 | - |
| | 11 | | -0.020 | - | - |
| | 15 | | - | -0.858 | - |
| Top ← Bottom | 2 | South Column | 0 | 0 | 0 |
| | 4 | | 0.001 | -0.244 | -0.010 |
| | 8 | | -0.006 | -0.707 | 0.008 |
| | 12 | | - | -0.873 | - |
| | 10 | | -0.025 | - | - |
| | 13 | | - | -0.836 | - |
| N ← S | 17 | Deck | - | - | -0.024 |
| | 6 | | -0.018 | -0.872 | 0.019 |
| | 16 | | - | - | -0.025 |
| | 9 | | -0.025 | -0.889 | -0.004 |
| | 7 | | -0.025 | -0.873 | -0.034 |

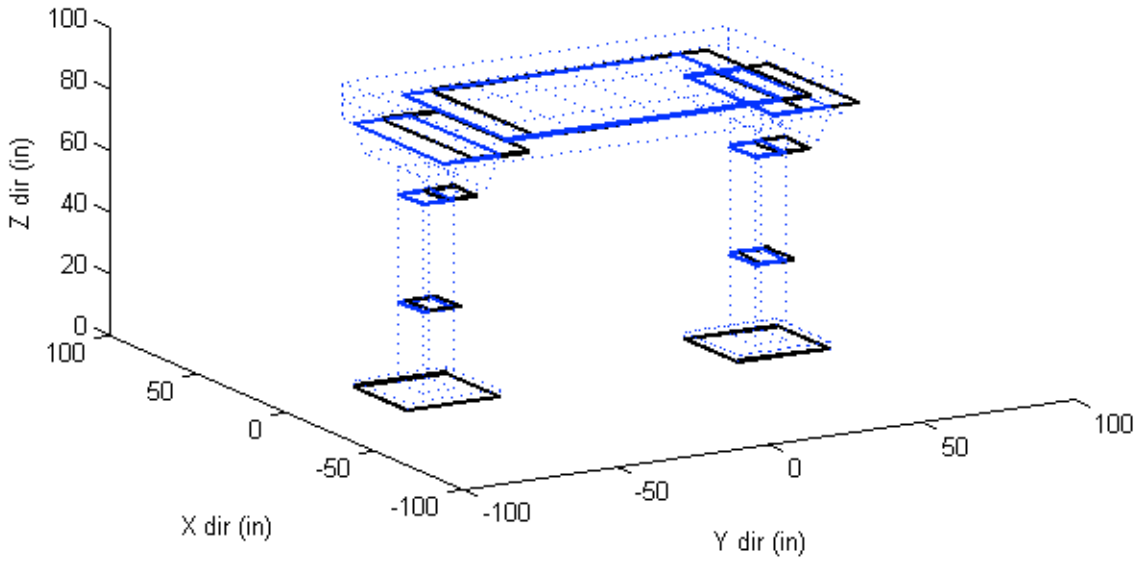

Test 15 – Torsional vibration mode

| Sensor # | | | Modal displacement | | |
|---|---|---|---|---|---|
| W → E | | | X | Y | Z |
| Top ← Bottom | 1 | North Column | 0 | 0 | 0 |
| | 3 | | -0.496 | 0.151 | 0.011 |
| | 5 | | -1.764 | 0.229 | -0.047 |
| | 14 | | - | -0.969 | - |
| | 11 | | -0.803 | - | - |
| | 15 | | - | 0.479 | - |
| Top ← Bottom | 2 | South Column | 0 | 0 | 0 |
| | 4 | | 0.368 | 0.176 | -0.248 |
| | 8 | | 1.738 | -0.139 | -0.045 |
| | 12 | | - | -1.502 | - |
| | 10 | | 0.437 | - | - |
| | 13 | | - | 0.671 | - |
| N ← S | 17 | Deck | - | - | 0.289 |
| | 6 | | 1.569 | 1.536 | -0.459 |
| | 16 | | - | - | 0.025 |
| | 9 | | 0.437 | 0.297 | 0.047 |
| | 7 | | -1.255 | -1.502 | -0.627 |

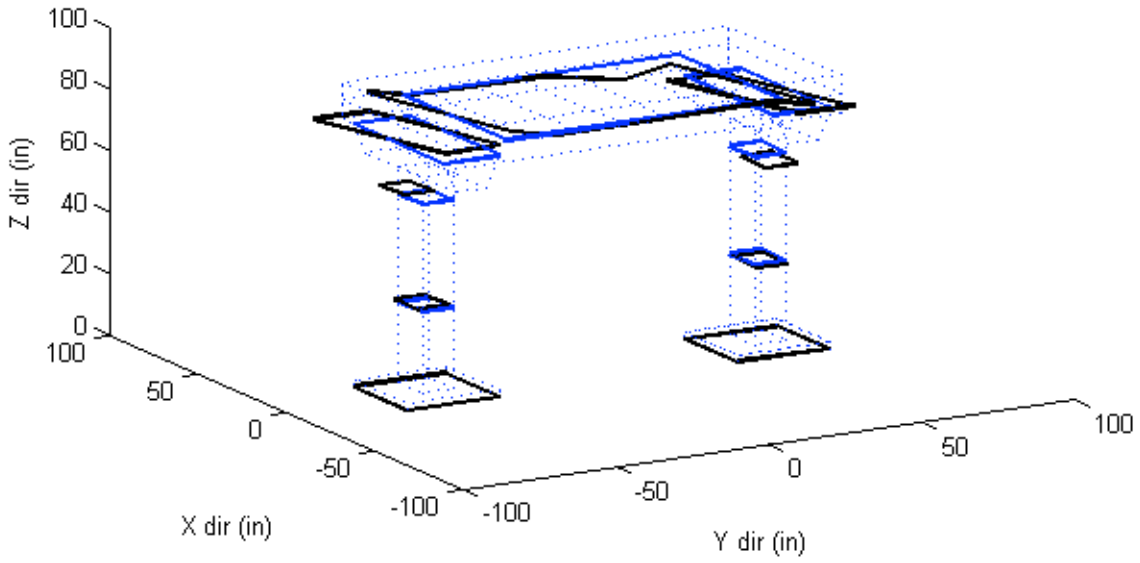

Test 15 – Vertical vibration mode

| Sensor # | | | Modal displacement | | |
|---|---|---|---|---|---|
| W → E | | | X | Y | Z |
| Top ← Bottom | 1 | North Column | 0 | 0 | 0 |
| | 3 | | -0.018 | 0.249 | -0.051 |
| | 5 | | -0.032 | 0.491 | -0.048 |
| | 14 | | - | 0.254 | - |
| | 11 | | 0.016 | - | - |
| | 15 | | - | -0.136 | - |
| Top ← Bottom | 2 | South Column | 0 | 0 | 0 |
| | 4 | | 0.009 | -0.226 | -0.092 |
| | 8 | | 0.036 | -0.395 | -0.081 |
| | 12 | | - | 0.114 | - |
| | 10 | | 0.026 | - | - |
| | 13 | | - | 0.249 | - |
| N ← S | 17 | Deck | - | - | -0.488 |
| | 6 | | 0.047 | 0.020 | -0.848 |
| | 16 | | - | - | -0.680 |
| | 9 | | 0.026 | 0.126 | -1.460 |
| | 7 | | 0.040 | 0.114 | -0.671 |

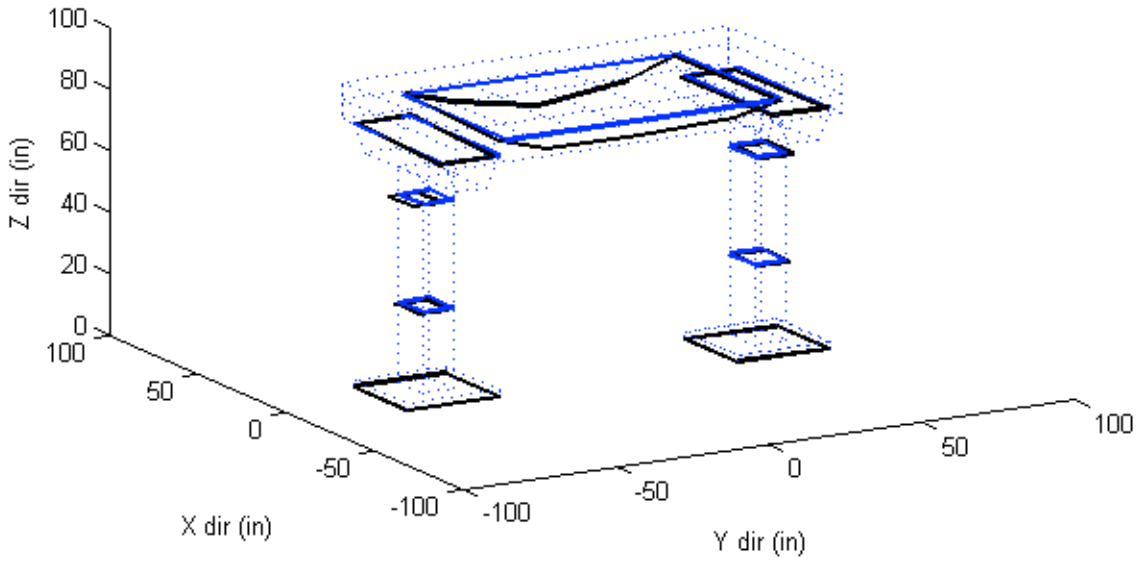

Test 16 – Lateral vibration mode

| Sensor # | | | | Modal displacement | | |
|---|---|---|---|---|---|---|
| | W → E | | | X | Y | Z |
| Top ← Bottom | 1 | | North Column | 0 | 0 | 0 |
| | 3 | | | -0.138 | -0.020 | 0.017 |
| | 5 | | | -0.686 | -0.062 | 0.024 |
| | 14 | | | - | -0.071 | - |
| | 11 | | | -1.083 | - | - |
| | | 15 | | - | -0.081 | - |
| Top ← Bottom | 2 | | South Column | 0 | 0 | 0 |
| | 4 | | | -0.192 | -0.019 | 0.004 |
| | 8 | | | -0.767 | -0.058 | 0.022 |
| | 12 | | | - | -0.069 | - |
| | 10 | | | -1.309 | - | - |
| | | 13 | | - | -0.087 | - |
| N ← S | 17 | | Deck | - | - | -0.139 |
| | | 6 | | 0.181 | -0.088 | 0.138 |
| | 16 | | | - | - | -0.136 |
| | 9 | | | -1.309 | -0.083 | 0.002 |
| | 7 | | | -1.241 | -0.069 | -0.129 |

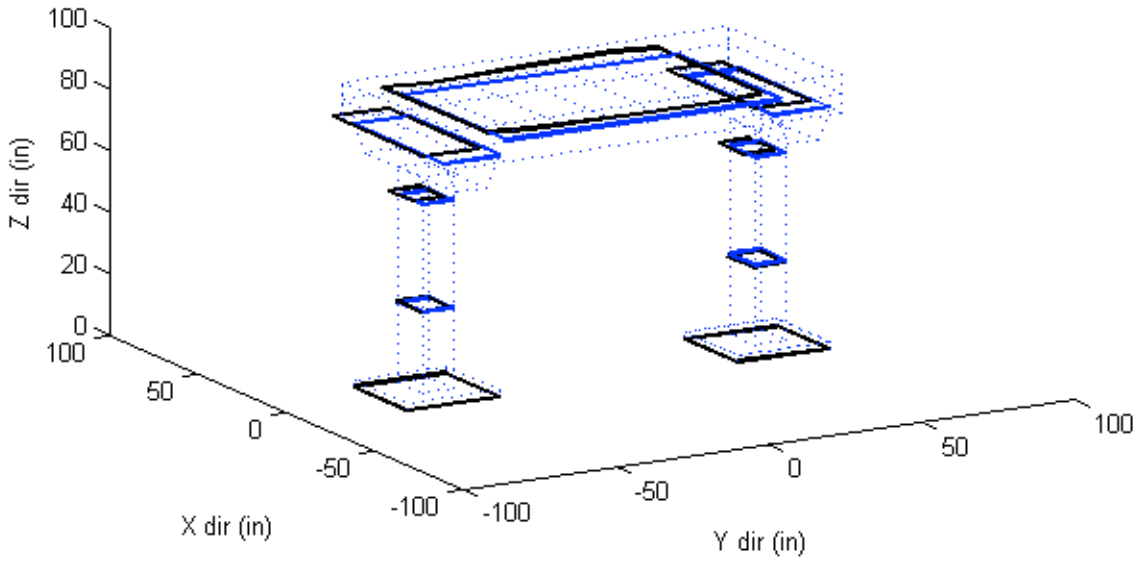

Test 16 – Longitudinal vibration mode

| Sensor # | | | Modal displacement | | |
|---|---|---|---|---|---|
| W → E | | | X | Y | Z |
| Top ← Bottom | 1 | North Column | 0 | 0 | 0 |
| | 3 | | - | -0.202 | 0.004 |
| | 5 | | -0.004 | -0.673 | 0.008 |
| | 14 | | - | -0.864 | - |
| | 11 | | 0.006 | - | - |
| | 15 | | - | -0.873 | - |
| Top ← Bottom | 2 | South Column | 0 | 0 | 0 |
| | 4 | | 0.006 | -0.226 | - |
| | 8 | | 0.011 | -0.700 | 0.004 |
| | 12 | | - | -0.879 | - |
| | 10 | | 0.003 | - | - |
| | 13 | | - | -0.827 | - |
| N ← S | 17 | Deck | - | - | -0.009 |
| | 6 | | 0.011 | -0.847 | 0.005 |
| | 16 | | - | - | -0.012 |
| | 9 | | 0.003 | -0.871 | -0.002 |
| | 7 | | 0.003 | -0.879 | -0.021 |

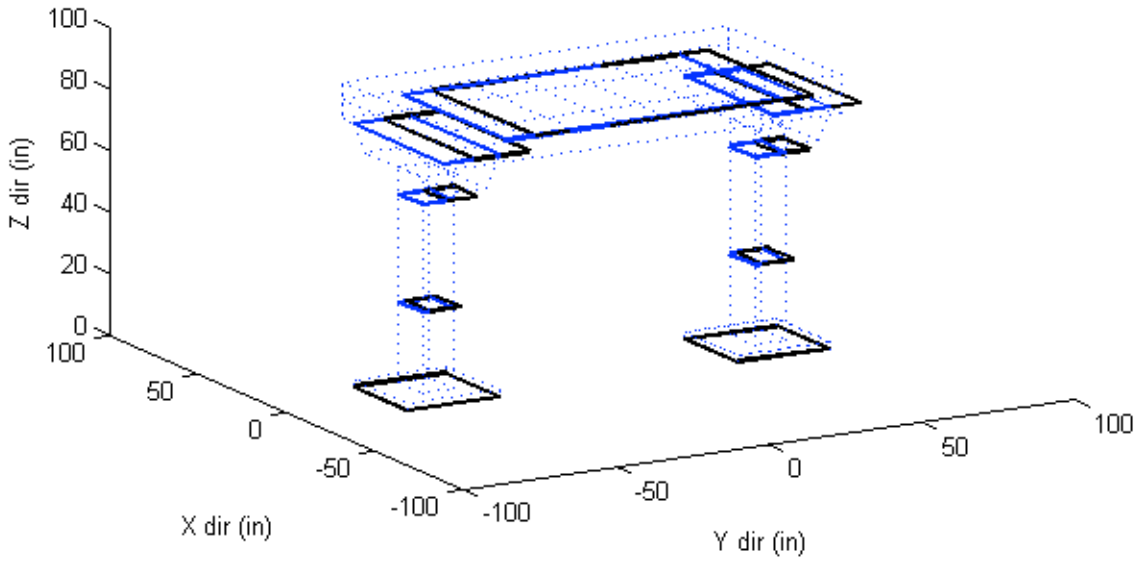

Test 16 – Torsional vibration mode

| Sensor # | | | | Modal displacement | | |
|---|---|---|---|---|---|---|
| | W → E | | | X | Y | Z |
| Top ← Bottom | 1 | | North Column | 0 | 0 | 0 |
| | 3 | | | -0.428 | 0.074 | 0.044 |
| | 5 | | | -1.544 | 0.119 | 0.118 |
| | 14 | | | - | -0.996 | - |
| | 11 | | | -1.489 | - | - |
| | | 15 | | - | 0.937 | - |
| Top ← Bottom | 2 | | South Column | 0 | 0 | 0 |
| | 4 | | | 0.410 | -0.056 | -0.013 |
| | 8 | | | 1.359 | 0.003 | -0.126 |
| | 12 | | | - | -1.171 | - |
| | 10 | | | 0.242 | - | - |
| | | 13 | | - | 0.858 | - |
| N ← S | 17 | | Deck | - | - | 0.245 |
| | | 6 | | 1.067 | 1.222 | -0.344 |
| | 16 | | | - | - | -0.082 |
| | 9 | | | 0.242 | -0.004 | 0.152 |
| | 7 | | | -1.209 | -1.171 | -0.558 |

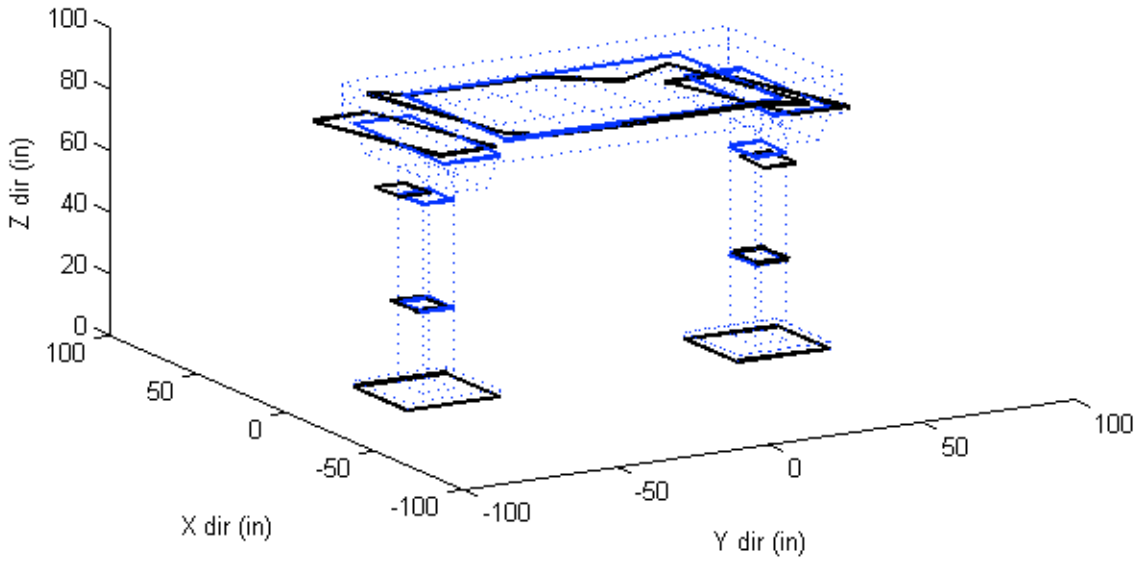

Test 16 – Vertical vibration mode

| Sensor # | | | Modal displacement | | |
|---|---|---|---|---|---|
| | W → E | | X | Y | Z |
| Top ← Bottom | 1 | North Column | 0 | 0 | 0 |
| | 3 | | 0.004 | 0.107 | -0.020 |
| | 5 | | -0.016 | 0.218 | -0.015 |
| | 14 | | - | 0.198 | - |
| | 11 | | -0.030 | - | - |
| | 15 | | - | -0.195 | - |
| Top ← Bottom | 2 | South Column | 0 | 0 | 0 |
| | 4 | | 0.014 | -0.134 | 0.051 |
| | 8 | | 0.024 | -0.204 | -0.037 |
| | 12 | | - | 0.039 | - |
| | 10 | | -0.030 | - | - |
| | 13 | | - | 0.187 | - |
| N ← S | 17 | Deck | - | - | -0.714 |
| | 6 | | -0.007 | 0.008 | -0.336 |
| | 16 | | - | - | -1.000 |
| | 9 | | -0.030 | 0.044 | -0.613 |
| | 7 | | -0.015 | 0.039 | -0.361 |

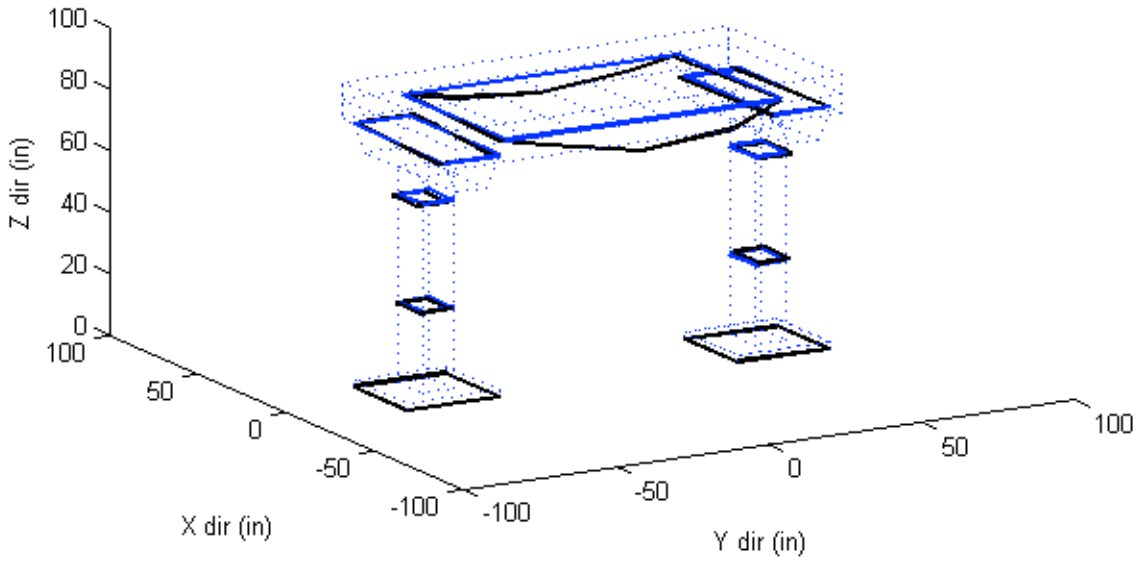

Test 17 – Lateral vibration mode

| Sensor # W → E | | | Modal displacement X | Y | Z |
|---|---|---|---|---|---|
| Top ← Bottom | 1 | North Column | 0 | 0 | 0 |
| | 3 | | -0.181 | -0.054 | 0.011 |
| | 5 | | -0.731 | -0.182 | 0.030 |
| | 14 | | - | -0.223 | - |
| | 11 | | -1.052 | - | - |
| | 15 | | - | -0.234 | - |
| Top ← Bottom | 2 | South Column | 0 | 0 | 0 |
| | 4 | | -0.179 | -0.071 | 0.014 |
| | 8 | | -0.720 | -0.194 | 0.025 |
| | 12 | | - | -0.228 | - |
| | 10 | | -1.333 | - | - |
| | 13 | | - | -0.238 | - |
| N ← S | 17 | Deck | - | - | -0.156 |
| | 6 | | -1.311 | -0.249 | 0.138 |
| | 16 | | - | - | -0.159 |
| | 9 | | -1.333 | -0.244 | -0.004 |
| | 7 | | -1.229 | -0.228 | -0.159 |

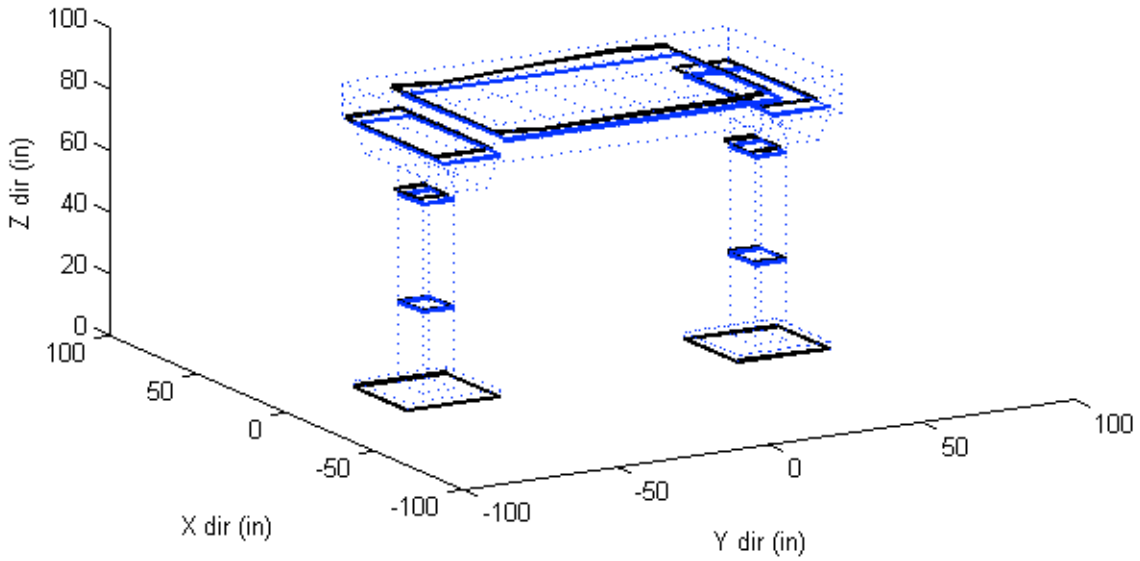

Test 17 – Longitudinal vibration mode

| Sensor # | | | Modal displacement | | |
|---|---|---|---|---|---|
| W → E | | | X | Y | Z |
| Top ← Bottom | 1 | North Column | 0 | 0 | 0 |
| | 3 | | - | -0.217 | 0.005 |
| | 5 | | 0.002 | -0.678 | 0.007 |
| | 14 | | - | -0.862 | - |
| | 11 | | 0.012 | - | - |
| | 15 | | - | -0.863 | - |
| Top ← Bottom | 2 | South Column | 0 | 0 | 0 |
| | 4 | | 0.006 | -0.244 | 0.003 |
| | 8 | | 0.017 | -0.702 | 0.004 |
| | 12 | | - | -0.885 | - |
| | 10 | | 0.013 | - | - |
| | 13 | | - | -0.818 | - |
| N ← S | 17 | Deck | - | - | -0.003 |
| | 6 | | 0.025 | -0.845 | - |
| | 16 | | - | - | -0.006 |
| | 9 | | 0.013 | -0.884 | -0.002 |
| | 7 | | 0.010 | -0.885 | -0.016 |

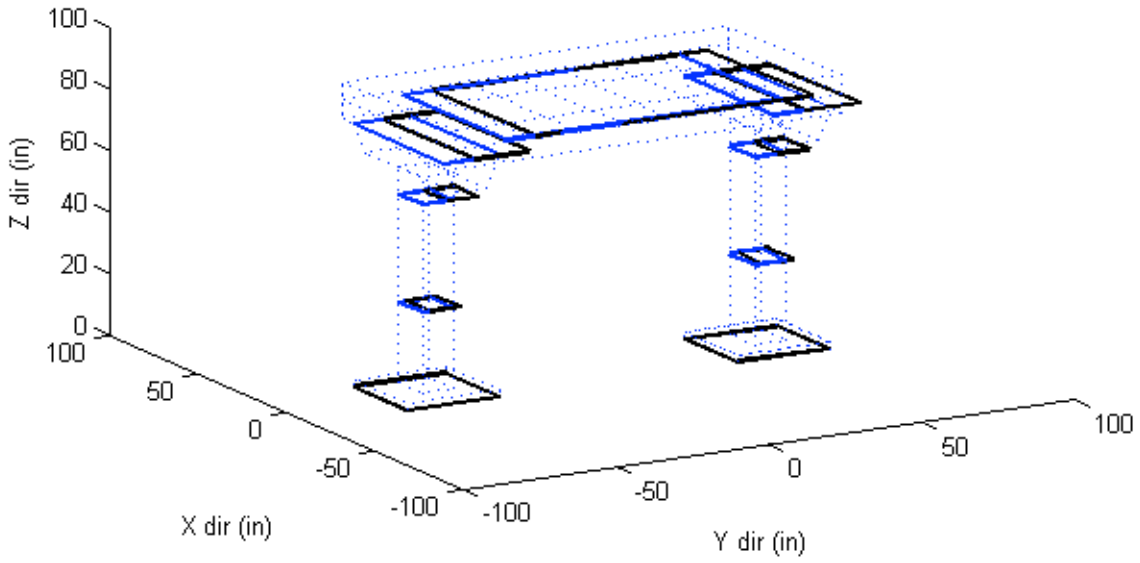

Test 17 – Torsional vibration mode

| Sensor # | | | Modal displacement | | |
|---|---|---|---|---|---|
| W → E | | | X | Y | Z |
| Top ← Bottom | 1 | North Column | 0 | 0 | 0 |
| | 3 | | -0.393 | 0.194 | -0.031 |
| | 5 | | -1.668 | 0.313 | 0.025 |
| | 14 | | - | -0.606 | - |
| | 11 | | -1.149 | - | - |
| | 15 | | - | 1.235 | - |
| Top ← Bottom | 2 | South Column | 0 | 0 | 0 |
| | 4 | | 0.515 | -0.019 | 0.069 |
| | 8 | | 1.512 | 0.180 | -0.225 |
| | 12 | | - | -0.895 | - |
| | 10 | | 0.546 | - | - |
| | 13 | | - | 1.067 | - |
| N ← S | 17 | Deck | - | - | 0.295 |
| | 6 | | 1.433 | 1.825 | -0.481 |
| | 16 | | - | - | -0.004 |
| | 9 | | 0.546 | 0.242 | -0.028 |
| | 7 | | -1.049 | -0.895 | -0.537 |

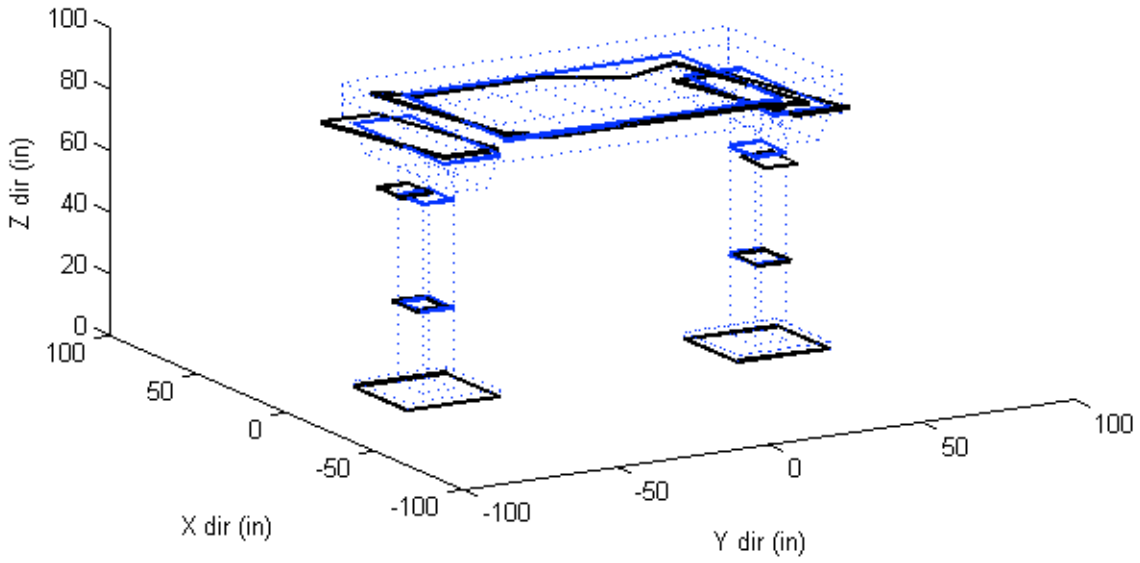

Test 17 – Vertical vibration mode

| Sensor # | | | Modal displacement | | |
|---|---|---|---|---|---|
| W → E | | | X | Y | Z |
| Top ← Bottom | 1 | North Column | 0 | 0 | 0 |
| | 3 | | 0.014 | 0.106 | -0.028 |
| | 5 | | 0.009 | 0.208 | -0.017 |
| | 14 | | - | 0.175 | - |
| | 11 | | 0.020 | - | - |
| | 15 | | - | -0.215 | - |
| Top ← Bottom | 2 | South Column | 0 | 0 | 0 |
| | 4 | | 0.028 | -0.159 | -0.021 |
| | 8 | | 0.066 | -0.258 | -0.029 |
| | 12 | | - | 0.015 | - |
| | 10 | | 0.018 | - | - |
| | 13 | | - | 0.139 | - |
| N ← S | 17 | Deck | - | - | -0.695 |
| | 6 | | 0.034 | -0.041 | -0.375 |
| | 16 | | - | - | -1.000 |
| | 9 | | 0.018 | -0.004 | -0.767 |
| | 7 | | 0.015 | 0.015 | -0.417 |

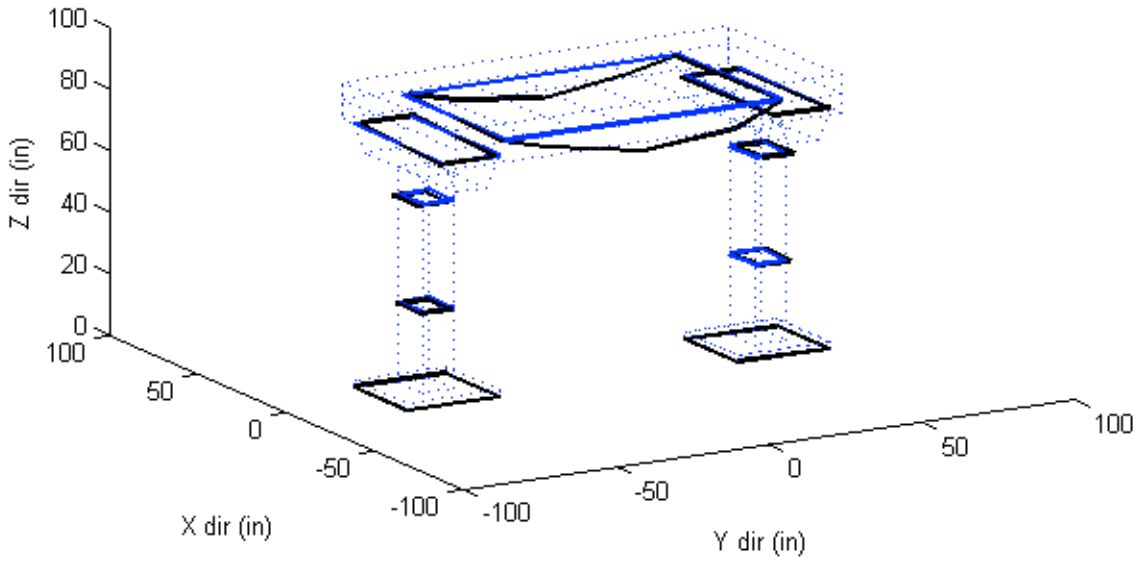

Test 18 – Lateral vibration mode

| Sensor # | | | | Modal displacement | | |
|---|---|---|---|---|---|---|
| | W → E | | | X | Y | Z |
| Top ← Bottom | 1 | | North Column | 0 | 0 | 0 |
| | 3 | | | -0.150 | 0.024 | 0.009 |
| | 5 | | | -0.648 | 0.069 | 0.018 |
| | 14 | | | - | 0.098 | - |
| | 11 | | | -0.999 | - | - |
| | | 15 | | - | 0.075 | - |
| Top ← Bottom | 2 | | South Column | 0 | 0 | 0 |
| | 4 | | | -0.250 | 0.024 | -0.001 |
| | 8 | | | -0.874 | 0.078 | 0.009 |
| | 12 | | | - | 0.109 | - |
| | 10 | | | -1.317 | - | - |
| | | 13 | | - | 0.073 | - |
| N ← S | 17 | | Deck | - | - | -0.111 |
| | | 6 | | -1.403 | 0.086 | 0.135 |
| | 16 | | | - | - | -0.109 |
| | 9 | | | -1.317 | 0.091 | 0.004 |
| | 7 | | | -1.189 | 0.109 | -0.104 |

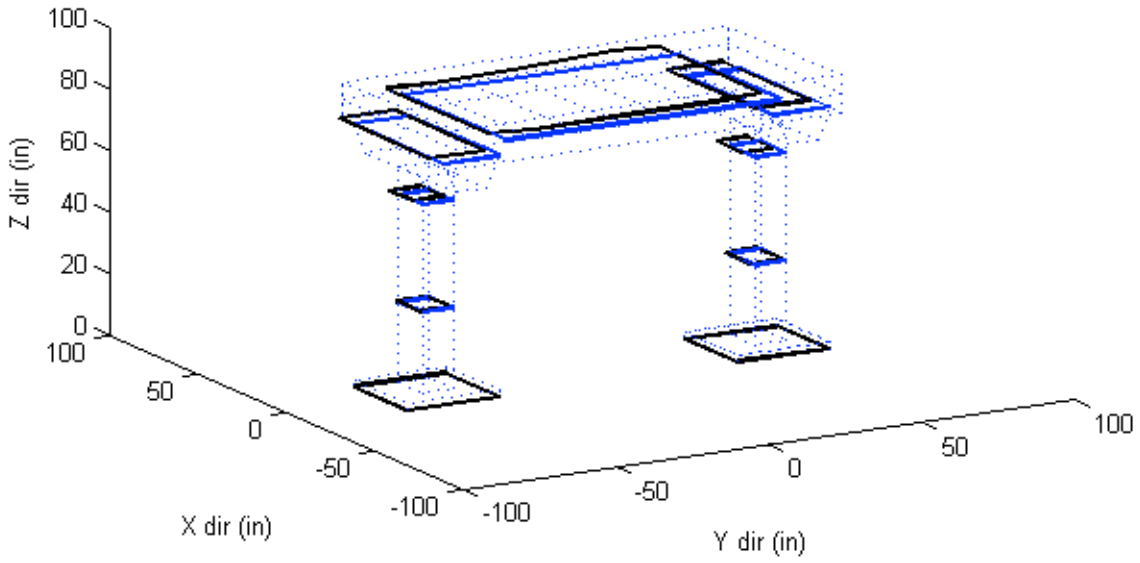

Test 18 – Torsional vibration mode

| Sensor # | | | Modal displacement | | |
|---|---|---|---|---|---|
| W → E | | | X | Y | Z |
| Top ← Bottom | 1 | North Column | 0 | 0 | 0 |
| | 3 | | -0.657 | -0.035 | 0.129 |
| | 5 | | -1.745 | 0.022 | 0.356 |
| | 14 | | - | -0.911 | - |
| | 11 | | -1.794 | - | - |
| | 15 | | - | 1.003 | - |
| Top ← Bottom | 2 | South Column | 0 | 0 | 0 |
| | 4 | | 0.450 | 0.243 | 0.089 |
| | 8 | | 1.089 | 0.261 | -0.267 |
| | 12 | | - | -0.920 | - |
| | 10 | | -0.289 | - | - |
| | 13 | | - | 1.090 | - |
| N ← S | 17 | Deck | - | - | 0.227 |
| | 6 | | 0.636 | 1.086 | -0.087 |
| | 16 | | - | - | -0.186 |
| | 9 | | -0.289 | 0.029 | 0.034 |
| | 7 | | -1.420 | -0.920 | -0.585 |

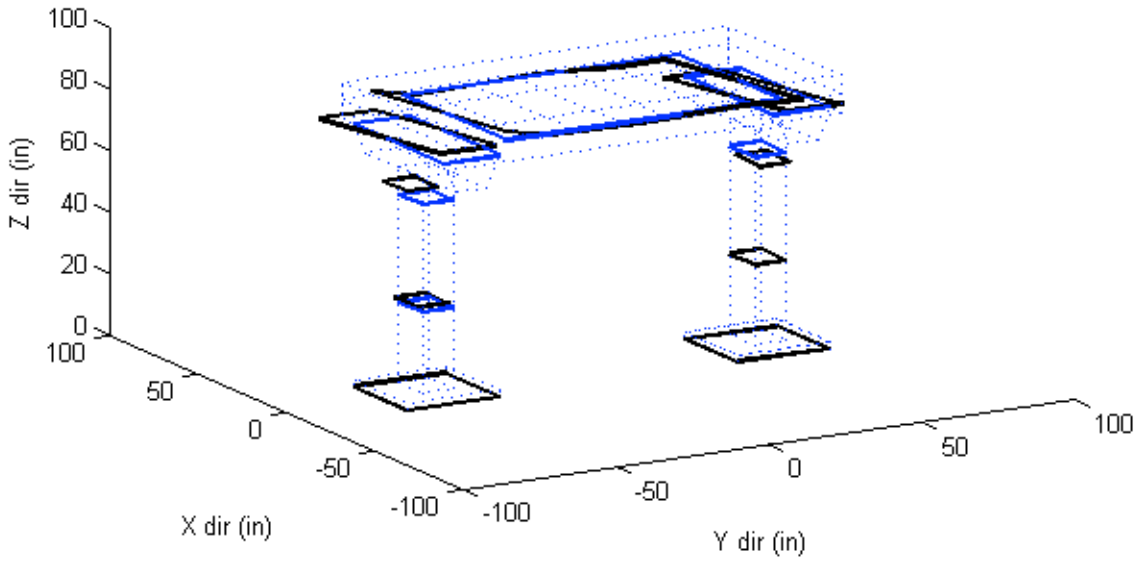

Test 19 – Vertical vibration mode

| Sensor # | | | Modal displacement | | |
|---|---|---|---|---|---|
| | W → E | | X | Y | Z |
| Top ← Bottom | 1 | North Column | 0 | 0 | 0 |
| | 3 | | 0.043 | 0.077 | -0.002 |
| | 5 | | 0.040 | 0.168 | 0.009 |
| | 14 | | - | 0.195 | - |
| | 11 | | -0.001 | - | - |
| | 15 | | - | -0.175 | - |
| Top ← Bottom | 2 | South Column | 0 | 0 | 0 |
| | 4 | | 0.013 | -0.095 | 0.019 |
| | 8 | | 0.026 | -0.161 | -0.023 |
| | 12 | | - | 0.036 | - |
| | 10 | | 0.011 | - | - |
| | 13 | | - | 0.143 | - |
| N ← S | 17 | Deck | - | - | -0.705 |
| | 6 | | 0.006 | -0.007 | -0.213 |
| | 16 | | - | - | -1.000 |
| | 9 | | 0.011 | 0.023 | -0.482 |
| | 7 | | 0.021 | 0.036 | -0.279 |